# Ice sheet melt and the Atlantic Ocean

Jelle van den Berk

**Ice sheet melt and the Atlantic Ocean**
PhD dissertation, Utrecht University, The Netherlands

Jelle van den Berk
Royal Netherlands Meteorological Institute
R&D Weather and Climate Modelling

ISBN:978-94-6419-457-9
Printed by: Gildeprint – Enschede

ICE SHEET MELT AND THE ATLANTIC OCEAN

Smeltende poolkappen en de Atlantische oceaan

(met een samenvatting in het Nederlands)

Proefschrift

ter verkrijging van de graad van doctor aan de Universiteit Utrecht op gezag van de rector magnificus, prof. dr. H. R. B. M. Kummeling, ingevolge het besluit van het college voor promoties in het openbaar te verdedigen op donderdag 31 maart 2022 des ochtends te 10.15 uur

door

JELLE VAN DEN BERK

geboren op 22 september 1981
te Amsterdam

PROMOTOREN: Prof. dr. ir. W. Hazeleger

Prof. dr. S. S. D. Drijfhout

COMMISSIELEDEN: Prof. dr. ir. H. A. Dijkstra

Prof. dr. E. van Sebille

Prof. dr. T. Eldevik

Prof. dr. D. Swingedouw

Dr. F. de Jong

## Abstract

The ocean is nestled in between the continents and exchanges heat and water with the atmosphere. The wind pushes against the water and aids the heat exchange. The Atlantic part of the ocean stretches from the Arctic in the far north to the beginning of the Southern Ocean around Antarctica, connecting these two cold areas with the warmth of the equatorial region. The ocean is not uniformly salty. Currents, evaporation and precipitation, rivers and icebergs continually change the salinity at the ocean surface and to depth. One of these currents is the so called Atlantic Meridional Overturning Circulation (AMOC) and consists of a northward flowing shallow branch and a deeper southward branch and is part of the entire Atlantic Ocean.

The AMOC is the result of the effects of wind and heat loss to the atmosphere in the cold North. The upper ocean needs to have a sufficiently high salinity for the upper AMOC branch to feed the lower branch. Under climate change the polar ice sheets will melt at an increasing rate and more freshwater will be led to the ocean surface, which leads to a freshening of the upper ocean. There is a risk that the AMOC will decrease in strength or shuts down entirely.

Melting of the polar ice sheets can be easily mimicked in climate models by adding freshwater to the ocean surface. The salt distribution changes by the currents, like the AMOC, at the surface, and eventually spreads to depth and further from the poles. The Atlantic Ocean loses salt by adjustment in the ocean salt transports through Bering Strait and the interface with the Southern Ocean. The AMOC itself remains relatively unaffected, though the connection between the shallow branch and the deeper branch changes by shifting to the North, into the Arctic.

The absence of drastic changes in the AMOC strength is remarkable when compared against with the distant past when the AMOC oscillated between vigorous and weakened states. No clear picture has emerged how such abrupt transitions in AMOC strength came about, and whether current climate change AMOC stability is at risk. What is clear is that climate models represent the AMOC and its critical transitions in various ways. The response of the Atlantic Ocean is complicated and the future of the AMOC remains uncertain.

## Samenvatting

De oceaan is genesteld tussen de continenten en wisselt warmte en water uit met de atmosfeer. De wind stuwt het water op, en helpt de uitwisseling van warmte. Het Atlantische deel van de oceaan strekt zich uit van de Poolzee in het uiterste noorden tot het begin van de Zuidelijke Oceaan rond Antarctica, en verbindt daarmee deze twee koude gebieden met de warmte rond de evenaar. De oceaan is niet overal even zout. Stromingen, verdamping en neerslag, rivieren, en ijsbergen veranderen continu het zoutgehalte aan de oceaanoppervlakte en naar de diepte toe. Eén van deze stromingen is de zogenaamde Atlantische Meridionale Omkerende Circulatie (AMOC) en bestaat uit een noordwaartse ondiepe stroom en een dieper zuidwaartse stroom en bestrijkt vrijwel de gehele Atlantische Oceaan.

Het in stand houden van de AMOC is een gevolg van een samenspel van wind en het warmteverlies aan de atmosfeer in het koude noorden. Belangrijk is dat de bovenlaag van de oceaan zout genoeg is zodat de ondiepe tak van de AMOC de diepere kan blijven voeden. Met klimaatverandering smelten ook de poolkappen en wordt er zoetwater naar de oceaan geleidt, wat tot verzoeting van de ondiepe laag leidt. Er bestaat dan een risico dat de AMOC minder sterk wordt of geheel stopt.

Het smelten van de poolkappen kan eenvoudig in klimaatmodellen worden nagedaan door zoetwater aan het oceaanoppervlak toe te voegen. De zoutverdeling verandert door de stromingen, zoals de AMOC, niet alleen aan het oppervlak, maar verspreidt zich uiteindelijk ook naar de diepte en verder van de polen. De Atlantische Oceaan verliest zelfs zout door een aanpassing van de zout transporten door de Straat van Bering en de uitwisseling met de Zuidelijke Oceaan. De AMOC zelf blijft relatief ongemoeid, hoewel de verbinding tussen de ondiepe en de diepe tak verandert door verschuiving naar het noorden, verder de Poolzee in.

Het uitblijven van drastische veranderingen in de AMOC sterkte is op zich opmerkelijk gezien het gedrag uit het verre verleden waar de AMOC oscilleerde tussen een sterke en een zwakke toestand. De invloed van zoetwater door, met name Groenlands, ijs verlies zou hier bepalend zijn geweest. Er is nog geen eenduidig beeld hoe dit soort abrupte overgangen in AMOC sterkte tot stand kwamen en of stabiliteit van de AMOC door de huidige klimaatverandering een risico is. Wel is duidelijk dat klimaatmodellen de AMOC en dergelijke overgangen op verschillende manieren weergeven. De reactie van de Atlantische Oceaan is gecompliceerd en de toekomst van de AMOC blijft onzeker.

# Contents

# List of Figures

# List of Tables

# 1 Introduction

The ocean covers most of Earth's surface and its large scale circulation affects climate and weather patterns. The ocean is affected by climate in turn and ongoing climate change also has its effects on the circulation patterns in the ocean, as well as the heat an salt that are carried along. The temperature and salinity determine the density of sea water. The density distribution of sea water is also a driver of large scale ocean circulation: the so-called thermo-haline circulation (THC). A warmer atmosphere therefore directly affects the ocean because it directly affects the thermal properties of sea water.

The sun irradiates the atmosphere and Earth's surface and through feedbacks determines its temperature (e.g. Stocker, 2011); in the past variations in solar irradiance has affected global temperature and the thermo-haline circulation of the world's ocean. In particular, it has been suggested that the periodic shifts between warm and cold (ice ages) were brought about by rapid transitions involving the thermo-haline circulation that dramatically changed the global heat distribution (see e.g. Bradley, 1999 for an introduction to paleoclimatology). Such past climate change is characterised by an abrupt reorganisation of the large scale ocean circulation by being forced across a threshold, after which a new stable state is reached (Rahmstorf, 2002).

Current changes to the atmospheric concentration of greenhouse gases (e.g. increases in $CO_2$) result in more heat being trapped in the atmosphere; this also affects the ocean and could lead to abrupt changes in circulation like in the past. The large scale circulation in the Atlantic Ocean in particular is thought to be pivotal in bringing about abrupt climate change (Intergovernmental Panel on Climate Change, 2014a).

Below, some important concepts and features of the ocean are discussed. Though the chapters that follow have been published as separate articles, and can be read independently by an informed reader, this introductory chapter provides some background to links these together.

## 1.1 The Atlantic and Arctic ocean

The Atlantic Ocean is delimited by Europe and Africa along its eastern boundary and the Americas along its western boundary. To the south we find the open ocean boundary

with the Southern Ocean, toward Antarctica. The Arctic Ocean lies to the north, and is connected to the Pacific Ocean at Bering Strait.

The ocean varies in salinity, temperature, pressure, and has persistent flow patterns (the currents). The shallow ocean layers are more active than the deep, and both the atmosphere and the land masses affect that motion. The salinity of the ocean is not everywhere the same; it is affected by the precipitation that lowers it, or the evaporation that increase it. The ocean circulation also maintains imbalances of salt; therefore, anything that affects circulation can affect the salt distribution in the ocean, and this includes the wind patterns (Stewart, 2008).

### 1.1.1 Wind-driven circulation patterns as surface currents

The ocean and atmosphere interact with each other, and the effects of one can feedback to the other. This can be directly seen in the wind-driven circulation. The wind pushes the ocean surface, and the forced currents move on the spinning Earth with the windstress curl determining whether the flow is clockwise (in the midlatitudes) or counter-clockwise (in the higher latitudes). The characteristic patterns seen in Figure 1.1 emerge primarily because of Earth's rotation leading to the Coriolis force that alter the flow path on the globe's surface (Gill, 1982; Stewart, 2008). The closed patterns are the ocean's gyres and they are constrained by the land masses that force a recirculation of the flow. There is a stark contrast between the two hemispheres; in the North Atlantic the continents impose zonal boundaries that force the circulation back onto itself, but the Southern Ocean has an unrestricted subpolar flow (blue) that goes round Antarctica. In the North Atlantic, the subpolar gyre circulation is counter clockwise and it is interrupted by Greenland and Iceland, giving it its typical shape.

With the continent in place in the west[1], further motion in that direction is blocked. A pressure gradient force, in the west-east direction, balances the flow and forces it to move along the continent: the western boundary currents.

The gyres separate and re-route surface water, but the difference in latitude also means the surface temperatures are different between the subpolar and subtropical gyres, which is important for density-driven flow.

### 1.1.2 Density-driven circulation

The North Atlantic subpolar gyre is important circulation system, not just for the surface circulation, but also for the deeper flow. The Nordic Seas and North Atlantic subpolar gyre are part of the same wind-driven gyre, but the topography of Iceland and Greenland disrupt the recirculation (Figure 1.1). The location of Greenland and the bottom topography are important determinants of the deeper circulation in particular because of their influence on the surface salinity (Figure 1.2) and heat distribution.

[1] This is not true in the Southern Ocean, and gives a dynamics similar to what we see in the atmosphere, or more saliently in the gas giants such as Jupiter and Neptune.

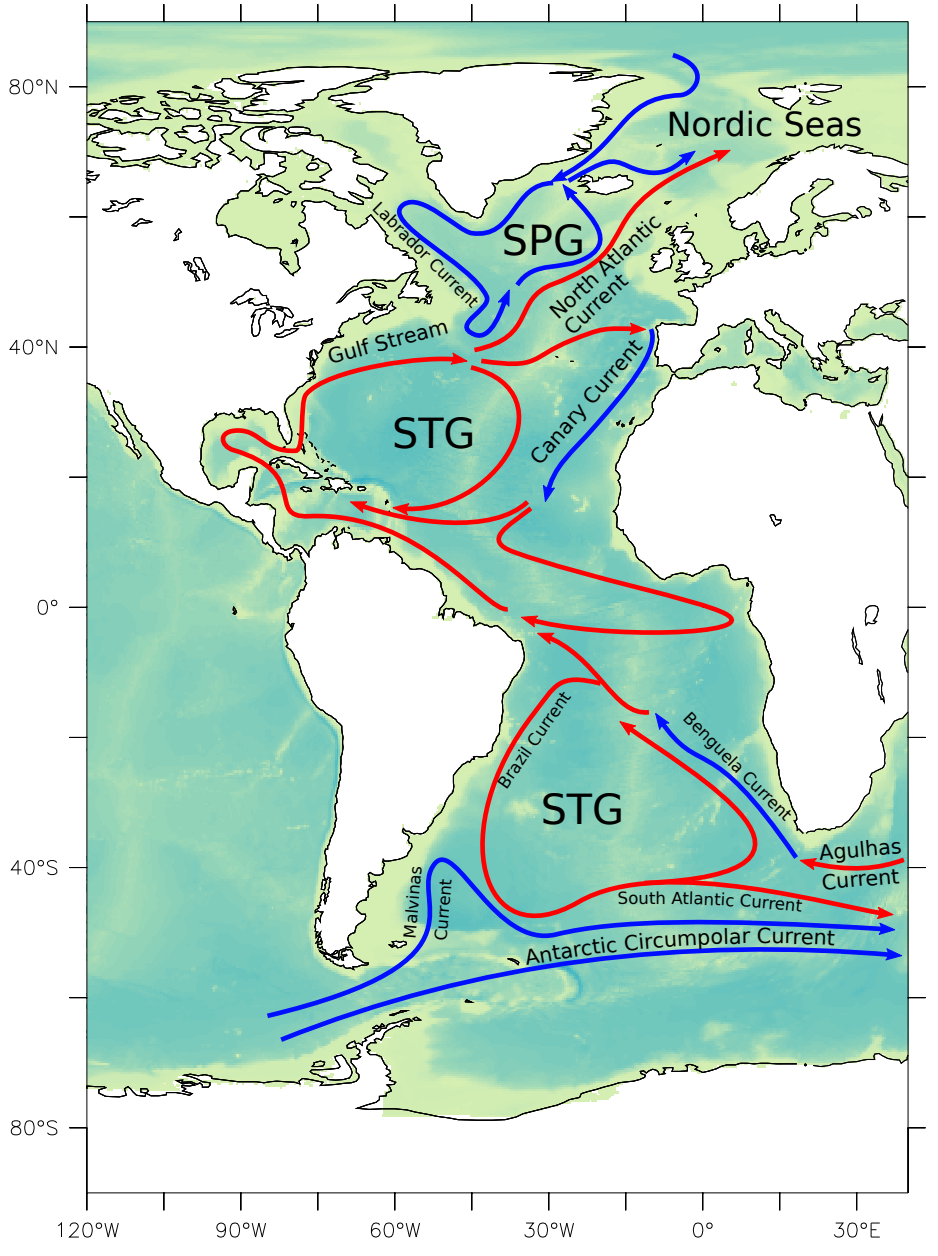


Figure 1.1: Sketch of surface currents in the Atlantic ocean. In red the warm currents and in blue the cold currents. There are threes gyre regions indicated, the cold subpolar gyre (SPG) in the North Atlantic and for each hemisphere a Subtropical gyre (STG). The southern hemisphere counterpart tot the North Atlantic subpolar gyre is the Antarctic Circumpolar Current (ACC) which is not zonally constraint by a continent. Drawn after Figure 8.8 in Garrison (2011) and Figures 9.1 and 9.2 in Talley (2011).

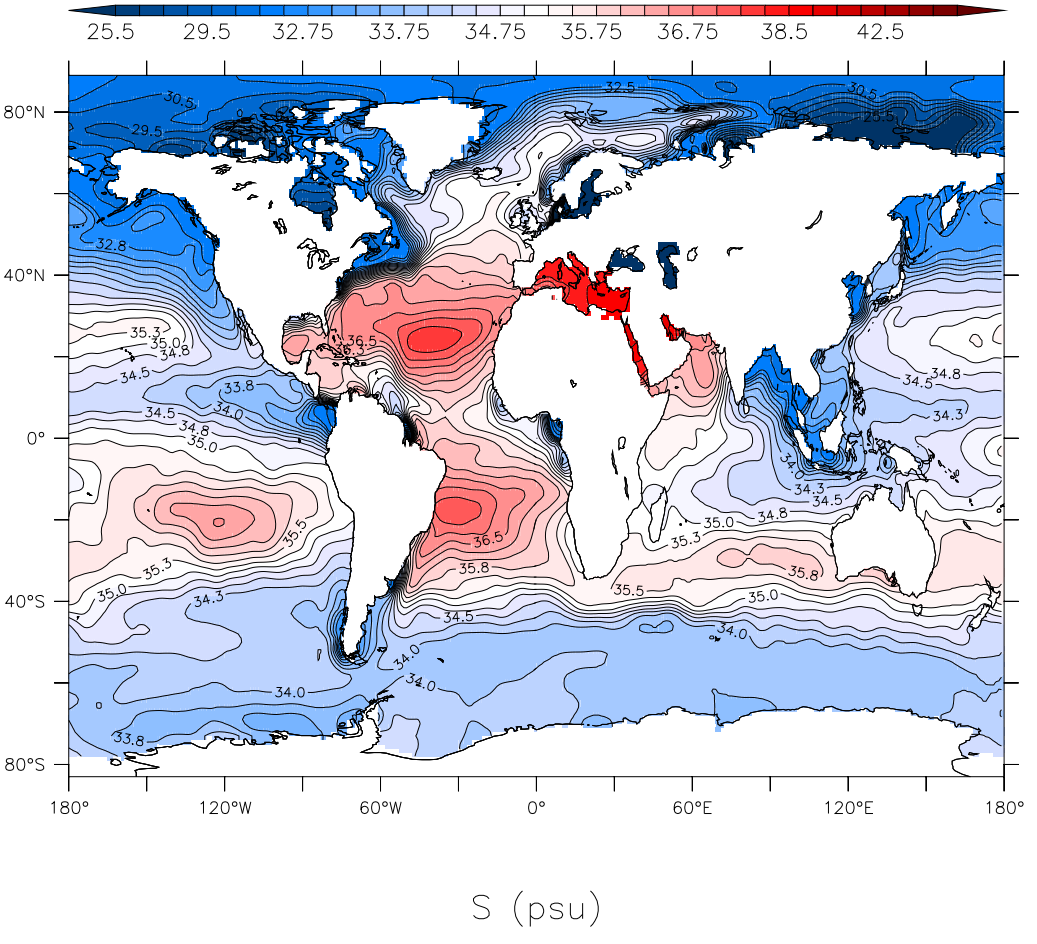


Figure 1.2: Depth-averaged salinity of the world ocean. The Atlantic subtropics are saltier than the rest of the Atlantic (the reference white-point has been chosen to highlight this). Based on the mean of the twentieth century EN4 reanalysis data salinity profile data (Good et al., 2013; Gouretski and Reseghetti, 2010).

The North Atlantic subpolar gyre sea water loses heat to the cold atmosphere, increasing its density (a buoyancy loss) of the surface water. The surface layer becomes denser than the water beneath it, which is an instability that is removed when the density of the water column is homogenised. This mixing of stratified layers is called convective overturning and the material properties of sea water are very important for this process, because temperature and salinity determine the density of sea water (the relation between temperature and salt to density is not simple). If the mixing reaches into the deeper layers, such as in the North Atlantic high latitudes, this mixing is called deep convection. Deep convection means formation of water with higher density due to heat loss to the atmosphere (which is very cold and dry locally—in particular during winter—because of low flux density of irradiation: there is a net loss of radiation to space) is transferred to the deeper ocean. If there is a convergence of flow, such as the inner subpolar gyre, or its northward flow against the northern boundary (particularly Greenland), convective overturning will result in a sinking of water (conservation of mass). The boundary currents in the Labrador and Irminger Seas in are therefore thought to be regions where this deep water formation (DWF) takes place (Spall and Pickart, 2001; Spall, 2008). This pile-up cannot continue unrestricted, a pressure gradient force against the topography at depth will redirect the sinking. The result is the deeper water shows a preference in the rotating frame of the spinning Earth to move toward the western boundary (because of the mirror-image situation of the northern vs the southern hemisphere, this is true on both sides of the equator but due to the land masses an asymmetry is introduced). A southward flow, pressed against the American continent, emerges (Stewart, 2008).

This is a very rough description of how the deep western boundary current is sustained by high latitude buoyancy loss. With more freshwater the density of sea water decrease because the salinity lowers. The high salinity water needed comes from the South Atlantic and is transported north, along the wind-driven currents. A large part of this salty water comes from the Indian Ocean where evaporation removes a lot of the freshwater, increasing the salinity (Stewart, 2008).

### 1.1.3 The Atlantic Meridional Overturning Circulation

The Atlantic Meridional Overturning Circulation (AMOC) is a northward flow of warm, saline waters in the upper 1 kilometre, and a cold, slightly less salty return flow at depth and is connected to the processes described above. The AMOC transports a considerable amount of heat from the southern hemisphere to the northern hemisphere, in particular toward the European continent. The Gulf Stream is part of the AMOC and affects the European weather in particular (Palter, 2015) as well as making the European climate more clement overall.

It was once thought that the deeper ocean is more or less static, with very little motion below the wind-driven layer. Measurements in the 1800s changed that view when it became apparent that there is both vertical and horizontal motion in the deep ocean (Lenz, 1845). (See Richardson, 2008 for a history of the AMOC.) Water moving north

from the Southern Ocean to the Arctic, across the Atlantic, travels south again at greater depth. The northward flow is primarily wind-driven, but the deeper flow cannot be directly connected to the winds because the wind-driven layer is at most a few hundred metres thick.

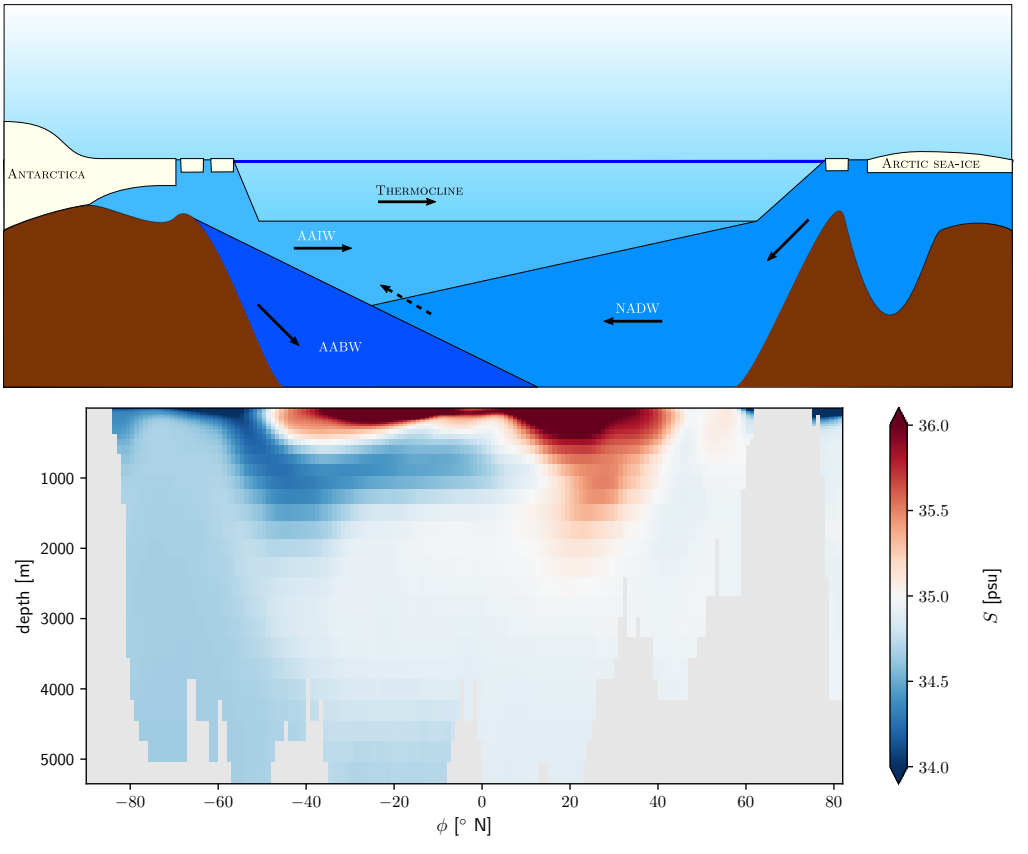


Figure 1.3: Top: sketch of latitudinal sections of the Atlantic and the relevant water masses. North Atlantic Deep Water (NADW) and Antarctic Intermediate Water (AAIW) compete with each other. Bottom: salinity along the 30°W section along the Atlantic (mean of the twentieth century EN4 reanalysis data; Good et al., 2013; Gouretski and Reseghetti, 2010).

The winds over the Southern Ocean drive a surface flow northward, resulting in the pulling up of deeper waters (water is pushed in the horizontal and needs to be replaced by water from the deep). This effect might be the main driver of the volume exchange between the Antarctic Intermediate Water (AAIW) and the North Atlantic Deep Water (NADW) (Nikurashin and Vallis, 2012), and would therefore be a driver of the AMOC (Marshall and Speer, 2012). The amount of salt that enters and leaves the Atlantic is also an important variable because of its potential effects on the thermo-haline circulation.

Warm salty water from the Indian Ocean makes its way into the South Atlantic through the Agulhas Current into the South Atlantic subtropical gyre (Figure 1.1). From the Indian Ocean salty water moves past Cape Agulhas into the Atlantic Ocean, under strong influence of the westerly winds that control this Agulhas 'leakage'. On the western side of the South Atlantic, colder water arriving through Drake Passage also is taken up in the gyre. These surface currents are important contributors to the shallow thermocline water that move north in the South Atlantic (Figure 1.3). In this thesis, there is little focus on the Pacific Ocean route, but more on Indian Ocean contribution; although the relative importance for the Atlantic salinity budget of both is not yet clear from observations (Drouin and Lozier, 2019). The Atlantic salt budget is important because North Atlantic contains the downward flow of the AMOC and connects its surface branch to the deeper branch.

In the North Atlantic subpolar gyre, the salty water loses heat tot the atmosphere and its density increases. In the subpolar gyre region deep water formation (DWF) takes place during the winter months as the water column becomes unstable because the density of the top layer increases sufficiently to become larger than the density of the deeper layer. This is mainly due to the difference in salinity of the two layers. Convection sets in, and more NADW is formed. This is a 'pushing' of the overturning due to the deep water formation. Both the pulling effect in the Southern Ocean and the pushing in the North Atlantic sustain the overturning circulation. The relative importance of the drivers of the AMOC is, however, not a settled matter; see Kuhlbrodt et al. (2007) for a discussion.

Heat (thermo) and freshwater (haline) fluxes alter ocean water density, resulting in a buoyancy flux at the surface and also drives the circulation. The thermo-haline circulation is an inseparable part of the overturning, but is not directly driven by windstress. There are several types of freshwater fluxes that can affect the buoyancy. In Figure 1.3 two water masses are depicted that are part of the overturning, North Atlantic Deep Water, and Antarctic Bottom Water (AABW). The former is sourced in the North Atlantic subpolar gyre and Nordic Seas, the latter primarily in the Weddell Sea near Antarctica. The NADW spreads southward as the deep western boundary current (not depicted) and in the Antarctic Circumpolar Current strong winds pull water from the deep. These two water masses are in competition in the sense that there is production of each in opposite hemispheres that flow into the Atlantic at depth as buoyancy-driven flows. At the surface, winds also affect the currents and drive warm, salty water northward again (Rahmstorf, 2000; Kuhlbrodt et al., 2007), the wind-driven gyres are a part of this circulation. This very rough conceptual image of the Atlantic overturning can be kept in mind during later discussions about the AMOC.

The Atlantic is also connected to the Pacific Ocean through Bering Strait, with fresher Pacific water entering the Arctic. To the south, the South Atlantic is connected with the Southern Ocean, which is in contact with all the major oceans. At the edge we find the most southern tip of Africa, Cape Agulhas the latitude of which is a boundary of the Atlantic. Any attempt to consider the Atlantic Ocean on its own is therefore always an oversimplification, and at the very least these 'interfaces' with the rest of the world

ocean need to be considered. Figure 1.4 shows that salinity flux at the section at the latitude of Cape Agulhas is a balance between the northward flowing upper limb and the southward flowing NADW in the lower limb. The southward flowing NADW is slightly more saline and the northward flowing upper limb has an AAIW component that is slightly fresher than the averaged over the section. The balance between these two components determines whether the circulation imports or exports salt (or equivalently exports or imports of freshwater) into the South Atlantic (see Weijer et al., 2019 for a review and a details relating to Figure 1.4).

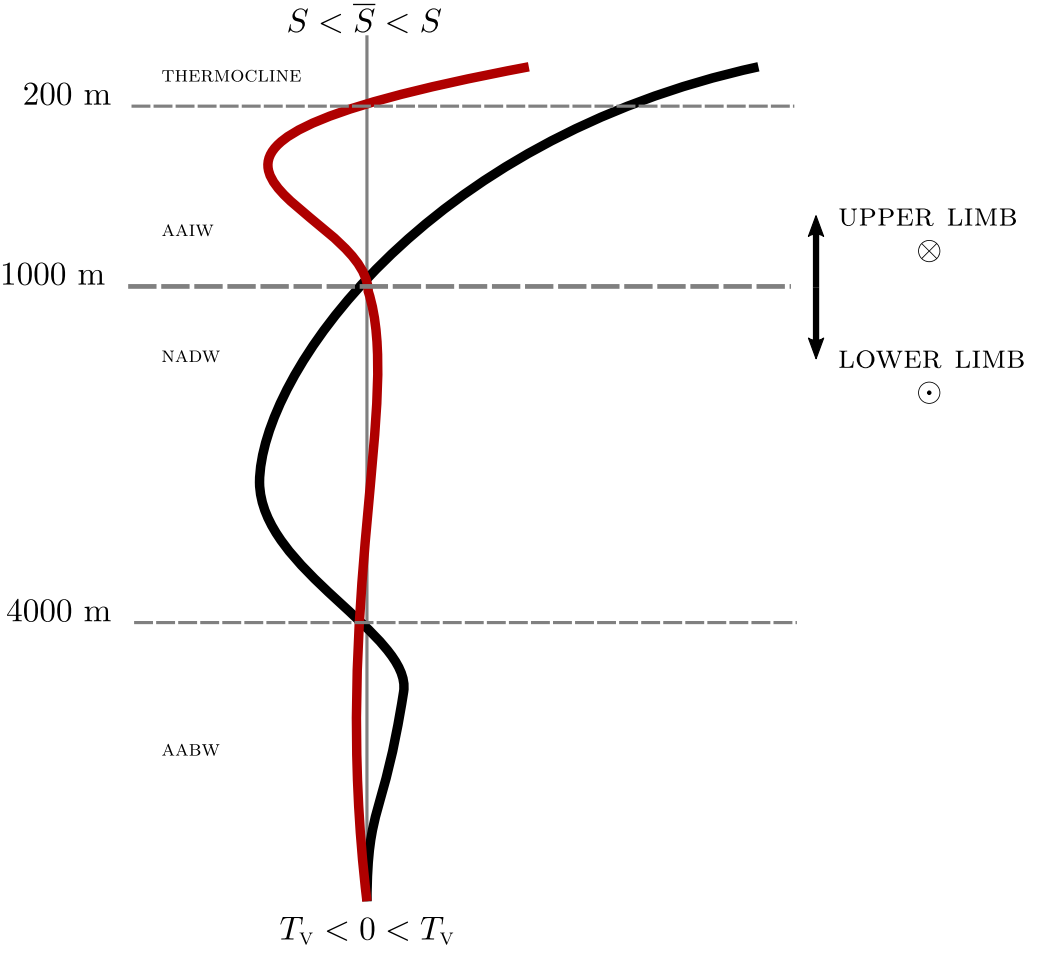


Figure 1.4: Sketch of the salinity ($S$, red) and zonally integrated transport ($T_V$, black) at the Atlantic zonal section at the latitude of Cape Agulhas (34°S). The depths are indicative. To the left of the central values (average salinity and transport = 0) are the water masses labelled. The overturning limbs are indicated on the right. Depending on these profiles, the overturning imports or exports salt from the Atlantic. (After Figure 5 in Weijer et al., 2019.)

Within the Atlantic there are opposing freshwater transports as, for instance, seen in a reanalysis dataset using a quarter degree eddy-permitting ocean model forced with ERA-Interim meteorology from 1989-2010 (Figure 6 in Valdivieso et al., 2014). A total transport of 0.35 Sv enters the South Atlantic compared to the Bering Strait throughflow, and consists of compensating components. One component is 0.1 Sv being transported in the opposite direction (towards the south pole) by the overturning circulation: an export of freshwater from the Atlantic. The gyre circulations contributes 0.25 Sv northward, eddies transport another 0.1 Sv northward, and there is a northward throughflow of 0.1 Sv (= 0.45 Sv and the opposite 0.1 Sv makes 0.35 Sv).

A study by Talley (2008) calculates comparable meridional freshwater transports from measurements of absolute geostrophic velocities and Ekman transport. Freshwater transports are given at 32°S (a few hundred kilometres north of the latitude of Cape Agulhas) and show a total freshwater inflow of 0.28 $\pm$ 0.04 Sv relative to the Bering Strait throughflow as the sum of 0.06 $\pm$ 0.02 Sv freshwater through Bering Strait and 0.20 $\pm$ 0.02 Sv by the South Atlantic gyre circulation. The overturning component can be taken as the sum of three nearly cancelling conversions of water masses into the NADW layer (a total of 0.02 $\pm$ 0.02 Sv); the (saline) Benguela current surface water removes (-0.05 $\pm$ 0.01 Sv), and the (fresh) AAIW (0.01 $\pm$ 0.01 Sv) and AABW (0.01 $\pm$ 0.01 Sv) add freshwater to the NADW from the Southern Ocean, leaving the NADW on the Southern Ocean side as a very small component in Atlantic freshwater budget. However, no eddy freshwater transport can be derived from this calculation which is estimated to be of comparable magnitude to the overturning component in Valdivieso et al. (2014). The quantities of the components that determine the freshwater balance in the South Atlantic are therefore uncertain. The results of Talley (2008) indicate the NADW freshwater balance is closed within the Atlantic and Arctic. The results of Valdivieso et al. (2014) indicate a coupling with the Southern Ocean is needed to do so.

The chapters that follow are about salt, where it goes when the polar ice sheets melt under the projected climate change, and how ocean circulation—in particular the AMOC—is affected. The remainder of this chapter will provide some background to the processes involved in climate change and also provides some context for the results presented later.

## 1.2 A changing climate is a changing ocean

A high level in $CO_2$ made Earth a balmy place millions of years ago (the Cretaceous period) with tropical forests on (what is today) Antarctica (Falcon-Lang and Cantrill, 2001). The sea-level was as much as a hundred metres higher than today because the ice-caps were not there and $CO_2$ levels were higher (Foster et al., 2017; Bradley, 1999). The sea-level reached even lower levels than today (Murray-Wallace and Woodroffe, 2014). This situation was a reality a few tens of thousand of years ago during the last ‘ice age’.

Our current living conditions still resemble this glacial period more than the warmer period that came before.

The level of atmospheric $CO_2$ can rise by, for instance, a release of carbon sequestered in the surface (Lee et al., 2013) or 'outgassing' by the ocean (Lauderdale et al., 2016). The latter can occur when the ocean warms and its capacity to absorb $CO_2$ diminishes. There is therefore a positive feedback between ocean warming and atmospheric $CO_2$ increase. Through sea level rise, the surface area of land for vegetation to grow changes. With a higher sea level, there is less land, and with a lower sea level there is more land. Vegetation takes up carbon and therefore adds another positive feedback between the ocean and atmospheric $CO_2$. Processes internal to the climate can lead to run-away ice growth due to excess precipitation on, in particular, Antarctica and the climate changes to a much colder state. These are examples of how the ocean has been important in past switching between climate states.

An increase in gases that alter the radiative properties of Earth's atmosphere ('greenhouse gases') can shift conditions more in the direction of a warm Earth. A similar process is ongoing today by anthropogenic $CO_2$ emissions over the past century and a half at a rate faster than ever occurred in the past. This can be seen in Figure 1.5 where the last 50 million years of $CO_2$ and temperature are shown. The last 800 thousand years can be reconstructed from ice cores (Jouzel et al., 2007; Bereiter et al., 2015; Brook and Buizert, 2018) and oxygen isotopes (Lisiecki and Raymo, 2005) and the most recent measurements are taken directly from the atmosphere (Rohde and Hausfather, 2020; Meinshausen et al., 2017; Tans and Keeling, 2021; Keeling et al., 1976). The record before 800 thousand years ago has greater uncertainty (not plotted) and the $CO_2$ values shows are from an optimal fit (after Loess filtering, see Foster et al., 2017) and deviates from the temperature record (Zachos et al., 2008; Lisiecki and Raymo, 2005). No ice core records are available before approximately 1 million years ago and proxy data from fossil plant remains are used and have wider measurement spreads that lead to greater uncertainty with age (tens to hundreds of ppm $CO_2$ as seen in Foster et al., 2017). Glacials and Earth's precession in agreement with timescale of 30k years (Jouzel et al., 2007); older measurements show values averaged on even larger timescales [2].

The striking difference between past variation and the current increase in $CO_2$ is the rate at which this change occurs. Where past glacial-interglacial periods saw adjustment on thousands of years, the change in $CO_2$ over the pas hundred years already exceeds the past changes (current levels of $> 400$ ppm $CO_2$ have not been seen in millions of years—see Figure 1.5). We therefore cannot simply look to the past to predict the future: the climate currently adjusts on much shorter timescales than it has had to do ever before and the effects of systems with greater inertia, such as the ocean, are simply unknown. The immediate effect on the atmosphere, on the other hand, is clear.

[2]The ice cores variation was matched with oxygen isotope variation (Lisiecki and Raymo, 2005) records ($\times$ 0.5 to scale to global values from a fit) and mean global value to recent values (14.1), from Rohde and Hausfather, 2020 (14.774). Hansen et al., 2013 gives a prescription to match (marine) isotope records from the distant past (Lisiecki and Raymo, 2005 and Zachos et al., 2008) to temperature.

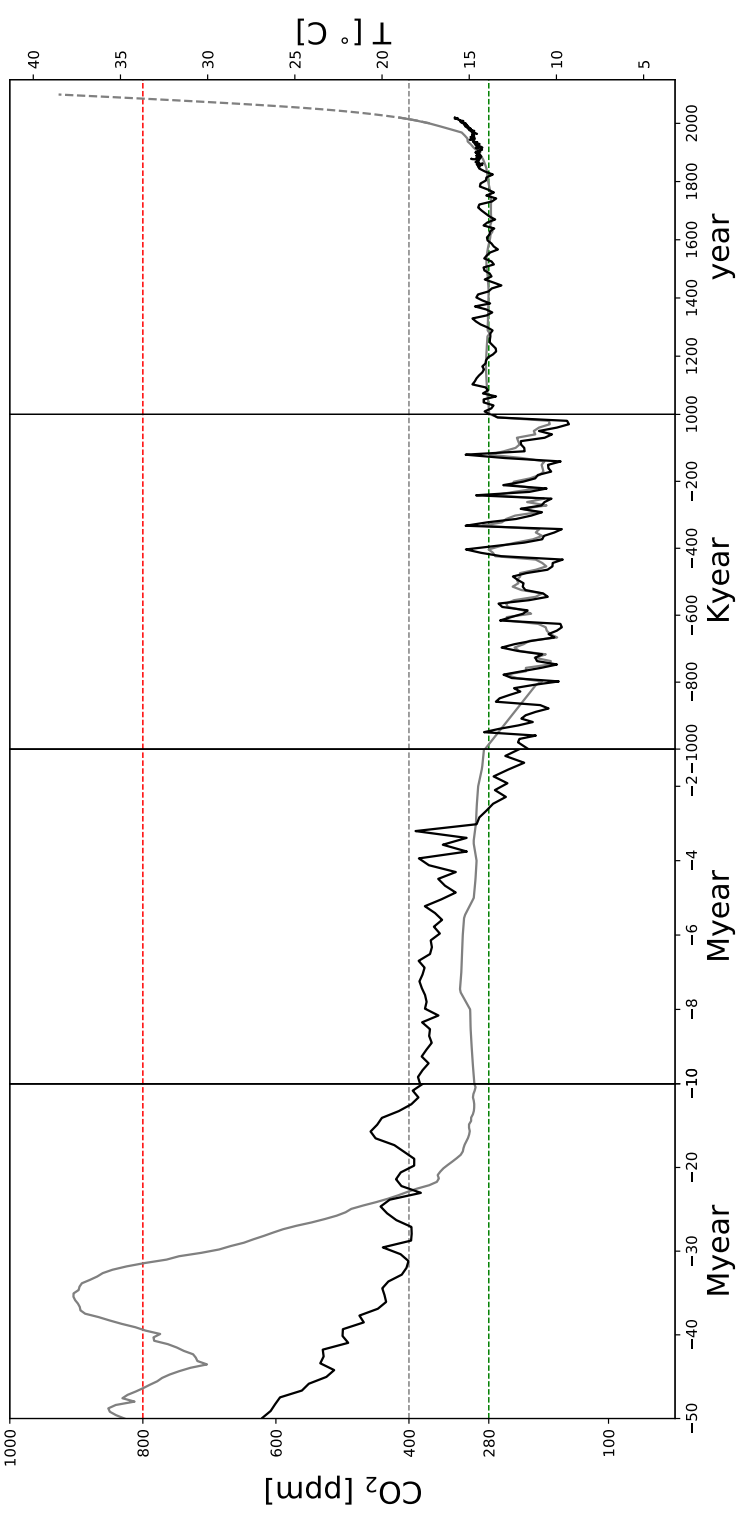


Figure 1.5: The last 50 million years has seen levels of $CO_2$ and temperatures above and below current values. Black lines show the global annual mean temperature record en grey lines the $CO_2$ record (dashed line is the RCP8.5 projection).The four panels shown span the 50-10 million years ago, 10-1 million years ago, 1 million - the year 100, and the year 1000 to present (hence the differences in scale on the x-axis). The green dashed line indicates the historic mean $CO_2$ value of 280 ppm, and the red dashed line 400 ppm $CO_2$.

An increased $CO_2$ concentration in the atmosphere makes it more opaque to infrared radiation in its absorption bands. This only leads to a noticeable change in the higher atmosphere, however. The mean free path of infrared radiation in the, relatively, thick lower atmosphere is quite short. It is only when density falls sufficiently that the mean free path becomes long enough for the atmosphere to become transparent to this radiation (e.g. Liou, 2002; Hartmann, 2016). With more $CO_2$ the altitude where this occurs increases (Figure 1.6). Radiation is then lost to space from an—on average—higher altitude, where it is colder. The amount of energy lost then becomes less and the effective temperature of Earth rises—this leads to a higher temperature in the lower atmosphere (Vallis, 2019). Higher temperatures in the lower atmosphere lead to smaller temperature difference with the seawater, and the atmosphere will absorb less heat from the ocean. The ocean stores more heat with a greater radiation imbalance at the surface and has been a large factor in mitigating the warming.

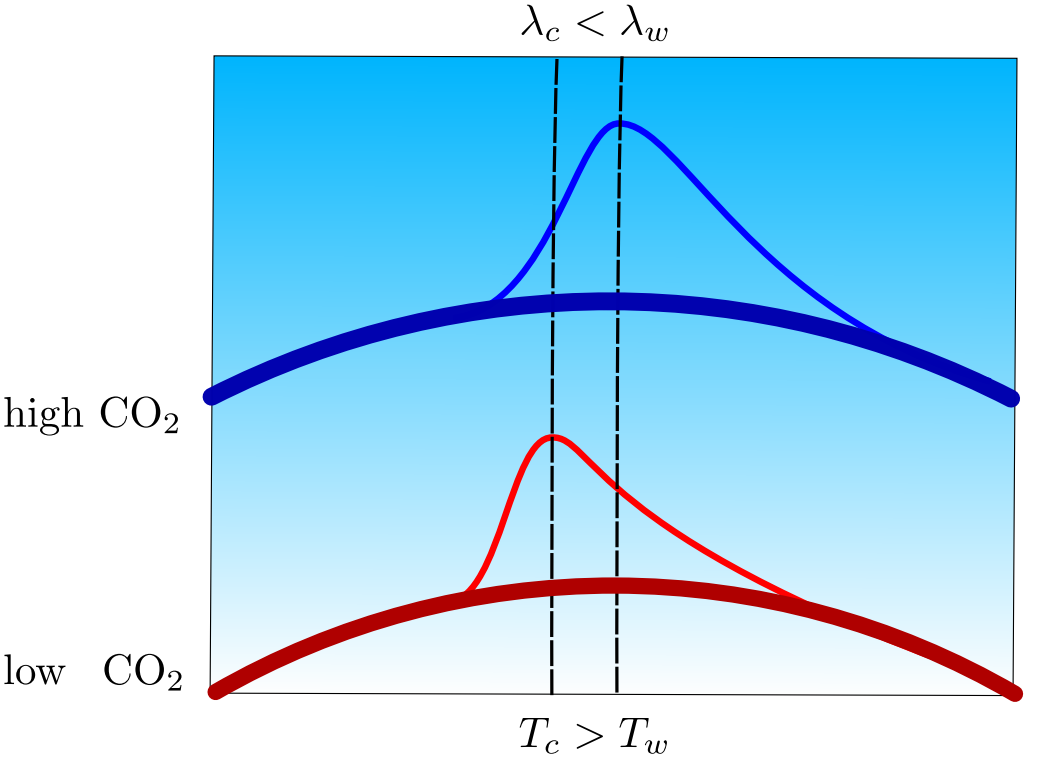


Figure 1.6: Sketch of the change in radiative characteristics of the atmosphere. As $CO_2$ increases the optical depth of the atmosphere decreases, it becomes more opaque. The characteristic height at which long wave radiation escapes to outer space increases. At greater height the temperature is lower ($T_c > T_w$) and the black-body radiation curve has its mode at longer wavelength ($\lambda_c < \lambda_w$) and effectively radiates away less heat.

The ocean is affected in more ways than just the changing sea level when the atmosphere warms. Also, the ocean circulation connects with the atmosphere in different ways. The ocean has absorbed most of the increased heat trapped by Earth's atmosphere and a third of the $CO_2$ emitted so far (Khatiwala et al., 2013; Von Schuckmann et al., 2020). The amount of heat continuing to be absorbed and released is, then, important to the heat budget of the atmosphere and consequently on land. The ocean's heat capacity is, however, larger by three orders of magnitude and over 90% of the warming so far has been absorbed by the ocean (Intergovernmental Panel on Climate Change, 2014b).

A large heat capacity also means the deep ocean takes up heat over a longer timescale, leading to a greater temperature gradient with the deep from surface heating (stratification, with lighter water at the top and denser water below). During the past 50 years the stratification of the ocean has increased (Li et al., 2020). An increased stratification shields the deeper ocean from the shallow layers by inhibiting the vertical exchange of, among others, heat and $CO_2$. The amount of heat that needs to be lost to the atmosphere to reach the same buoyancy loss in the deep water formation regions then increases. Should the ocean warm up everywhere at the same rate, the amount of heat that needs to be lost would remain more or less the same (from near-linearity in the density function). It is therefore the ocean that determines the longer term climate response; and increasing our understanding of its possible future state is important to understand the effects of global climate change.

Forcing the climate will change the state of the ocean, with different regions seeing different effects. In Figure 1.7 this is illustrated by showing the changes in water masses in the $(S, \theta)$. The bottom-left panel shows a colour-coding of ocean regions and in the top panels the distribution on 2005 (left) and 2100 (right) in the coupled climate model (CCM) EC-Earth when forced with the RCP8.5 emission scenario. The Arctic shows a depletion of very cold water, but the Southern Ocean appears relatively unaffected. Observations in the Beaufort Gyre and Chukchi Sea already show warming and increased sea ice loss during the past decades (Timmermans et al., 2018).

Figure 1.8 shows the $(S, \theta)$ changes in terms of volume. The top panel shows the state in 2005 with the signature 'rivers' of deep water masses in deep purple (with large volume). The bottom panel shows the difference with the state in 2100 with blue indicating a reduction in volume and red an increase. Warming shows itself as a shift upward in the diagram; changes in salinity are a sideways shift. The high volume water masses are reduced in volume due to warming, but also salinity changes. Increases are typically in water masses closer to the surface (low volume). Investigating where and how changes in, especially, salinity come about in the ocean under climate change is important to understand the long term effects of climate change. The effects of polar ice sheet melt is lacking in Figures 1.7 and 1.8, which might be an important driver of ocean change.

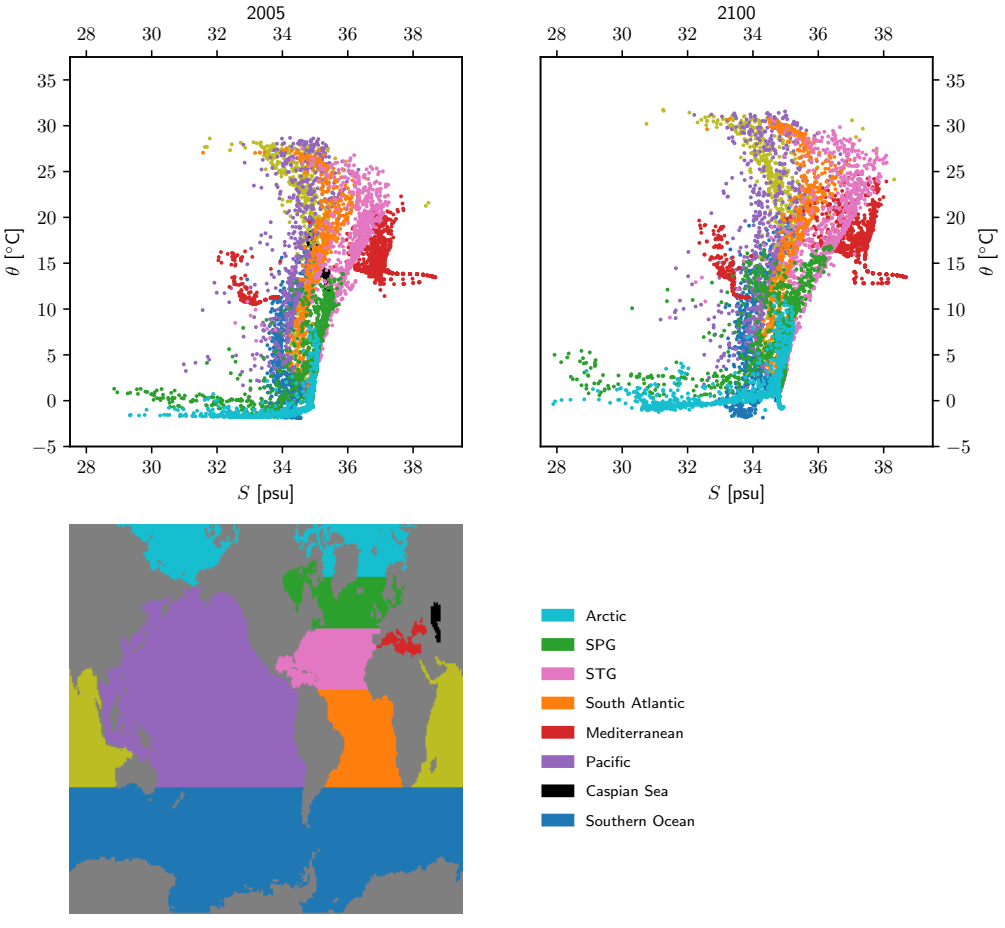


Figure 1.7: Scatter diagram of water masses in the $(S, \theta)$ plane from EC-Earth under RCP8.5 forcing. The colour coding refers to the division of the world ocean (extending to depth) in the lower left panel on the EC-Earth model grid. The top left panel shows the annual mean distribution in 2005, and the top right its counterpart in 2100. Up to 1000 randomly selected values are shown for each division.

### 1.2.1 Meltwater scenarios

Higher surface temperatures increase the melt rate of the ice sheets. When the climate is balanced the precipitation that increases the ice sheets mass is in equilibrium with the mass loss. Warmer ocean water increases the melt rate at the base of the glaciers and ice sheets at the pole: the basal melt. This freshwater loss is taken up by the ocean. The ice can also melt directly and flow into the ocean—this is called run-off. A third form of mass loss has to do with the glaciers and ice sheets breaking apart. This can occur

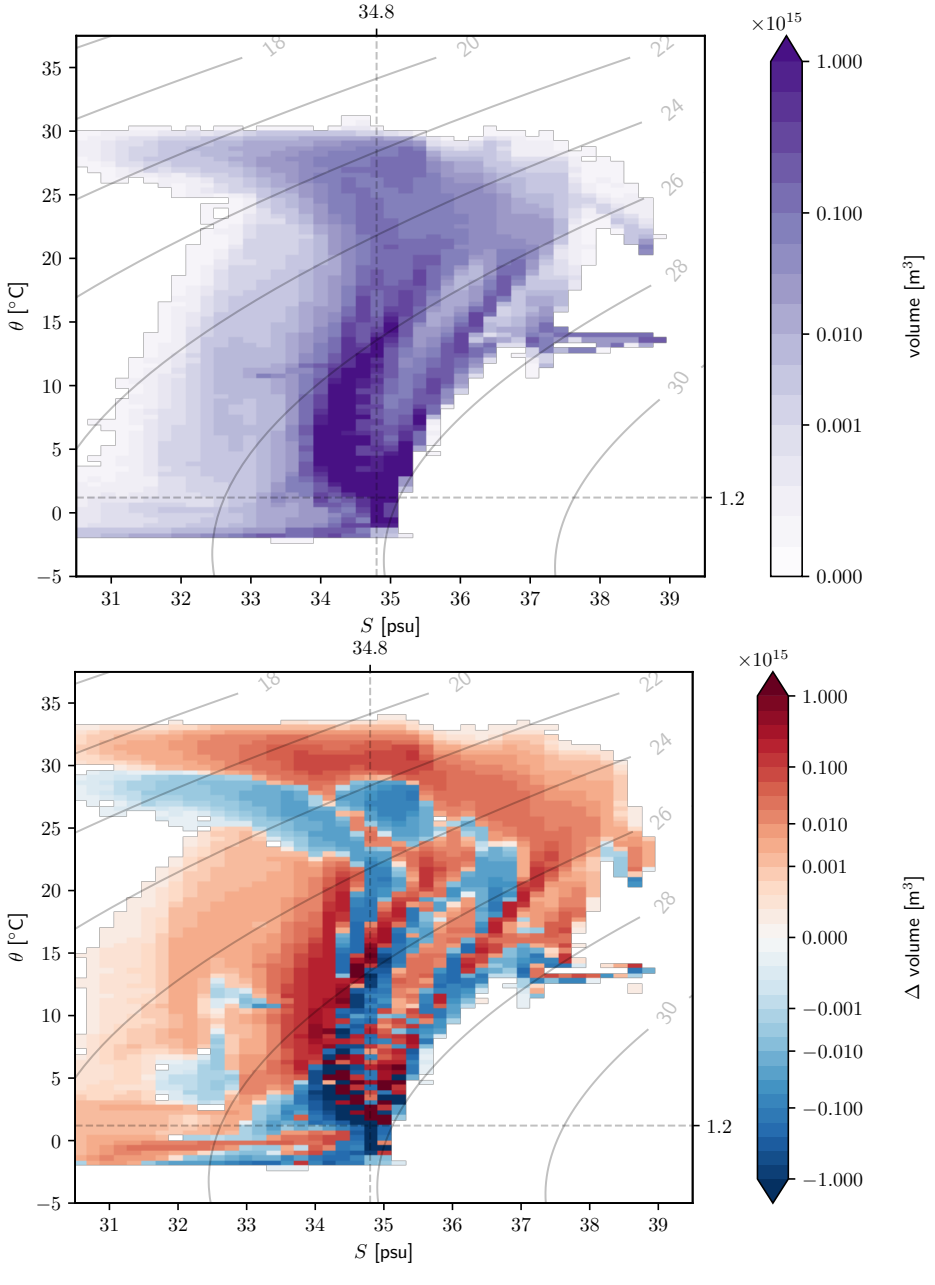


Figure 1.8: Top: volume distribution of water masses in the $(S, \theta)$ plane from EC-Earth (annual mean 2005). Bottom: Difference in volume distribution of water masses in the $(S, \theta)$ plane from EC-Earth between 2100 and 2005. Red indicates an increase in the type of water, and blue a decrease. In both panels dashed lines indicated the most common water mass type (cold, deep water) and grey lines indicate $\sigma_0$ density classes.

rapidly with large chunks of ice plunging into the ocean as icebergs. The West Antarctic Ice Sheet (WAIS) in particular is susceptible to these sudden events because there is little bedrock to check the sliding ice as the meltwater lubricates the grounding line (Joughin et al., 2014). Observations (Figure 1.9, Helm et al., 2014) show that the elevation of the Greenland and Antarctic ice sheets have decreased in the last decade; that is, the mass loss has increased. Recent observations (Shepherd et al., 2019; Sørensen et al., 2018) indicate an increasing imbalance in the Antarctic and Greenland ice sheets.

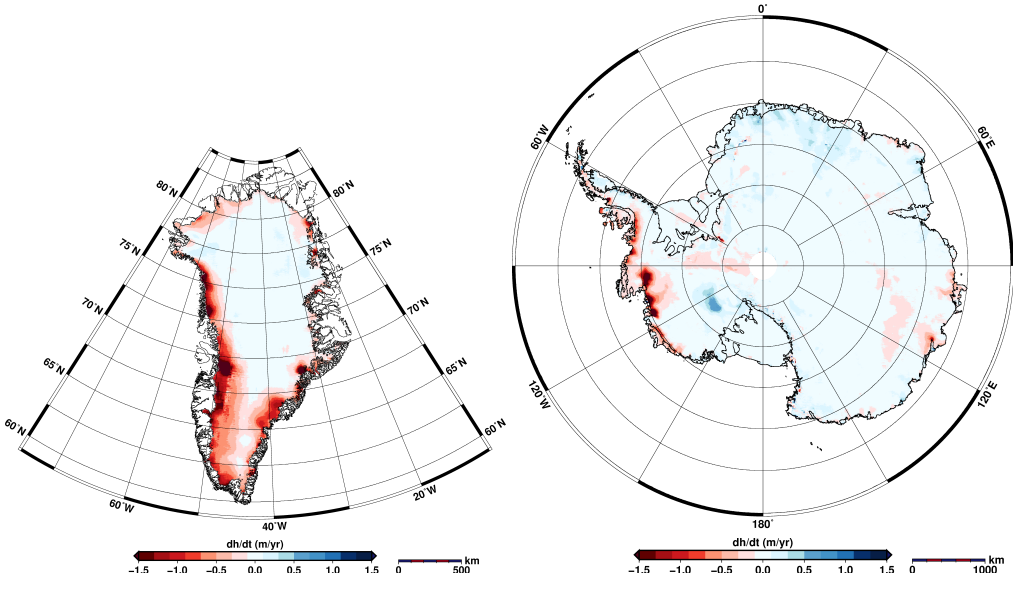


Figure 1.9: Map of elevation change between January 2011 and January 2014 for Greenland (left) and Antarctic (right) indicating ice sheet mass loss (from Helm et al., 2014). Measured with ESA's Cryosat.

Most CCMs do not model ice sheet mass loss, and the CMIP set of experiments do not have them as a requirement (Taylor et al., 2012). Clearly, this is a deficiency. It cannot be easily addressed, however, because an ice sheet model greatly adds to the complexity of the climate simulator and it should also model the past observed mass loss to be considered realistic and this adds to the difficulty in 'tuning' the parametrisation of a CCM to accurately model the current climate. Scenario story lines about the polar mass loss can help in a similar way the emission scenarios help with modelling future climate change. Although it is not known where and how much mass loss will occur, anticipated events that are part of change scenarios constrain quantitative projections into the future. This is true for emission scenarios and also for polar melt scenarios.

The collapse of the WAIS is such a story point that drastically increases the amount of freshwater added to the ocean surface in a short amount of time. The collapse of an entire Antarctic ice sheet is an abrupt event and will instigate other change, in particular lowering the surface salinity of the ocean, which may trigger further change that can also

be abrupt in their transition time. The weakening, and possible collapse, of the AMOC is one of them. The mechanism can directly affect the AAIW formation by increasing buoyancy in its formation regions; or, indirectly, through the salt advection (transport by the ocean flow) to the north and inhibiting deep water formation of the NADW in the North Atlantic subpolar gyre and Nordic Seas regions. This is one of the reasons why these mass loss events should be taken along in climate simulations, and they are an important source of uncertainty that have been largely overlooked.

### 1.2.2 Abrupt changes

The current climatological epoch is called the Holocene (from 10.000 years BCE), and has been a very stable era. There have not been any cataclysmic events such as floods (the draining of lake Agassiz into the Arctic is thought to have affected the AMOC before the Holocene—Murton et al., 2010), droughts (earlier droughts seem to have guided early human migration from Africa—Scholz et al., 2007), or super-volcano eruptions that shroud the entire planet in volcanic ash and dust (Krakatoa in 1883 produced a Tsunami, but did not have such far reaching global effects as, for instance, the volcanic eruption in Yellowstone 640 thousand years ago; see Chang et al., 2007). It is therefore not surprising that civilisation progressed rapidly, setbacks were minimal and environmental changes gradual.

Rising $CO_2$ could lead to conditions similar to several million years in the past, during the Pliocene (3 million years ago, Bartoli et al., 2011). Current changes, however, are more rapid that ever seen before. Any (physical) adjustment that results from this change would take place much faster than previous climate changes. They will be fast, not just on geological timescales, but also on biological timescales. The biosphere, including humanity, would see the world change within only a few generations—more abrupt than ever before—with evolutionary adaptation being unable to keep up. There is a risk of Earth rapidly transitioning to a new climatic state and the ocean might be instrumental in this process. The Atlantic overturning is one of the 'tipping elements' listed in Lenton et al. (2008) and its collapse, or 'tipping', to another stable state would mean little to no northward transport and disrupt the circulation and the oceanic heat transfer to the northern hemisphere.

Variations in the deep water formation rate have been linked to past AMOC variability (Broecker et al., 1985) and has been suggested to be sensitive to increased $CO_2$ emissions (Broecker, 1997) and changes in the freshwater budget of the Atlantic (Rahmstorf, 1996). Simulations of the AMOC under substantial changes of atmospheric $CO_2$ concentrations (larger than current levels) show that the thermo-haline circulation, and with it the AMOC, reduces to a very weak state (Stouffer and Manabe, 2003). A transition from the normal, vigorous AMOC to a weak AMOC is seen at a critical threshold of the atmospheric $CO_2$ concentration. These two modes of the AMOC are supposedly brought about by non-linear effects that result from a positive feedback called the salt-advection feedback. The original idea of the salt-advection feedback (Stommel, 1961)

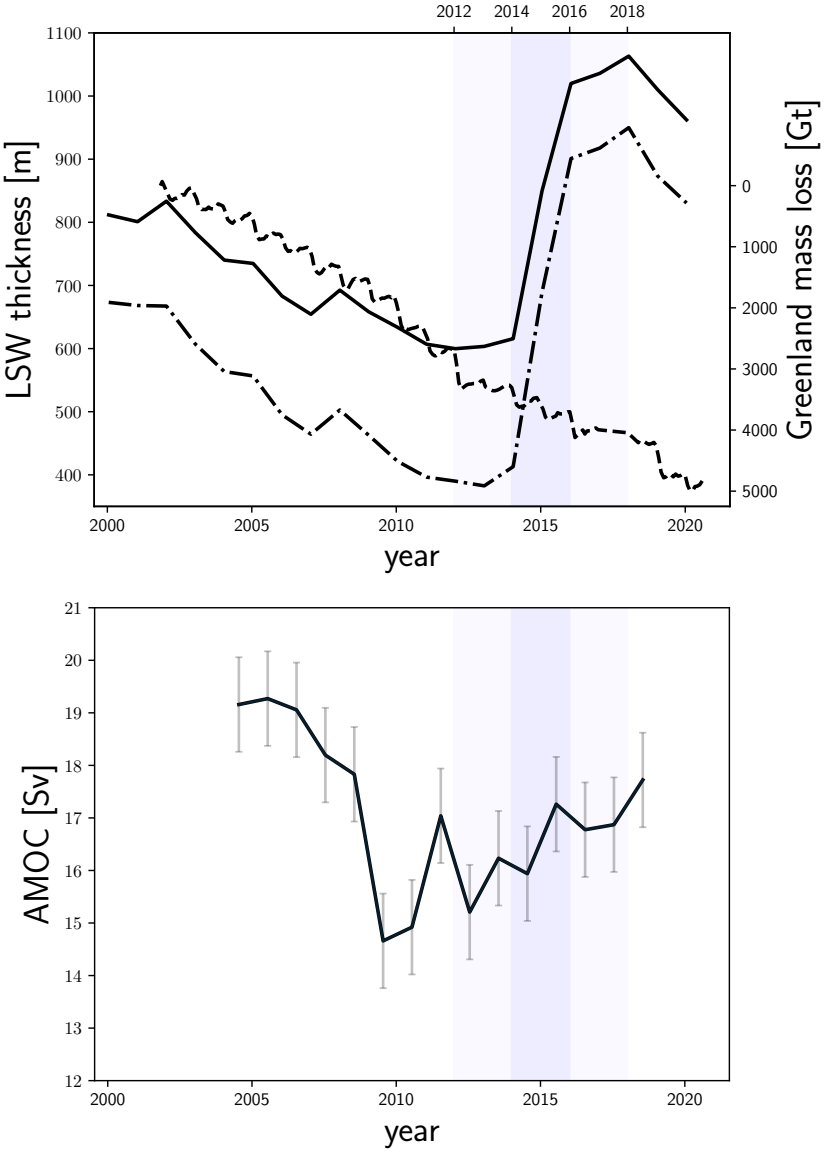


Figure 1.10: Top: Labrador Sea water (LSW) thickness estimates (solid line by summation of density classes, dash-dotted line by summing only connected layers to provide an upper and lower bound), and Greenland mass loss (dashed line) derived from the Grace satellite observations (Sasgen et al., 2020). The shaded area indicates where the freshwater from Greenland is not aligned with the LWS. Bottom: direct measurements (annual averages) of the AMOC strength index at 26.5°N by the RAPID array (Moat et al., 2020b). The indicated uncertainty is the estimated 0.9 Sv for annual means given in McCarthy et al. (2015).

is that a change in the overturning strength results in a change in the Atlantic freshwater (or salt) budget because the overturning circulation transport freshwater to or from the Southern Ocean in its steady-state.

If a weaker AMOC imports more freshwater, the freshwater budget of the Atlantic increases and further weakens the AMOC, which is a positive feedback mechanism. The AMOC weakens because the surface salinity in the deep water formation regions in the North Atlantic and Arctic decreases due to dilution with the increase in freshwater. Should the AMOC export more freshwater when weakening, the salinity increases and deep water formation can be expected to increase with it. In this case a negative feedback would stabilise the thermo-haline circulation. Which of the two possible feedback mechanisms determines the response of the AMOC is not clear, though observations indicate that the AMOC imports freshwater (Garzoli et al., 2013) and the positive salt-advection feedback is important and might lead to a rapid change to a weak AMOC state at a critical climate threshold. Melting ice sheets release freshwater into the ocean and could be the main driver of a critical cessation of deep water formation if the melt increases at a sufficiently fast rate that the excess cannot be exported from the Atlantic.

The maximum of the AMOC is a one dimensional index that is commonly used to measure the overturning strength. In Figure 1.10 the annual average of direct measurements taken by the RAPID array (Moat et al., 2020b) are shown. The array measures the transport at 26.5°N and indicates a variable AMOC over the past decades. Figure 1.10 also shows the Labrador Sea water (LSW) thickness derived from EN4 salinity/temperature profile data (Good et al., 2013; Gouretski and Reseghetti, 2010) as well as Greenland mass loss derived from satellite measurements (Sasgen et al., 2020). From temperature and salinity the density class can be determined (McDougall et al., 2009). Using 27.74 - 27.8 g $m^{-3}$ as the density anomaly class ($\sigma_0$) corresponding to LSW gives a partitioning of the measurements in the Labrador Sea region (see Yang et al., 2016 for a similar analysis). In Figure 1.10 an upper and lower limit of the LSW thickness is given. A lower limit only includes continuous measurements from the deep, while the upper limit includes all layers.

The correlation between the time series is suggestive of a physical connection; both between the Greenland adding freshwater to the Labrador Sea and decreasing the LSW formation (a deep water formation process), and with the AMOC strength. The blue highlights in Figure 1.10 indicate a period of apparent de-coupling between the Greenland mass loss and LSW formation; the LSW thickness was increasing 2012 - 2018 (also noted by Yashayaev and Loder, 2017) while the RAPID measurements show in increase in AMOC strength. The Labrador Sea is in the western North Atlantic subpolar gyre, and it has been noted that during 2012 - 2016 the eastern part underwent substantial freshening (Holliday et al., 2020). The east/west organisation of the freshwater budget in the SPG is important because of its effect on the deep water formation, a driver of the AMOC (the simulations in Chapter 4 also show this).

The actual freshwater forcing required and the pathways through which it affects the deep water formation are still open questions (Gillard et al., 2016). Recent measurements

in the North Atlantic subpolar gyre by the Overturning in the Subpolar North Atlantic Program (OSNAP, Lozier et al., 2017; Li et al., 2017) indicate that the Labrador Sea is not as important to the AMOC as the Irminger Sea and Iceland basin (Lozier et al., 2019). Modern climate models, however, show the majority of deep water formation to take place in the Labrador Sea as a result of open ocean convection (Heuzé, 2017). This discrepancy between observations and models is an important uncertainty because it directly relates to a (major) driver of the AMOC, and, consequently, its stability.

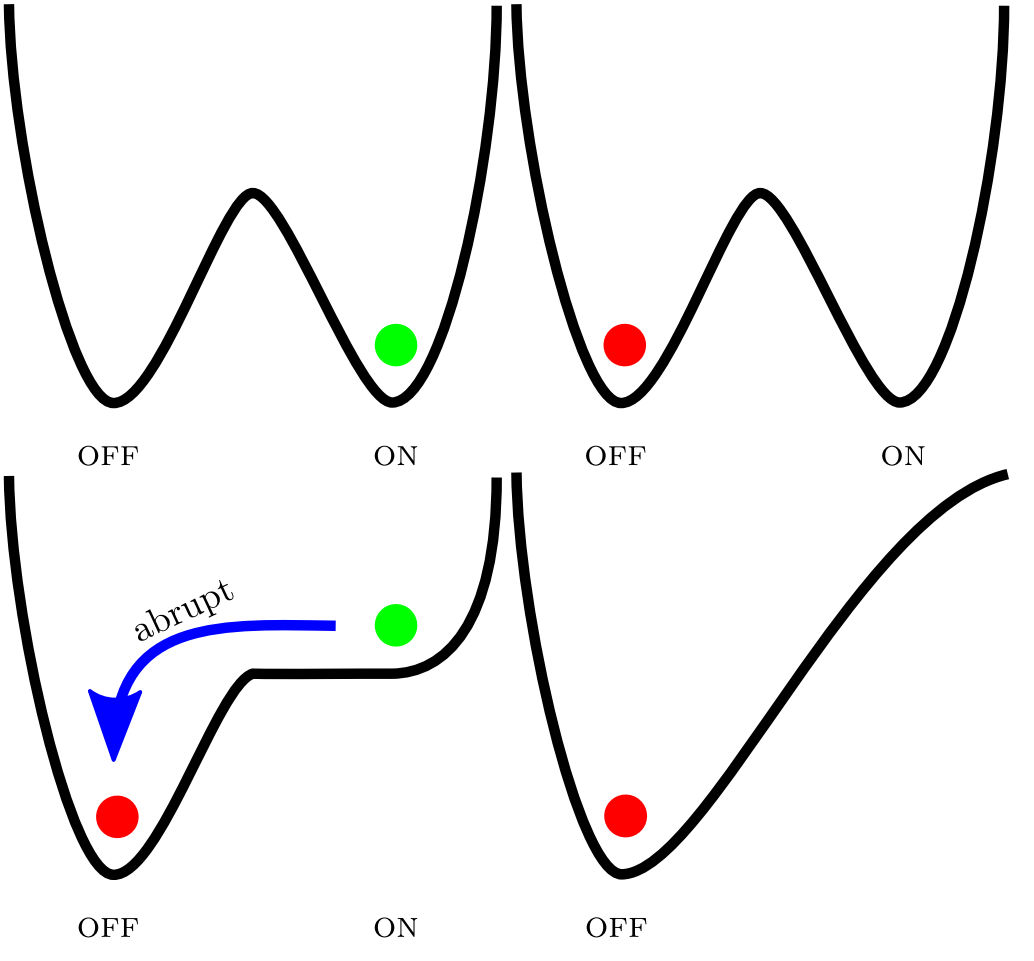


Figure 1.11: Sketch of changes in the AMOC stability regimes. From a stable bimodal regime (top) to an unstable bimodality being forced into a stable unimodal off state (bottom). The probability of switching from the top-left to the top-right state is very small. A freshwater forcing could change the shallow on state well and force the potential to a potential with only a single well; the switch to the off state then becomes inevitable because the on state ceases to exist (a topological change in the potential).

The SPG might therefore be an important component of the ocean regarding the strength of the AMOC, in particular its response to changes in salinity due to Greenland mass loss. The AMOC index can be used as a variable in a conceptual model of a system with two stable states constrained by a background potential. In Figure 1.11 a change in the background potential changes its shape, and finally only allows for a single state to exist: the stable off state of the AMOC. The change in the potential is driven by increasing freshwater forcing that shuts down the deep water formation in the SPG region which is consequently exacerbated through the positive feedback of salt advection.

Observations appear to indicate early warning signals as fingerprint of an AMOC slowdown that reached a point of loss of stability, possible close to a critical state transition (Boers, 2021). Specifically, critical slowing down (Dakos et al., 2008) can be understood as the AMOC sampling a basin of attraction of its state-space that has widened, leading to a larger variance of the signal. Although this does not mean another stable 'off' state will be reached soon, the AMOC does appear to have undergone changes that have brought it further from its pre-industrial state and closer to critical transition.

## 1.3 Outline and research questions

The four chapters that follow have each been published as separate articles in journals and can be read on their own. The first chapter describes a way to force a coupled climate model (CCM), which consists of an ocean and an atmosphere model component, with freshwater release from the polar ice sheets; the two after that investigate the effects on salt distribution and ocean circulation that results using the CCM EC-Earth. The fourth proposes a low-dimensional model to describe AMOC collapses in an ensemble of less complicated models than used in the previous chapters. Climate models used to models the current climate and the climate in the 21$^{st}$ do not predict such a collapse though, but this may be due to model deficiencies. The final chapter presents a synthesis and speculates about possible directions for further research. A short description and research question for each chapter is given below.

**Chapter 2 (A realistic freshwater forcing protocol for ocean-coupled climate models)** outlines an approach to determine an ocean freshwater forcing field under the RCP8.5 emission scenario. CCMs typically do not have ice sheet modules (although a new ensemble of experiments, ISMIP6, will use ice sheet models coupled to CCMs in the future—Nowicki et al., 2016). Without an ice sheet module there is no simulation of the loss and regrowth of mass that takes place continuously on Greenland and Antarctica. For a steady-state situation such an idealisation will have little impact. However, when we wish to simulate the effect of an ever increasing mass loss of those ice sheets this lack is an unacceptable deficiency. A pragmatic remedy is to estimate the freshwater application to the ocean as a result of the ice sheet's mass loss extrapolation from individual sources (ice sheet, glaciers, and icebergs), which is the subject of Chapter 2. A high-

end scenario of mass loss from the Greenland and Antarctic ice sheet is used to derive projections up to the year 2100 and some initial results are presented. This chapter was published as Van den Berk and Drijfhout (2014).

– *How can the effects of melting ice sheets be effectively mimicked in an ocean model that does not have a module to simulate interactive ice sheets?*

**Chapter 3 (Atlantic salinity budget in response to Northern and Southern Hemisphere ice sheet discharge)** presents results from simulations with the CCM EC-Earth using the freshwater forcing protocol described in Chapter 2. The rising $CO_2$ and the freshwater forcing pattern increase in magnitude from our starting point 2005 until the year 2100, after which the forcing fields are reversed in time until 2195 to return to the 2005 levels. Eventually, the freshwater contribution from Antarctica exceeds that of Greenland, and adds an increasing freshwater contribution toward 2100. We call this a ramp-up/ramp-down experiment. Effects that take more time to reach equilibrium, such as the AMOC, will then show an asymmetric response after the pivot year 2100. This chapter was published as Van den Berk et al. (2019).

– *In what way is Atlantic Ocean salinity distribution affected by melting ice sheets?*

**Chapter 4 (Circulation adjustment in the Arctic and Atlantic in response to Greenland and Antarctic mass loss)** also uses the meltwater scenario projection of Chapter 2, and uses the same ensemble of simulations in Chapter 3 but focuses more on the changes taking place within the Atlantic Ocean.

The response of the ocean cannot be simply expressed as changes occurring at Bering Strait and the section at Cape Agulhas (connecting to South America). The internal dynamics of the Atlantic are important to the Atlantic salt budget. This chapter was published as Van den Berk et al. (2021b).

– *How is the salt distribution and ocean circulation in the Atlantic affected by climate change and melting ice sheets, in particular AMOC stability?*

**Chapter 5 (Characterisation of Atlantic Meridional Overturning hysteresis using Langevin dynamics)** focuses on the possibility of an AMOC collapse, but does not use the freshwater forcing protocol in the previous chapters as no collapse was observed in the EC-Earth ensemble or in simulations of comparable models that were available. Simulations of simpler models with a collapsing AMOC, called climate models of intermediate complexity (EMICs), however, were available. The low-dimensional Langevin model allows for comparison between models that display an AMOC collapse—a important climate tipping point. This chapter was published as Van den Berk et al. (2021a).

– *Can a quantitative description be given for an AMOC collapse as seen in climate models?*

**Chapter 6** presents some possible extensions of the Langevin model in Chapter 5 and some preliminary results relating to the possibility of AMOC collapse under the current transient forcing and why it has been absent in CCM simulations. The distinction between simulations under transient forcing and equilibrated simulations is discussed.

– *How far away is the AMOC from a collapse according to current climate simulations?*

**Chapter 7** returns to the questions posed above with a summary of the results, an outlook on further research, and a critique.

## Acknowledgements

Thanks go out to Clifford Chuwah, Wilco Hazeleger, and Sybren Drijfhout for helpful comments, suggestions, and corrections that have improved this chapter.

# 2 A realistic freshwater forcing protocol for ocean-coupled climate models

## 2.1 Introduction

It is expected that the ice stored on Greenland and Antarctica will diminish during the coming century. The estimates of the amount so far have varied widely (Katsman et al., 2011; Pfeffer et al., 2008; Rignot et al., 2011; Thomas et al., 2009). Nonetheless it seems pertinent to incorporate this mass loss in coupled climate models (CCMs) when making projections of future climate change. A rising global mean temperature is expected to enhance mass loss of both the Greenland and the Antarctic ice sheet (Gregory and Huybrechts, 2006). Most of the current CCMs lack an interactive ice sheet model to handle these processes dynamically. As we should take into account this mass loss, we have to model the response of the ice sheets in CCMs in another way. Our intent is to provide a prescription of how this can be done for any ocean model.

An ice sheet's surface mass balance (SMB) is the amount of water gained minus the amount lost. Many processes affect the SMB of an ice sheet; those mentioned in Shepherd et al. (2012) are solid and liquid precipitation, surface sublimation, drifting snow transport, erosion and sublimation, meltwater formation, re-freezing, retention, and run-off. An increased melt might lubricate a glacier and increase its rate of retreat, leading to more iceberg calving (see Greve and Blatter, 2009, for an introduction to the dynamics of glaciers).

Most CCMs do not couple with an interactive ice sheet model and can not be expected to model these mass loss processes due to a warming climate. By prescribing the mass loss, this defect can be compensated for. A prescription based on a plausible high-end sea level rise scenario is presented with the purpose to be easily implemented in a CCM.

Parametrisations of ice sheet melting do exists (Beckmann and Goosse, 2003; Wang and Beckmann, 2007), but are limited in their scope and applicability to any particular climate model. A similar problem exists with the parametrisation of iceberg calving (Al-

ley et al., 2008; Amundson and Truffer, 2010), where it is often cumbersome to include these parametrisations in an ensemble of different models.

Our manuscript is organised as follows. We begin with identifying the processes at work and their locations. A motivation for the freshwater projections is given in Sections 2.2 – 2.3. Details of how the projections should be implemented is explained in 2.A. The effects on sea surface height are discussed in Section 2.4. We end with a summary.

### 2.1.1 Model description

We will show some results using the CCM EC-Earth (Hazeleger et al., 2010; Hazeleger et al., 2012) which does not include an interactive ice sheet module. EC-Earth consists of three computational components. The atmosphere is modelled with the Integrated Forecast System (IFS), cycle 31r1 which has a resolution of 62 layers in the vertical and triangular truncation at wavenumber 159 (ECMWF, 2006, effectively resolving $\approx$ 130 km gridded). The ocean is modelled by the Nucleus for European Modelling of the Ocean (NEMO) developed by the Institute Pierre Simon Laplace at a resolution of approximately 1° in the horizontal ($\approx$ 110 km) and 42 levels in the vertical (Madec, 2008). The two are synchronised along the interface every three model-hours by the OASIS3 coupler developed at the Centre Européen de Recherche et de Formation Avancée en Calcul Scientifique (Valcke et al., 2004). The ocean model is further extended by a sea ice module of Louvain-la-Neuve (LIM) (Fichefet and Morales Maqueda, 1997; Bouillon et al., 2009).

The iceberg output used as forcing (Marsh et al., 2015) is derived from a modified version of the Bigg et al. (1996) and Bigg et al. (1997) iceberg model, developed by Martin and Adcroft (2010) and coupled to ORCA025, an eddy-permitting global implementation of the NEMO ocean model Madec, 2008, to simulate the trajectories and melting of calved icebergs from Antarctica and Greenland in the presence of mesoscale variability and fine scale dynamical structure.

Icebergs are treated as Lagrangian particles, with the distribution of icebergs by size derived from observations (see Bigg et al., 1997 and Table 1). The momentum balance for icebergs comprises the Coriolis force, air and water form drags, the horizontal pressure gradient force, a wave radiation force, and interaction with sea ice. The mass balance for an individual iceberg is governed by bottom melting, buoyant convection at the side walls and wave erosion (see Bigg et al., 1997).

This configuration has been run for 14 years, and the associated freshwater fluxes used here are averages over years 10-14. Southern Hemisphere calving and melting rates are in near balance after 10 years, but further decades of simulation would be needed for global balance, due to slower equilibration of calving and melting in the Northern Hemisphere. An average pattern of icebergs is our primary interest, which is why we settled for a relatively short integration time.

## 2.2 Mass loss processes and their locations

For our purposes a detailed treatment of various mass loss processes is not necessary, because only the amount of freshwater release applied to the ocean is of interest. Nevertheless, the many different processes that affect the SMB indicate that uncertainties are to be expected and distinction between mass loss processes and geographical locations needs to be made Shepherd et al., 2012.

The most obvious response to increased atmospheric temperatures is the melting of ice. This mass loss can be associated with adding freshwater directly offshore of the coast of the region where the melt takes place. We designate this freshwater source as *run-off*, or $R$ for short. Run-off is contrasted with another form of mass loss that produces icebergs. The calving of icebergs from glaciers we call *ice discharge*, or $D$. The important difference is that icebergs are free floating chunks of ice and can drift to other locations and melt.

This last observation prompts us to introduce the distinction between *near* ($N$) and *far* ($F$) freshwater forcing. A near forcing is always adjacent to the coast of origin and a far forcing is not restricted like this.

The output of the iceberg drift and melt simulation gives us the location and relative magnitude of the far source of freshwater forcing. We assume spatial patterns on an annual cycle for these contributions, with magnitudes varying in time. The scaling factors are provided by the mass loss projections in the two polar regions.

Glaciers not only calve blocks of ice, but (relatively) warm ocean water will also melt tidewater glaciers when the two are in contact. This is called basal melt ($B$) and takes place within the shelf cavity. The ice discharge not melted away we call the *ice flux* ($I$). Basal melting affects all glaciers and ice shelves but the extent is determined by the local temperature of the water. Floating ice shelves loose mass by the relatively warm ocean water compared to the freezing point (Rignot and Jacobs, 2002). This melt contribution to freshwater release into the ocean is relatively small compared to other forms of melt. Mass loss as a result of floating ice shelves does not contribute to sea level rise (Jenkins and Holland, 2007). However, in general (in equilibrium) this mass loss is balanced by ice discharge from the grounded part of the glacier. If basal melt actually forms a significant part of the ice discharge from the glaciers the full $D$ can not be treated as only due to iceberg calving. A fraction of $D$ is released as freshwater run-off at the glaciers' calving face and the remainder is left available to drift away in the form of icebergs. A certain fraction of $D$ is added to $N$ with the remainder allocated to $F$. (For a schematic overview of these labels see Figure 2.1.)

In this section we will identify the regions we wish to treat separately on the basis of the different characteristics of mass loss (processes) that differentiate them. We start by noting that Greenland and Antarctica are the locations of the polar ice caps and proceed from there. We list important characteristic values (at present day) where appropriate. In particular these will be basal melt fractions (the fraction of the iceberg melted away

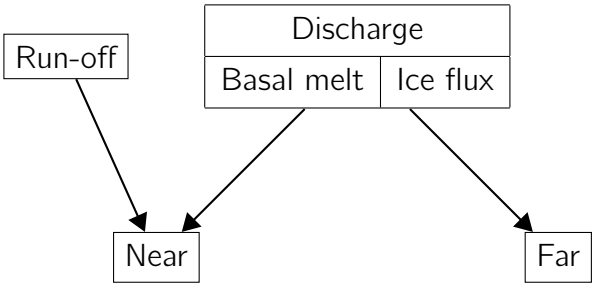


Figure 2.1: Schematic overview of mass loss processes and their re-labelling.

before it is adrift, or $\mu$), and mass loss. Projections of future development of mass loss are constructed in Section 2.3.

Both Greenland and Antarctica are covered by ice sheets, but also differ substantially. Firstly, Antarctica stores a considerably larger amount of ice (Hanna et al., 2008; Van den Broeke et al., 2011). Secondly, Greenland melt is expected to increase with a decreasing surface mass balance (Hanna et al., 2008), whereas Antarctica could also gain mass in the future (Church et al., 2013). A third reason to distinguish between the two regions is the type of glacier present. On this basis we subdivide further and segment Greenland and Antarctica in smaller sections, each with their own storyline.

### 2.2.1 Greenland

Greenland is expected to experience increased surface melt as well as increased iceberg calving from its tidewater glaciers (Katsman et al., 2008). The three main tidewater glaciers we need to consider are Jakobshavn Isbræ in the west and Kangerdlugssuaq and Helheim in the east (Rignot and Kanagaratnam, 2006; see Figure 2.10 for their locations). Smaller tidewater glaciers are located in the north. Glaciers with relatively small discharge values are ignored (Katsman et al., 2011). The glaciers in Table 2.1 not explicitly mentioned are simply taken to be part of the region listed. A distinction must be made between the glaciers with termini that are expected to retreat to above sea level and those that are not expected to do so during the coming century. The foremost example of a glacier whose terminus will not retreat is Jakobshavn Isbræ, but the northern glaciers' topography also prevent this (Katsman et al., 2008). We then arrive at separate scenario projections, which roughly divide Greenland into three regions. The first ($n_{\mathrm{i}}$) will consist of the northern tidewater glaciers and Jakobshavn Isbræ, which have non-retreating termini. The second region ($n_{\mathrm{ii}}$) covers the eastern tidewater glacier. These do have retreating termini. The third ($n_{\mathrm{iii}}$) region is the remainder, where surface melt is the primary mass loss process. The glaciers that make up regions i and ii are listed in Table 2.1.

| | glacier | $D_{\text{init}}$ (Gt/yr) | |
|---|---|---|---|
| region i | | | |
| | (a) Jakobshavn Isbræ | 27 | |
| | (b) Petermann | 12.2 | |
| | (c) Ryder | 4.3 | |
| | (d) Nioghalvfjerdsbræ | 14.3 | |
| | (e) Zachariæ Isstrøm | 11.7 | |
| | | | 69.5 |
| region ii | | | |
| | (f) Helheim | 26.2 | |
| | (g) Ikertivaq | 10.3 | |
| | (h) Storstrømmen | 6.8 | |
| | (i) Daugaard-Jensen | 10.5 | |
| | (j) Kangerdlugssuaq | 27.9 | |
| | | | 81.7 |

Table 2.1: Greenland tidewater glaciers used to define regions i and ii.(See Rignot and Kanagaratnam, 2006, for an overview for Greenland glacial mass loss.)

### 2.2.2 Recent Greenland melt

There are three major glaciers in Greenland that will be considered here: Helheim, Kangerdlugssuaq and Jakobshavn. Of these, Helheim and Kangerdlugssuaq do not have developed ice tongues[1] (Thomas et al., 2009). Jakobshavn does have an ice tongue and for this reason a substantial basal melt fraction is to be expected there. A related reason is that Jakobshavn has a sill before its flux gate that can trap the (warm) water that moves past it, and it is hypothesised that this helps to increase the glacier's flow rate (Holland et al., 2008; Rignot et al., 2010), supported by the findings of (Motyka et al., 2011). A basal melt fraction of $\mu = 0.29$ for the Jakobshavn Isbræ was found (Motyka et al., 2011) before its ice tongue broke off in 2003. The ice tongue inhibits calving, but due to a larger surface area, also enhances basal melt. More recent observations indicate that the area of the glacier that is thinning is reaching ever further inward (Thomas et al., 2009). This is found to be the case for the three major Greenland glaciers, but Kangerdlugssuaq

[1] A floating protrusion of ice from a glacier which has a relatively large surface area exposed to the ocean water.

and Helheim show great variability (Thomas et al., 2009). Glaciers that are part of the hydrological cycle, but are not expected to increase their mass loss (see Katsman et al., 2011), are ignored.

Other measurements of basal melt flux of three of Greenland's western glaciers are given in Rignot et al. (2010). The glaciers run deep and have shallow sills that limit exchange of water with the adjoining ocean. A range of $\mu = 0.2 - 0.8$ is found for the summer basal melt. These glaciers might not be representative for the larger western Greenland region, and the large variation in melt fraction indicates critical dependence on local circumstances.

On the basis of these findings, we will assume the same basal melt fractions for two of the three regions of Greenland. We assume that the northern part suffers no basal melt, because of the relatively low thinning rates found there (Thomas et al., 2009). The other two regions are associated with (mostly) tidewater glaciers, and the geographical similarity implies that we also expect similar temperature rise in sea water. The authors of Thomas et al. (2009) find that especially glaciers with bed topography well below sea-level (hundreds of metres) are thinning rapidly.

The values given in Rignot et al. (2010) are for summer only. Assuming two seasons of equal duration we take halve of these values to be appropriate annual means. The average ($\mu = 0.25$) is also comparable to the earlier quoted value of 0.29 for Jakobshavn Isbræ in the mid 1980s. If we assume, on the basis of thinning rates, that a similar basal melt rate applies here we can use 0.25 for the relevant Greenland regions ($n_{\mathrm{ii}}$ and $n_{\mathrm{iii}}$).

### 2.2.3 Antarctica

Like Greenland, Antarctica has varying geography that leads to a different treatment of each subregion. In Katsman et al. (2008), three areas that are at risk of enhanced mass loss are identified. The first is the Amundsen Sea Embayment (ASE i, taken to correspond to Pine Island and Twaites), which feeds the West Antarctic Ice Sheet (WAIS). The second area consists of Totten glacier, Cook ice shelf glacier and Denman glacier (ii), which are large marine ending glaciers feeding the east Antarctic Ice Sheet (EAIS). The final region (iii) is the North Antarctic Peninsula (N-AP). Other ice shelves that might be at risk are the Filchner Ronne and Brunt ice shelf (Hellmer et al., 2012). As will be shown below, our implementation can easily take into account initial mass loss, if such a storyline is considered appropriate.

### 2.2.4 Recent Antarctica melt

Basal melt rates have been determined for various Antarctic glaciers in Rignot and Jacobs (2002). The values we use are the grounding line ice flux and a downstream flux gate, as given in their Table 1. If no basal melt were to occur, then the difference between these two quantities would be zero (assuming no accumulation or other ablation occurs as these authors do). The difference is then equal to the amount of melt that has occurred

between the grounding line and the gauge flux gate. We will name this difference $\Delta\phi$ and let $\mu = \Delta\phi/D$. We will summarise the findings in Rignot and Jacobs (2002) per region in the following paragraphs. We only discuss those regions and glaciers that are expected to show a (substantial) increase in discharge by Katsman et al. (2011). Those glaciers that are ignored do not contribute to additional melt, but can still play a (substantial) part in the hydrological cycle.

**WAIS** The West Antarctic Ice Sheet (taken to correspond to the glaciers Pine Island, Thwaites, Smith and Crosson, and Kohler and Dotson in Rignot and Jacobs (2002)) shows $\Delta\phi = 59.5$ Gt/yr. The same region showed an ice discharge, $D = 215$ Gt/yr. The melt ratio for this region is $\mu_{s_{\mathrm{i}}} = 59.5/215 \approx 0.30$. More recent measurements (Rignot et al., 2013) indicate that a larger melt ratio perhaps is more appropriate. However, we will keep the lower value here.

**EAIS** The value given for the eastern ice sheet region is $152 - 93.3 = 58.7$ Gt/yr of basal melt, or $\mu_{s_{\mathrm{ii}}} = 0.15$ (Rignot and Jacobs, 2002).

**N-AP** The northern peninsula region is not explicitly taken into account in Rignot and Jacobs (2002), but the area geographically closest to it (Evans and Ronne ice shelf) is given to have a basal melt rate of 31.7 Gt/yr, and the corresponding region in Rignot et al. (2008) (IH', English Coast) has a 1996 ice discharge of 78 Gt/yr. We then find $\mu_{s_{\mathrm{iii}}} = 0.40$. The basal melt ratios for the Antarctic ice discharge are substantial and regionally dependent on local temperature. This is elaborated in Rignot and Jacobs (2002) where a 1K increase leads to an increase of 10 m/yr in the basal melt rate.

| | Greenland | | | Antarctica | | |
|---|---|---|---|---|---|---|
| | $n_{\mathrm{i}}$ | $n_{\mathrm{ii}}$ | $n_{\mathrm{iii}}$ | $s_{\mathrm{i}}$ | $s_{\mathrm{ii}}$ | $s_{\mathrm{iii}}$ |
| $\mu$ | 0 | 0.25 | 0.25 | 0.30 | 0.15 | 0.40 |

Table 2.2: Overview of melt ratios $\mu$ for the Antarctic and Greenland scaling regions.

For Jakobshavn Isbræ we found a considerable basal melt fraction, on par with the value found in the western Antarctic. The putative values for the six scaling regions (three GreenlandGreenland| and three Antarctic regions that have mass loss values controlled independently from each other) considered are listed in Table 2.2.

### 2.2.5 Deposition area of freshwater release

The amount of basal melt is strongly connected to the characteristics of the donor glacier and for this reason it would be unreasonable to simply spread this freshwater along the

entire Greenland coast. We restrict the deposition to an area close to the source glacier, and prescribe it as a mass flux at the surface. The details of the horizontal distribution are given in Section 2.A.

In Greenland, the major tidewater glaciers are Jakobshavn in the west, and Kangerdlugssuaq and Helheim in the east. The total amount of Greenland ice discharge is based on Rignot and Kanagaratnam (2006) where a list of glaciers is provided. The location of the given glaciers can be used to determine where the basal melt component of the freshwater flux is to be placed. The same procedure can be used for Antarctica. The discharge values we use are taken from Rignot et al. (2008).

Because basal melt manifests itself as a freshwater forcing already at the calving face, the corresponding fraction of $D$ should be applied to the coastal gridcells. The effect is that the amplitude of the ice discharge diminishes regionally, and is replaced by an *effective* run-off component in the form of the near forcing. The far forcing will be given by iceberg melt and is typically further from the coast.

## 2.3 Mass loss scenarios and projections

A scenario consists of a storyline of some events to come (Katsman et al., 2011). A projection is the future evolution of a particular variable (mass loss) based on a certain scenario. In the case of sea level rise, this implies a quantification of the amount of additional water at a particular point in time (often the year 2100) added to the ocean. Since we not only want to consider an accumulated loss, but also the progression in time, we will suggest time dependent projections of mass loss for each region identified above. First we treat the implications of the storyline given in Katsman et al. (2011) for Greenland followed by the one for Antarctica. The conversion values in Table 2.3 can be used to convert between common units. For each scaling region a separate projection will be given.

| | Gt/yr | mm/yr | Sv |
|---|---|---|---|
| Gt/yr | 1 | 360 | $3.15 \cdot 10^4$ |
| mm/yr | $2.78 \cdot 10^{-3}$ | 1 | 87.4 |
| Sv | $3.17 \cdot 10^{-5}$ | 0.0114 | 1 |

Table 2.3: Some conversion factors for the density of (fresh) water at 0° C and 1 atm. For example, a 1 Sv sustained run-off over the course of a year is equivalent to a global mean sea level rise of 87.4 mm.

The basal melt seems to relate directly to calving rates and not so much to surface melt (Holland et al., 2008; Pritchard et al., 2009). For this reason we will take the calving rate,

when found to increase slowly, to grow with a constant factor in basal melt projections below.

The basal melt rate is tightly coupled to the local temperature, and in absolute terms to the extent of the ice sheet. When the adjoining ice sheet collapses the amplitude of the ice discharge goes up tremendously, but the basal melt cannot be expected to follow. Therefore, we can only attribute a certain fraction of $D$ to $B$ as long as the ice sheet is in place (and its surface area is unchanging). After a collapse, or even for a non-linear increase in ice discharge (which will not scale exponentially after a collapse if linked to temperature), the basal melt needs to be re-evaluated. We suggest to set it to zero if a very non-linear event occurs, or allow for a linear increase afterwards (cf. the WAIS in Section 2.3.2).

Here, we provide a description of a set of projections of ice sheet mass loss which follow a high-end scenario of ice loss from the Greenland and Antarctic ice sheets (Katsman et al., 2011), to be used in conjunction with a Representative Concentration Pathway, RCP8.5 scenario (Taylor et al., 2012). For other RCP scenarios that involve ice mass loss can be used by adjusting the appropriate scaling.

### 2.3.1 Greenland

Greenland is at risk to experience both increased surface melt and glacier retreat (Katsman et al., 2008). The latter is particularly relevant for the Jakobshavn glacier which has already shown considerable retreat (Holland et al., 2008). The processes at work are assumed being the same for the glaciers in region i, and continue to linearly increase the retreat rate during the coming century. As a result, by the year 2100 the rate has been estimated to be four times the current value (Katsman et al., 2011). In region ii, the same progression is assumed, but a retreat to above the waterline is expected by 2050, after which the mass loss rate returns to 1996 values (Rignot, 2006).

The increased global mean temperature is enhanced by local feedback processes with a factor 1.6 (Gregory and Huybrechts, 2006), leading to a greater susceptibility of overall melt and enhanced iceberg calving in region iii. The effect is assumed to cause an increase of sea level rise, which scales linearly with the local temperature increase (Katsman et al., 2011).

#### Projection of run-off $R$

Ice cap run-off is expected to increase linearly with time. Greenland's contribution is expected to be largest of all regions experiencing melt, because its ice mass is more prone to melt due to its location and the temperature feedback with the surrounding ocean (Katsman et al., 2011).

The IPCC's AR5 (Church et al., 2013) (see their Table 13.5, the RCP8.5 scenario) provides a high-end upper limit estimate of 0.13 m sea level rise caused by the decrease of Greenland's surface mass balance (SMB). Pfeffer et al. (2008) estimate that Greenland's

SMB can provide 71 mm and Antarctica 10 mm of sea level rise. The glaciers and ice caps not associated with these two regions are expected to yield 80 mm. Currently, only Greenland's SMB is lessening (Bamber et al., 2012; Shepherd et al., 2012).

Greenland run-off is given by Bamber et al. (2012) as 416 Gt/yr ≅ 0.013 Sv. Figure 13.9 in the AR5 (Church et al., 2013) indicates that $R$ is expected to increase. If we assume a linear melt rate increase (during the 21st century), we obtain $1.3 \cdot 10^{-2}$ mm/yr$^2$, or a time dependent rate of (converted with Table 2.3)

$$R(t) = 0.013 + (2.96 \cdot 10^{-4} \cdot t) \text{ Sv} \tag{2.1}$$

for Greenland's run-off $R$. The variable $t$ is the number of years since 2000. Run-off is a forcing to be applied to (Greenland's) coastal gridcells in the model used. A simulation of Greenland's run-off also shows a linear progression (Mernild and Liston, 2012). The projection of $R$ is shown in Figure 2.2. The value of 0.013 Sv is assumed to be the value appropriate for hydrological balance and does not contribute to any rise in sea level.

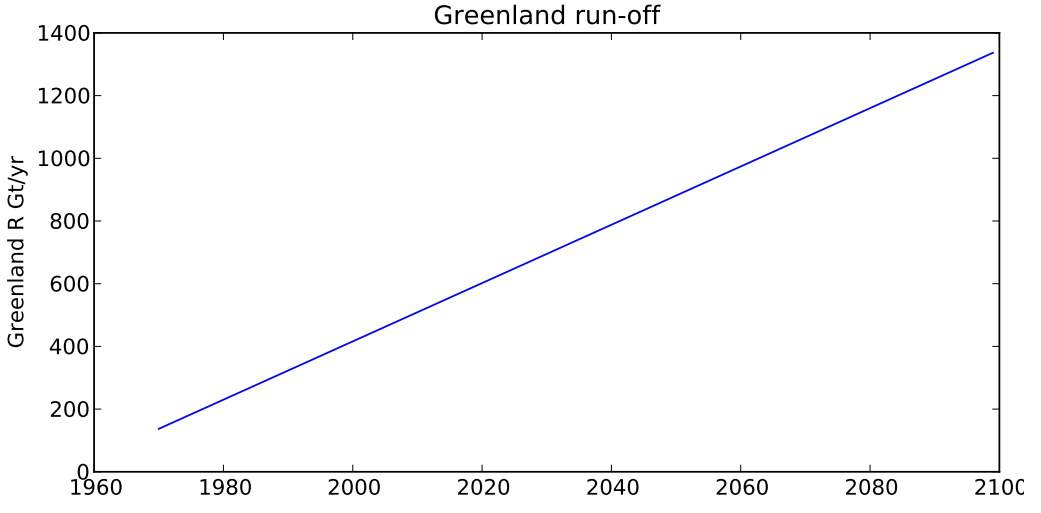


Figure 2.2: Mass loss for Greenland run-off (R).

### Projection of discharge $D$

Here we give prescriptions for ice discharge in the scaling regions that we distinguish. The initial rate is presumed to be balanced before the epoch ($t \equiv 0$), while the excess value forms the additional imbalance. The initial rate is model specific, we will address this issue below in Section 2.A.2. The time index $t$ is to be the number of years since 2000 in all expressions that follow.

**Greenland i** The northern glaciers and—in particular—Jakobshavn Isbræ are expected to show a fourfold increase in their rate of the retreat by 2100 (Katsman et al., 2011).

Their behaviour is the same in the east and south (see below), except that these termini are not expected to retreat to above sea level and in the north retreat does not stop during the 21st century. A fraction of 0.18 of the current mass loss is allocated to these regions on the basis of recent mass loss values (see Rignot and Kanagaratnam, 2006, for an overview for Greenland glacial mass loss),

$$D_{n_{\mathrm{i}}}(t) = 69.5 \cdot \left[\frac{3}{104}(t+4)+1\right] \ \mathrm{Gt/yr}. \tag{2.2}$$

The total sea level rise is 10 cm by 2100.

**Greenland ii** A doubling of the rate of retreat of the eastern and southern tidewater glaciers by 2050 followed by a return to the balanced rates of 1996 (with 0.21 the fraction of 1996 mass loss, see Table 2.1) gives,

$$D_{n_{\mathrm{ii}}}(t) = 81.7 \cdot \begin{cases} 1/54 \cdot (t+4)+1 & t \le 50 \\ 1 & t > 50 \end{cases} \ \mathrm{Gt/yr}. \tag{2.3}$$

**Greenland iii** We use the updated values from IPCC's fifth assessment report (Church et al., 2013), instead of the fourth (Meehl et al., 2007) which was used in Katsman et al. (2008) and Katsman et al. (2011).

An increase of Greenland's discharge $D$ (without the two tidewater glacier areas discussed above) by 2100 is expected due to enhanced run-off caused by a 4 K global-mean atmospheric temperature rise (Katsman et al., 2008). The effect is assumed to give an increase of sea level rise of 0.21 mm/yr for each degree the local temperature increases; this was the increase observed during the period 1993 – 2003 (Katsman et al., 2011). If we assume that $R$ and $D$ contribute equally to this rise, we find a value of 0.1 mm/yr steady rise in 2000 and 0.32 (= 1/2 × 0.4 mm/yr/K × 1.6 global temperature rise increase) additional rise due to increasing temperature. Here the value 0.4 mm/yr/K is given in Katsman et al. (2008) as the mass balance sensitivity with respect to local temperature, the adjustment factor relates this again to global mean temperatures. We find $4/100 \times 0.32 \cdot t$ mm/yr for a linear increase in local Greenland temperature, or (with Table 2.3)

$$D_{n_{\mathrm{iii}}}(t) = 36 + (4/100 \times 115 \cdot t) \ \mathrm{Gt/yr}. \tag{2.4}$$

The scaling functions for each of the above three regions are shown in Figure 2.3.

### Prescription of near-deposition $N$

The near-deposition of freshwater comprises the melt run-off $R$ and the basal melt rate $\mu \cdot r_n$. The basal melt is location dependent. So far we have collected Jakobshavn and the northern tidewater glaciers together on the basis of the similar processes at work. Measurements of thinning rates indicate that not all of Greenland's glaciers show basal melt (Thomas et al., 2006). We should then split up region i into Jakobshavn which does

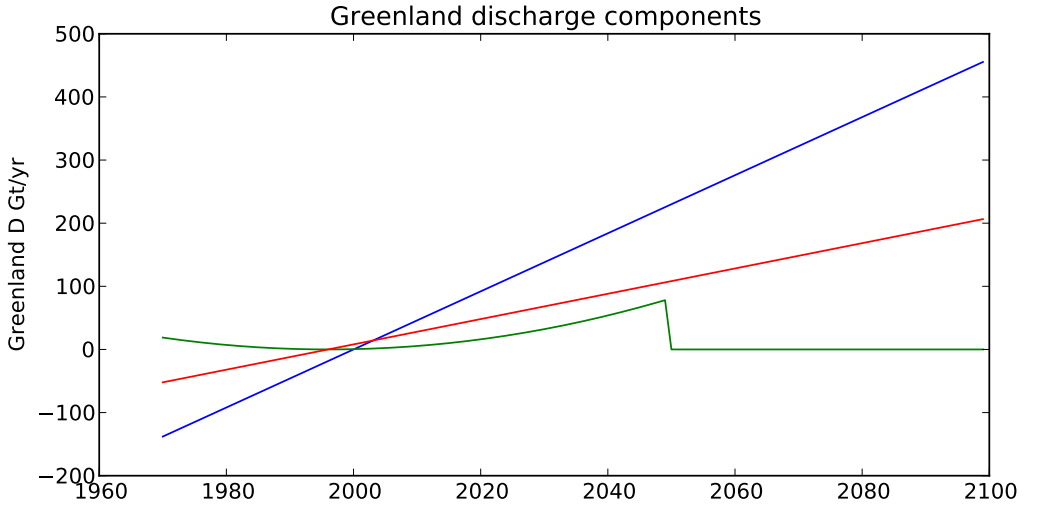


Figure 2.3: Scaling functions of the components of ice discharge ($D$) for Greenland. In blue $D_{n_{\mathrm{i}}}$, green $D_{n_{\mathrm{ii}}}$, red $D_{n_{\mathrm{iii}}}$.

feature basal melt and the northern tidewater glaciers that do not. We label the two ia and i\a respectively. From Table 2.1 we see that Jakobshavn had a discharge of 27 Gt in 1996, leaving 42.5 Gt for the remaining glaciers. The expressions become

$$N_{n_{\mathrm{ia}}}(t) = 27 \cdot \mu_{\mathrm{i}} \cdot \left[\frac{3}{104}(t+4)+1\right] \ \mathrm{Gt/yr}, \tag{2.5}$$

where $\mu_{\mathrm{i}} = 0.25$ for Jakobshavn and

$$N_{n_{\mathrm{i\backslash a}}}(t) = 0 \tag{2.6}$$

for the northern glaciers' $N$ (which is the value given in Table 2.2 before we made an exception of Jakobshavn). The expressions for the near-depositions in the other two regions have the same numerical value for the basal melt fraction ($\mu_W = \mu_E = 0.25$, where the subscripts indicate west and east, respectively) and can be directly expressed in terms of the ice discharge rate, which leads to

$$N_{n_{\mathrm{ii}}}(t) = \mu_{\mathrm{ii}} \cdot r_{n_{\mathrm{ii}}}(t) \tag{2.7}$$

for the south/eastern region (ii) and

$$N_{n_{\mathrm{iii}}}(t) = \mu_{\mathrm{iii}} \cdot r_{n_{\mathrm{iii}}}(t) \tag{2.8}$$

for the third region.

**Prescription of far-deposition $F$**

The amount of ice calved and not melted at the base is allowed to drift. This is the amount that we will distribute according to the pattern produced by the iceberg drift simulation detailed below in 2.A.1. Taking the split of region i into account we have

$$F_{n_{\mathrm{ia}}}(t) = 27 \cdot (1 - \mu_W) \cdot \left[\frac{3}{104}(t+4) + 1\right] \ \mathrm{Gt/yr}, \tag{2.9}$$

for Jakobshavn's $F$ and

$$\begin{aligned} F_{n_{\mathrm{i}\setminus\mathrm{a}}}(t) &= 42.5/69.5 \cdot r_{n_{\mathrm{i}}}(t) \\ &= 42.5 \cdot \left[\frac{3}{104}(t+4) + 1\right] \ \mathrm{Gt/yr}, \end{aligned} \tag{2.10}$$

for the northern glaciers' $F$. Here, we have assumed $\mu$ to remain constant throughout time, effectively allowing the melt amount to scale with the ice discharge rate. Because the rate changes only linearly, this is not an unreasonable assumption. We merely assume that a larger ice mass is present when $D$ increases. In the case of Antarctica (see below), this assumption breaks down when collapsing ice sheets need to be taken into account.

### 2.3.2 Antarctica

The high-end scenario we use (Katsman et al., 2008) includes an accelerated outflow of the Amundsen Sea Embayment, with a collapse in the year 2030 after which the loss rate remains constant at eight times the current value. The loss is assumed to increase exponentially up to the breakpoint. A similar progression is assumed to hold for the glaciers in east Antarctica, except that the difference in grounding prevents a retreat as advanced as for the ASE. After 2030 the mass loss increases with a greater exponential rate. The Peninsula region is assumed to experience enhanced melt and glacier flow with a similar progression as the EAIS region, but the quantity is much less.

**Projection of discharge $D$**

A projection to match the storylines involves constructing a parametrisation of the loss rate. To be able to do so the current loss rates are required.

**Antarctica i** The severe scenario includes a collapse of the West Antarctic Ice Sheet, the inclusion of which is based on expert judgement (Katsman et al., 2011). The collapse of the Larsen-B ice shelf has shown such an event to cause an increase of $2-6\times$ the speed of the shelf's feeding glaciers (Scambos et al., 2004). If we assume this speed-up factor to also hold for the WAIS with respect to current feeding rates, a total sea level rise in the order of 0.25m by 2100 is expected (Katsman et al., 2011). The storyline assumes that by 2030 a 50% excess discharge has taken place and the collapse is initiated. The

removal of the ice shelf increases (near instantaneously) the calving rate by a factor 8 of the balanced discharge value[2]. This positive feedback causes the glaciers to calve at an exponential rate. With a 237 Gt/yr of outflow calving and 177 of input for Pine Island and Twaites glacier—this is also the base rate added for full ice flux values, taken from Rignot et al., 2008 (their Table 1) and a sustained acceleration of 1.3%/yr,

$$D_{s_{\mathrm{i}}}(t) = \\ 237 + \begin{cases} 237 \cdot \left[(1.013)^t - 1\right] & t \leq 30 \\ 177 \times 7 & t > 30 \end{cases} \mathrm{Gt/yr}. \tag{2.11}$$

**Antarctica ii** The eastern glaciers are expected to retreat like those in the western part except that east Antarctica rests on a high plateau. The eastern glaciers are then thought to be less susceptible to collapse (Rignot, 2006) because marine glaciers will not be able to retreat so easily. The outflow of ice of the eastern ice sheet is 785 Gt/yr (Rignot et al., 2008) and 388 (= 87 + 207 + 94, from Table 1 in Rignot et al., 2008) Gt/yr is due to the glaciers bounded by the ice sheet (this is the base calving rate). Katsman et al. (2011) assume the same initial storyline as for the western sector. After this period exponential growth is expected. The integrated contribution to sea level rise by 2100 would be 0.19 m. Under these constraints we find 0.0385 in the exponent for the post-2030 rate,

$$D_{s_{\mathrm{ii}}}(t) = 388 + \\ 388 \cdot \begin{cases} (1.013)^t - 1 & t \leq 30 \\ \left[(1.013)^{30} - 1\right] \cdot e^{0.0385 \cdot (t-30)} & t > 30 \end{cases} \mathrm{Gt/yr}. \tag{2.12}$$

**Antarctica iii** Assuming an effect of 0.05m sea level rise by 2100 Katsman et al. (2008), with again assuming the same structure of the equation for the region ii, we find 0.0375 for the exponential rate,

$$D_{s_{\mathrm{iii}}}(t) = 107 + \\ 107 \cdot \begin{cases} (1.013)^t - 1 & t \leq 30 \\ \left[(1.013)^{30} - 1\right] \cdot e^{0.0375 \cdot (t-30)} & t > 30 \end{cases} \mathrm{Gt/yr}. \tag{2.13}$$

The scaling functions for the discharge amount associated with each of the above three regions are shown in Figure 2.4.

The combined discharge rates are shown in Figure 2.5. An accumulation balancing rate of 107 Gt/yr is given by Rignot et al. (2008). The effect of increased snow accumulation on Antarctica during the immediate future (as indicated by observations Church et al., 2013) would mean a larger potential value for $D$. Measurements from Rignot and Kanagaratnam (2006) and Rignot et al. (2008) are shown as well in Figure 2.5. More

[2]Katsman et al. (2011) quote 8 as an upper bound, and $8 = 6 \times 237/177$, the fraction of the 2000 outflow to the input. The balance value they speak of is the input rate.

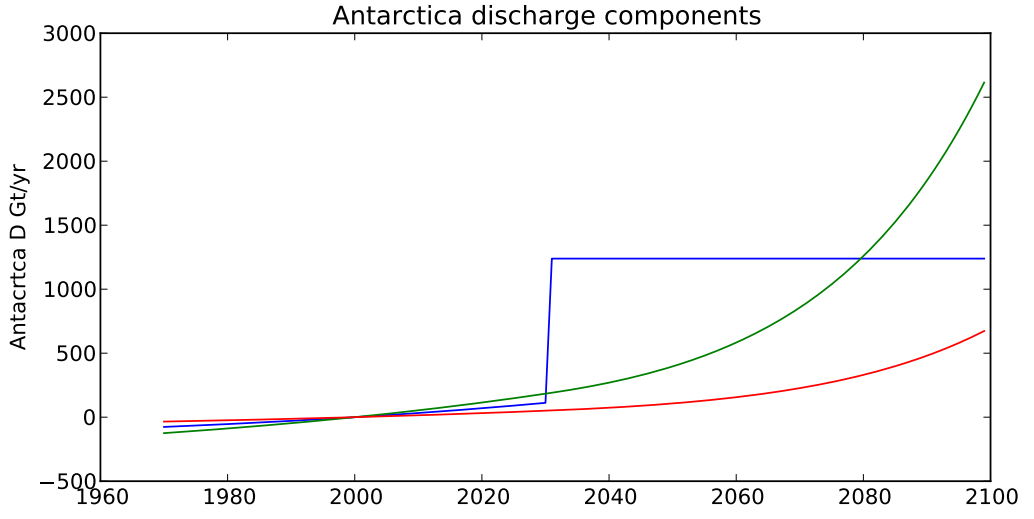


Figure 2.4: Scaling functions of the components of ice discharge ($D$) for Antarctica. In blue $D_{s_{\mathrm{i}}}$, green $D_{s_{\mathrm{ii}}}$, red $D_{s_{\mathrm{iii}}}$.

recent overviews (Shepherd and Wingham, 2007; Shepherd et al., 2012) show considerable variation in the Greenland and Antarctic mass balance measurements. Because the sampling was performed during different periods and does not include all ice sheets, we have left these from further consideration.

**Prescription of near-deposition** $N$

The progression of $D$ in Figure 2.4 shows the collapse of the West Antarctic Ice Sheet. The discharge rate increases dramatically with this event. With the ice sheet gone, calved icebergs drift more easily. We expect basal melt to decrease then. On the other hand, more land ice is in contact with the ocean, which should increase the absolute amount of melt taking place. Without any way of quantifying either effect, we suggest that after a collapse event the basal melt amount returns to pre-collapse levels. The expression becomes

$$N_{s_{\mathrm{i}}}(t) = \begin{cases} \mu_{\mathrm{i}} \cdot D_{s_{\mathrm{i}}}(t) & t \leq 30 \\ \mu_{\mathrm{i}} \cdot D_{s_{\mathrm{i}}}(30) & t > 30 \end{cases} \quad \mathrm{Gt/yr} \tag{2.14}$$

for the WAIS (region i), where $\mu_W = 0.30$. Similar considerations to those above lead us to keep the amount of basal melt steady at the 2030 levels for the other two regions, which then give the exact same form as Eq. 2.14 with the appropriate $\mu$ values (Table 2.2).

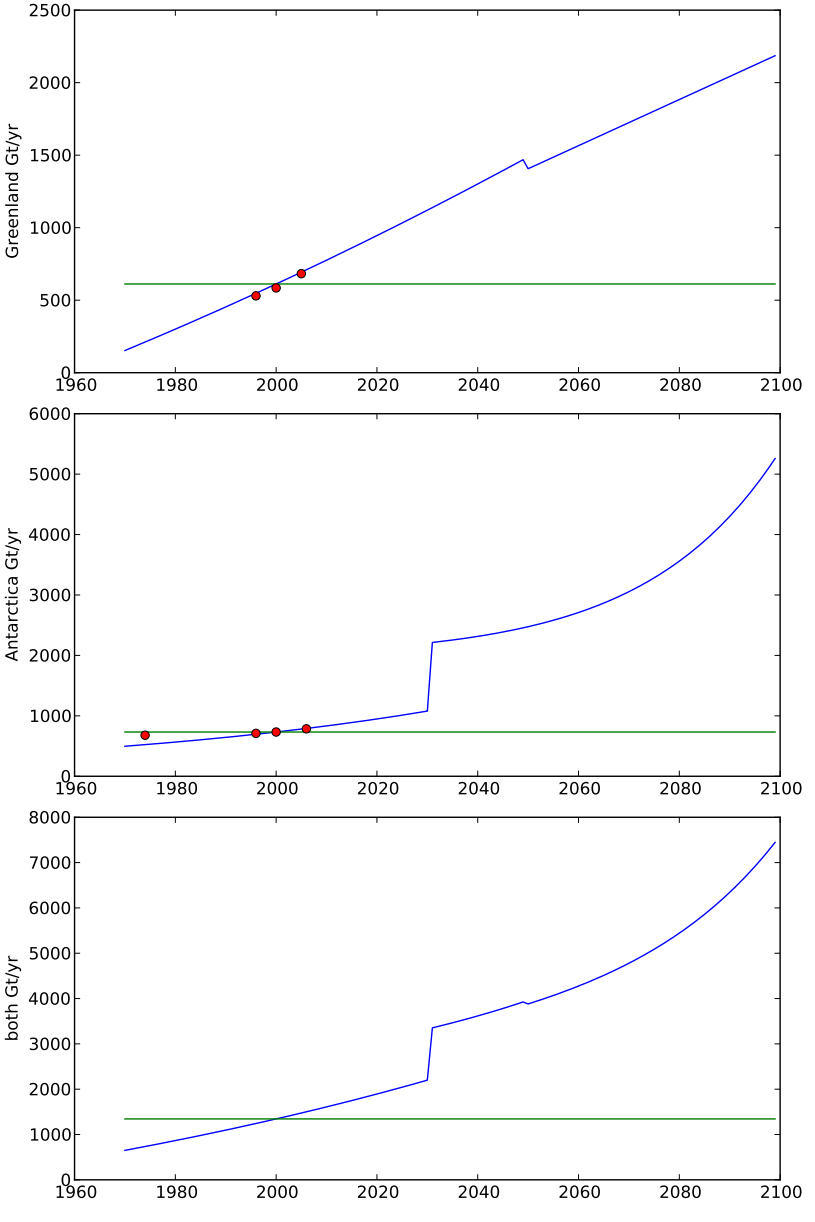


Figure 2.5: Mass loss for Greenland, Antarctica and their sum. The horizontal lines show the equilibrium values. Some measurements are shown as well. These were taken from Rignot et al. (2008) for Antarctica and from Rignot and Kanagaratnam (2006) for Greenland. The Greenland values were obtained by assuming the mass balance differences are entirely attributable to ice discharge changes in regions i and ii. Uncertainties in the original measurements are $\sim 10\%$.

**Prescription of far-deposition $F$**

Far-deposition is allocated to all mass loss not already claimed by basal melt. The expression for Antarctic $F$ is then simply

$$F_s(t) = \begin{cases} (1-\mu_s)\cdot D_s(t) & t \le 30 \\ D_s(t) - \left(\mu_s \cdot D_s(30)\right) & t > 30 \end{cases} \quad \text{Gt/yr.} \tag{2.15}$$

for all three regions with $\mu_s$ replaced by the appropriate basal melt fraction and $r_s$ the corresponding discharge rate.

Table 2.4 gives a summary of the melt scenario features on which our projections are based.

### 2.3.3 Comparison with other projections

In Table 2.5 a breakdown of mass loss expressed as sea level equivalent is given. We can compare with some other severe scenarios, see Figure 2.6. The most recent scenarios are by Pfeffer et al. (2008), and by Katsman et al. (2011). A projection close to the values given by Pfeffer et al. (2008) as upper bounds would tax the rate of retreat of the tidewater glacier to nonphysical limits. The lower bound from Fettweis et al. (2013) only takes meltwater into account. The projections for ice discharge dominate this by an order of magnitude.

## 2.4 Effect on the sea surface

To illustrate the effect of the freshwater protocol outlined above, we ran a RCP8.5 experiment with the CCM EC-Earth (Hazeleger et al., 2010). One simulation was run without the extra freshwater forcing applied (*control*) and one with additional freshwater forcing included (*forced*) to allow for a sensitivity experiment. The control run is part of the CMIP5 archive and both runs use the RCP8.5 forcing a described in Taylor et al. (2012).

We expect the additional freshwater to immediately affect local sea surface height and through barotropic effects to propagate information throughout the world ocean (Stammer et al., 2011; Lorbacher et al., 2012). The freshwater might also affect ocean currents.

In the forced run the North Atlantic subpolar gyre remains weakly affected for a considerable time. It is not until 2075 that the mean sea level rise is comparable to the local rise in the gyre (not shown). The reason for this is that most of added the freshwater is taken away by boundary currents in the Northern Hemisphere. The same can be seen in other experiments of comparable resolution with Greenland freshwater release like Stammer et al. (2011), Kopp et al. (2010), Weijer et al. (2012), and Swingedouw et al. (2013a).

A climate model is a chaotic system and shows sensitivity to small variations in initial conditions. An ensemble of runs can bring out the so called internal variability. We have used such an ensemble of control runs to determine the variance in the SSH. In Figure 2.7

| | Region | Now | Future |
|---|---|---|---|
| SMB | Greenland | 416 Gt/yr | linear increase |
| Calving | northern tw. glaciers (i) | 69.5 Gt/yr | " |
| | eastern/southern tw. glaciers (ii) | 81.7 Gt/yr | linear increase until 2050, then return to current value |
| | other glaciers (iii) | 36 Gt/yr | linear increase |
| Basal melt | northern tw. glaciers (i) | 0 | 0 |
| | eastern/southern tw. glaciers (ii) | 0.25 | scale with calving rate |
| | other glaciers (iii) | 0.25 | " |
| SMB | Antarctica | in equilibrium | unchanged |
| Calving | WAIS (i) | 237 Gt/yr | acceleration until 2030, then kept constant |
| | EAIS (ii) | 388 Gt/yr | acceleration until 2030, then mild exponential increase |
| | N-AP (iii) | 107 Gt/yr | " |
| Basal melt | WAIS (i) | 0.30 | scale with calving rate until 2030, then kept constant |
| | EAIS (ii) | 0.15 | " |
| | N-AP (iii) | 0.40 | " |

Table 2.4: Summary of the melt scenario characteristics. Details are given in the text and figures.

| | Greenland (mm) | | | | | Antarctica (mm) | | | |
|---|---|---|---|---|---|---|---|---|---|
| | $R$ | $D_i$ | $D_{ii}$ | $D_{iii}$ | | $D_i$ | $D_{ii}$ | $D_{iii}$ | |
| 2000 | 0 | 0 | 0 | 0 | | 0 | 0 | 0 | |
| | | | | | 0 | | | | 0 |
| 2005 | 0.32 | 0.16 | 0.14 | 0.18 | | 0.11 | 0.18 | 0.049 | |
| | | | | | 0.80 | | | | 0.34 |
| 2020 | 5.2 | 2.6 | 1.2 | 1.6 | | 1.9 | 30 | 0.84 | |
| | | | | | 11 | | | | 33 |
| 2030 | 11.6 | 5.8 | 2.4 | 3.2 | | 4.4 | 7.2 | 2.0 | |
| | | | | | 23 | | | | 14 |
| 2050 | 32 | 16 | 6.0 | 8.1 | | 73 | 23 | 6.2 | |
| | | | | | 62 | | | | 102 |
| 2100 | 130 | 64 | 6.0 | 30 | | 245 | 190 | 50 | |
| | | | | | 230 | | | | 485 |

Table 2.5: Comparison of sea level equivalent rise (mm) per contributor region for a selection of years. Discrepancies in the added numbers are due to round-off error. Columns 6 and 10 are the sums of columns 2 – 5 and 7 – 9 respectively.

the areas where the rise does not exceed $2\sigma$ are mapped onto the eustatic sea level, where the whitepoint is centred. The model allows for a free-surface adjustment which shows an increase of SSH with the addition of more freshwater as can be seen in the lower panel.

The response to the freshwater forcing is largely advective with the mean subpolar gyre circulation transporting the melt water southward. This can be seen by the comma shaped feature present in both panels and lying more to the east in the lower one. To the west and south of the subpolar gyre the sea surface anomaly is larger than within the gyre, or to the north. The west-to-east gradient in the North Atlantic with a strong anomaly along the northeast coast of North America, as noted in Kopp et al. (2010), can also be seen in the top panel of Figure 2.7.

The lower panel, which depicts the situation for the last five years of the century, shows an opposite pattern. Here, a positive anomaly on the eastern side of the Atlantic basin can be seen. The formation/inversion of this pattern is also present in the atmosphere-coupled run discussed in Stammer et al. (2011). A strong signal develops along the American coast and a signal similar to the one in the lower panel of Figure 2.7 can be seen after four decades (see also Swingedouw et al. (2013a) for a comparison between several models showing a similar pattern).

The additional freshwater does not impact the Atlantic Meridional Overturning Circulation (AMOC). In Figure 2.8 the annual mean of of its maximum value is shown

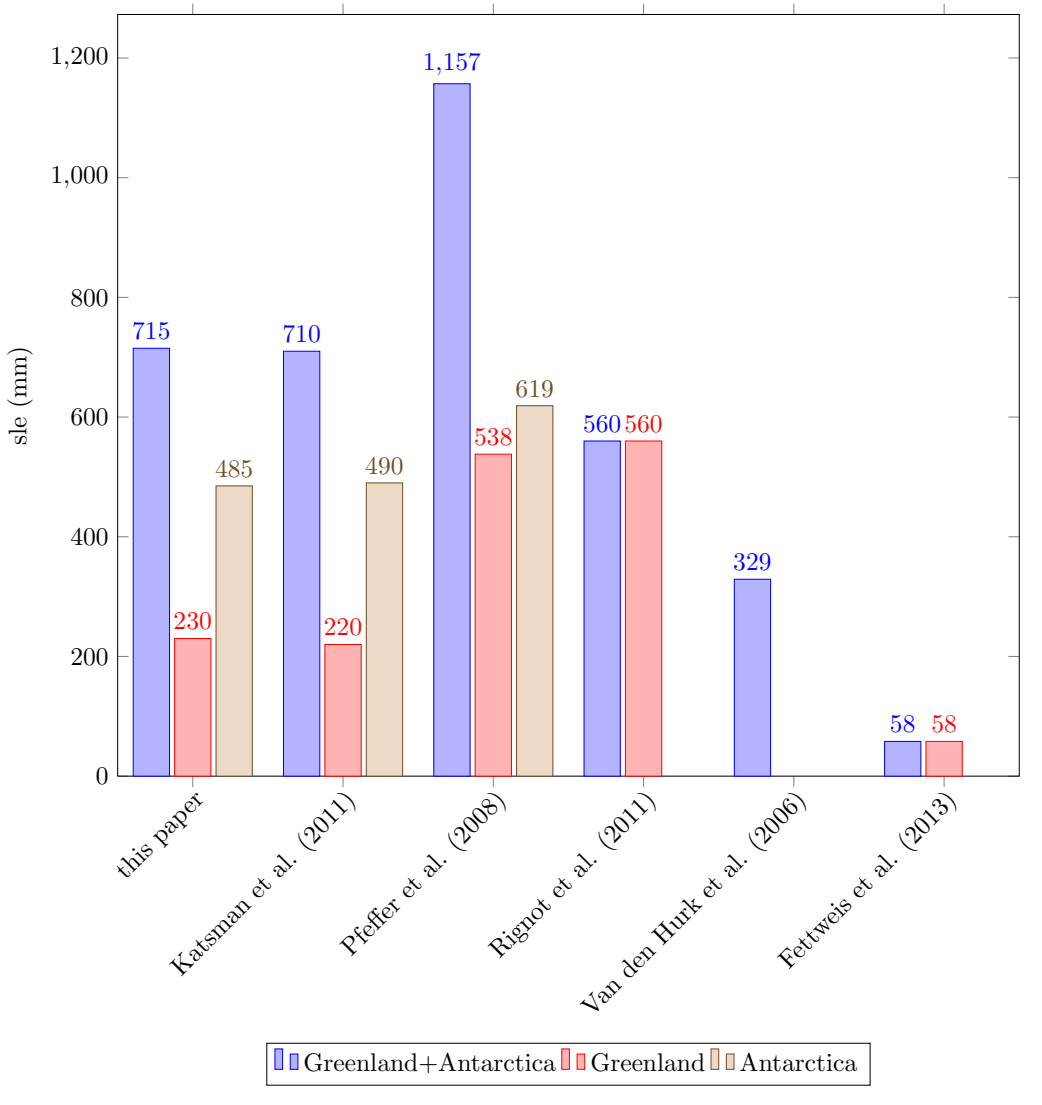


Figure 2.6: Histogram comparison of different mass loss projections. The cited sources are Katsman et al. (2011), Pfeffer et al. (2008), Rignot et al. (2011), Van den Hurk et al. (2007) and Fettweis et al. (2013).

for the RCP8.5 only run (green) and with the freshwater added (blue). The difference (red) indicates little difference between the two. The maximum mixed layer depth (not shown) shows some decrease in the Labrador region and an increase north of Iceland, but this effect is highly variable. We surmise that most of the freshwater does not reach the convection regions and has little impact on dense water formation. We cannot ascertain

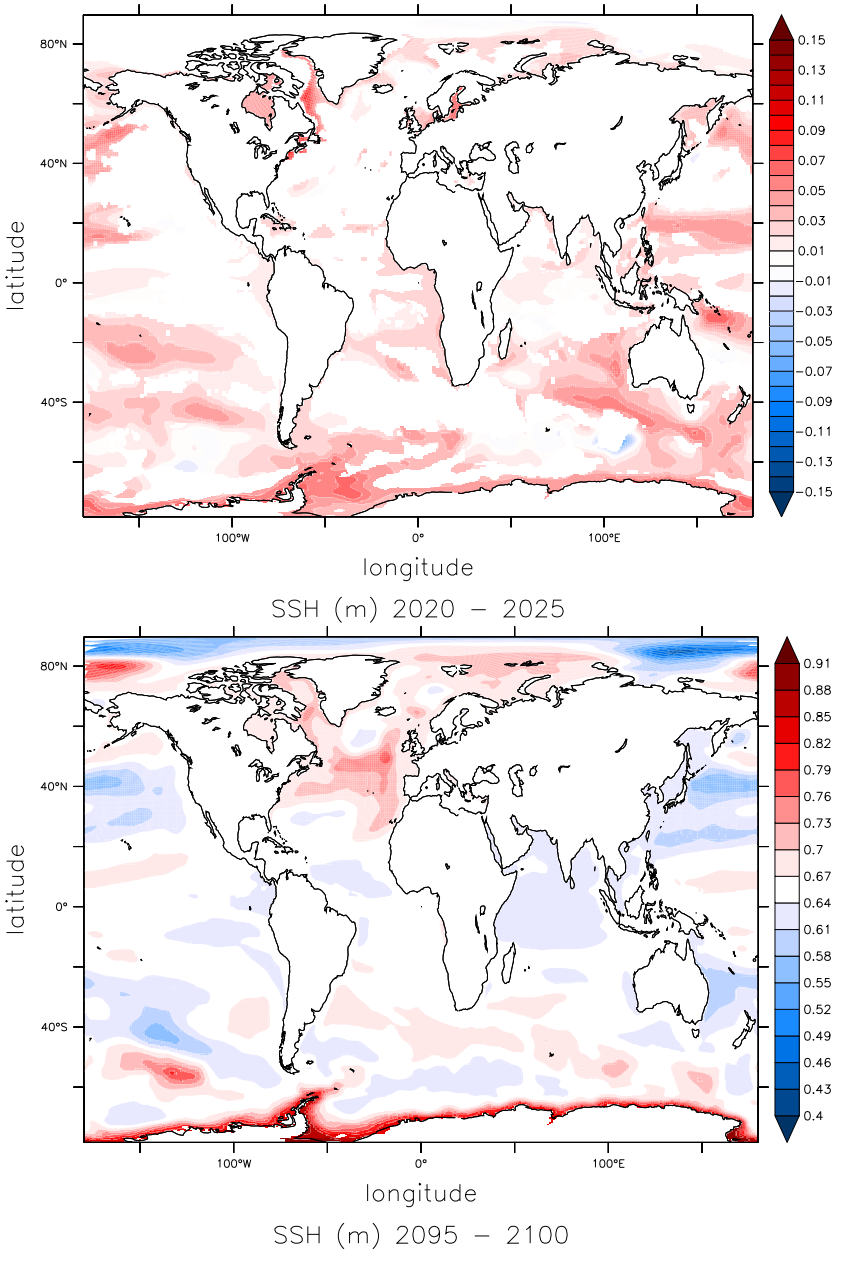


Figure 2.7: Top panel: sea surface height anomalies of 5-year averages for the indicated period. Lower panel: the situation in 2095 (the whitepoint corresponds to the eustatic sea level rise). The Arctic consistently lags behind the rest of the ocean in rise. Non-significant rises (at the $2\sigma$ level with respect to an ensemble of RCP8.5 forced control runs) are mapped onto the eustatic level, the whitepoint.

whether spatial changes occur as a result of this (i.e. the possible shifting north of the convection regions).

The signal in the eastern North Atlantic is described in Swingedouw et al. (2013a) where the authors show that the leakage (i.e. removal of freshwater that then does not re-circulate) relates to the meridional tilt of the separation between the subpolar and the subtropical gyre. The leakage via the Canary Current (the eastern branch of the pattern) diminished the amount of freshwater that is transported to the convection sites in the Labrador Sea and Nordic Seas and could then affect the intensity of deep convection if the leakage is sufficiently large. This also occurs in EC-Earth.

The long-term pattern of freshwater in our forcing field as shown in Figure 2.7 resembles the observed anomaly in sea level rise near the Antarctic ice shelves shown in Figure 1 in Rye et al. (2014). The only conspicuous difference is that we have a somewhat larger melt in the northern peninsula region. The gross Antarctic sea level rise pattern in Rye et al., 2014 is also present in our simulation. In the Southern Hemisphere, the freshwater released along the coast of Antarctica spreads northward and is thereafter taken up by the Antarctic Circumpolar Current (ACC), spreading it in a band around Antarctica. The same pattern around Antarctica can be seen in the simulation described in Lorbacher et al. (2012), where the fast response to Antarctic melt occurs on a timescale of mere days. This is remarkable because the fast response is due to barotropic waves and not directly related to the long-term response. In Figure 3 in Rye et al. (2014) the sea level rise in a model output indicates locally larger relative rise than is in our simulation.

## 2.5 Discussion

Recent experiments with high resolution, eddy-resolving, models (Weijer et al., 2012; Spence et al., 2013; Den Toom et al., 2014) indicate qualitative differences in large-scale circulation compared with coarse-resolution ones ($\sim 1°$) like EC-Earth. The circulation shows different ventilation pathways (Spence et al., 2013) of North Atlantic Deep Water (NADW), which is not surprising given the finer topography and different diffusion value needed. Also, deep convection regions persist longer at higher resolution (Weijer et al., 2012; Spence et al., 2013). The entrainment along the western boundary lasts longer compared to a low resolution model which favours a more immediate transport to the deep convection zones (Spence et al., 2013). The short term response in a high resolution model can be different, but this does not necessarily mean a significant difference in behaviour on decadal timescales (Weijer et al., 2012). Caveats like these suggest that a significant improvement in realism can be expected when high resolution models are coupled with atmospheric models (Den Toom et al., 2014), which has not been feasible so far.

Nevertheless, our run does show similarities with higher resolution (Den Toom et al., 2014). We can compare with the results of another freshwater forcing experiment in the same vein, which indicates only little impact on the large-scale circulation (Marsh et al.,

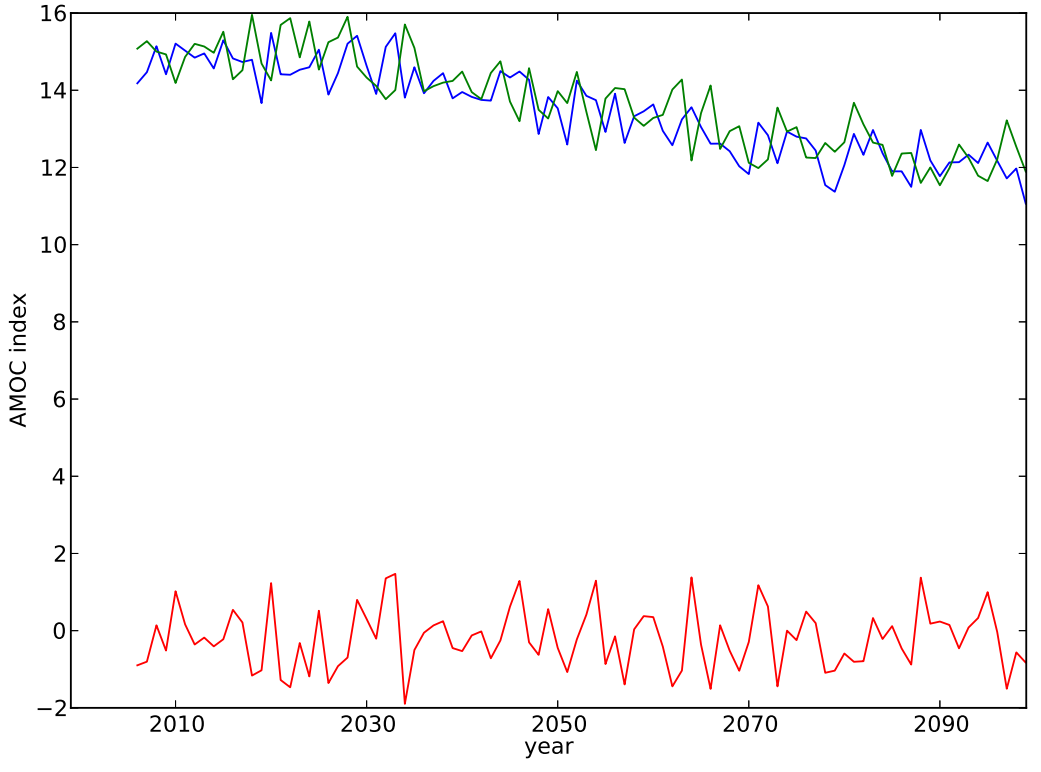


Figure 2.8: The maximum of the annually averaged Atlantic Meridional Overturning Circulation. Blue shows the run with freshwater forcing, green without, and red the difference between the two.

2010). There, the additional freshwater accumulates west of Greenland and leaves the subpolar gyre largely unaffected. The same effect is seen in our simulation (Figure 2.7).

Ice mass loss like in our scenario does not lead to significant decrease in the height of the ice sheet. We therefore do not expect any changes in the feedbacks between the ice sheet and the atmosphere. Since retreat of glaciers does affect the interaction with the ocean (at least locally), some feedbacks will be affected by ice melt. We try to account for one of these, basal melt, but a detailed treatment requires more advanced modelling.

Climate scenarios contain a lot of uncertain elements. Such scenarios are also subject to change. By being as precise as possible we hope to accommodate future scenarios.

## 2.6 Summary

We have presented a simple, yet flexible way to apply a patterned freshwater forcing to the ocean surface based on realistic, yet high-end, Greenland and Antarctica mass loss scenarios. The projection of run-off ($R$), basal melt ($B$), and ice discharge ($D$) in excess

of balanced values—which have not been met in Greenland for the past twenty years—show an increase in the calving rates of both the Antarctic and Greenland glaciers. The final contributions of excess production of $R$, $B$ and $D$ remain within the maximum bounds determined by Pfeffer et al. (2008). In the scenario we used, it was assumed that a collapse of the West Antarctic Ice Sheet occurs, which will accelerate mass loss tremendously before mid-century. The total mass loss from the two large ice sheets becomes dominated by the ice discharge contribution.

The sea surface height in the subpolar gyre in the North Atlantic is affected only little, with a smaller than average increase throughout the 21$^{st}$ century. The area around Antarctica sees a steady increase on the other hand, and maximal values can be found there. This is due to the large forcing in the region associated with iceberg calving in the scenario.

The protocol we have proposed aims to provide an affordable way to extent the current numerical models to deal with melting ice sheets. Effects like a realistic spatial pattern of freshwater accumulation are encouraging.

## Acknowledgements

Thanks go out to Wilco Hazeleger, Roderik van de Wal, Camiel Severijns, and especially Caroline Katsman, for useful comments and suggestions. The authors also thank Bob Marsh and Vladimir Ivchenko for contributing their iceberg simulation. This work was funded by the European Commission's 7th Framework Programme, under Grant Agreement number 282672, EMBRACE project.

## 2.A Implementation

In the previous sections we developed a description for time series of location dependent freshwater forcing, derived from projections of meltwater run-off ($R$), basal melt ($B$), and iceberg calving ($D$). Because these quantities are either applied to a location near the source or further away from it, we constructed the $N$ and $F$ prescriptions. The scaling regions' mass loss can be scaled independently according to the above scenarios. To implement the projections we have to account for any freshwater forcing already applied in the model. Most climate models balance snow accumulation on Greenland and Antarctica with a prescribed run-off. We propose to start at time zero (year 2000) with a freshwater flux that balances the already prescribed flux in the model, only changing the spatial distribution. Afterwards we allow for a growing imbalance between snow accumulation and freshwater gain according to our melt projections.

### 2.A.1 Iceberg drift

The far-deposition $F$ of freshwater forcing needs a prescribed annual pattern. Output of a simulation of iceberg drift by Marsh et al. (2015) provides this pattern and the amount of melt loss. These authors have determined the amount of meltwater from icebergs at every cell on the grid of a $2° \times 2°$ ocean model Madec (2008). The pattern thus obtained is an annual one. We subdivide the iceberg pattern in a Northern and a Southern Hemispheric region. We assume that all freshwater flux found north of the equator is attributable to Greenland mass loss and likewise all found south of the equator is attributable to Antarctic sources. Because the forcing pattern (Figure 2.9) alone does not contain any information about the original source of icebergs, the scaling of the far-deposition $F$ can only be applied per hemisphere.

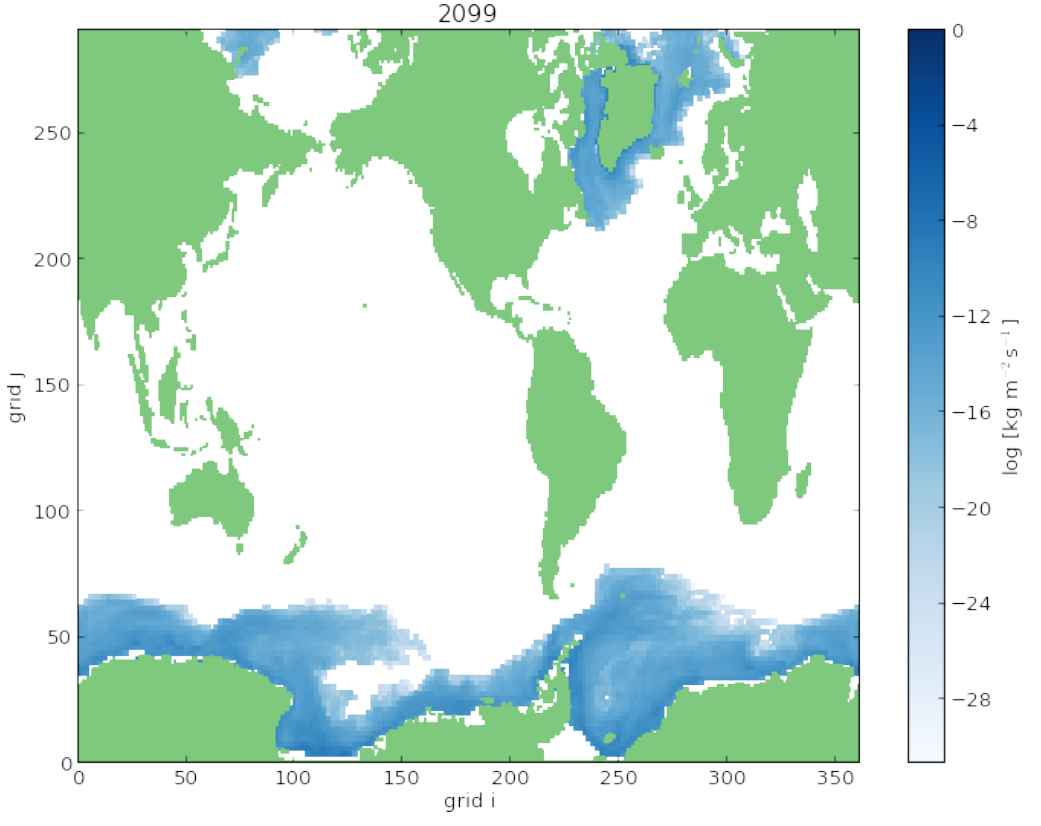


Figure 2.9: Annual average of the iceberg pattern used to distribute the far-deposition $F$ of freshwater forcing amount in EC-Earth. Darker blue indicates a greater relative amount is deposited.

The basal melt pattern only varies within a single year, meaning we can scale the seven region dependent contributions of $N$ according to their individual annual prescription.

The spatial pattern of freshwater forcing from iceberg melting is obtained from the output of an iceberg tracking simulation. Because only the pattern is of interest (the total amount of mass loss due to icebergs is normalised), we do not need to regrid the iceberg melt in a strictly conservative way, but only approximately. Instead we simply locate the original gridcell nearest to a target gridcell and use the value it has (we do scale with the area of each gridcell).

### 2.A.2 Scaling and distribution

Our starting point is maintaining (approximate) continuity with historical conditions. We demand that our scenarios for $t = 0$ (year 2000) have equal amounts of freshwater forcing as the total of prescribed run-off around Greenland and Antarctica in the model forcing. We note that the observational estimates for present day mass loss (in our scenarios the value at t=0) may differ from the model's total sum. When replacing these, we maintain the relative ratios for basal melt, iceberg calving and run-off obtained from the observations, but rescale the total observed mass loss to match the total in the model. The relative contributions in the scenario projections are given in Table 2.6.

| | Greenland | | | | Antarctica | | |
|---|---|---|---|---|---|---|---|
| | $D_{n_{\mathrm{i}}}$ | $D_{n_{\mathrm{ii}}}$ | $D_{n_{\mathrm{iii}}}$ | $R$ | $D_{s_{\mathrm{i}}}$ | $D_{s_{\mathrm{ii}}}$ | $D_{s_{\mathrm{iii}}}$ |
| amount (Gt/yr) | 69.5 | 81.7 | 36 | 416 | 177 | 388 | 107 |
| fraction | 0.69 | 0.12 | 0.14 | 0.06 | 0.26 | 0.58 | 0.168 |

Table 2.6: The initial ($r_0$) run-off and ice discharge values (in Gt/yr, total of 1274.54 Gt/yr) and their fractional share of the Antarctic or Greenland part (or hemispheric share). The total initial amount of freshwater forcing should be kept the same at time = 0 to ensure hydrological balance in the model.

#### Run-off

In our scenario only Greenland experiences run-off. This will be distributed equally along Greenland's coastal gridcells, a single cell wide. Any Antarctic run-off would be negligible with respect to other melt loss processes, since a mass increase seems more likely (Church et al., 2013).

### Iceberg melt flux

We cannot distinguish the origin of icebergs any finer than from which hemisphere they originate. We simply sum the far-deposition for north and south and scale the iceberg melt flux in each half of the globe,

$$F_n(t) = F_{n_{\mathrm{ia}}}(t) + F_{n_{\mathrm{i}\backslash\mathrm{a}}}(t) + F_{n_{\mathrm{ii}}}(t) + F_{n_{\mathrm{iii}}}(t) \tag{2.16}$$

$$F_s(t) = F_{s_{\mathrm{i}}}(t) + F_{s_{\mathrm{ii}}}(t) + F_{s_{\mathrm{iii}}}(t). \tag{2.17}$$

The fractions listed in Table 2.6 provide the relative weights that each region should have. In the final expressions for $F$, the initial values reported in Section 2.4 are replaced with the fractions of total mass loss due to ice discharge specific to the model.

### Basal melt deposition

To provide a correct deposition of the basal melt freshwater we need to take the relative strength of discharge into account. We take the values for the ice discharge as presented in Rignot and Kanagaratnam (2006) for Greenland and assign the locations given to the nearest gridcell in a mask of the grid layout as used in our model. Masks are then made for the relevant Greenland and Antarctic regions, so that we are able to independently control the melt intensity of each.

For each region a collection of point sources is defined to determine the basal melt freshwater release location in Figure 2.10. In the case of a glacier this would be a single point, in a region such as the North Antarctic Peninsula several points. By associating an area of deposition (set to a default of 2000 km$^2$ for each point source) with each source, we can enumerate the nearest gridcells and subtract their area until exhaustion of the deposition area. We use the Euclidean distance to weigh the relative amount of meltwater that is to be deposited in each gridcell. A cell nearer to the source receives more mass. The point sources and associated variable values are given in Table 2.7 for Greenland and in Table 2.8 for Antarctica. In this way a zone of deposition can be defined. The basal melt pattern consists of six regional contributions, each with an independent scaling (scaling region).

In addition, we wish to take the presence of sills into account because they might act as a barrier and trap water. For each gridcell that is enumerated, we define the line of gridcells between it and the source cell (a linear equation of the latitude/longitude coordinates). We then attempt to locate the sill as the barrier nearest to the source. A barrier is defined as an ocean gridcell where the depth is less than the depth associated with the cell closer to the source in the line, effectively a bump in the bottom topography. All gridcells belonging to the line before the sill are used as the deposition area. The typical number of cells per point source is one or only a few gridcells for a $1° \times 1°$ grid.

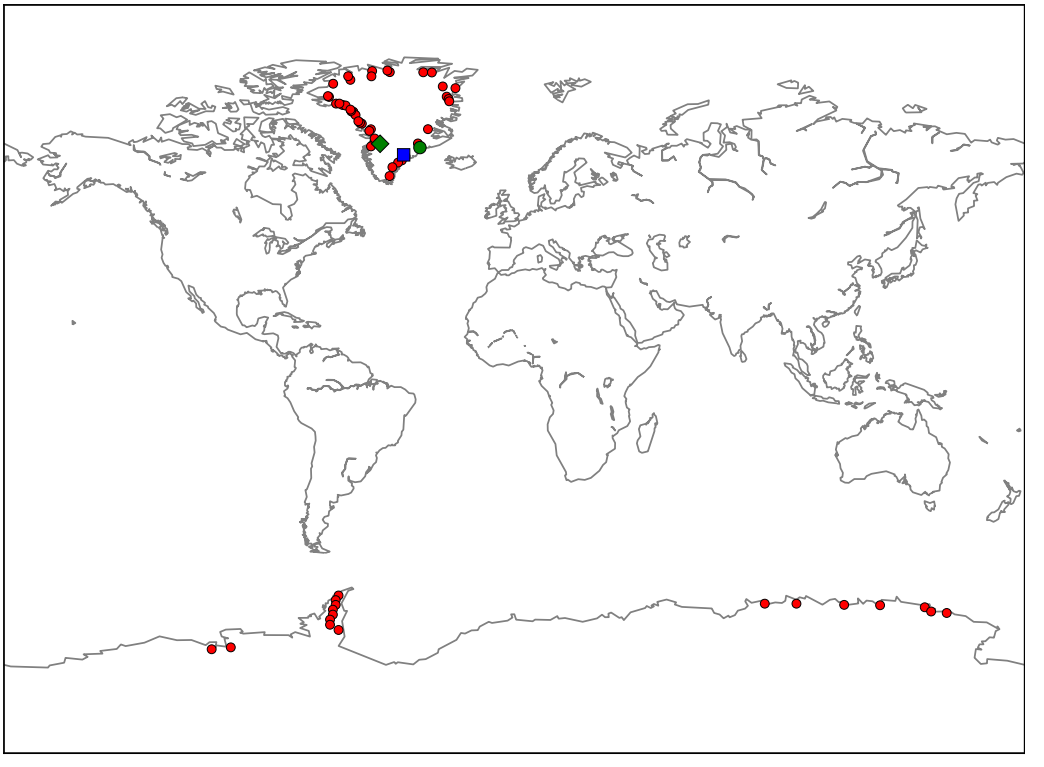

Figure 2.10: Points used to determine mass deposition areas. Indicated with a green diamond is Jakobshavn, with a blue square Kangerdlugssuaq, and with a green circle Helheim. Actual freshwater fluxes (e.g. run-off) are not shown.

### 2.A.3 Seasonality

Surface melt does not occur throughout the year, but tends to be limited to summer. We model this restriction with a seasonality function, for which we assume a step distribution $\sigma$. For the Northern Hemisphere we take summer to start in May, ending in September, and for the Southern Hemisphere beginning in November, ending in March. We correct for this by scaling annual values with a factor 2.4 (=12/5) during summer. During summer the function is 'on' and otherwise 'off',

$$\sigma(t) = \begin{cases} 2.4 & \text{summer(t)} \\ 0 & \text{winter(t).} \end{cases} \tag{2.18}$$

The seasonality function must be multiplied with $N$. Care must be taken that the total amount of mass loss in a year remains the same as in the original prescription.

### 2.A.4 Synthesis

The final product is a time series of freshwater forcing per gridcell. No explicit reference during run time of the simulation is needed to the various expressions and regions we have distinguished here. All gridcells where no value is defined receive a value of 0, and all separately scaled contributions are summed to a single time dependent pattern. This time series can now be used as a forcing field to mimic a realistic freshwater forcing as the result of, not only meltwater, but also iceberg calving and the basal melt associated with them.

The recipe consists of the following steps

1. remove the existing freshwater forcing associated with Greenland and Antarctica;
2. set the $r_0$ values to match the loss in any previous freshwater forcing to maintain balance;
3. for each region in Greenland and Antarctica: mask region and multiply with the projection value;
4. for the Northern and Southern Hemisphere: sum the projections in each (according to Eqs 2.16 and 2.17) and scale the hemispheric pattern with this sum; the forcing is applied to the surface as additional water with local temperature;
5. apply the sum of the series as a freshwater forcing to the ocean model.

## 2.B Mass loss point sources

| region | position ($\phi$, $\lambda$) | size (km$^2$) | $D$ (Gt/yr) | name |
|---|---|---|---|---|
| $D_{n_{ia}}$ | (68.9, -47.3) | 8000 | 27 | Jakobshavn Isbræ |
| | (69.1, -49.4) | | | |
| | (69.2, -48.2) | | | |
| | (69.2, -47.7) | | | |
| $D_{n_{ii}}$ | (77.6, -23.9) | 6000 | 6.8 | Storstrømmen |
| | (77.2, -23.2) | | | |
| | (76.8, -22.9) | | | |
| | (71.8, -30.5) | 2000 | 10.5 | Daugaard-Jensen |
| | (68.2, -33.3) | 4000 | 27.9 | Kangerdlugssuaq |
| | (69.0, -34.0) | | | |
| | (66.7, -39.0) | 4000 | 26.2 | Helheim |
| | (66.4, -38.4) | | | |
| | (65.5, -39.7) | 2000 | 10.3 | Ikertivaq |
| $D_{n_{iii}}$ | (65, -41) | 6000 | 67.4 | |
| | (64, -43) | | | |
| | (62, -44) | | | |
| | (68.4, -50.6) | 2000 | 10.7 | Nordenskiold |
| | (70.0, -49.3) | 2000 | 10.9 | Sermeq Kujatdleq |
| | (71.5, -51.1) | 2000 | 2.7 | Kangerdlugssup |
| | (71.8, -50.6) | 2000 | 12.1 | Rinks |
| | (72.8, -53.8) | 4000 | 8.6 | Upernavik |
| | (73.0, -54.4) | | | |
| | (73.3, -55.0) | 2000 | 4.7 | Nunatakavasaup |
| | (74.4, -56.0) | 2000 | 7.1 | Igdlugdlip |
| | (74.9, -56.7) | 6000 | 10.9 | Hayes |
| | (75.0, -56.8) | | | |
| | (75.0, -57.4) | | | |
| | (75.1, -57.6) | 4000 | 1.3 | Steenstrup |
| | (75.4, -57.8) | | | |
| | (76.1, -59.5) | 2000 | 8.5 | Kong Oscar |
| | (76.2, -60.5) | 2000 | 8.5 | Peary/Docker |
| | (76.4, -62.9) | 2000 | 3.3 | Gades |
| | (76.4, -61.7) | 2000 | 64.4 | |

Table 2.7: Point sources used to define the basal melt regions in Antarctica. Several points can belong to a single glacier if it is extended over a large area. The area is the surface in km$^2$. The discharge values were taken from Rignot and Kanagaratnam, 2006.

| region | position ($\phi$, $\lambda$) | size (km$^2$) | $D$ (Gt/yr) | name |
|---|---|---|---|---|
| $D_{s_i}$ | (-75.2, -100) | 4000 | 87 | WAIS |
| | (-75.5, -106.7) | | | |
| $D_{s_{ii}}$ | (-66.8, 88.3) | 4000 | 87 | EAIS |
| | (-66.8. 99.5) | | | |
| | (-67, 116.3) | 4000 | 94 | |
| | (-67.1, 129) | | | |
| | (-68.7, 152.5) | 6000 | 237 | |
| | (-67.5, 144.8) | | | |
| | (-68.4, 147) | | | |
| $D_{s_{iii}}$ | (-65, -62) | 16000 | 107 | N-AP |
| | (-66, -63) | | | |
| | (-67, -63) | | | |
| | (-68, -64) | | | |
| | (-69, -64) | | | |
| | (-70, -65) | | | |
| | (-71, -65) | | | |
| | (-72, -62) | | | |

Table 2.8: Point sources used to define the basal melt regions. The area is the surface in km$^2$.

# 3 Atlantic salinity budget in response to Northern and Southern Hemisphere ice sheet discharge

## 3.1 Introduction

The climate warms due to anthropogenic emissions of greenhouse gasses and, as a consequence, the ice sheets on Greenland and Antarctica are expected to loose mass (e.g. Joughin and Alley, 2011). Mass losses may increase further due to non-linear effects associated with ice sheet interactions with the atmosphere and ocean (see Hanna et al., 2013, for an overview). Upper limit estimates go as far as a 1 m global mean sea level rise from Antarctica alone by 2100 and > 10 m by 2500 (DeConto and Pollard, 2016). The response to ice cap melting in the climate system is not well understood, since most climate models used for projections do not incorporate the complex interactions that lead to increased ice loss from the ice sheets. In principle, coupled climate models (CCMs) could simulate such mass loss by including ice sheet (see Vizcaino, 2014) and iceberg modules that simulate calving and iceberg drift in response to changing atmospheric and ocean temperatures. The current generation of CCMs used in the CMIP5 ensemble, and likely used in the CMIP6 ensemble (Eyring et al., 2016), is not equipped with such modules and therefore cannot simulate the mass loss of ice sheets to the ocean interactively with the other components of the climate system.

An alternative to explicit modelling ice mass loss is to prescribe the freshwater release from the large ice sheets to the ocean by estimating the amount of mass loss under present and future conditions. Examples of such approaches are Bakker et al. (2016), Marsh et al. (2010), Swingedouw et al. (2013a), Stammer (2008), Stammer et al. (2011), and Weijer et al. (2012) where Greenland meltwater was applied to Greenland coastal grid cells of numerical ocean models. The latter three studies have the intensity of the forcing vary around the coast to reflect the non-uniform meltwater run-off. In Stammer (2008) mass loss from Antarctica was also included (with a similar approach in Stammer et al., 2011, using a coupled atmosphere-ocean model). Also, in each study the total amount of

freshwater release was varied within a range of values to determine the sensitivity of the ocean circulation to a set of idealised forcing scenarios.

In this paper the effect of a more plausible freshwater release scenario to the ocean is assessed for the coming century using a coupled-climate model (Van den Berk and Drijfhout, 2014). After the year 2100 the forcing reverses, which is clearly no longer realistic, but would reveal effects operating on multi-decadal or centennial timescales. Different from earlier studies is the use of a spatial pattern of freshwater release occurring for a large part outside the coastal area to reflect the meltwater deposition due to iceberg drift. This pattern has the effect that less meltwater is directly applied around the coasts of Greenland and Antarctica and more freshwater reaches the open ocean where deep water formation takes place in the coupled model, potentially affecting the global circulation. We vary the amount of freshwater release over time (with a seasonal cycle) in accordance with the RCP8.5 emission scenario (Riahi et al., 2011; Taylor et al., 2012). The increase is not uniform, with separate areas, such as the West Antarctic Ice Sheet and individual glaciers, having different projections. The mass loss from Antarctica is typically three to four times larger than the mass loss associated with Greenland, reaching more than 1 Sv ($=10^6$ m$^3$ s$^{-1}$) towards 2100.

Earlier work that compared the effects of Greenland and Antarctic mass loss (e.g. Stouffer et al., 2007; Hu et al., 2013) noted that the Southern Ocean winds induce a northward transport that transfers Antarctic meltwater northward and that the resultant sea-surface salinity and Atlantic Meridional Overturning Circulation (AMOC) responses are different when the two freshwater sources are taken separately. In the model used here, the AMOC response is rather weak (Sterl et al., 2012), with low sensitivity to warming and freshening (Van den Berk and Drijfhout, 2014). The salinity changes, on the other hand, can be very intricate and non-linear. Here, we will focus on the Atlantic and Arctic salinity budget and how barotropic and baroclinic mass and freshwater/salt fluxes over the boundaries (i.e. Bering Strait and a zonal section near Cape Agulhas) are modified by the freshwater release. In particular, coupled climate model studies forced with realistic amounts of Greenland meltwater loss do not simulate a strong response of the AMOC (Swingedouw et al., 2013a; Weijer et al., 2012; Van den Berk and Drijfhout, 2014), and also the model used here features a rather weak response.

The aim of this paper is, therefore, to evaluate how the ocean, and in particular the distribution of salt, responds to a plausible high-end scenario of freshwater release against a background of global warming, and to which extent the response to Northern Hemisphere (NH; Greenland) and Southern Hemisphere (SH; Antarctica) mass sources reinforce or counteract each other. Also, it is investigated whether non-linear or non-reversible effects arise by simulating a century of decreasing $CO_2$ concentrations and freshwater release (ramp-down) after a century of increase (ramp-up) following the RCP8.5 emission scenario. The ramp-up and ramp-down scenarios used are exactly symmetric about the year 2100.

The paper is structured as follows. Section 3.2 consists of an overview of the simulations done. In Section 3.3 the framework of the analysis is presented. In Section 3.4

the main results from the analysis are shown. A discussion and final conclusions are presented in Section 3.5.

## 3.2 Experiments

Figure 3.1 shows the forcing profiles used to prescribe atmospheric $CO_2$ and freshwater forcing (from the polar ice sheets) to the ocean (or 'hosing'). Till 2100 there is an increase in both forcings, followed by a symmetric decrease of the forcing, ending in 2195. These two phases are labelled 'ramp-up' and 'ramp-down' (see also Sgubin et al., 2014 for a similar experimental set-up). The atmospheric forcing follows the RCP8.5 scenario (Taylor et al., 2012) during the ramp-up, the freshwater forcing is as described in Van den Berk and Drijfhout (2014). The scenario follows a high-end mass loss scenario from Greenland and Antarctica, but is less extreme than, e.g., DeConto and Pollard (2016).

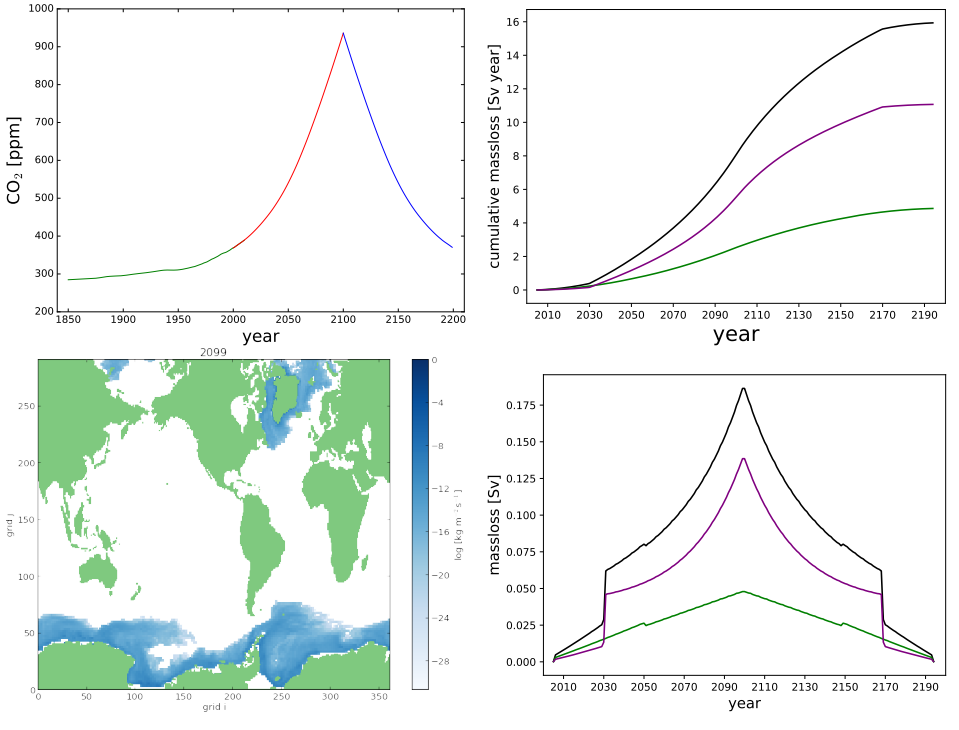


Figure 3.1: Top: The two forcing profiles applied in our simulations. Top-left panel: atmospheric $CO_2$ concentration. Top-right panel: cumulative global freshwater forcing (global: black, northern hemisphere: green, southern hemisphere: purple). Bottom-left: iceberg melt pattern (see Van den Berk and Drijfhout, 2014, for technical details). Bottom-right: melt rates; the top-right panel shows the time-integrated curves of these.

This forcing profile is idealised and the symmetry of the profile is clearly unrealistic. The motivation for using this symmetric forcing profile is to investigate possible non-linear effects, as the mechanisms responding to the linear increase in forcing, which operate on different timescales, will decouple after the reversal point in 2100 (see also Boucher et al., 2012). In particular, mechanisms that almost instantaneously follow the forcing will still behave symmetrically, while those which respond with a lag will deviate from the forcing trend. The simulations start in 2005 after a spin-up of 440 years with pre-industrial atmospheric forcing and historical forcing from 1850 to 2005 (see Sterl et al., 2012, for details). The simulations are continued until 2195.

| | $CO_2$ | NH melt | SH melt | members |
|---|---|---|---|---|
| C | + | - | - | 4 |
| H | + | + | + | 4 |
| N | + | + | - | 1 |
| S | + | - | + | 1 |

Table 3.1: Overview of experiments and their included forcing. The control experiment $C$ does not include the meltwater forcing, but $H$ includes forcing in both hemispheres. Northern Hemisphere-only freshwater forcing ($N$) and Southern Hemisphere-only freshwater forcing ($S$) each have a single member, $C$ and $H$ each have four.

Table 3.1 gives an overview of the simulations. We performed an ensemble of 4 control runs with only the atmospheric forcings changing according to the RCP8.5 scenario (ensemble $C$), and a similar-sized ensemble in which the freshwater forcing is applied to the run in $C$ (ensemble $H$). Simulations $N$ and $S$ are single runs with a forcing like in the first run of $H$, but with the freshwater forcing only applied to either the Northern or Southern Hemisphere. All output variables are recorded as monthly mean output.

The experiments are performed with the CCM EC-Earth. EC-Earth consists of three components. The atmosphere and land surface are modelled with the Integrated Forecast System (IFS–cycle 31r1) which resolves 62 layers in the vertical and uses a triangular truncation at wavenumber 159 (ECMWF, 2006, effectively resolving $\approx$ 130 km). The ocean is modelled by the Nucleus for European Modelling of the Ocean (NEMO) developed by the NEMO European Consortium at a resolution of approximately 1° in the horizontal ($\approx$ 110 km) and 42 levels in the vertical (Madec, 2008). The effect of mesoscale eddies is parameterised with an eddy-induced advection term (Gent and Mcwilliams, 1990). Both the horizontal diffusivity and the eddy-induced advection term use a constant diffusivity parameter of $10^3$m s$^{-2}$ NEMO is equipped with a free surface formulation for the ocean surface, implying that freshwater release adds volume to the ocean, instead of using a virtual salt flux. Ocean and atmosphere are synchronised along the interface every three model-hours by the OASIS3 coupler developed at the Centre

Européen de Recherche et de Formation Avancée en Calcul Scientifique (Valcke et al., 2004). The ocean model is coupled to a sea ice model developed by the University of Louvain-la-Neuve (LIM2) (Fichefet and Morales Maqueda, 1997; Bouillon et al., 2009). The general characteristics of EC-Earth simulations are described by Hazeleger et al. (2012); Sterl et al. (2012) shows more detail on the ocean aspects.

## 3.3 Methods

The total freshwater flux into the ocean surface ($F$) is $F = -E + P + R + I + M$, with $E$ evaporation, $P$ precipitation, $R$ run-off, $I$ meltwater from sea ice, and $M$ the meltwater we apply as a forcing. For a global domain with only a free surface there must be changes in volume due to freshwater fluxes, but the salt content must remain conserved. The salt balance is expected to differ by latitude. Apart from the extra freshwater forcing applied in the model, the salinity is affected by ocean advection and changes in the other terms in $F$. A change in volume transport will change the advected amount of salt, as will a change in the local salinity. Below we derive some quantities that help differentiate between these components. EC-Earth's ocean component, NEMO, uses a linear free surface formulation: a closure term related to changes in sea surface height (SSH) is needed to close the salt budget. This term could be interpreted as a change in the salt content of the upper layer, and as such is an artefact of the lack of a true free surface of the model.[1] For a zonally bounded box $B$ with surface $a$, depth $H$ and sea surface height of $\eta$, conservation of salt then leads to the balance (see also Treguier et al., 2012),

$$\begin{aligned}\frac{\partial \zeta_B}{\partial t} &= \frac{\partial}{\partial t} \iint_a \int_{-H}^{\eta} S \, dz \, dx \, dy \\ &= \iint_a \int_{-H}^{\eta} \left(-\rho_0 \nabla \cdot \left(V_n - V_s\right) S + \nabla F_D\right) \, dz \, dx \, dy + \zeta_i. \end{aligned} \tag{3.1}$$

Here $\zeta$ is the salt content, $S$ the salinity, $\rho_0$ the reference density of sea water in the model, $V$ the meridional velocity, $F_D$ salt diffusion, and $\zeta_i$ salt forcing due to brine rejection. Because salt can only be transported across the north ($n$) and south ($s$) ocean sections these are explicitly present. The ocean component in our model formulates the (linear) free surface (Roullet and Madec, 2000) and only involves advection and diffusion below

[1] The surface elevation does not change the vertical metric ($dz/dk$—meaning the metric field is static and not dependent on the surface elevation as it should be for a real free surface formulation).

$z = 0$,

$$\frac{\partial}{\partial t} \iint_a \int_{-H}^{\eta} S\,dz\,dx\,dy = \iint_a \int_{-H}^{0} \frac{\partial S}{\partial t} dz\,dx\,dy + \iint_a S \frac{\partial \eta}{\partial t} dx\,dy$$

$$\approx \int_b \int_{-H}^{0} \left(-\rho_0 \cdot \left(V_n - V_s\right) S + F_D\right)\, dz\,dx + \zeta_i \tag{3.2}$$

$$\zeta_0 + \zeta_\eta = \zeta_n + \zeta_s + \zeta_D + \zeta_i. \tag{3.3}$$

The velocities $V_s$ and $V_n$ are the meridional velocities at the northern and southern boundaries of a box. The salt content is now split into the components, indicated by the given subscripts ($\zeta_0$ for volume, $\zeta_\eta$ for surface, $\zeta_{n,s}$ for advection, $\zeta_D$ for diffusion, and $\zeta_0$ for brine rejection). Meltwater and other surface fluxes do not affect the total amount of salt in the ocean, but does add to its volume.

Salt advection through the basin is primarily a result of the overturning, gyres, and a net barotropic flow. We define three variables describing the changes in salt advection (see appendix 3.A for details on notation used below). We start with advection by the overturning component, i.e. an analogue of $M_{\text{ov}}$ (Rahmstorf, 1996),

$$\Delta\zeta_{\text{ov}}(t) = \int_{t_0}^{t} \iint_b \left(\langle V\rangle_x - \langle V\rangle\right) \langle S\rangle_x \, dxdz\, dt. \tag{3.4}$$

Here, $\langle\rangle$ is a zonal averaging operator and is defined in the Appendix.

Similarly, Eq. 3.5 is associated with the azonal component of salt advection, i.e. advection by the gyre and an analogue of $M_{\text{az}}$ (Rahmstorf, 1996) of the salt content $\zeta$;

$$\Delta\zeta_{\text{az}}(t) = \Delta \int_{t_0}^{t} \iint_b \delta^x V \cdot \delta^x S \, dxdz\, dt, \tag{3.5}$$

and the remainder is advection by the net barotropic flow, resulting from Bering Strait transport and the integrated net freshwater forcing between Bering Strait and the relevant latitude (i.e the running integral of $P + R - E$),

$$\Delta\zeta_{\text{zo}}(t) = \Delta\zeta(t) - \left(\Delta\zeta_{\text{ov}}(t) + \Delta\zeta_{\text{az}}(t)\right). \tag{3.6}$$

Salt advection can change because the volume transport changes, or because the salinity changes. The salt advection anomaly into a box can be split into two quantities (where

$H$ for hosing series, $C$ for control),

$$\Delta \int_b SV\,dz\,dx = \int_b \left(S_H - S_C\right)\frac{V_H + V_C}{2} + \left(V_H - V_C\right)\frac{S_H + S_C}{2} dz\,dx$$
$$= \left(\Delta^S + \Delta^V\right)\int_b SV\,dz\,dx. \tag{3.7}$$

The operator $\Delta^S$ retains the anomalous salinity, but uses the average of the volume transport, while $\Delta^V$ averages the salinity profile while retaining the anomalous volume transport. These two operators indicate whether the change in salt advection is primarily due to salinity changes or volume changes.

For a single (zonal) section $b$ the cumulative effects on salt, transported across a section $b$, have a similar expression to Eq. 3.7 as its time-integral,

$$\Delta\zeta(t) = \int_{t_0}^{t}\iint_b SV\ dxdz\ dt$$
$$= \Delta^S \int_{t_0}^{t}\iint_b SV\ dxdz\ dt + \Delta^V \int_{t_0}^{t}\iint_b SV\ dxdz\ dt. \tag{3.8}$$

Eq. 3.8 decomposes the changes in salt transport into a part that is driven by changes in salinity (keeping the volume transport constant) and into a part that is driven by changes in volume transport, keeping the salinity constant. Below, these two terms will be indicated as being the 'salinity-driven' and 'volume-driven' part of the salt transport anomaly, respectively. (All decompositions are calculated at the model gridpoint level.)

## 3.4 The salt redistribution

We start our analysis by showing the global response in sea surface salinity to freshwater forcing from the large ice-sheets in four chunks of 45 years (see also e.g. Morrill et al., 2014; Otto-Bliesner and Brady, 2010; Stouffer et al., 2007, for similar work in other models). As stated before, for a description of the mean ocean state in EC-Earth, see Sterl et al. (2012).

### 3.4.1 The spatial pattern of redistribution

In Figure 3.2 the panels display ensemble-averaged differences between runs $H$ and $C$ (Table 3.1). Figure 3.2 shows that low salinity waters from the East and West Greenland Current pile up at the eastern boundary of the subtropical gyre. The distribution around the subpolar gyre (SPG) and the eastern boundary current of the subtropical gyre (STG),

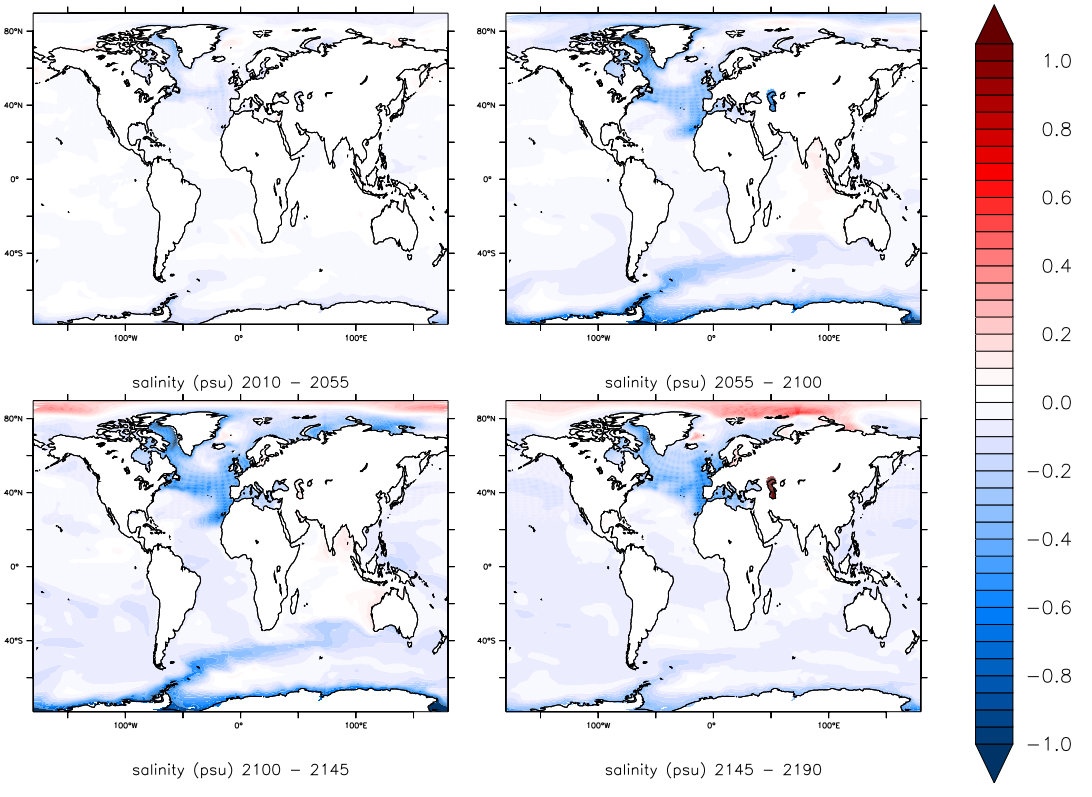


Figure 3.2: Surface salinity anomaly ($H - C$), means of indicated time ranges, ensemble averages.

i.e. the Canary current, indicates that the redistribution is advective in nature. The low-salinity water partly follows the pathway of the boundary currents and mid-latitude jet, which divides the subpolar and subtropical gyres, and is partly affected by surface Ekman flow. The low salinity signature along the Canary current has been also observed in the hosing experiments of Swingedouw et al. (2013a), which contains further details of how the salinity anomaly in the North Atlantic develops. Low salinity waters are also found around the coast of Antarctica. At the Antarctic Peninsula in particular there is a patch of low salinity waters which spreads further northward and eastward, and there is some indication of these waters being carried into the South Atlantic. A rapid adjustment takes place, as is evident from the congruence in the transport signals at both Bering Strait and the Agulhas section. This cannot be due to advection, but only through wave adjustment. This becomes especially visible after 2050. The conspicuous increase of sea surface salinity in the Arctic is not due to changes increases in sea ice growth, but has an advective origin as will become apparent below.

Figure 3.3 shows the same for the depth-averaged salinity. By comparing the two figures it becomes clear that, while along the boundaries of the subpolar gyre the sur-

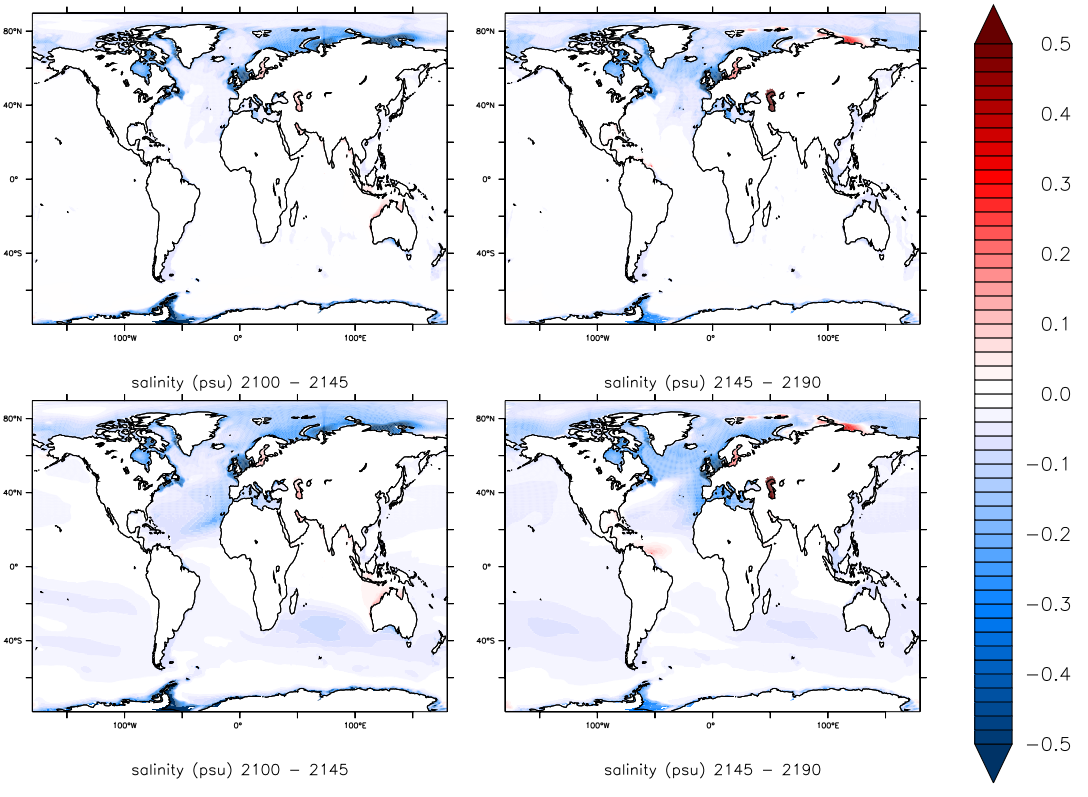


Figure 3.3: Top: depth-averaged salinity anomaly($H-C$). Bottom: top 1000m averaged salinity anomaly($H-C$). Means of indicated time ranges, ensemble averages.

face signal weakens in the last 45 years due to reducing freshwater input, the depth-averaged signal keeps increasing in the subpolar gyre region. During this period the time-integrated freshwater input still increases. Also, the signal is more mixed over the whole subpolar gyre. Apparently, during the last 45 years, more of the surface signal is vertically mixed or subducted reducing the net freshwater anomaly in the surface layers. Also, it becomes apparent that the northward spreading of the anomaly originating from Antarctica remains more confined to the surface layers and must be primarily transported by the Ekman flow.

### 3.4.2 The basin-wide Arctic-Atlantic salt export

The zonally-averaged salt anomaly in the Atlantic shows that after 50 years most of the freshening occurs primarily in the subtropical gyre (Figure 3.4, between $10°N$ and $45°N$). This implies that the subtropical gyre receives more freshwater from the north than it transports to the south, leading to convergence of freshwater. After about 100 years, the South Atlantic freshens as well, preceded by a mild salinification during the

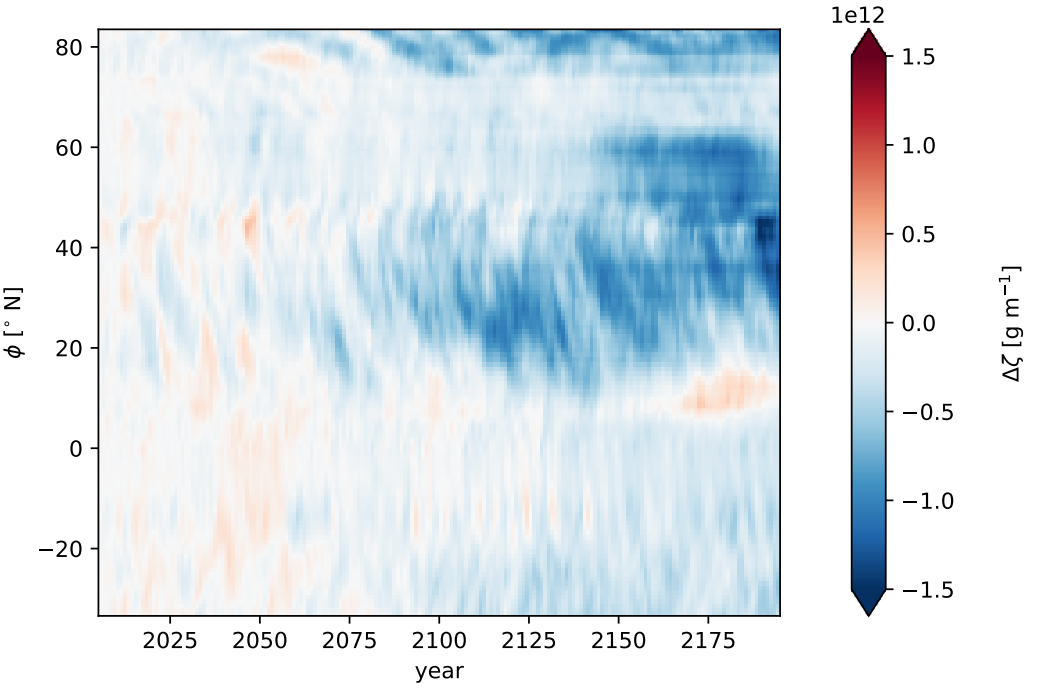


Figure 3.4: Time-latitude diagram of the anomaly ($H - C$) of ensemble averaged salt content in the Arctic-Atlantic basin.

initial 50 years. Later, we will show that this freshening originates from the Antarctic. The subpolar gyre (between $45°N$ and $65°N$) remains relatively unaffected until 2150 when considerable freshening starts, on par with subtropical gyre freshening.

A small part of the change in salinity (and salt content through changes in advection) is due to a response in evaporation and precipitation. After 50 years, a reduction in the precipitation north of the equator appears, with an excess in precipitation south of it (not shown). This pattern is indicative of a southward shift of the Intertropical Convergence Zone (ITCZ). A shifting ITCZ is a known effect for a warmer climate in which the AMOC slows down, reducing the relatively high NH surface temperatures compared to the SH (see e.g. Stouffer et al., 2006. The effects of the ITCZ shift, however, appear minimal compared to the freshwater forcing from the ice sheets and will not be discussed further (but see e.g. Zhang and Delworth, 2005). As a result, the basin-integrated effect of changes in EPRI are minor in the Arctic-Atlantic salinity budget (dotted line in Figure 3.5). Remarkably, the Atlantic is not only diluted by the freshwater from the Greenland ice cap (Figure 3.5), there is also a net salt export from the basin, which starts after five decades of forcing. As a result, the decrease in salinity is much stronger than dilution by the northern forcing would imply (left panel), even though part of the excess volume is transported out of the basin. There is no change in the salt transport across the Strait of Gibraltar (not shown). This leaves Bering Strait and the section at Cape Agulhas

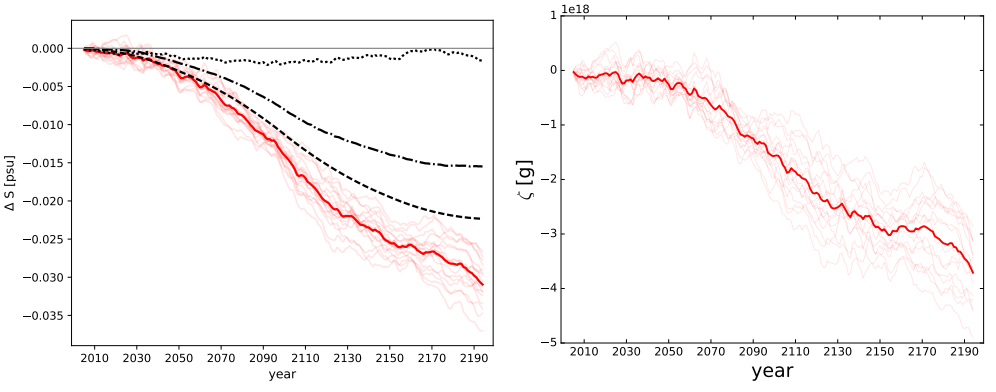


Figure 3.5: Left panel: the anomaly $(H - C)$ of average salinity in the Arctic-Atlantic. More freshwater is taken in than is to be expected from the Greenland freshwater (dashed line), than can be explained from the increase in surface elevation (dash-dotted line), or the net freshwater anomaly into the ocean (dotted line). Right panel: the salt content in the basin. Ensemble averages are plotted in a darker hue. Individual anomalies are plotted to indicate the ensemble spread.

as the two locations where net salt exchange can adjust. The connection between Bering Strait and South Atlantic volume transport has been noted before by, e.g. Reason and Power (1994), De Boer and Nof (2004), and Hu et al. (2008). These studies focus on the effects of closing Bering Strait on the overturning. Bering Strait is thought to have been closed during paleo-climatic times such as glacial periods (Hu et al., 2008). A closed Bering Strait leads to a more unstable overturning (Hu et al., 2012; Hu et al., 2015). The freshwater import via Bering Strait can be affected by Greenland meltwater, even reversing to an export (Hu et al., 2011). We, however, are interested in the connection during present and near-future times with Bering Strait in its current state. To this end we analyse the salt distribution in the transient response in greater detail (and with a more appropriate melt scenario) than has been done in the literature so far.

The inference from Figure 3.5 that salt is exported from the Atlantic by advective processes is confirmed by decomposing the salt balance into its components as in Eq. 3.1. It is then found that salt loss is indeed due to anomalous salt advection (the green and black line $\approx$ red) out of the basin (Figure 3.6). Sea ice and other coupled processes only affect the salt content in the basin very little. To determine which parts of the circulation are responsible for the salt loss we split the anomalous salt advection into components.

### 3.4.3 A decomposition of salt advection

The anomalous salt advection can be split into three dynamic components, which reflect changes in salt transport by the overturning, gyre, and barotropic circulation, respectively (Eqs 3.4, 3.5, 3.6). This decomposition is shown in the left panel of Figure 3.7. The

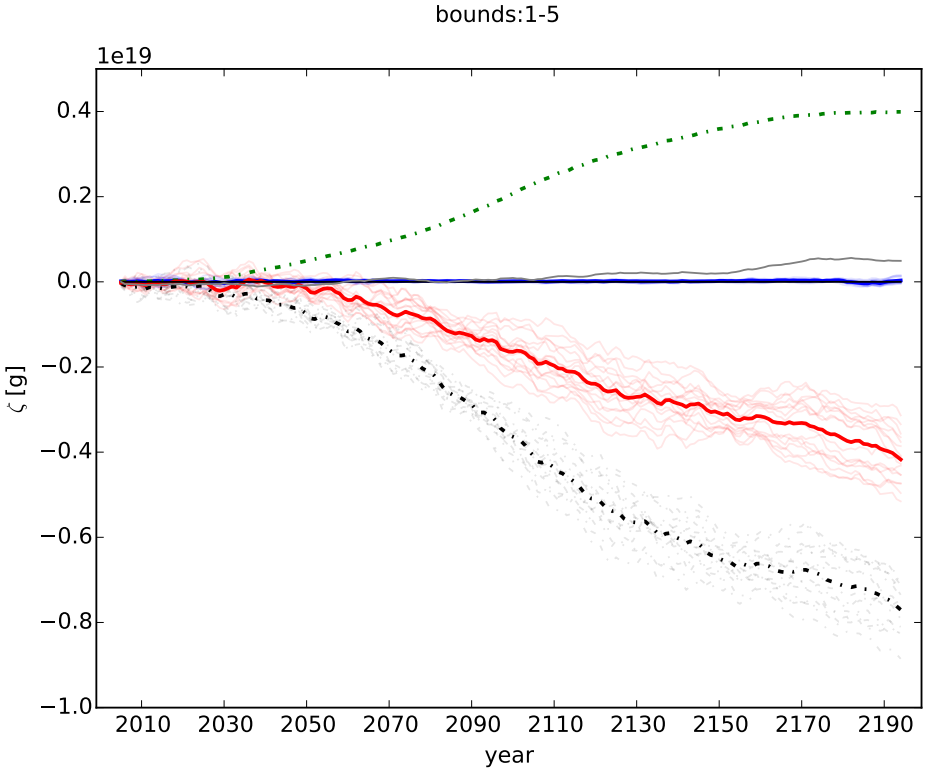


Figure 3.6: Anomaly $(H - C)$ of salt content in the Arctic-Atlantic basin by contribution. The components are the anomaly values of the terms in Eq. 3.3. In solid red $\Delta\left(\zeta_n + \zeta_s\right)$, the advected salt through the basin. In dash-dotted black $\Delta\zeta_0$, the salt in the fixed volume. In dashed green $\Delta\zeta_\eta$, the surface elevation accumulation term. The sea ice contribution $\Delta\zeta_i$ in blue, and in grey the remainder ($\approx \zeta_D$, diffusion, mixing and accumulated numerical errors). Ensemble averages are plotted in a darker hue.

anomalous salt advection can also be split into components reflecting changes in either volume transport or salinity (Eq. 3.8). This is shown in the right panel of Figure 3.7 for each of these three dynamic components.

The two baroclinic components (overturning and gyre) are responsible for 75% of the salt export at the end of the simulation, with the remaining 25% due to barotropic flow. Figure 3.7 shows that the overturning is associated with anomalous transport of salt out of the basin. The overturning component itself remains relatively unaffected during the ramp-up (blue dashed line, right panel). Thus, the AMOC response to hosing is relatively weak in this model; $\mathcal{O}$(1 Sv). This implies that the change in salt transport by the overturning is primarily due to changes in salinity (dashed red line, right panel). Because there is no overturning component in Bering Strait, the overturning at the Agulhas section either imports fresher water or exports saltier water. With a freshening of the surface

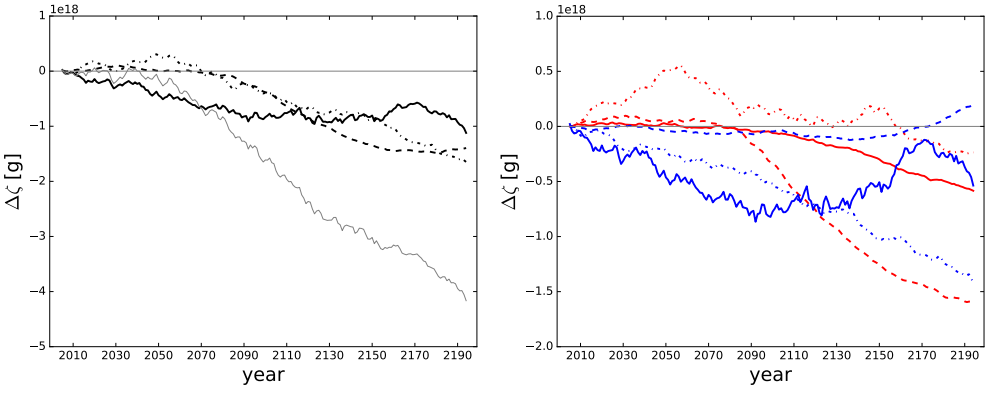


Figure 3.7: Left panel: anomaly ($H-C$) of net advected salt into the Arctic-Atlantic basin decomposed into a barotropic (solid line), overturning (dashed line), and gyre (dash-dotted line) components. The grey line is their sum and equal to the total salt advection (red line in Figure 3.6). Right panel: The three components in the left panel split into S (red) and V (blue) components. All lines are the ensemble averages of the runs. Note the difference in scale between the two panels.

due to the applied forcing, the expected response is a freshening of the inflow. Given the timing, this change must be associated with the arrival of freshwater, originating from the Antarctic Ice Sheet, at the southern boundary of the Atlantic.

It is only during the last half of the 22$^{nd}$ century that volume-driven changes affect the salt transport by the overturning. The overturning weakens and exports less salt from the Atlantic, counteracting the dilution of salt in the basin. It should be noted that this response, occurring after 2150, does not exclude changes in the volume transport (weakening) of the overturning, which occurs before 2150. It merely indicates that such changes have not yet reached the Agulhas section during the first century and a half. The gyre component in Figure 3.7 is dominated by volume-driven changes. The gyre imports freshwater into the South Atlantic and the increase in import indicates a strengthening of the gyre at the Agulhas section, see Section 3.4.5 for details.

The barotropic component also exports salt from the basin, both through a stronger volume transport and increased salt contrast between Bering Strait inflow and outflow across the Agulhas section (Figure 3.7). Net volume transport changes across the basin in Figure 3.8a result from a difference between changes in Bering Strait transport and transport across the section at Cape Agulhas. The mass loss due to divergence of the barotropic flow is at least an order of magnitude larger than changes in freshwater flux between ocean and atmosphere. The result is a steady export of water out of the basin due to an imbalance between the two barotropic transport terms. This transport divergence partly counteracts the volume increase due to adding freshwater from Greenland. The divergence in volume transport means that either the outflow across the Agulhas section increases, or it decreases less than the inflow through Bering Strait. The mass advection

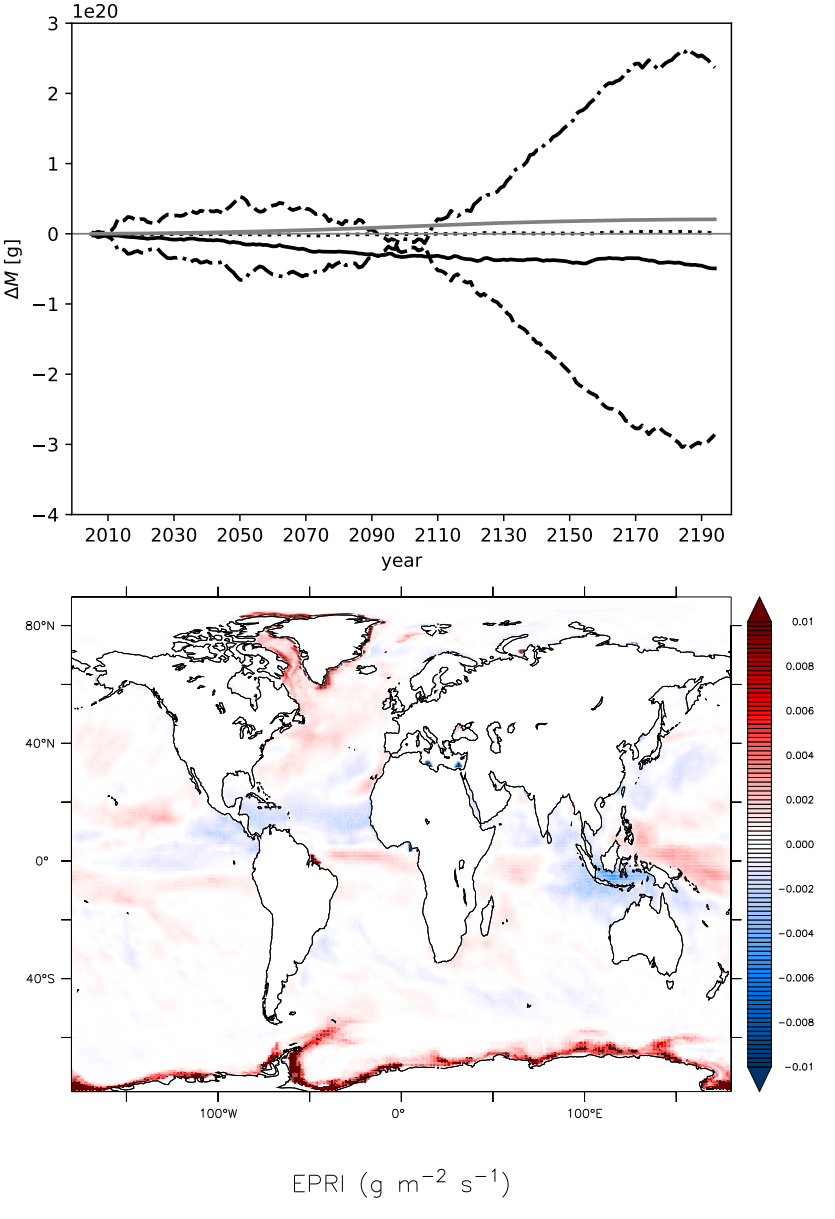


Figure 3.8: Top panel: Anomaly ($H - C$) of time-integrated mass transport into the Arctic-Atlantic basin. The solid line is the basin-integrated divergence (net transport through the basin), which is the difference between Bering Strait in the North (dashed line) and Cape Agulhas in the south (dash-dotted line). The EPRI contribution (dotted line) is negligible. The grey line is the Greenland freshwater forcing. Bottom panel: the ramp-down EPRI pattern plus forcing.

in Figure 3.8a shows that the transport increases across both sections during the first 50 years, but decreases after that time. The bottom panel in Figure 3.8 illustrates why the atmospheric response in EPRI is basin-integrated negligible over the Arctic-Atlantic basin. The anomalous EPRI field shows clearly the sign of a displaced ITCZ, with a southward shift occurring in the Atlantic. The net effect (i.e. net EPRI anomaly) integrated over the tropical belt, however, is small. This is consistent with the weak response of the AMOC.

The export of salt by the barotropic component especially increases during the ramp-up (solid black line in Figure 3.7), and is steady during the ramp-down. We see that the initial salt export from the Atlantic by the barotropic flow is volume-driven and the effect of salinity changes only sets in during the ramp-down. In this phase (i.e. after 2100) the two effects largely cancel. It should be noted that the effect of volume-driven response in barotropic flow on the salinity budget is different than in Hu et al. (2011), where a reduction in Bering Strait throughflow was found to lead to an increase salinity. Here, changes in Bering Strait inflow and outflow across the Agulhas section are not in balance. The effect on salinity is not driven by the barotropic flow becoming stronger or weaker, but by the divergence between inflow and outflow, with the outflow being larger, hence export of volume and salt. This change in barotropic response is again associated with the arrival of freshwater from Antarctica at the southern boundary of the Atlantic.

The main drivers of the salt export from the Atlantic are thus a dilution due to water imported by the overturning across the Agulhas section because of the arrival of freshwater from the Antarctic, an increase in the volume-driven export by the South Atlantic gyre, and a divergent barotropic transport across the basin, which partly compensates the volume increase due to freshwater input. We conclude that the salt export from the Atlantic is a compound effect involving all three different circulation types.

### 3.4.4 Bering Strait changes

Results from previous sections and from existing literature (De Boer and Nof, 2004; Hu et al., 2007; Hu et al., 2012; Weijer et al., 2001; Hu et al., 2015; Reason and Power, 1994) indicate an important role for Bering Strait in the adjustment of the salt budget in the Atlantic in response to high latitude freshwater perturbations.

The flow through Bering Strait starts increasing salt and mass into the basin, while the flow across the Agulhas section decreases salt and mass even more, indicating that both barotropic flows increase. After 50 years the barotropic salt transport anomaly changes sign at each section, indicating the barotropic flow has become less than the control run $C$. However, at each moment in time the salt (and mass) transport are divergent, that is, mass and salt are exported from the basin. The mass export is a response to the volume added to the Atlantic by Greenland freshwater release. This added volume alters the sea surface height (SSH) difference between the Atlantic and Pacific.

The Pacific typically features higher sea level than the Atlantic, with the pressure drop across Bering Strait driving a northward flow through Bering Strait (Aagaard et al., 2006). The initial increase in barotropic flow through Bering Strait must be due to an in-

crease in sea level gradient, either by a Pacific-side increase, or an Arctic-side decrease. Initially, Greenland meltwater is carried southward via currents and wave adjustment, while Antarctic meltwater is carried northward into the Pacific along the eastern boundary, also likely dominated by wave adjustment processes via boundary and Kelvin waves. As a result, the Arctic does not gain volume, while SSH does increase in the Pacific (Figure 3.9). After 40-50 years the SSH anomaly—coupled to a negative salinity anomaly—is carried by the North Atlantic Drift and Norwegian Current into the Arctic, reversing the anomalous SSH gradient across Bering Strait. This drives the sign reversal in salinity and mass transport anomaly through Bering Strait and across the Agulhas section seen in Figure 3.8.

Though the large-scale changes in north-south SSH gradient are the driver of the Bering Strait throughflow flowing down the pressure gradient, within the Bering Strait the flow should largely obey geostrophy. Geostrophy is ensured by the warmer and lighter Pacific surface layer outcropping at the eastern side of Bering Strait, while the colder water in the Arctic is connected with the western boundary of the Arctic. As a result, the north-south gradient in SSH is transmitted to the east-west SSH gradient within Bering Strait. This effect is illustrated by Figure 3.10, which shows the change in total transport versus geostrophic transport. The match is not completely perfect, as the flow is partly frictionally controlled, but the signals in both transports are still in qualitative agreement. Wind and density gradient contributions, shown as the Ekman transport anomaly and the baroclinic transport anomaly, are negligible.

### 3.4.5 The South Atlantic subtropical gyre response

The South Atlantic is separated from the Southern Ocean by a strong front associated with the Antarctic Circumpolar Current (ACC), known as the Subtropical Front (STF) (Peeters et al., 2004). At the STF, the Agulhas Return Current (ARC) encounters the ACC, with the winds exerting a strong influence on the position of the STF (Biastoch et al., 2009; De Boer et al., 2013; Durgadoo et al., 2013). Across the STF a large salinity and temperature gradient exists. In addition, the SH supergyre (the flow that connects the three wind-driven gyres in the SH in terms of barotropic volume transport) strengthens in the Indian and Atlantic sector in response to hosing. The strength of the SH supergyre and the position of the STF are strongly controlled by the wind; this response leads to the question whether the changes in transport can be attributed to changes in wind stress.

During the first 50 years, the gyre imports more salt into the South Atlantic due to a more saline inflow, partly counteracted by a spin-up of the South Atlantic subtropical gyre, which, as a whole, imports freshwater (Figure 3.7). In those first 50 years the wind response shifts the STF to the south and enhances the SH supergyre. Thereafter, the barotropic streamfunction continues to show consistent anomalies that enhance the South Atlantic subtropical gyre (Figure 3.11). The associated change in windstress does not only show an increase in winds, but also a noticeable southward shift of the westerlies. This is in contradiction with Menviel et al. (2010), who showed that an increase

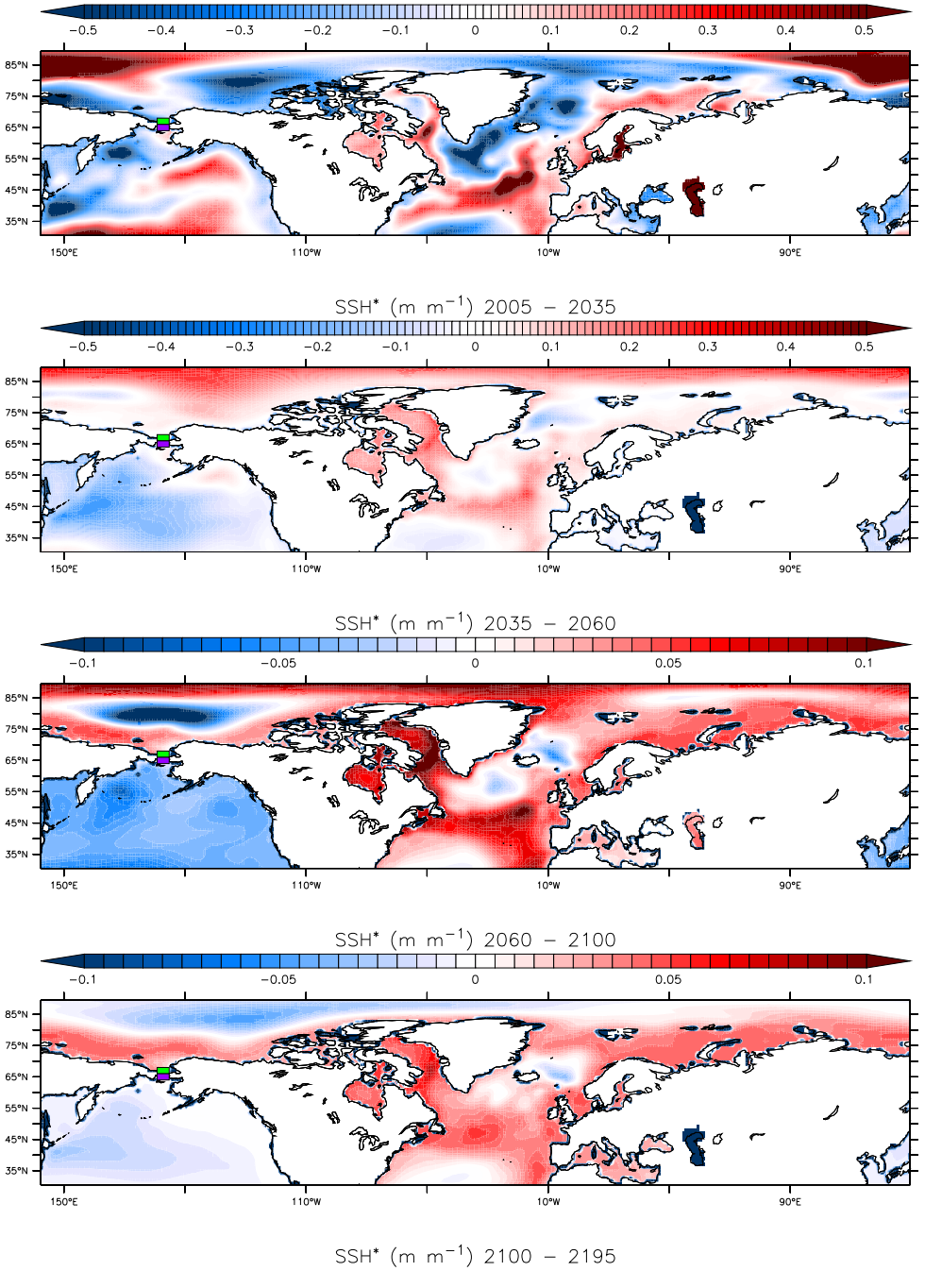


Figure 3.9: means of SSH/⟨SSH⟩(globally averaged) - 1 for the indicated time ranges; anomaly of $(H - C)$.

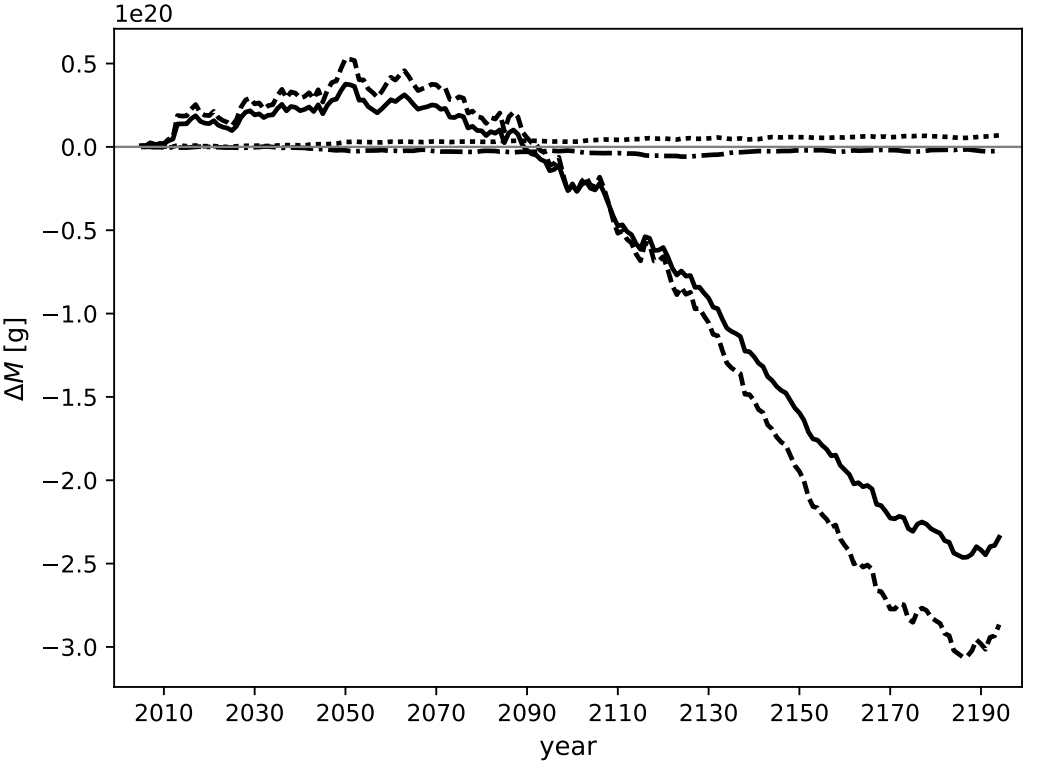


Figure 3.10: Bering ($H-C$) geostrophic transport anomaly (solid line), compared against the total transport anomaly (dashed line). The baroclinic contribution (dash-dotted line) and Ekman transport (dotted line) are negligible.

in SH sea ice shifts the wind northward. Here, the Antarctic ice sheet releases large amounts of freshwater. This not only increase sea ice but also reduces buoyancy near the Antarctic continent due to large-scale freshening of surface waters, reducing, instead of increasing the meridional density gradient between pole and equator, and changing the density pattern. It is beyond the scope to explain the wind response to this type of surface forcing here, but the reversed change in equator-to-pole density gradient may partly explain the opposite shift in westerlies, as found in Menviel et al. (2010). As a result, Agulhas leakage does not decrease, but increases instead (Sijp and England, 2008).

To quantify these effects, we relate the increased volume transport to the Sverdrup balance and gyre spin-up associated with buoyancy forcing. In this case the section is chosen at 35°S, between 20°E and 20°W. We should stress that, because of the non-linearities associated with Agulhas leakage, we do not expect the South Atlantic subtropical gyre to be fully controlled by local windstress and buoyancy forcing, nor the strength of the Agulhas leakage feeding into this gyre (Beal et al., 2011).

Figure 3.12 clearly illustrates that buoyancy forcing plays no role, and that during the first 100 years the change in volume transport is adequately described by changes in Sverdrup transport associated with the wind response to increased meridional temperature gradients. After 100 years, however, the increase in volume transport becomes considerably larger than the change in Sverdrup transport, indicating that this change is associated with non-local effects further upstream (roughly at the same time the overturning starts to freshen the entire basin).

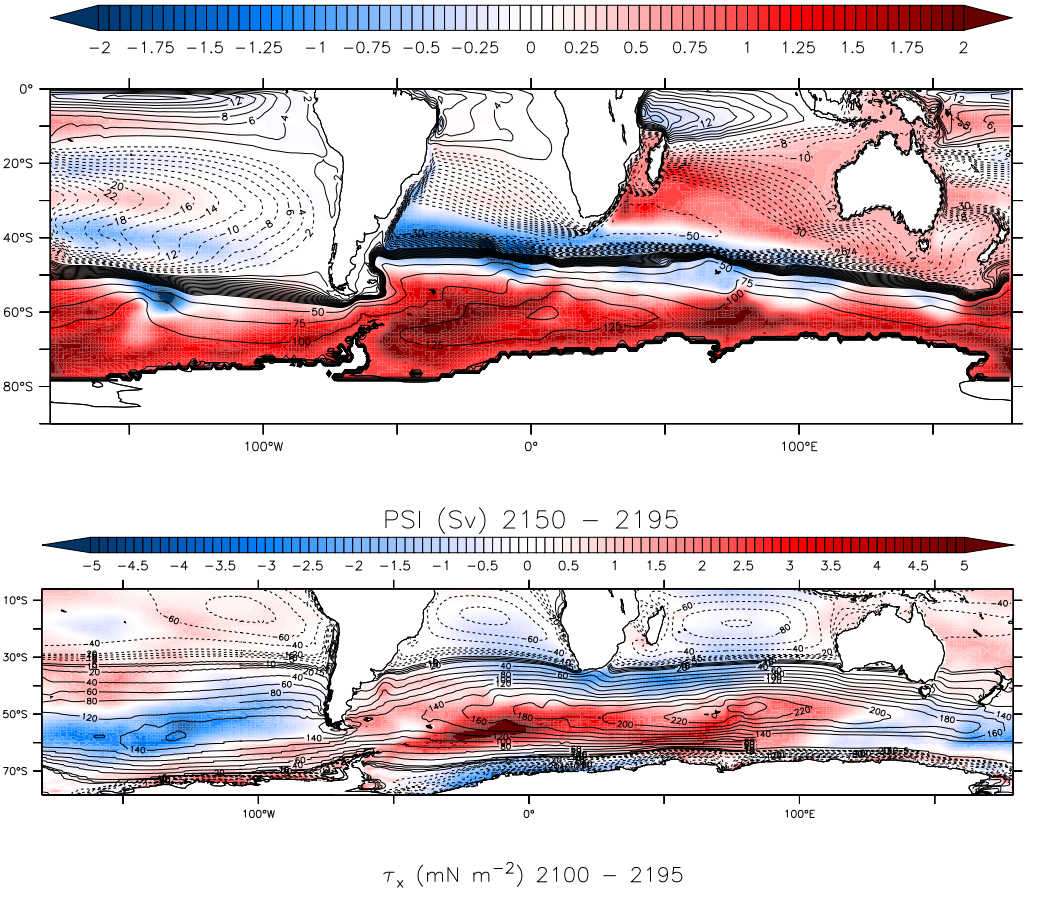


Figure 3.11: Barotropic streamfunction anomaly (top), mean of the range 2150-2195. Zonal windstress (middle, bottom), means of the ranges 2050-2100 and 2100-2195. Ensemble averages $H - C$, with the climatological mean overlaid as contours.

### 3.4.6 The different response to NH and SH sources

The results shown so far indicate a different role for both NH and SH freshwater sources on the Atlantic salt budget. The $H$ set of simulations cannot distinguish between the

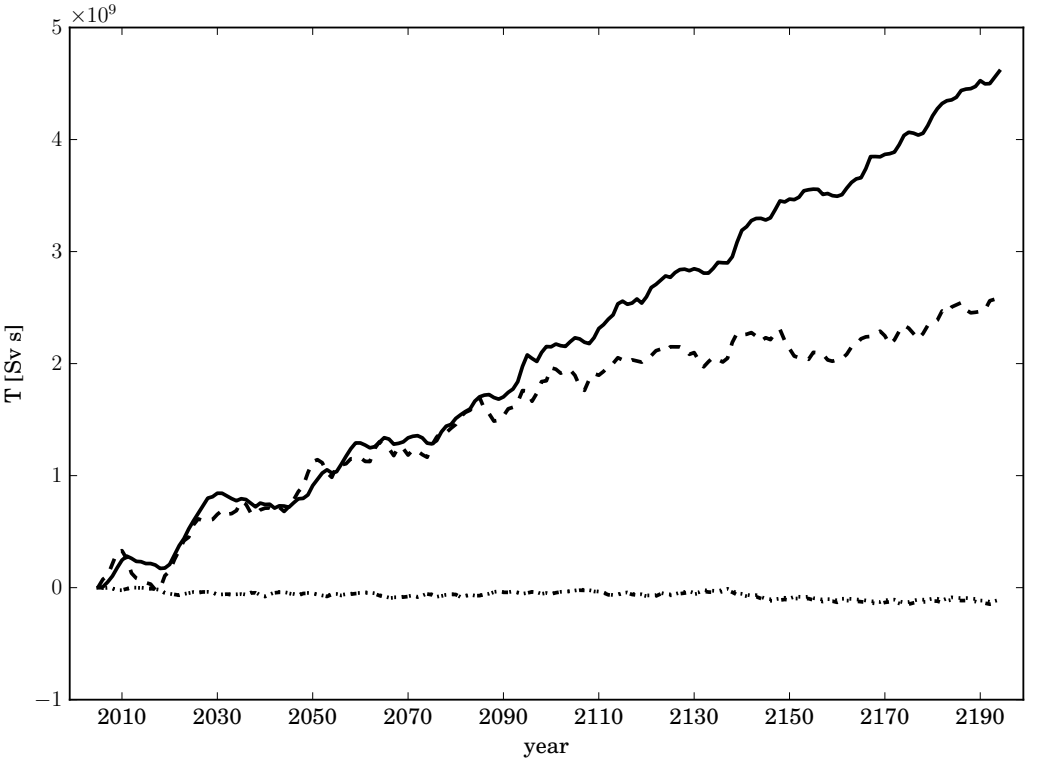


Figure 3.12: Time-integrated Sverdrup transport anomaly (dashed), time-integrated anomaly of the negative of the extreme of the barotropic streamfunction (solid), and buoyancy forcing changes at 100 m (dash-dotted) and 200 m (dotted). Ensemble average of $H - C$.

impact of both sources of freshwater. To be able to do so, simulations with separate NH and SH freshwater forcing were conducted ($N$ and $S$).

In Figure 3.13 the barotropic transport anomalies are shown for NH forcing ($N - C$) and SH forcing ($S - C$) only. The barotropic component already shows the opposite effect of the forcing on salt import/export into/from the Atlantic and Arctic basins in the two experiments. With only Antarctic freshwater forcing, there is a steadily increasing salt import. With only Greenland freshwater forcing, there is a salt export from the Atlantic. In the NH forcing experiment, Greenland freshwater anomalies are advected with some time delay into the Arctic, similar to the full freshwater anomaly experiment. At the same time as in $H - C$, the SSH gradient across Bering Strait starts to decrease and, as a result, the transport through Bering Strait, decreases as well. The throughflow across the Agulhas section follows this response. The reduced barotropic throughflow is associated with a diminished import of fresher water and also less export of saltier water. The reduced inflow, however, outweighs the reduced outflow in terms of salt and mass balance.

Figure 3.13 clearly demonstrates this for the salt balance. The mass balance (not shown) displays the same behaviour.

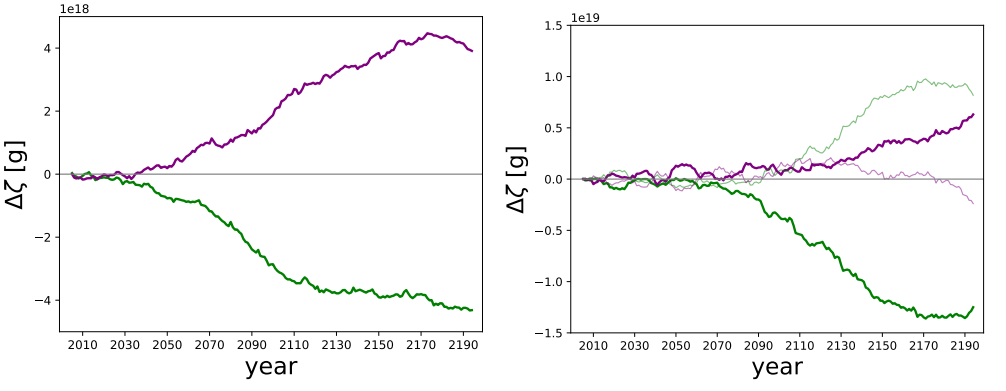


Figure 3.13: Left panel: Salt increase in Arctic-Atlantic basin by barotropic flow advection for Northern Hemispheric melt (green) and southern Hemisphere melt (purple) scenarios. Right panel: Anomaly $N - C$ in green and $S - C$ in purple of time-integrated barotropic salt advection component, split in northern (Bering Strait, darker hue) and southern (Agulhas section, lighter hue) boundary contributions.

This reduction in barotropic transport implies a positive feedback by Greenland meltwater on freshening the Atlantic and Arctic basins. Direct freshening occurs by adding freshwater to the ocean and this added volume reduces the inflow of mass and salt across Bering Strait. Although the barotropic flow across the Agulhas section also decreases, this decrease is smaller than the Bering Strait transport. As a result, salt transport divergence by the barotropic flow occurs in response to volume added from the Greenland ice sheet.

Note that even though the Pacific water entering through Bering Strait is fresher than the Arctic water, the positive feedback above relates to the mass advection through the Strait. In terms of salinity, a reduction in Bering Strait on its own is a negative feedback because less freshening through the strait takes place (Hu et al., 2011).

In the SH forcing experiment the opposite occurs. Added volume from Antarctica reaches the North Pacific with some time delay, enhancing the barotropic flow through Bering Strait.The effect on the salt balance is also the opposite of the one seen in the NH forcing experiment (Figure 3.13). Flow through Bering Strait and across the Agulhas section both increase under SH forcing, but the increase across the Agulhas section is smaller than the increase of Bering Strait transport. As a result, the response of the barotropic flow is now a convergence of salt into the Arctic-Atlantic basin.

In the experiment $H$, with both NH and SH forcing, we saw a net freshening by the barotropic component. Ultimately, the effect of NH forcing outweighs the effect of SH forcing in terms of salt divergence in the Atlantic, even though the SH forcing in terms of added volume to the ocean is much stronger than the NH forcing (by roughly a factor four

in our scenario). Also, we found that the NH forcing leads to a positive feedback on the freshwater budget, amplifying the freshening in the Arctic-Atlantic basin. In Figure 3.14 the geostrophic transport is compared against the total transport for $N-C$ and $S-C$. For $N$ there is even better agreement between geostrophic transport and the total transport than in $H$ (forcing in both hemispheres), while in $S$ the agreement is slightly less, even though wind and density gradients do not contribute significantly in each case. So, the Bering Strait response is driven by changes in sea surface height, which are attributed to wave adjustment to the freshwater release, although attribution in this case is difficult because of the large variability in sea surface height, making it difficult to identify the boundary/Kelvin waves included in the wave adjustment process.

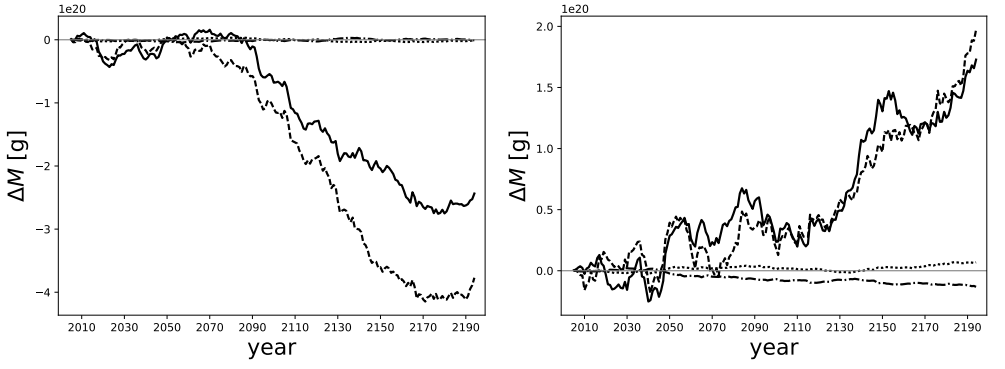


Figure 3.14: Counterparts of Figure 3.10 for $N-C$ (left) and $S-C$ (right). The Bering geostrophic transport anomaly (solid line) is compared against the total transport anomaly (dashed line). The baroclinic contribution (dash-dotted line) and Ekman transport (dotted line) are negligible.

## 3.5 Discussion and conclusion

Freshwater forcing, derived from a Greenland and Antarctic ice sheet melt scenario, was applied to the ocean in a coupled climate model, otherwise forced by an RCP8.5 scenario until 2100 (ramp-up) and a reversal in greenhouse gas concentrations and freshwater forcing after 2100 (ramp-down). It was found that the Atlantic exports both excess freshwater (volume anomalies) and salt during the latter half of the 21$^{\text{st}}$ and the 22$^{\text{nd}}$ century. The salinity decrease in the Atlantic and Arctic is more than would be expected from a mere dilution response from the freshwater forcing. In addition to the dilution, the salt transport across the Atlantic boundaries changes in such a way that additional freshening occurs.

In response to the freshwater forcing, the net volume transport across zonal sections at the latitude of Cape Agulhas and through Bering Strait develop almost similar anomalies. Initially transports increase, but after 50 years they start decreasing. At the same time

a small residual imbalance between these two transports develops, becoming larger in time, with a larger outflow anomaly at the southern boundary than the inflow anomaly through Bering Strait. This net flow divergence in the Atlantic allows export of part of the excess volume of freshwater released from the Greenland Ice Sheet to the Southern Ocean across the Cape Agulhas section.

Splitting the salt advection into three dynamic components indicates not only a barotropic response, but also that the baroclinic gyre and overturning effects have a major share in the export of salt. During the first 50 years the salt export due to barotropic circulation changes is compensated by the South Atlantic subtropical gyre importing saltier waters (not shown). The positive salinity anomaly is subsurface and not visible in the sea surface salinity anomaly shown in Figure 3.2. After 2070, when freshwater from the Antarctic Ice Sheet arrives at the eastern boundary of the South Atlantic, both gyre and overturning components freshen the basin. The baroclinic signal is almost solely determined by changes at the Agulhas section, while the barotropic signal is a residual between the inflow in the north and outflows in the south.

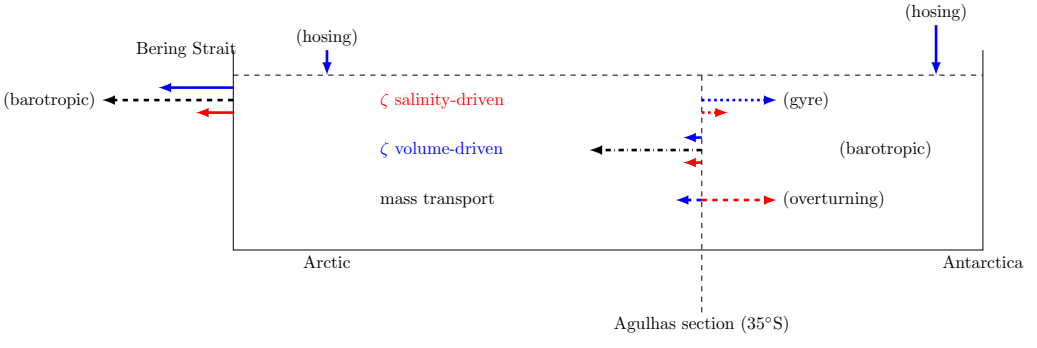


Figure 3.15: Summary diagram indicating the (long-term integrated—at 2195) salt and mass transport changes in the Arctic-Atlantic basin (H-C) in response to freshwater releases due to ice cap mass loss. Colours and line styles correspond to those in Figures 3.8 and 3.7.

In Figure 3.15 a summary of the long-term integrated effects of the hosing scenario are depicted. Larger arrows indicated a larger response, but they are not to scale. Black arrows indicate the mass transport, blue the volume-driven salt transport, and red the salinity-driven salt transport.

The freshwater from the Greenland and Antarctic ice sheets results in an adjustment of the Atlantic on longer timescales than studied here. The simulations show the beginning of this process and an equilibrium-response would take much longer time. Nevertheless, the experiments discussed here show a delicate interplay between the impact of Greenland meltwater and Antarctic meltwater release that can have opposing effects in the Atlantic. For instance, freshwater from Antarctica and freshwater from Greenland have opposite effects on the large-scale north-south density gradient, and this gradient

is often used as a metric for the strength of the AMOC (Thorpe et al., 2001). Also, meltwater release from the Antarctic Ice Sheet might negatively impact Antarctic Bottom Water formation, and a reduced deep overturning cell might impede weakening of the AMOC through the bipolar seesaw effect (Green and Schmittner, 2015; Seidov et al., 2001; Stocker and Johnsen, 2003). The nature of the ramp-up/ramp-down experiment we have performed is by no means a realistic future scenario and was designed such that processes that take a long time to adjust become more apparent in the ocean response to freshwater forcing (e.g. the North Atlantic gyre responses). As a result, the integrated quantitative effects occurring in the model are far from a realistic future response to more realistic meltwater scenarios. Qualitatively, however, we have been able to demonstrate various—sometimes opposing—dynamic adjustments and feedbacks occurring in response to freshwater from both northern and southern sources.

After five decades the response at the Southern boundary changes sign. A slower, advective, oceanic response overtakes the effect of salinification by transporting Antarctic freshwater, associated with enhanced mass loss from the Antarctic Ice Sheet, to the South Atlantic and the whole Atlantic starts to freshen, even though the Agulhas leakage and the supergyre transport keep increasing. Also, the imbalance in barotropic transport affects the salinity budget in the Atlantic. Initially, Bering Strait transport increases less than the outflow across the Agulhas section from Africa to South America does. After 50 years, however, both start decreasing, with the response at Bering Strait being stronger than that of the Agulhas section. The initial increase appears due to SSH anomalies from added volume from Antarctica quickly arriving in the North Pacific, while similar anomalies resulting from added volume from Greenland initially travel southward. After 50 years, part of the volume excess originating from Greenland reaches the Arctic, being advected by the North Atlantic and Norwegian Current and spread further by the Beaufort Gyre.

While initially the SSH gradient over Bering Strait increases, after 50 years it starts to decrease. The integrated response to these barotropic changes is that the Atlantic freshens. It should be emphasised that this response cannot be explained by an increase or decrease in barotropic throughflow or Bering Strait inflow, since in such case the response in salinity would be opposite to the response in barotropic flow Hu et al. (2011). The salt export is due to the consistent divergence of barotropic flow, i.e. outflow across the Agulhas section increases more or decreases less than Bering Strait inflow.

Bering Strait can be important for the stability of the AMOC. After an AMOC collapse, recovery is more difficult with a closed Bering Strait (Hu et al., 2007; Hu et al., 2012). A closed Bering Strait traps low salinity anomalies in the Arctic, possibly destabilising the overturning, as shown in previous studies (e.g. Reason and Power, 1994; De Boer and Nof, 2004; Hu et al., 2015). In many coarse resolution models, Bering Strait is not well resolved, however. The model used here has one degree horizontal resolution, and Bering Strait features a realistic width and depth, allowing geostrophic processes to dominate over frictional processes. With a volume transport of $\sim$ 1 Sv, the modelled Bering Strait throughflow is in agreement with observed values (Woodgate et al., 2006).

A main conclusion from this paper is that melting ice sheets do not merely dilute the ocean and increase sea level. A much more complicated picture arises where both barotropic and baroclinic effects play a role. The salinity of the Atlantic depends not just on the dilution effects of Greenland meltwater, but also on the dynamic effects brought about by the Antarctic meltwater. The imbalance that develops between the mass flux anomaly at Bering Strait and at the zonal section at the latitude of Cape Agulhas eventually leads to additional freshening of the Atlantic (both through salinity and volume transport changes) beyond what would be expected from Greenland meltwater alone.

The freshwater releases from Greenland and from Antarctica have a distinctly different effect on the volume transports and salt balance of the Atlantic. In the case of SH meltwater forcing, the SSH gradient over Bering Strait increases, and subsequently the barotropic throughflow across the Arctic-Atlantic basin increases. Transport at the Agulhas section responds in a very similar way, but the increase is slightly less, leading to net convergence and salinification of the basin. With only NH meltwater forcing, the SSH gradient across Bering Strait decreases, with, again, transport across the Agulhas section following the decrease, but being slightly weaker. The result is a decrease and net divergence of the barotropic flow, leading to overall freshening of the basin.

Our study indicates that coupled ocean-atmosphere processes are of minor importance for the adjustment of the salt budget in the Atlantic in response to freshwater sources, while coupled processes are important in driving South Atlantic circulation changes. A resultant shift of the ITCZ is noted, but hardly affects the salt budget, when integrated over the whole Arctic-Atlantic basin, as areas of positive and negative EPRI response cancel out. Also, wind stress changes over the Southern Ocean affect the SH supergyre. Even though the model used is a state of the art coupled model for long climate integrations, there are limitations as well. Because the advection of the meltwater is likely affected by mesoscale eddies, both in the subpolar North Atlantic and by the Agulhas leakage bringing the meltwater from the Antarctic into the South Atlantic, the full effects of melting ice sheets on the Atlantic salt balance are difficult to quantify in our relatively coarse resolution model. The model uses the Gent-McWilliams parametrisation scheme, which is an idealisation (with a constant thickness diffusivity). The choice of eddy parametrisation can affect the results (e.g. Eden et al., 2009). We also do not know to what extent the melt scenario used here will be applicable to the real world. It is nonetheless clear that feedbacks in the Southern Ocean are of importance. The Southern Hemisphere forcing will eventually dominate the Northern Hemisphere forcing, because a larger volume of meltwater can be released from the Antarctic Ice Sheet compared to the Greenland Ice Sheet; the potential contribution from Antarctica to global sea level rise can be much larger than Greenland's in a high-end scenario (DeConto and Pollard, 2016; Katsman et al., 2011; Le Bars et al., 2017).

## Acknowledgements

This work was funded by the European Commission's 7th Framework Programme, under Grant Agreement number 282672, EMBRACE project. The authors thank Frank Selten for useful suggestions. The anonymous referees have contributed substantial improvements to the manuscript, for which the authors are also grateful.

## 3.A Salt transport split

A zonal-depth variable (like on the zonal sections we consider in this paper) can be decomposed into a depth anomaly with respect to the zonal average and the remainder, $V = \delta^x V + \langle V \rangle_x$, where

$$\langle V \rangle_x = \int V \, \mathrm{d}x \Big/ \int \mathrm{d}x = \frac{1}{w_x} \int V \, \mathrm{d}x,$$
$$\delta^x V = V - \langle V \rangle_x.$$

Note that $V$ and $\delta^x V$ are 2-dimensional, while $\langle V \rangle_x$ only has the dimension of depth. We can split into these components,

$$\begin{aligned} S \cdot V &= (\delta^x S + \langle S \rangle_x) \cdot (\delta^x V + \langle V \rangle_x) \\ &= \delta^x S \cdot \delta^x V + \delta^x S \cdot \langle V \rangle_x + \delta^x V \cdot \langle S \rangle_x + \langle S \rangle_x \cdot \langle V \rangle_x; \end{aligned}$$

but the cross terms integrate to zero, because (integrating over a section $b$)

$$\iint_b \delta^x V \cdot \langle S \rangle_x \, \mathrm{d}x\mathrm{d}z = \iint_b \delta^x V \, \mathrm{d}x \langle S \rangle_x \, \mathrm{d}z$$
$$\int_b \delta^x V \, \mathrm{d}x = \int_b V \, \mathrm{d}x - \langle V \rangle_x \int_b \mathrm{d}x \equiv 0.$$

We are then left with only two terms. We let

$$\zeta_{\mathrm{az}} = \iint_b \delta^x V \cdot \delta^x S \, \mathrm{d}x\mathrm{d}z,$$

which is sensitive to azonal (not barotropic or overturning, but gyre related). The remaining term leaves

$$\begin{aligned} \iint_b \langle V \rangle_x \cdot \langle S \rangle_x \, \mathrm{d}x\mathrm{d}z &= \iint_b \left( \langle V \rangle_x - \langle V \right) \langle S \rangle_x \, \mathrm{d}x\mathrm{d}z + \iint_b \langle V \rangle \langle S \rangle_x \, \mathrm{d}x\mathrm{d}z \\ &= \zeta_{\mathrm{ov}} + \zeta_{\mathrm{zo}}, \end{aligned}$$

where we use $\langle V \rangle$ for the barotropic (section-averaged) value of $V$. The two remaining terms are sensitive to the overturning and barotropic changes, respectively.

# 4 Circulation adjustment in the Arctic and Atlantic in response to Greenland and Antarctic mass loss

## 4.1 Introduction

In a warming climate, the increase in atmospheric temperature will also affect the ocean and cryosphere (Pörtner et al. (In press) provides a synthesis of current research on this topic). Apart from heating up the ocean, ice melt—in particular from the Greenland and Antarctic ice sheets—will increase, leading to enhanced freshwater release to the ocean. The direct effect of this meltwater is a decrease in sea surface surface salinity and a rise in sea level (Bindoff et al., 2007). At low temperatures, the thermal expansion coefficient for sea water is low compared to the haline contraction coefficient (Aagaard and Carmack, 1989); for this reason, the impact on density of adding freshwater is largest in a cold environment, e.g. where mass loss from the Greenland and Antarctic ice sheets naturally occurs. A freshwater excess at the northern convection sites (Labrador Sea, Irminger Sea, Nordic Seas) could also have an impact on the ocean circulation by affecting the Atlantic Meridional Overturning Circulation (AMOC) and gyre circulation (Yang et al., 2016).

There is observational evidence that the AMOC has already been in decline since the last decade (Smeed et al., 2018) and this is supported by observed spatial patterns in sea surface temperatures (SSTs) (Caesar et al., 2018) that are also seen in climate models. More recent observations (Moat et al., 2020a), however, indicate the AMOC is no longer weakening. Additionally, Fu et al. (2020) argue that the current AMOC state is not different from several decades ago and show that within the North Atlantic subpolar gyre (SPG) a stable overturning persists in the eastern part of the basin, as opposed to the Labrador Sea, despite substantial upper-layer water property changes. Since it is unclear whether the observed AMOC weakening in the last decade was due to anthropogenic forcing or part of an internal variation, observations over a longer period are needed. Also, SSTs have changed; the North Atlantic has seen elevated SSTs in the recent several decades of up to 1°C (Bulgin et al., 2020). The spatial pattern of the SST tendencies is

not uniform and the largest differences have occurred recently. In particular, there is a cooling south of Greenland ('warming hole') and a stronger increase further south in the Gulf stream region. Mass loss from the polar ice sheets also has become apparent from changes in elevation (Helm et al., 2014). A sixfold increase in Greenland mass loss has been observed since the 1980s (Mouginot et al., 2019), and Antarctic mass loss has also accelerated over the past decades (Paolo et al., 2015).

Ice sheet mass could weaken or destabilise the AMOC and force it into a long-term 'off-state' (e.g. Rahmstorf, 1996). AMOC bistability was first shown to exist in a general circulation global climate model by Manabe and Stouffer (1988). A collapse of the AMOC can have drastic consequences such as cooling of the Northern Hemisphere and warming of the Southern Hemisphere (Vellinga and Wood, 2002). Such abrupt changes have also occurred in past AMOC switches and is seen in the Greenland ice core record (Dansgaard et al., 1982; Johnsen et al., 1992). In a study comparing the response in five climate models to a 0.1 Sv (1 Sv = $10^6$ $m^3$ $s^{-1}$) freshwater discharge from Greenland only (Swingedouw et al., 2013b); it was found that the AMOC was impacted, but that the weakening depends on the amount of leakage of the freshwater anomaly from the subpolar to the subtropical gyre. In a follow-up study (Swingedouw et al., 2015) it was shown that the AMOC response to the same amount of hosing decreased with global warming in an RCP8.5 scenario (Taylor et al., 2012) run. Increased stratification due to warming diminished the additional impact of increased stratification due to freshwater discharge in the subpolar gyre. Also, leakage of the additional freshwater to the subtropical gyre increased due to a northward shift of the storm tracks reducing the tilt of the subpolar-subtropical gyre front. In both studies the simulations were only a few decades long and the AMOC response was not yet equilibrated. The impact of freshwater discharge from Greenland on the Nordic Seas can also take place on a longer timescale than its impact on the Labrador and Irminger Seas, because in the former case the freshwater has to recirculate in the subtropical gyre before it reaches the north-east Atlantic, while in the latter case the freshwater already arrives within a few years. The different timescales for Greenland freshwater discharge affecting deep convection sites in the Labrador and Irminger Seas versus the Nordic Seas imply a possibly complex AMOC response to Greenland mass loss, operating at various timescales.

Deep convection in the Labrador, Irminger and Nordic Seas is tightly coupled to the AMOC, as shown by model experiments in which the AMOC weakens when deep convection declines in response to additional freshwater release (Stouffer et al., 2006; Brodeau and Koenigk, 2016; Drijfhout, 2015). This coupling is corroborated by analysis of the pathways of the lower branch of the AMOC (Lavender et al., 2000; Gary et al., 2011; Rhein et al., 2017) which shows that an interior pathway from the subpolar to the subtropical North Atlantic gyres carries a significant export of deep water. In addition, the AMOC slowdown may trigger a delayed positive feedback by amplifying the freshening over the convection sites through reduced northward transport of salty waters, away from the South Atlantic (Drijfhout et al., 2011; Jackson et al., 2013). On the other hand, after advection of the freshwater anomaly to the eastern side of the subpolar

gyre (Swingedouw et al., 2013b), the net effect on east-west density (and pressure) gradients of the added freshwater remains small, and this might imply a much weaker impact on zonally averaged northward volume transport than expected from the impact of deep convection alone.

The effect of freshwater discharge from Antarctica might also affect the AMOC and even strengthen it. It has been shown that multi-decadal to centennial timescales in ocean and climate models the AMOC often scales with a north-south pressure (density) gradient (Marotzke, 1997; Thorpe et al., 2001; Sijp et al., 2012). This implies that changes in the Southern Ocean can affect the AMOC as well, but on a longer timescale (Weijer et al., 2002; Weber and Drijfhout, 2007). A more rapid response through wave dynamics is, however, also possible (Swingedouw et al., 2009). A freshwater discharge from Antarctica in that case would act to reduce density and pressure in the south. The effect of Antarctic freshwater release would be to increase the north-south pressure (density) gradient and strengthen the AMOC. For this reason, it is important to study the AMOC response in a freshwater discharge scenario that accounts for both Northern and Southern Hemisphere sources instead of meltwater discharge from Greenland only (Swingedouw et al., 2013b; Weijer et al., 2012; Bakker et al., 2016; Haskins et al., 2020). The calving of icebergs affects spatial patterns of the mass redistribution, especially in the Southern Ocean (Starr et al., 2021).

Here we will investigate the response of the Atlantic circulation to freshwater release from both Northern and Southern Hemisphere sources combined and in isolation, to assess their impact, to what extent these impacts counteract or reinforce each other, and how they change over time. To clearly assess the influence of freshwater discharge from Antarctica in addition to discharge from Greenland, we rely on a scenario where, eventually, mass loss from Antarctica becomes larger (a factor of 2.5) than mass loss from Greenland, in agreement with a scenario in which the West Antarctic Ice Sheet starts to collapse (Joughin et al., 2014; Rignot et al., 2014; Feldmann and Levermann, 2015; Shepherd et al., 2019) when forced with the RCP8.5 emission scenario. The freshwater forcing scenario includes an iceberg distribution pattern (described in Van den Berk and Drijfhout, 2014) that distributes a freshwater release further away from the ice sheets. This distribution was derived from modelled iceberg drift under current conditions. After 2100 both types of forcing decrease to the initial 2005 values, to emphasise different timescales between forcing and response.

This paper is structured as follows. Section 4.2 summarises the experimental set-up and presents the framework of the analysis. In Section 4.3 the analysis is shown. A discussion of the main results and final conclusions are presented in Section 4.4.

## 4.2 Experiments

The forcing profiles for $CO_2$ concentration and meltwater release used here are shown in Van den Berk et al. (2019) and reproduced here as Figure 4.1. The freshwater release is

described in detail in Van den Berk and Drijfhout (2014). In summary, until year 2100

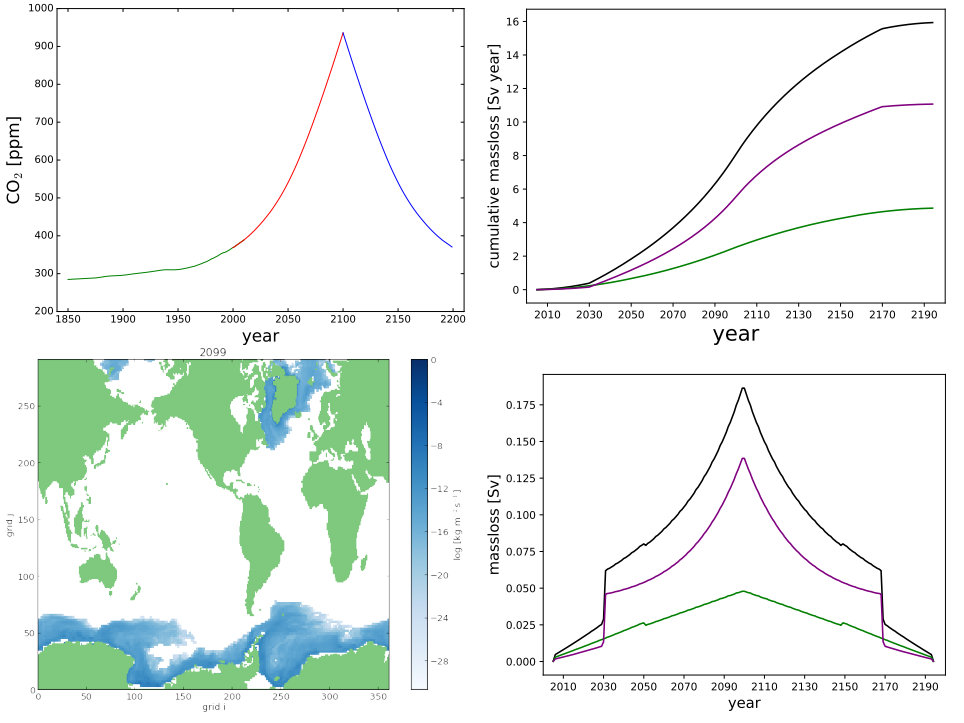


Figure 4.1: Top: The two forcing profiles applied in our simulations. Top-left panel: atmospheric $CO_2$ concentration. In green the historical phase (after which our simulation start), in red the 'ramp-up' phase with increasing $CO_2$, and in blue the 'ramp-down' phase as a counterpart to the ramp-up. Top-right panel: cumulative global freshwater forcing (global: black, northern hemisphere: green, southern hemisphere: purple). Bottom-left: iceberg melt pattern (see Van den Berk and Drijfhout, 2014, for technical details). Bottom-right: melt rates; the top-right panel shows the time-integrated curves of these. Reproduced from Van den Berk et al. (2019).

there is an increase in both forcing time series, followed by a time-symmetric decrease of the forcing until year 2195. The freshwater discharge from Greenland increases from 0 Sv in the year 2005 when the RCP scenarios start, to 0.07 Sv in year 2100; after which it decreases again to 0 Sv in 2195; for Antarctica the value in year 2100 is 0.17 Sv. These numbers lead to 71.5 cm sea-level rise in year 2100 due to mass loss from ice sheets only, which is large but not unrealistic. For instance, the value for the 83$^{\text{rd}}$ percentile (the upper bound of a likely range of 2/3) in a RCP8.5 scenario given in Bamber et al. (2019) is 102 cm. The two phases (before and after year 2100) are labelled 'ramp-up' and 'ramp-down' (see also Sgubin et al., 2014 for a similar experimental set-up. The atmospheric forcing follows the RCP8.5 scenario (Taylor et al., 2012) during the ramp-up; the freshwater forcing time series is described in more detail in Van den Berk and

Drijfhout (2014). The control experiment *C* does not include the freshwater forcing, while *H* includes freshwater forcing in both hemispheres. Northern Hemisphere-only freshwater forcing (*N*) and Southern Hemisphere-only freshwater forcing (*S*) each have one single member, *C* and *H* each have four members (see Table 4.1 for an overview of all runs). All output was saved as monthly mean values.

| | $CO_2$ | NH melt | SH melt | members |
|---|---|---|---|---|
| C | + | - | - | 4 |
| H | + | + | + | 4 |
| N | + | + | - | 1 |
| S | + | - | + | 1 |

Table 4.1: Overview of experiments and their included forcing. The control experiment *C* does not include the meltwater forcing, but *H* includes forcing in both hemispheres. Northern Hemisphere-only freshwater forcing (*N*) and Southern Hemisphere-only freshwater forcing (*S*) each have a single member, *C* and *H* each have four.

The experiments are performed with the Coupled Climate Model (CCM) EC-Earth which consists of three components. The atmosphere and land surface are modelled with the Integrated Forecast System (IFS–cycle 31r1) which resolves 62 layers in the vertical and uses a triangular truncation at wavenumber 159 (ECMWF, 2006, effectively resolving $\approx$ 130 km). The ocean is modelled by the Nucleus for European Modelling of the Ocean (NEMO) developed by the NEMO European Consortium at a resolution of approximately 1° in the horizontal ($\approx$ 110 km at mid latitudes) and 42 levels in the vertical (Madec, 2008). The two are synchronised along the interface every three model-hours by the OASIS3 coupler developed at the Centre Européen de Recherche et de Formation Avancée en Calcul Scientifique (Valcke et al., 2004). The ocean model is coupled to a sea ice modell developed by the University of Louvain-la-Neuve (LIM2) (Fichefet and Morales Maqueda, 1997; Bouillon et al., 2009). The general characteristics of EC-Earth simulations are described by Hazeleger et al. (2012); Sterl et al. (2012) describes the ocean aspects in greater detail. Sterl et al. (2012) note that the overturning strength shows 2 Sv fluctuations on decadal scales, and these variations are driven by ocean temperature variations. Wouters et al. (2012) note that AMOC fluctuations in EC-Earth are not directly forced by the atmosphere, but are delayed responses to the ocean being forced by the North Atlantic Oscillation (NAO, Hurrell, 1995) on a 60-year timescale.

In response to the freshwater forcing, the salt balance in the ocean is expected to differ by latitude as the freshwater spreads out through the ocean. Apart from the extra freshwater forcing applied, the salinity is affected by ocean advection and changes in evaporation, precipitation, run-off, and changes in sea ice volume (E-P-R-I). To gain insight into the processes that change the ocean's salinity we consider regional budgets

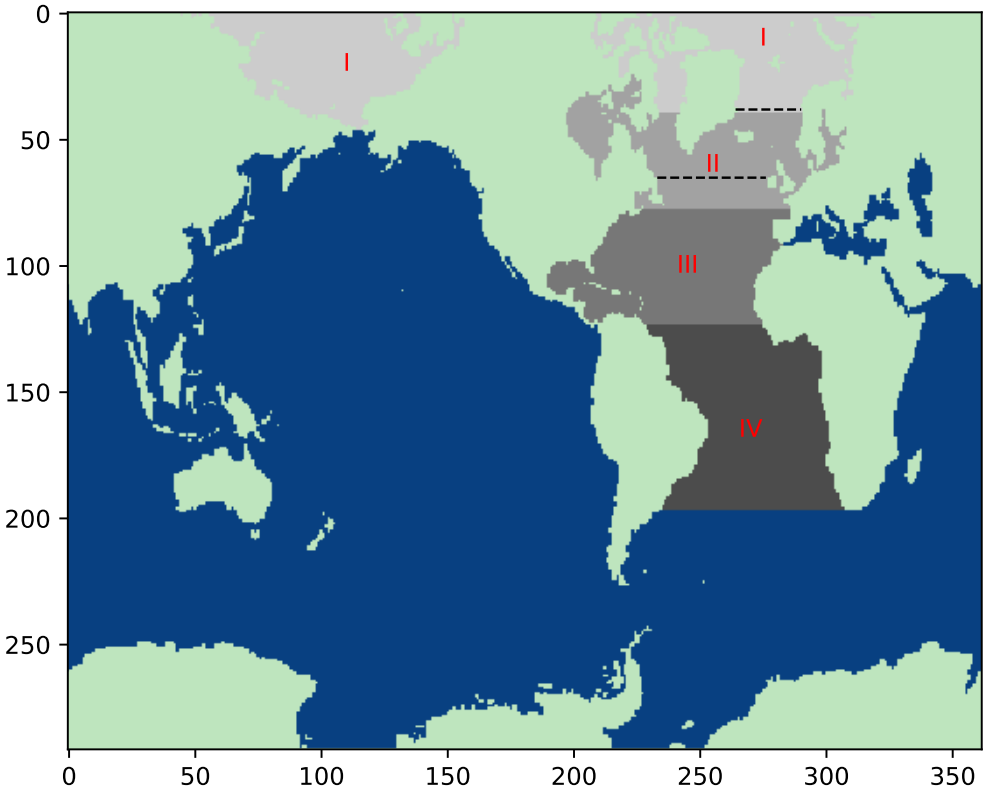


Figure 4.2: Basin partitioning on the model grid (ORCA 1). I: Arctic, II: subpolar gyre, III: subtropical gyre, IV: South Atlantic. Boundaries are at $34°S$ and $(9, 47, 67)°N$, ($67°N$ is the latitude of Bering Strait). These four areas extended to depth are referred to as boxes 1-4 in the text. Dashed lines indicate sections ate $70°N$ and $55°N$

.

according to the partitioning shown in Figure 4.2 which divides the Arctic-Atlantic basin into four boxes with five zonal sections as boundaries between them and the rest of the ocean. The first box is the Arctic ocean, and box 2 and 3 contain the subpolar and subtropical North Atlantic gyres, respectively; the fourth box is the remainder of the basin (South Atlantic) with the cut-off placed at the section connecting Cape Agulhas with South America. There is one meridional section through the Strait of Gibraltar in box 3.

In the next section, salt advection is decomposed into three components: overturning, azonal (gyre), and barotropic flow. Transport changes are also decomposed in a part driven by changes in volume transport and a part driven by changes in salinity. For more details, and the mathematical formulation of these components, we refer to Van den Berk and Drijfhout (2014) and Van den Berk et al. (2019).

## 4.3 The salt redistribution within the Atlantic basin

The freshwater from the forcing field is not uniformly spread throughout the World Ocean as shown in Figure 4.3. In the North Atlantic, the shape of the salinity anomaly on the subpolar/subtropical interface suggests that the subpolar gyre redistributes the freshwater from the forcing and that significant exchange with the subtropical gyre occurs (similar as seen in Swingedouw et al., 2013b). Near the Antarctic Peninsula, the Antarctic Circumpolar Current (ACC) distributes the freshwater originating from Antarctica northward in the Southern Ocean. Also, there is a lag of 50 years before salt is exported from the Southern Ocean into the South Atlantic across the Agulhas section (see Van den Berk et al., 2019).

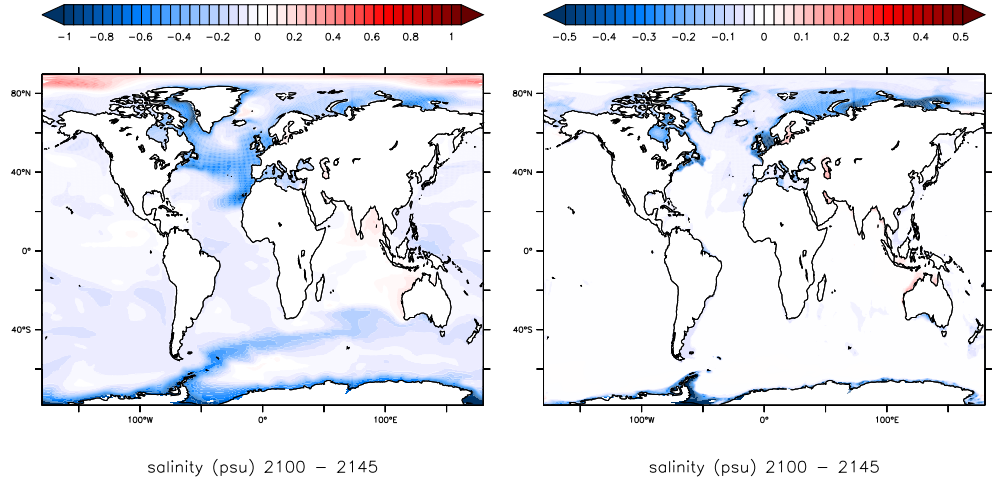


Figure 4.3: Left: Ensemble-averaged 45-year averaged surface salinity anomaly ($H - C$) and right: depth-averaged salinity anomaly ($H - C$) after 95-140 years of forcing. Note the difference in scale between the panels.

While the basin-integrated freshwater budget is dominated by adjustments at the southern boundary of the South Atlantic (Van den Berk et al., 2019), Figure 4.3 shows that the largest changes in freshwater transport occur within the North Atlantic. Freshwater changes induced by anomalous salt advection strongly differ per region, as is shown in the top panel in Figure 4.4.

The difference between the simulations with the freshwater forcing and the control runs is a residual signal for barotropic, overturning, and gyres salt transports. As is shown below, the barotropic and overturning transport residuals nearly cancel each other between the subpolar gyre (SPG) and subtropical gyre (STG), leaving a small net effect that is dominated by adjustment of the gyre in the SPG. Between the SPG and Arctic, however, there is a near cancellation between the gyre components, leaving a residual that is dominated by changes in barotropic and overturning transports. Below we first

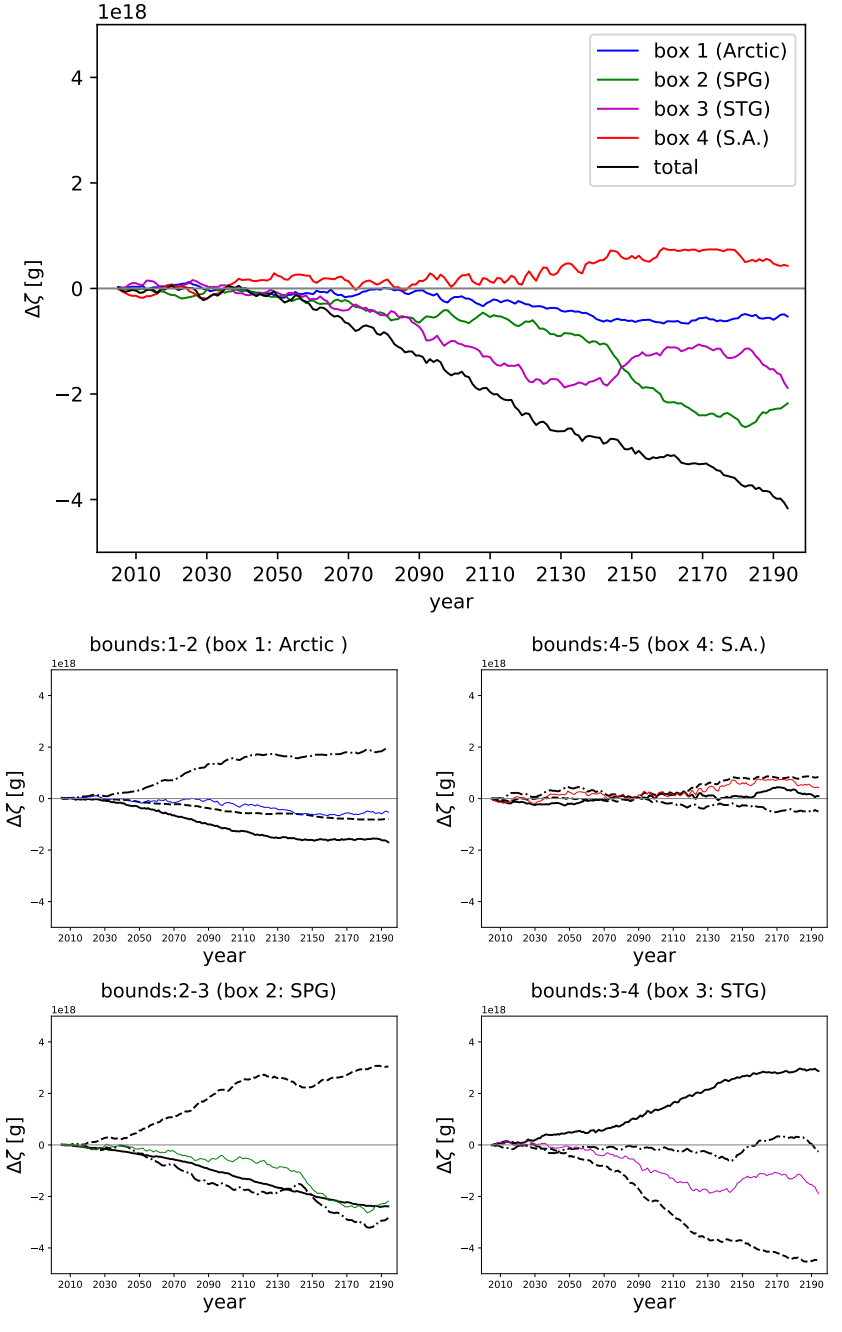


Figure 4.4: Anomaly ($H - C$) of time-integrated salt advection. Top panel shows the total salt advection anomaly across each box (i.e. depth-integrated north- south differences) and for the Arctic-Atlantic together. The panels below have the salt advection across the indicated box(es) split into three dynamic components: barotropic (solid line), overturning (dashed line), and azonal or gyre (dash-dotted line); sum values correspond to those in the top panel. Ensemble averages.

focus on the interaction between the Arctic and the North Atlantic subpolar gyre (Section 4.3.1). We proceed with the interaction between the North Atlantic subpolar and subtropical gyres (Section 4.3.2) that gives rise to the peculiar salt redistribution seen in the North Atlantic in Figure 4.3. The South Atlantic shows little response and will not be discussed in detail.

### 4.3.1 Salt exchange between the Arctic and subpolar North Atlantic

Figure 4.4 shows a counteracting signal in the gyre-driven salt advection between the Nordic Seas and the North Atlantic subpolar gyre. This change in transport is dominated by velocity changes in the subpolar gyre, as illustrated by Figure 4.5. This figure shows plots of the net salt advection for the four boxes decomposed into components associated with salinity (S) and velocity (V) changes. In the subpolar North Atlantic anomalous salt transport by the gyre freshens the North Atlantic by increasing the net export of salt to the Arctic where the gyre salinifies the basin (Figure 4.5, dash-dotted lines). To understand this further we investigate the change in vertically-averaged horizontal circulation in the North Atlantic. The subpolar gyre shows a decrease in strength in the west (as seen in the barotropic streamfunction in Figure 4.6), while the gyre circulation in the Nordic Seas becomes stronger. The gyre causes more salty water from the North Atlantic Current to be drawn into Arctic while the return flow in the East Greenland Current becomes fresher, explaining the salinity-driven component in salt-increase in the Arctic by the gyre (Figure 4.5, dash-dotted lines in left panels). This raises the question: which processes are responsible for the change in gyre strength? And more specifically, is the change purely an ocean-driven adjustment or does it involve atmospheric feedbacks?

#### Forcing and transport response

First, we investigate whether changes in buoyancy and windstress forcing can account for the change in gyre circulation. Between Scotland and Iceland the North Atlantic Current diverges into two main pathways; one branch feeds the subpolar gyre and another feeds the Nordic Seas by continuing past Iceland. The weakening of the subpolar gyre leads to warmer and saltier water bypassing the subpolar gyre and travelling, via the Norwegian Current, into the Nordic Seas. As a result, within the subpolar gyre SST decreases and heat loss to the atmosphere decreases, leading to a net heat gain by anomalous surface buoyancy fluxes (Figure 4.7). This is especially noticeable in the two main convection sites in the Labrador and Irminger Seas where we note a greater increase in downward buoyancy flux (less heat loss to the atmosphere) than in other parts of the subpolar gyre. In the Nordic Seas the opposite occurs, where the buoyancy flux increase is dominated by the thermal forcing (Figure 4.7). Note that the changes in the haline component of the buoyancy flux are much smaller and can be neglected in the anomalous response. Changes in sea ice due to the freshwater forcing are also negligible.

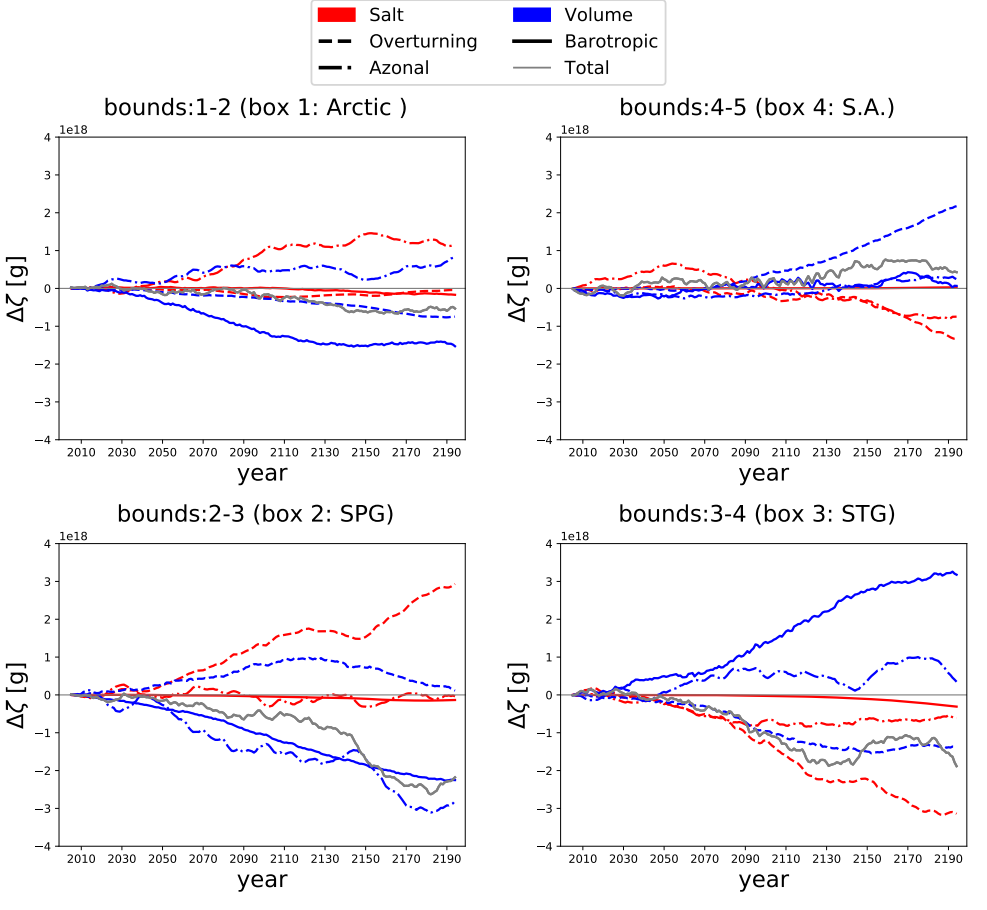


Figure 4.5: For indicated boxes, anomaly ($H - C$) of time-integrated salt advection decomposed into a barotropic (solid line), overturning (dashed line), and gyre (dash-dotted line) component, and each split further into S (salinity driven, red) and V (volume driven, blue) driven parts. Grey lines are their sums (total salt advection through the box). Ensemble averages.

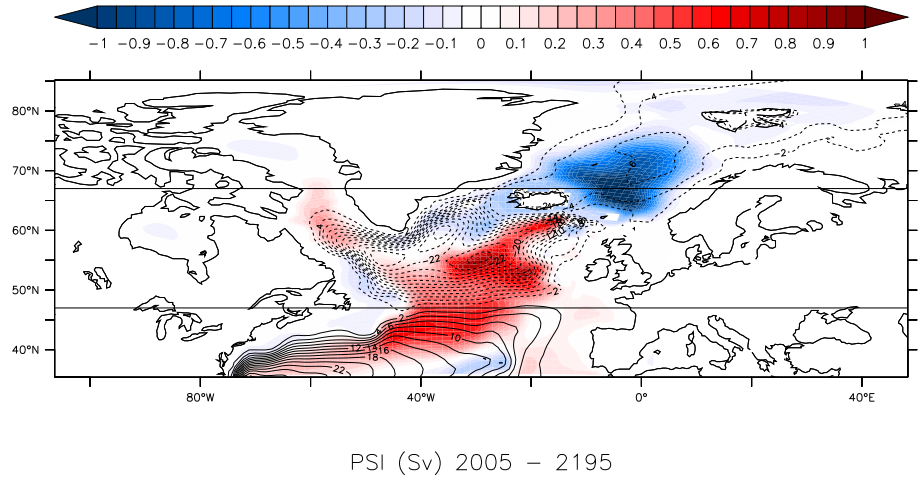


Figure 4.6: Barotropic streamfunction anomaly ($H - C$), with climatology imposed as contours (solid line as clockwise flow, dashed line as counter clockwise flow, horizontal lines indicate the separation of the STG/SPG), mean of years 2005-2195, ensemble average.

The surface buoyancy forcing can modify the potential vorticity of the flow and drive an anomalous gyre circulation (Luyten and Stommel, 1986; De Verdiére, 1989). To estimate the buoyancy forced change on gyre transport, the buoyancy flux is calculated from the net heat flux $Q_H$ [J s$^{-1}$ m$^{-2}$] and net freshwater flux (precipitation - evaporation) $P - E$ [kg m$^{-2}$ s$^{-1}$] (Karstensen and Lorbacher, 2011) as

$$B = \frac{g}{\rho_0}\left[\alpha\frac{Q_H}{C_H} + \beta(P-E)\frac{S}{1-S/10^3}\right],$$

with $\alpha$ [K$^{-1}$] and $\beta$ [kg g$^{-1}$] the thermal and haline expansion coefficients, respectively; $C_H$[J kg$^{-1}$ K$^{-1}$] is the heat capacity of sea water (taken as constant) and $S$ [psu] is the salinity. The units of $B$ are m$^2$ s$^{-3}$. The values of the expansion coefficients can be determined (at surface pressure $P = 0$) from the TEOS-10 polynomial approximations (McDougall et al., 2009). The buoyancy flux induces a vertical velocity at the base of the (upper) mixed layer in a simple two layer approximation (Luyten and Stommel, 1986). By defining a reduced gravity $g'$ between the first layer at depth $ML$, and the deeper ocean ($D$) below,

$$g' = g\frac{\rho_D - \rho_{ML}}{\rho_0},$$

we can relate a buoyancy forced interfacial velocity $W_b$ to the buoyancy forcing as

$$W_b = -B/g'.$$

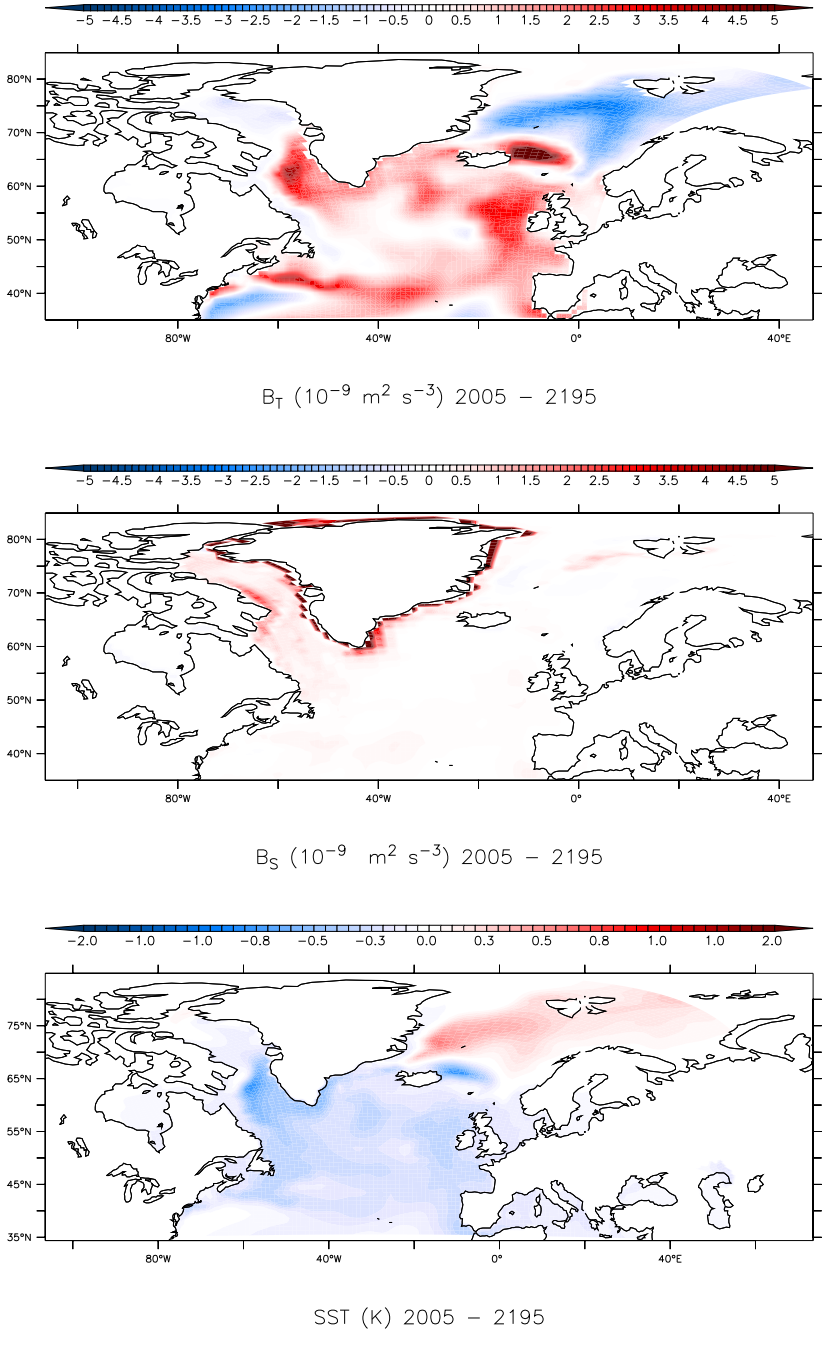


Figure 4.7: Mean thermal-buoyancy flux anomaly (top), haline-buoyancy flux anomaly (middle) and SST anomaly (bottom). The SST decreases in the SPG, leading to a decrease of heat flux into the ocean, which results in a lack of buoyancy loss in the SPG. The Nordic Seas show the opposite pattern. Mean of years 2005-2195, ensemble averages $(\boldsymbol{H} - \boldsymbol{C})$.

This velocity can then be used with the vertically integrated vorticity equation to estimate the contribution to the gyre's mass transport $V_b$ that is forced by heating or cooling:

$$\beta V_b = f \int_{x_e}^{x_\psi} W_b \, \mathrm{d}x. \tag{4.1}$$

These buoyancy forced changes in gyre transport occur via SST changes related to changes in circulation; that is, they act as a feedback on already initiated changes by another process which must be the wind-driven response of the gyre. We can determine the depth-integrated Sverdrup transport $V_w$ from the Sverdrup balance,

$$\rho_0 \, \beta \, V_w = \int_{x_e}^{x_m} \frac{\partial \tau_y}{\partial x} - \frac{\partial \tau_x}{\partial y} \, \mathrm{d}x, \tag{4.2}$$

with $\rho_0$ (= 1020 [kg m$^{-3}$]) the model reference density, $\beta$ [s$^{-1}$ m$^{-1}$] the meridional variation of the Coriolis-frequency, and $\tau$ the windstress vector [N m$^{-2}$]. We integrate from the East coast ($x_e$) to the extremum of the barotropic streamfunction ($x_m$) to avoid the boundary current in the West, where the Sverdrup balance ceases to hold. With these expressions we can compare the effects of wind and buoyancy forcing on transport changes in the gyre of the Nordic Seas and in the western subpolar gyre.

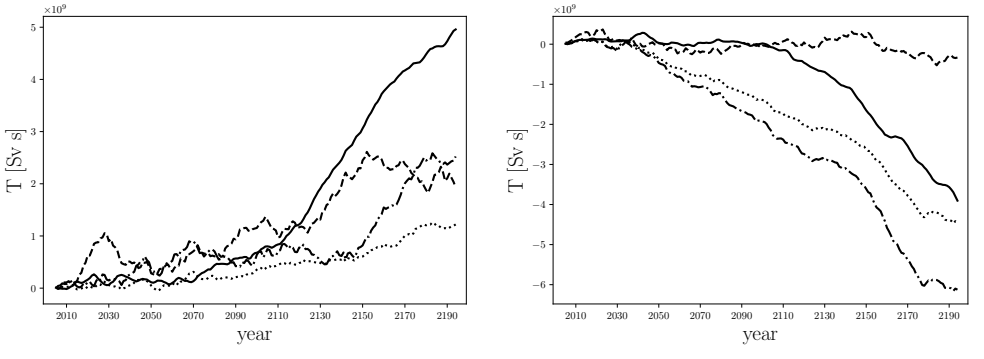


Figure 4.8: Time-integrated Sverdrup transport anomaly ($V$, section-integrated windstress curl scaled with $\rho_0\beta$, dashed line), time-integrated anomaly of the (extremum of the) barotropic streamfunction (excluding the western boundary current, solid line), and meridional transport due to buoyancy forcing changes (dash-dotted: 100 m, dotted: 200 m mixed layer depth, Eq. 4.1). Left panel: (70°N) East of Greenland to Norway. Right panel: 55°N (from Ireland to 25°W to avoid the recirculation cell in the SPG to the west of that longitude). Ensemble averages ($H - C$).

From Figure 4.8 it is apparent that the anomaly of the wind-driven Sverdrup transport (dashed line) in the Nordic Seas only partly explains the changes in the barotropic

streamfunction (left panel; solid line), which increases to 5 Sv in 2190 and yielding a positive trend that is still large in 2190. The change in gyre transport in the Nordic Seas can only be attributed for about 50% to changes in the wind; the other half is forced by changes in surface buoyancy flux. The change in subpolar gyre strength in the west (right panel) is of the opposite sign and in 2190 of the order of 4 Sv and also not equilibrated (still decreasing). It is almost completely forced by buoyancy forcing changes. In both cases the largest changes occur after 2100 when the forcing is decreasing, highlighting the decoupling between forcing and response and the role of internal feedbacks in the coupled climate system. In Figure 4.8 we have used mixed layer depths of 100 m and 200 m to determine the sensitivity of the estimated interfacial velocity due to surface buoyancy fluxes to the depth of this layer. It appears that at 70°N a mixed layer depth of 100 m gives a better fit, while at 55°N a mixed layer depth of 200 m does. It should be stressed that the gyre response to changes in buoyancy (and wind) forcing cannot be fully explained by the forcing at one particular latitude. The velocity changes are more complex than can be captured by a simple two-layer model and we cannot expect to fully close the volume transport changes per section with this (crude) method. A more detailed analysis such as done in Le Corre et al. (2020) might give further insight.

The (winter) wind-response in the Nordic Seas gyre is likely initiated by changes in SSTs and air-sea heat fluxes and thus consists of a coupled ocean-atmosphere feedback, which can be explained by the different SST responses between subpolar gyre in the west and the gyre in the Nordic Seas (Figure 4.9). The long-term change in wind stress over the North Atlantic in response to freshwater forcing from Greenland during a strong greenhouse emission scenario ($H - C$) shows increased westerlies at the latitude of Iceland and decreasing westerlies to the south of it centred around 55°N, with again an increase centred around 45°N. This corresponds to a southward shift of the westerly jet stream, but an enhancement of its northerly extension over the British Isles and Scandinavia (i.e. a reduced zonal extent) and a decrease of easterlies between Greenland and Iceland (Figure 4.9 a). This shift is dominated by the response in winter (Figure 4.9 b), with the exception of the increase in westerlies around 45°N which is dominated by spring and autumn (not shown). Over the length of the simulations the variance (dominated by the winter months) in the hosing ensemble ($H$) strongly decreases over the North Atlantic subpolar gyre (Figure 4.9 c). The pattern of change in inter-annual variance corresponds well with the NAO pattern, which has a similar pattern in all simulations (Figure 4.9 d shows the NAO in the control run $C$). The northern pole of the NAO-dipole overlaps with the spatial distribution of change in variance. Apparently the changes in variability are primarily due to the pattern of dominant North Atlantic atmospheric variability, the NAO, which has also been associated with the storm track variability (Hurrell, 1995; Hurrell et al., 2003).

Warming of the Nordic Seas peaks around 70°N; south of 67°N cooling prevails, and is associated with a weaker and fresher subpolar gyre. As a result, a positive northward SST-gradient anomaly weakens the overall north-south-temperature gradient, which reduces westerly winds south of 70°N, while north of 70°N the SST-gradient anomaly en-

hances the westerlies. This differential wind response then enhances the windstress-curl, and subsequently the Ekman pumping and northward Sverdrup transport across 70°N (Pedlosky, 1996).

In Figure 4.10 similar transports are seen as in Figure 4.8, but for $(N - C)$, indicating that the Greenland meltwater forcing is the dominant driver in the Nordic Seas-SPG seesaw effect. Also, in observations an effect of the subpolar gyre and Nordic Seas has already been suggested (Dukhovskoy et al., 2019), although it was argued that it could not be explained by Greenland meltwater discharge alone and the propagation of salinity anomalies from lower latitudes could also play a role. The increase in the wind-driven transport anomaly seen in Figure 4.8 is absent, but the observed change in volume transport is less well explained by the two-layer model for the runs with only 1 ensemble member. It could also be that the wind-response, at least partly, must be attributed to the arrival of the Antarctic freshwater anomaly impacting the North Atlantic gyres. This is supported by the fact that in $(S - C)$ the changes in volume transport in the northern North Atlantic and Nordic Seas oppose those seen in $(H - C)$, especially after year 2100 (not shown).

When the subpolar gyre weakens, isopycnal doming in the middle and the preconditioning for deep convection reduce, limiting the depth of the winter mixed layer. This response is thus consistent with reduced convection, while the response in the Nordic Seas gyre is consistent with increased deep convection. Freshening of the subpolar gyre can therefore push the system to a weaker circulation mode. The mechanism for gyre adjustment discussed here resembles the one found in conceptual and coupled climate models where it was demonstrated that the subpolar gyre may switch from a strong to a weaker mode due to feedback mechanisms involving the stratification in the gyre (Born and Stocker, 2013). Here, also coupled feedbacks through an atmospheric response are instrumental in the observed gyre changes. The opposite, however, might also occur: the decrease of convection could weaken the gyre, which in turn affects the salinity in the gyre centre. Because the salinity affects the convection, a positive feedback loop would be present (Born et al., 2016).

### 4.3.2 Changes in AMOC salt transport between subpolar and subtropical latitudes

The anomalies of the overturning salt-transports make the subpolar gyre saltier and the subtropical gyre fresher. The change in salinity is the main reason, not volume change (AMOC strength) (Figure 4.5, red dashed versus blue dashed lines). Enhanced northward salt transport by the overturning across the subtropical/subpolar gyre boundary in response to freshwater release from Greenland is surprising, as in general the surface waters contain larger freshwater anomalies than the deeper waters (compare the left and right panel in Figure 4.3). This suggests that below the surface more salt is transported northward.

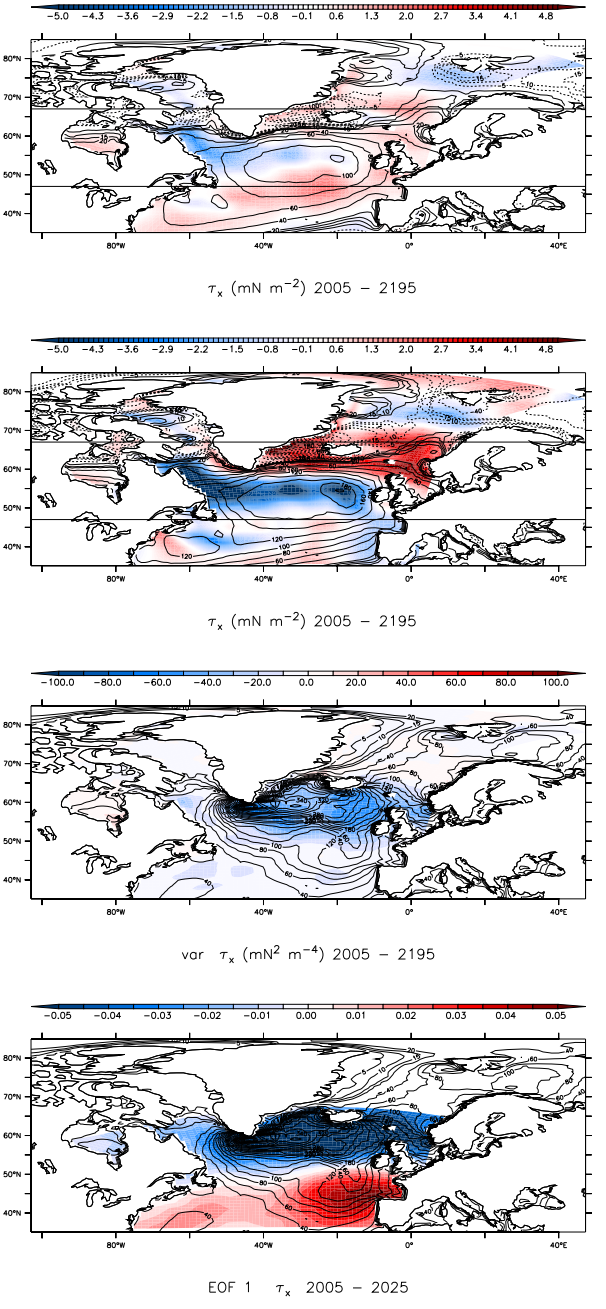


Figure 4.9: Top (a): mean value of the zonal windstress 2005 - 2195 for the winter months (December, January, February); annual mean climatology imposed as contours. Horizontal lines indicate the zonal sections of the SPG box (2). Middle-top (b): as above, but for the winter months (December, January, February) only. Middle-bottom (c): mean variance 2005 - 2195. Ensemble average ($H - C$); contours are annual mean values of 2005-2025. Bottom (d): First principle component (EOF) of 2005 - 2025 capturing 47% of the variance.

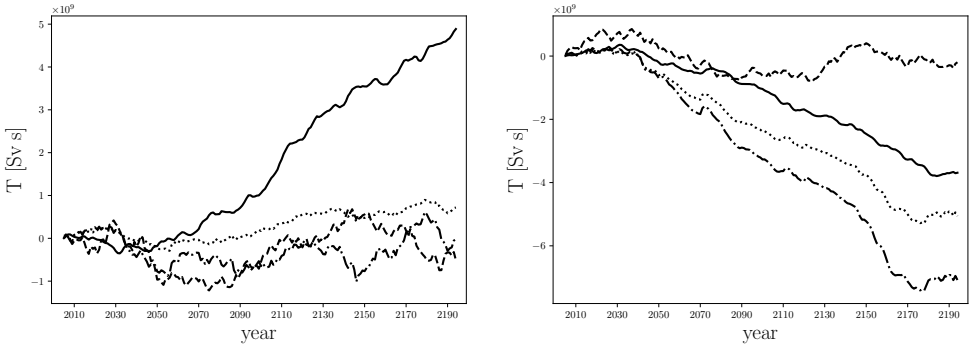


Figure 4.10: Time-integrated Sverdrup transport anomaly ($V$, section-integrated wind-stress curl scaled with $\rho_0\beta$) (dashed line), time-integrated anomaly of the (extremum of the) barotropic streamfunction (excluding the western boundary current, solid line), and meridional transport due to buoyancy forcing changes (dash-dotted: 100 m, dotted: 200 m mixed layer depth, Eq. 4.1). Left panel: (70°N) East of Greenland to Norway. Right panel: 55°N (from Ireland to 25°W to avoid the recirculation cell in the SPG to the west of that longitude. Ensemble averages ($N - C$).

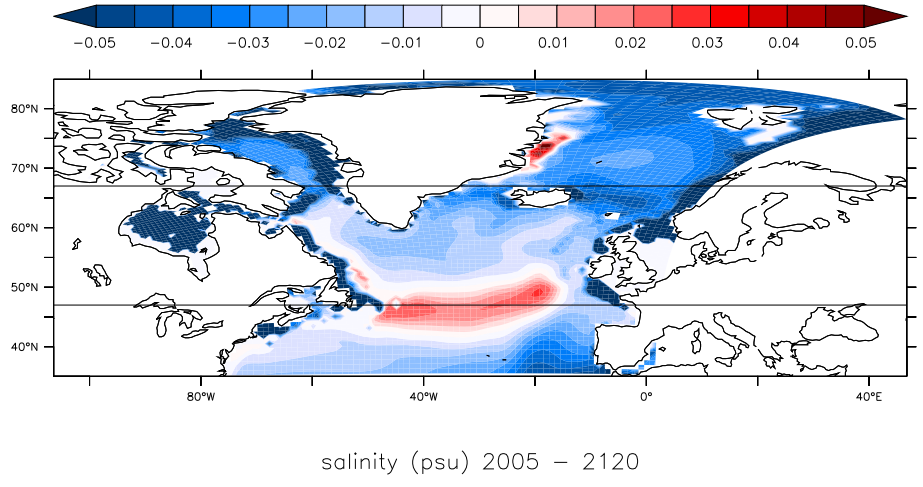


Figure 4.11: Averaged salinity anomaly ($H - C$) over 100 m – 1000 m depth, mean of years 2005 – 2120. Horizontal lines indicate the zonal sections of the SPG box (2). Ensemble average.

In Figure 4.11 it can be seen that a subsurface increase in salinity along the section between the two gyres is the cause for the enhanced northward salt transport by the overturning circulation. The surface has become fresher due to the freshwater release, but the first 1000 m below the surface have become saltier. Comparing with Figure 4.6, we see that the subtropical gyre increases (spin-up) and expands while the subpolar gyre weakens and contracts (spin-down). As a result, the inter-gyre boundary shifts to the North, leaving a positive salinity anomaly along the section chosen to coincide with the gyre boundary in the control run as seen in Figure 4.11. The shift in gyre boundary, which is also the boundary between high and low salinity waters, is associated with a small latitudinal band in which the northward salt transport by the overturning circulation increases.

The overturning circulation also further salinifies the subpolar gyre and freshens the subtropical gyre through changes in velocity (Figure 4.5, blue dashed lines). At first sight this is surprising because the AMOC transports salt from the STG to the SPG, a weakening of the AMOC in response to freshwater hosing is expected to result in subpolar freshening and subtropical salinification. The change in AMOC, however, is more subtle.

**The change in the AMOC**

Over most of the Atlantic, the AMOC initially does not weaken in response to the freshwater forcing but slightly increases in strength. This is illustrated by Figure 4.12 showing a mild increase ($\sim$ 0.5 Sv) at most latitudes during the first 50 years, after which the AMOC starts decreasing.

In Figure 4.13 the mean mixed layer depth anomaly ($H - C$) for 2005 - 2195 is plotted, together with the mean value for 2005 - 2100 under RCP8.5 (ensemble $C$). The mixed layer becomes shallower mainly in the Labrador Sea and Nordic Seas in the control simulations. The additional freshwater forcing widens the deep water formation region in the Labrador Sea and shifts it in the Nordic Seas. Also, there is not a significant change in AABW production under the freshwater forcing judged from the mixed layer depth changes in the Southern Ocean (not shown). Consistent with a lack of response in the Southern Ocean, we do not find a bipolar seesaw effect, unlike results from other model studies (e.g. Swingedouw et al., 2009). The AMOC decreases in the control run ($C$) and the freshwater forcing weakens it further, inhibiting the recovery (and overshoot) seen in the ramp-down phase.

The initial increase in AMOC strength cannot be understood by how the freshwater along the northern boundary of the Atlantic affects the density (i.e. the freshening seen in Figure 4.3). To first order, net sinking and AMOC strength scale with the east-west density gradient along the northern boundary of the SPG (Spall and Pickart, 2001). The added freshwater induces a negative density anomaly that first affects the western side of the boundary. As a result, the east-west density gradient should increase (which is also seen in Figure 4.14), while the AMOC decreases. The argument of Spall and Pickart (2001), however, assumes a direct link between pressure and density gradients, which is only correct under steady-state. Here, a transient source of freshwater is used as a forcing,

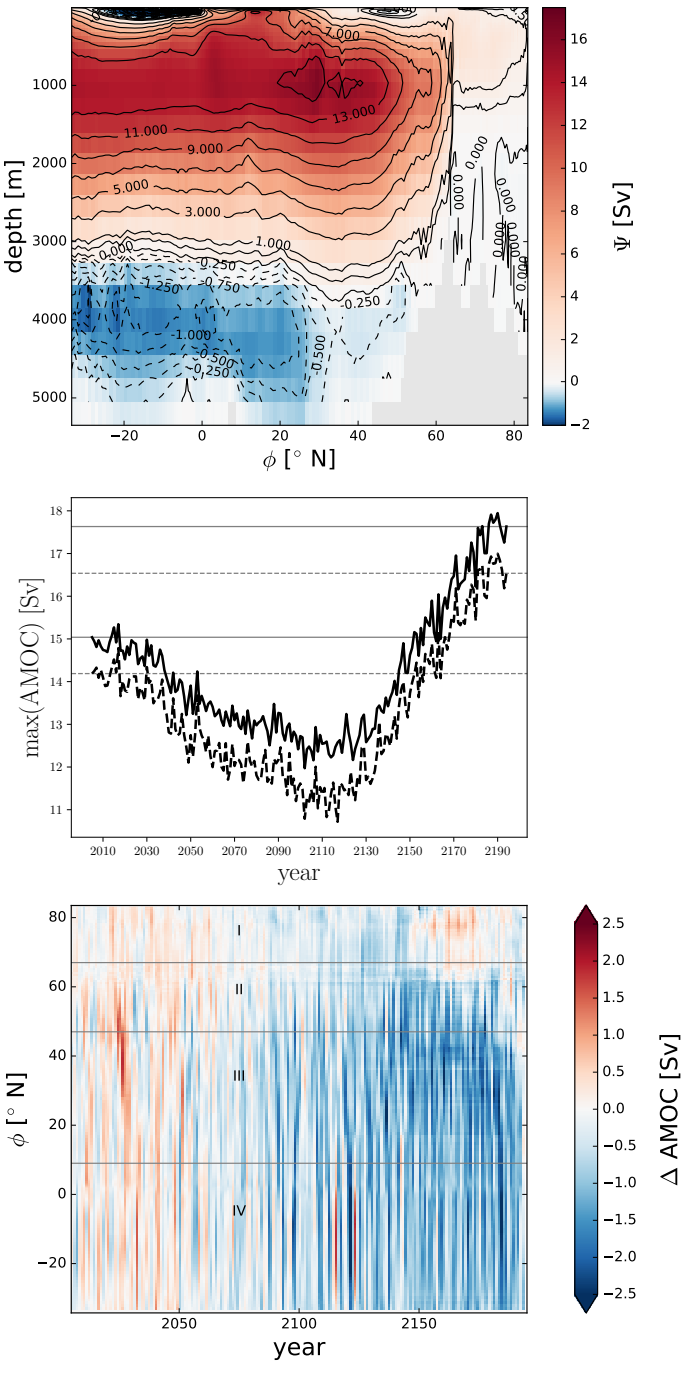


Figure 4.12: Top panel: climatology of the Atlantic overturning. Middle panel: AMOC index maximum, solid line at all Atlantic latitudes, dashed line at RAPID location 26.5°N (horizontal lines indicate initial and final values). Bottom panel: time-latitude diagram of the anomaly of the AMOC maximum; maxima are taken below 500 m depth for ensemble averages of $H - C$.

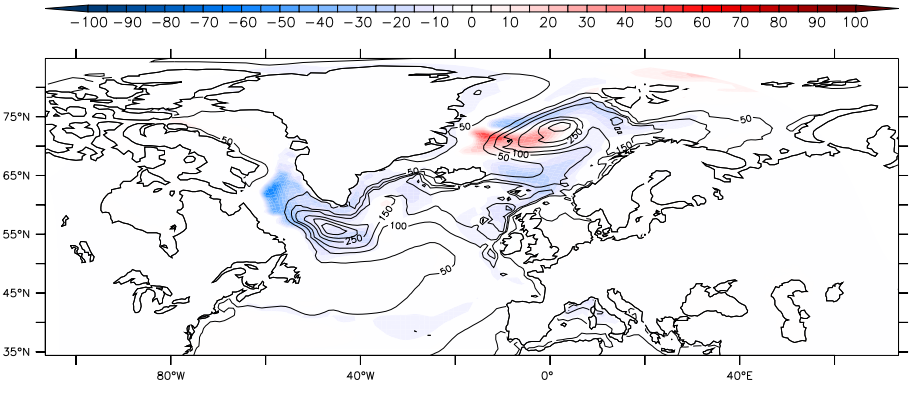


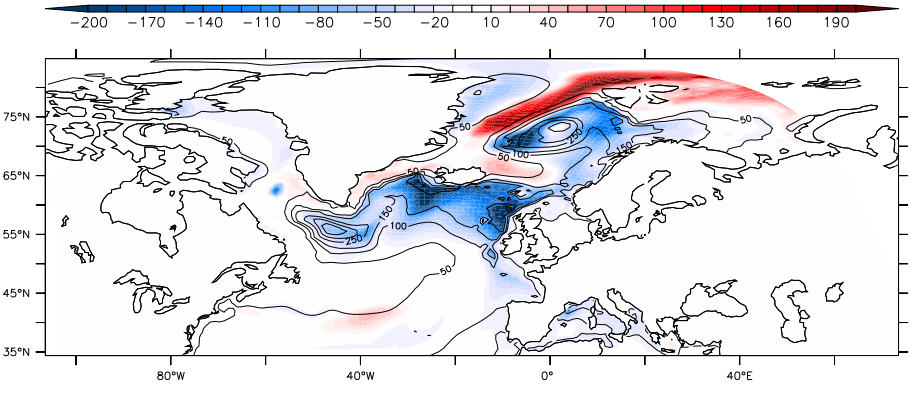


Figure 4.13: Top (a): Mean mixed layer depth anomaly ($H - C$) for 2005 - 2195. Bottom (b): reference annual mean anomaly between 2100 and 2005 under RCP8.5 ($C$). Ensemble averages. Contours indicate annual mean climatological values.

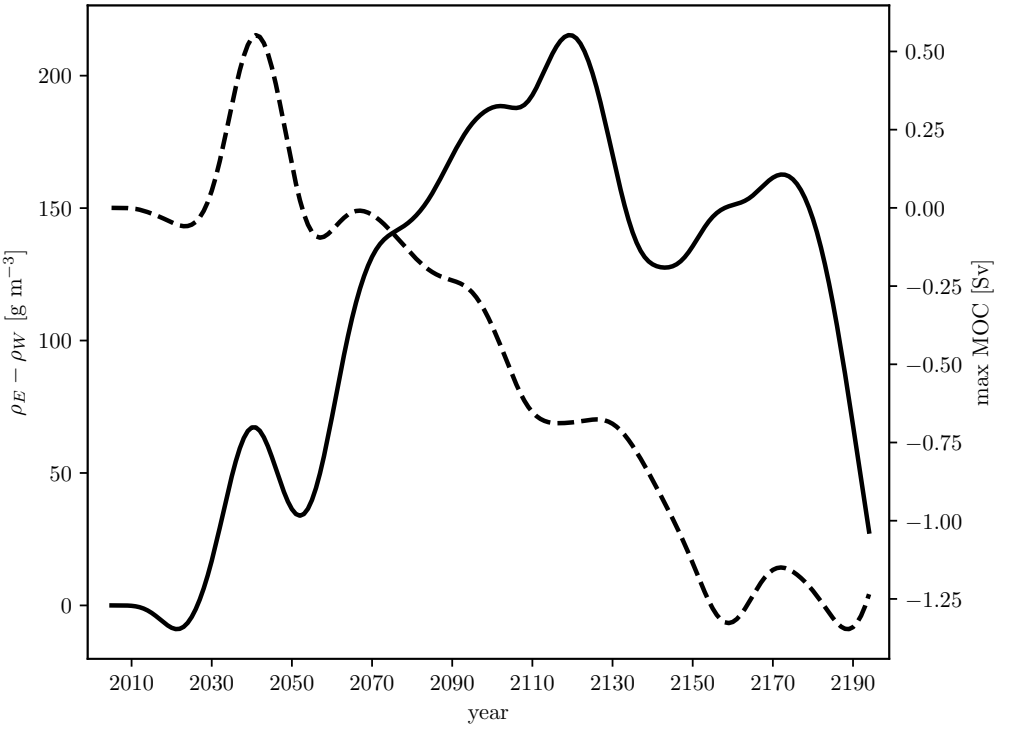


Figure 4.14: Solid line is the average potential density anomaly of the East - West difference at the Atlantic section at 60°N of the first 1000 m. The middle 60% of the basin is removed, leaving an eastern and a western side as boundaries. The dashed line is the maximum AMOC over all Atlantic latitudes as shown in Figure 4.12. Both lines are shown with a 30-year smoothing (Butterworth filtering) of the time-series applied; ensemble averages ($H - C$).

directly impacting sea surface height (SSH). As a result, the transient freshwater-signal in SSH (volume change) affects east-west pressure gradients as well as the freshening of the water column, and may compensate density changes in a different way as the SSH response to freshening when there is no net volume change in the ocean. Apart from freshening at the western side associated with meltwater release from Greenland, the North Atlantic density fields is also affected by a change in the North Atlantic Current advecting more warm water along the eastern boundary, with less warm water entering the western subpolar gyre, associated with the spin-up of the gyre in the Nordic Seas and a slow-down of the gyre in the western SPG. The surface SSH gradient between the east and west initially overcompensates the decrease in upper 1000 m density gradient in the sense that it rises faster in the east than in the west, while upper 1000 m density declines faster in the west than in the east (see also Figure 9 in Van den Berk et al., 2019 for the spread

of the SSH signal). In short, the surface SSH signal spreads faster than the subsurface density anomaly. Figure 4.3 shows that the subpolar gyre advects the freshwater anomaly, as it arrives from the Greenland coast, back to the eastern part of the subpolar gyre, between Ireland and Iceland. As a result, the freshwater anomaly affects both the West and the East, leaving a small imprint on the net sinking and there is even a small initial increase in the AMOC (Figure 4.14). Only after the year 2050, when the halocline in the Labrador and Irminger Sea becomes strong enough to reduce deep convection there, does the density in the western part of the basin become more strongly affected than in the eastern part and the AMOC starts to decline, now in anti-correlation with the density difference between eastern and western boundary (Figure 4.14). This time delay in AMOC decline is comparable with the circulation timescale of the gyre (Born and Mignot, 2012). Note that the decline in AMOC is smaller than in Swingedouw et al. (2013b), which is consistent with the smaller Greenland meltwater discharge amount used in this study.

The weak AMOC response to hosing is thus explained by a small change in east-west density and pressure gradients in the North Atlantic due to a switch in convection location. While the freshwater release affects Labrador and Irminger Sea convection, re-stratifying and weakening the western subpolar gyre, this is compensated by enhanced deep convection in the Nordic Seas. Figure 4.12 indeed shows an increase of the overturning during the first half of the ramp-up, especially in the Nordic Seas, followed by a small decrease in overturning. The overturning increase in the eastern North Atlantic is indeed coupled to an increased gyre circulation in the Nordic Seas, with a decrease in the western subpolar gyre (Figure 4.6), which is consistent with the results described in Zhang et al. (2011).

**Changes in AMOC salt transport further south**

Both a decreasing AMOC and a decrease in salinity of the upper limb relative to the lower limb contribute to the freshening of the subpolar and subtropical North Atlantic; but remarkably, the salinity driven component of the net salt export by the overturning changes sign after year 2100: up to year 2100 it was importing less freshwater, albeit weakly. This switch is mainly due to changes at the southern boundary of the subtropical gyre (Box 3, Figure 4.5) related to freshening of the upper 1000 m of the South Atlantic due to the arrival of meltwater discharge from Antarctica after year 2100. In EC-Earth, the AMOC imports freshwater across the southern boundary of the South Atlantic, a well-known model bias (Mecking et al., 2017). While the weakening AMOC imports less freshwater across the southern boundary of the South Atlantic (Figure 4.5), the water that is imported is getting fresher, especially after year 2100. As a result, the overturning circulation salinifies the South Atlantic by weakening and exporting less salt to the north, but freshens the South Atlantic by importing fresher waters from the Southern Ocean (Box 4, Figure 4.5 blue and red dashed lines). The decrease in salt import in the South Atlantic, together with a weaker AMOC, leaves a positive salinity imprint on

the North Brazil Current with large-scale freshening further south (Figure 3 in Van den Berk et al., 2019). Freshening in the North Atlantic results in freshening of the whole Atlantic, despite the South Atlantic counteracting North Atlantic freshening with an increase in salinity (red line in top panel of Figure 4.4), which is however smaller than the freshening in the North Atlantic. However, integrated over the whole basin, this partial compensation is insufficient to counteract the overall freshening (black line in top panel of Figure 4.4) and the anomalous transport by the overturning circulation (dashed lines in lower panels of Figure 4.4) acts to freshen the Arctic-Atlantic basin through increased freshening of the waters that cross the Agulhas section at 34°S (note that a large fraction of the black line in the top panel of Figure 4.4 can be explained by the dashed black in in the bottom panels being passed relatively unaffected through the South Atlantic as seen in the right middle panel).

## 4.4 Summary and discussion

We investigated the effects of a high-end future climate projection for mass loss from the Greenland and Antarctic ice sheets. While in response to meltwater discharge the whole Atlantic freshens, freshening occurs unevenly over the sub-basins, with largest freshening in the North Atlantic and even larger, almost compensating adjustments taking place between subpolar and subtropical gyres, while there is little change in the South Atlantic. The two gyres in the subpolar North Atlantic and Nordic Seas respond most strongly. A spin-up of the gyre in the Nordic Seas occurs, in conjunction with a weakening and re-stratification of the western part of the North Atlantic subpolar gyre, after the freshwater release decreases Labrador and Irminger Seas convection. A similar seesaw—or shift—between eastern and western convection sites has been described by e.g., Wood et al. (1999) and Swingedouw et al. (2013b). It causes a weak AMOC response to a Labrador and Irminger Sea convection decrease. As a result, the net deep water formation in the model used (EC-Earth) is not particularly sensitive to Greenland meltwater forcing. A reason for this is the effective re-routing of freshwater by the subpolar gyre away from the convection regions in the West, keeping the decrease in convection there limited. The advective pathways of meltwater release from Greenland, however, may depend on the horizontal resolution of the model and eddy-resolving models might show more freshwater transport from the boundary currents to the sites of deep convection, especially in the Labrador and Irminger Seas (Lohmann et al., 2014; Yang et al., 2016). Higher resolution is also important for resolving the boundary currents around Greenland, as these determine where Greenland's meltwater is transported to (Gillard et al., 2016). Thus, the AMOC response to meltwater release is determined by how important Labrador and Irminger Seas convection are, relative to convection in the Nordic Seas, and how effective the seesaw between eastern and western convection sites operates (Lozier et al. (2019) discusses the importance of Labrador Sea convection for the AMOC). To what extent

the response shown here is model-dependent is unknown and should be investigated by further studies using different climate models with different horizontal resolution.

We should also note some limitations regarding the use of a freshwater forcing field. The meltwater scenarios implicitly account for feedback effects to the freshwater release, but not explicitly the effects on the atmosphere or the secondary effects on the ocean. Interactions with the solid Earth such as isostatic adjustment are already excluded by the model formulation because of the longer timescales involved. The thermal effects are not modelled with a prescribed freshwater forcing. In particular, as the ice sheet melts, more freshwater reaches the oceans and increases stratification, which shallows the halocline. Consequently, more heat is retained near the ocean surface and would increase the basal melt rate. This is a deficiency of only using a freshwater forcing. Another important feedback lacking without a dynamic ice sheet is the interaction with the atmosphere. The geometry of the ice sheet does not change and therefore cannot affect the melt-elevation feedback where a decrease in height of the ice sheet leads to even greater melt due to the warmer temperature at the lower surface after melt. An overview of these feedbacks and others is given in Fyke et al. (2018). Coupling a dynamic ice sheet model to EC-Earth would model some of these feedbacks, but the realism of the resulting effects is not clear.

The effectiveness of the seesaw depends on the feedbacks associated with the gyre spin-up in the Nordic Seas and gyre spin-down in the western subpolar gyre to the south. For instance, Swingedouw et al. (2013b) attribute this seesaw between subpolar gyre and Nordic Seas to the increased import of warm and salty Atlantic waters in the Nordic Seas as a result of pathway changes in the North Atlantic Current when obduction in the subpolar gyre no longer occurs. The weakened subpolar gyre leads to a shift in the North Atlantic Current and subpolar-subtropical gyre boundary, with the subtropical gyre expanding and the subpolar gyre contracting. Associated with this shift, deep convection decreases in the subpolar gyre and increases in the Nordic Seas, leading to lower SSTs in the West (less heat transported from the deep ocean to the surface) and higher SSTs in the Nordic Seas associated with increased vertical heat transport to the surface. In our simulations this change in SSTs induces a coupled ocean-atmosphere feedback that further spins-up the Nordic Seas gyre and spins-down the subpolar gyre. The anomalous SST-gradient associated with this response enhances the westerlies, especially between 65°N and 70°N, and the associated increase in windstress curl further enhances the spin-up of the Nordic Seas gyre. In addition, the anomalous SSTs also affect air-sea fluxes, and the resulting buoyancy forcing acts to further enhance the gyre in the Nordic Seas and to weaken the subpolar gyre in the west. An analysis based on paleo proxies indicates that this seesaw may have played an important role in, especially, the cold phases of Dansgaard-Oeschger oscillations (Wary et al., 2017). A comparison of CMIP5 models (Deshayes et al., 2014), however, shows inconsistent circulations patterns of the subpolar gyre, indicating results are model-dependent. This is another reason more studies—using a variety of models—are needed to assess which response is robust and can be validated by observations. Additionally, it should be noted that the climate model used (EC-Earth) has a bias in the South Atlantic which results in an incorrect sign of $M_{\mathrm{ov}}$ (Rahmstorf,

1996; Sgubin et al., 2014) (positive, whereas measurements indicate a negative sign Garzoli et al., 2013). A different value for $M_{ov}$ would affect our analysis and the response to the freshwater forcing might be stronger than seen here, especially before 2100.

Observations already suggest subpolar gyre freshening associated with Greenland meltwater discharge and subsequent decrease in Labrador Sea Water thickness (Yang et al., 2016), though natural variability and other freshwater sources from the Arctic play a role as well in the subpolar gyre freshening. In Böning et al. (2016) it was argued that Greenland meltwater discharge may have affected deep convection in the Labrador Sea since year 2010. Claims of earlier signs of Greenland meltwater discharge affecting the AMOC are difficult to sustain, given the signal-to-noise level of this freshwater source against natural variability. The authors also argue that the spreading of the meltwater discharge is intimately linked to mesoscale transport processes, implying that a low-resolution model as used here may not well represent the correct spreading pathways of the meltwater discharge. Another issue is the vertical mixing of the freshwater anomaly. In Dukhovskoy et al. (2019) it is argued that in a regional high-resolution model the mixing is too large for the meltwater discharge to explain the observed signal.

Although we do not see a clear mode switch in the subpolar gyre from a strong to a weak state it appears that similar feedbacks involved in the bistability of the subpolar gyre as described in Born and Stocker (2013) do act to weaken the gyre here. The interior pathways of the most northerly AMOC flows are due to buoyancy loss in the Nordic Seas and an increased inflow in the Nordic Seas can reduce the subpolar gyre further south (Zhang et al., 2011). This is also seen in Sgubin et al. (2017), where CMIP5 models were analysed for abrupt convection collapse events in the Labrador Sea; models showing such a collapse under future anthropogenic emission scenarios most often feature a surprisingly weak AMOC response due to a coincident enhancement of deep convection in the Nordic Seas. The seesaw pattern between the subpolar North Atlantic and Nordic Seas may also explain the remarkable insensitivity of the AMOC to Greenland meltwater discharge. Compared with hosing experiments in which the whole AMOC collapses (Stouffer et al., 2006; Drijfhout, 2015), our experiments seem to require larger volumes of freshwater to inhibit both Labrador/Irminger Sea deep convection and deep convection in the Nordic Seas. It appears that the freshwater does not reach the Nordic Seas when smaller volumes of hosing are applied, allowing for the enhanced deep convection there to compensate the decreased convection in the Western subpolar gyre. However, a more dedicated experimental set-up and analysis is needed to confirm this hypothesis and fully understand how the spreading of the meltwater may depend on the volume of discharge. In particular, a coupled ice sheet model to capture the main feedback processes between ice sheet, ocean, and atmosphere is desirable.

Meltwater from the Antarctic ice shelf was shown to affect the salt-balance of, in particular, the South Atlantic after 100 years by increasing the Southern Hemisphere supergyre and the amount of Agulhas leakage entering the South Atlantic (Van den Berk et al., 2019). The AMOC was only marginally affected by this; although the implied changes in north-south density gradient could support AMOC recovery on top of the

compensation signal of enhanced deep convection in the Nordic Seas. In this study we were interested to see whether the Southern Hemisphere impact on the AMOC may become stronger on longer timescales. Unfortunately, the present experimental set-up did not allow us to study adjustment processes beyond the year 2195. Haskins et al. (2019), however, did show such impact of slow adjustment in the South Atlantic on AMOC evolution; in particular it helped AMOC recovery after North Atlantic hosing experiments. It has been suggested in Jüling et al. (2018) that high-resolution models will show faster spreading pathways and adjustment processes; if so, the Antarctic meltwater would also impact the AMOC faster.

The AMOC response to both sources of meltwater thus depends on how the advective processes are represented in a model, and a hierarchy of resolutions would be useful to tease out differences and determine which responses are robust model features. Although the signal of Antarctic freshwater release in the North Atlantic is much smaller than in the South Atlantic, we found clear signs that the adjustments of the gyres in the subpolar North Atlantic and Nordic Seas were affected by salinity changes originating father south in the Atlantic.

## Acknowledgements

This work was funded by the European Commission's 7th Framework Programme, under Grant Agreement number 282672, EMBRACE project. The authors thank the three anonymous referees for their valuable comments and suggestions that have improved the manuscript greatly.

# 5 Characterisation of Atlantic Meridional Overturning hysteresis using Langevin dynamics

## 5.1 Introduction

The Atlantic Meridional Overturning Circulation (AMOC) is an important circulation in the Atlantic ocean. It is also an important part of the climate system overall due to the heat it transports from the South Atlantic to the North Atlantic (Ganachaud and Wunsch, 2000; Vellinga and Wood, 2002). The AMOC therefore has a substantial influence on the (western) European climate and a weakening of the AMOC might cause changes in the European climate and weather. The AMOC has also been identified as one of Earth's 'tipping elements' where a rapid change on markedly faster times scales could take place in the (near) future (Lenton et al., 2008). The AMOC is partly buoyancy driven by the deep water formations in the North Atlantic subpolar gyre which produces the North Atlantic Deep Water (NADW) (e.g. Rahmstorf, 2000). The AMOC might be bi-stable in nature which means it admits an 'off' state, with little or no transport from north to south, as a counterpart to its current 'on' state (Broecker et al., 1985).

Palaeoclimate records of the last glacial period show a rapid switching of temperature, which might be associated with the presence/absence of a vigorous AMOC as exists today (Dansgaard et al., 1993). The possibility of a bistable AMOC being the cause of these rapid changes has been noted (Broecker et al., 1990). With the current climate warming rapidly, the stability of the AMOC is of particular interest (Collins et al., 2013) and climate modelling projections indicate the AMOC strength will decrease under an increase of $CO_2$. Recent measurements show the AMOC has decreased in strength (Smeed et al., 2018). An understanding of the possibly bistable nature of the AMOC is therefore relevant to understand the consequences of climate change. See Weijer et al. (2019) for a review on AMOC bistability.

The Langevin equation has been posited before as suitable to capture the essential dynamics of an AMOC collapse (Ditlevsen and Johnsen, 2010; Berglund and Gentz, 2002). It has also been used elsewhere as the basis for describing the dynamics of climate sub-

systems (Kwasniok and Lohmann, 2009; Livina et al., 2010) and the AMOC in particular (Kleinen et al., 2003; Held and Kleinen, 2004). A fourth order potential function is used in Ditlevsen and Johnsen (2010) and Berglund and Gentz (2002) because it is the minimum required for having three distinct solutions (double wells). This potential function has two parameters which are presumed to be functions of the freshwater forcing. Variation in the freshwater forcing is assumed to directly drive changes in AMOC strength by changing the potential function in the Langevin equation. Although the hysteresis loops of the AMOC include both a collapse and a resurgence point, we will only attempt to model the collapse from the stable 'on' branch to the stable 'off' branch.

Though the Langevin equation has played a role in the conceptual picture of bistability and tipping points in the climate, it has not been used to actually fit the parameters to a (simulated) AMOC collapse. Here, we attempt to construct a simple model based on the Langevin equation and fit its dynamics to salt-advection driven collapse trajectories of the AMOC seen in climate models (Rahmstorf et al., 2005). The result is a set of parameters that quantitatively describe the AMOC collapse process. This derived model defines a low-dimensional manifold that captures the essential AMOC collapse characteristics. To the extent that the low-dimensional model is successful in capturing the more complex model this method could also be used to predict the parameter range where in a model a collapse would occur. At present, however, it is intended to provide a characterisation of the collapse that will allow comparison between climate models.

Section 5.2 sketches the theoretical background of the Langevin equation and of the salt-advection mechanism. In Section 5.3 we fit the proposed Langevin model to the AMOC collapse trajectories seen in a set of climate models of intermediate complexity (EMICs) taken from Rahmstorf et al. (2005). We end with a discussion and conclusions in Section 5.4.

## 5.2 The Langevin model

An increase in surface air temperatures, or an increased surface freshwater flux by changes in precipitation minus evaporation, will decrease the buoyancy in the shallow layer of the deep water formation regions in the North Atlantic subpolar gyre. The deep water formation is reduced, and the southward meridional flow reduced. In principle, this mechanism can reduce the AMOC to zero gradually if fully buoyancy-driven. A salt-advection feedback mechanism that leads to a bimodal AMOC was proposed by Stommel (1961). In this mechanism, salinity anomalies in the North Atlantic are amplified by the overturning flow, which in turn controls the North Atlantic salinity. Positive anomalies are strengthened and negative anomalies weakened; this results in a positive feedback between the salinity anomalies and the overturning. Bistability, consisting of a strong and a weak AMOC state, and possible abrupt transitions result.

Figure 5.1 shows a conceptual picture of the two stable AMOC (index) states. The AMOC is a scalar variable obtained by integrating the overturning transport and selecting

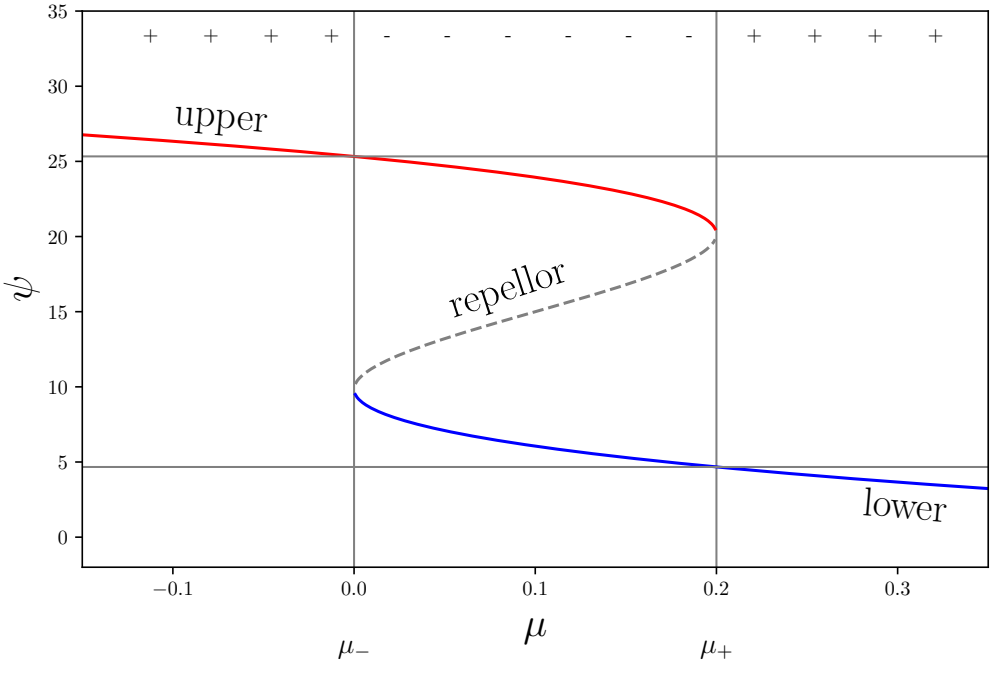


Figure 5.1: Example bifurcation diagram of the AMOC ($\Psi$) in response to a control variable $\mu$. The red branch is the on-state (upper), blue the off-state (lower). The upper branch deforms when closer to the bifurcation points which are connected though the repellor (dashed line). The two bifurcations points are indicated as $\mu_+$ (collapse point) and $\mu_-$ (resurgence point). Top $\pm$ symbols indicate unimodal (+) or bimodal ($-$) regime.

its maximum value (typically located in the subtropical North Atlantic). In red, the upper branch is drawn up to the collapse point where a bifurcation occurs. The real AMOC in the current climate moves along this branch from the left, to the right, towards its (assumed) collapse point. The branch in blue is the counterpart of the upper branch and represents the off state of the AMOC and ends in another bifurcation point to the left where the AMOC jumps back to full strength. The dashed line (repellor) separates the two basins of attraction associated with the two stable branches (attractors). At the bifurcation point one of the two basins of attraction vanishes and a qualitative change takes place in the potential function (the number of solutions for a given value of the freshwater forcing $\mu$ goes from 3 to 1).

Below we will derive a model based on the Langevin equation that captures the essential dynamics of a bimodal AMOC under a freshwater forcing $\mu$.

### 5.2.1 Multiple stable AMOC states

The conceptual picture of the AMOC being a zero-dimensional variable that is driven by stochastic forces trapped in a potential is similar to that of a particle's motion described by Langevin dynamics (Lemons et al., 1908). The Langevin equation (Gardiner, 2004; Ditlevsen and Johnsen, 2010),

$$\dot{x} = -\partial_x U_\mu(x) + \sigma\eta \tag{5.1}$$

describes the position of a noise-driven particle ($x$) trapped in a potential function $U$. The stochastic term is a white noise process ($\eta$) scaled with an intensity parameter $\sigma$. At first we will ignore the stochastic nature of the AMOC collapse process and focus on the deterministic behaviour.

The double well potential seen in Figure 5.1 has been extensively studied and applied, also in a quantitative way. But to our knowledge it has not been quantitatively applied to AMOC hysteresis using the Langevin equation in complex numerical climate models before.

AMOC bistability has, however, been studied quantitatively in e.g. Boulton et al. (2014) using transient runs. In Poston and Stewart (1978) an extensive treatment is given why, in addition to a scaling and shifting, only two parameters are sufficient to describe the bistability. More precisely, the third order term and the fourth order coefficient can be eliminated. The two remaining coefficients in the polynomial describe the critical behaviour, not just locally near the critical points, but the entire trajectory under a suitable transformation. A direct consequence is that only partial information, in the form of a piece of the trajectory, should suffice to describe the entire trajectory (the full hysteresis loop).

The potential function takes the form (Gardiner, 2004; Ditlevsen and Johnsen, 2010)

$$-U(x) = -\frac{1}{4}x^4 + \frac{\beta}{2}x^2 + \alpha x. \tag{5.2}$$

The two parameters $\alpha, \beta$ are functions of the freshwater forcing $\mu$. The AMOC state variable $\Psi$ requires an affine transformation (Cobb, 1980),

$$\begin{aligned} \alpha &= \alpha(\mu) \\ \beta &= \beta(\mu) \\ x &= (\Psi - \lambda)/\nu. \end{aligned}$$

To fit the model trajectories we need to find expressions for $\alpha$ and $\beta$, and suitable values for the transformation parameters $\lambda$ and $\nu$. In the literature $\alpha$ is referred to as the normal factor, and $\beta$ the splitting factor (Poston and Stewart, 1978). In the bifurcation diagram the value of $\nu$ is approximately the distance in $\Psi$ between the bifurcation point on the top branch to the bifurcation point on the lower branch. Similarly, the value of $\lambda$ is approximately the $\Psi$ value between the bifurcation points at $\mu_\pm$. The transformation

uses $\lambda$ to shift the trajectory and $\nu$ to scale it. Below we describe the potential visually and state additional constraints that follow from the demand that the freshwater forcing is the only variable that determines the dynamical behaviour.

### 5.2.2 Potential description

In Figure 5.2 an overview of the qualitatively different forms of potential are shown ($-U(x)$, right panels) together with their derivative functions ($-\partial_x U$, left panels). Dots indicate the location of critical points and are related to the number of wells in the potential. The top panels show the typical bimodal form ($I$) with two stable states and one unstable one in the middle. Below these are the three possible unimodal states ($E$). These occur for forcing values to the left of $\mu_-$ and to the right of $\mu_+$. The panels $B_1$ and $B_2$ are the submanifolds that separates the unimodal regime from the bimodal regime. These two meet in the cusp point $P$, as shown in the bottom panels. See Poston and Stewart (1978) for further details.

In Figure 5.3 the stability diagram is shown where the areas indicated are those with qualitatively different behaviour seen in Figure 5.2. See also Poston and Stewart (1978) for similar diagrams. The cusp point $P$ is the singular point where no proper solution can exist because only the trivial solution (all parameters are valued 0) is allowed here (both bifurcation points $\mu_\pm$ and AMOC strength are at zero). The two parameters are $\alpha$ and $\beta$ and are the two coefficients in the potential function. Their values change because of their dependency on the forcing value ($\mu$).

Our aim is to arrive at a description that matches a series of $\mu$ values across the stability diagram. The two parameters $\alpha, \beta$ are independent but can be parameterised by other variables that map them to observations. If parameterised by a single variable, the values of ($\alpha$, $\beta$) across the stability surface are a one-dimensional subset, as suggested by the AMOC index. On one side of the cusp point, along the splitting axis ($\beta$), only a unimodal regime exists, while on the other side two regimes exist with the modes at relative distances apart.

### 5.2.3 Constraints

With a varying $\alpha$ there exist an interval between two critical points ($\alpha_\pm$) in between which the distribution is bimodal and unimodal outside that interval. Because the AMOC trajectory is 1-dimensional and $\mu$ is also 1-dimensional, there must be a relation between $\alpha$ and $\beta$ that reduces dimensionality from two to one dimensions. When passing through the critical point $\alpha_+$, the number of potential wells goes from two to one. Similarly, moving through $\alpha_-$ changes the number of wells from one to two (for given $\mu_\pm$). The two critical points of $\partial_x U$, $\mu_\pm$, can be found analytically for $\mu_\pm$ real and being degenerate solutions. It can be shown (Birkhoff and Mac Lane, 1970, p. 106) that the discriminant $D = 27\alpha^2 - 4\beta^3 = 0$ (i.e. real solutions) needs to be solved for $\alpha$ to obtain the two critical solutions that relate $\alpha$ and $\beta$. It is at these solutions that the number of critical

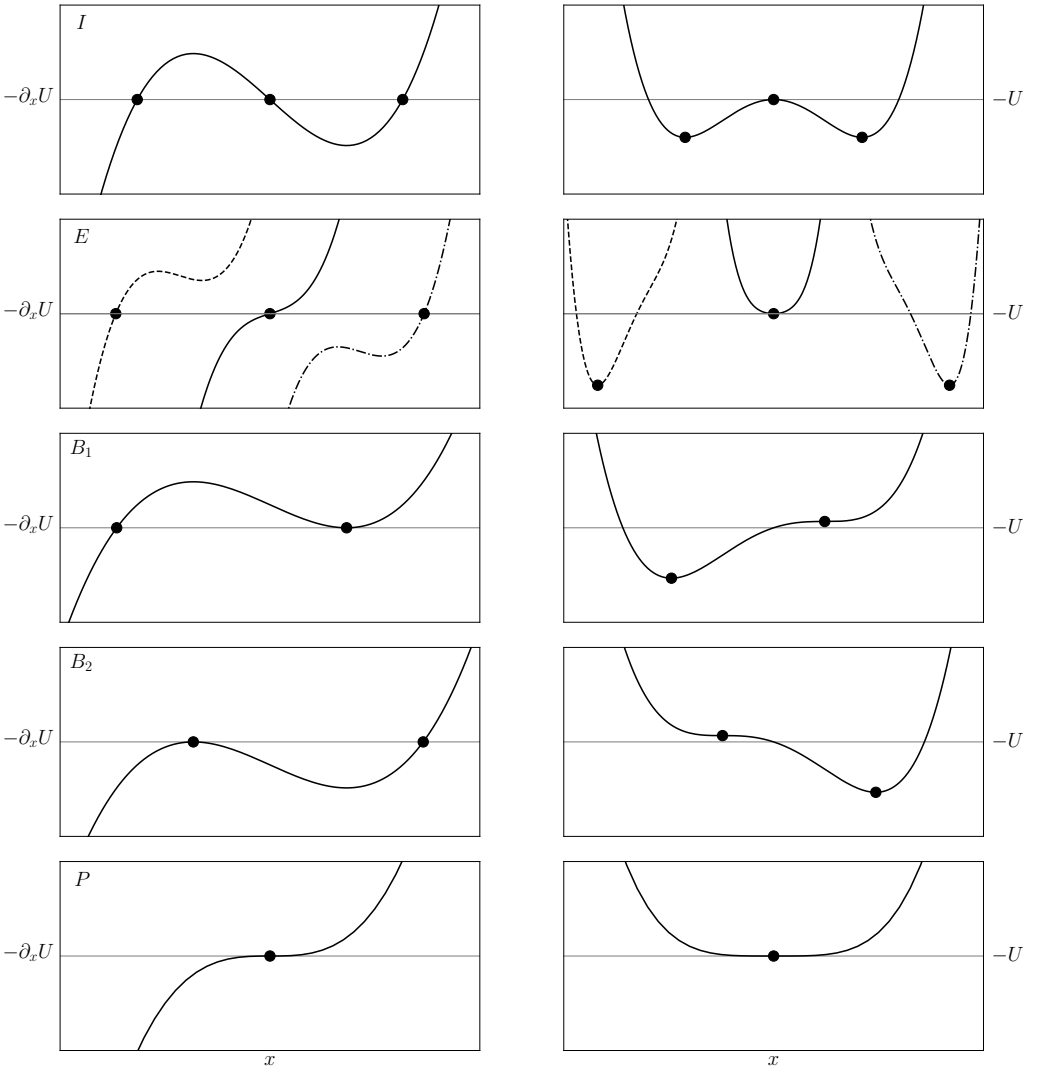


Figure 5.2: Sample potentials (right) and their derivatives (left) for (top to bottom) the three possible varieties of bimodal state ($I$), three types of unimodal state ($E$), the two pathological cases where $D = 0$ ($B_1$ and $B_2$), and the cusp catastrophe point ($P$). Dots indicate the critical points. (Scaling is not uniform between panels. Note the choice of negative sign of the potential $U$.)

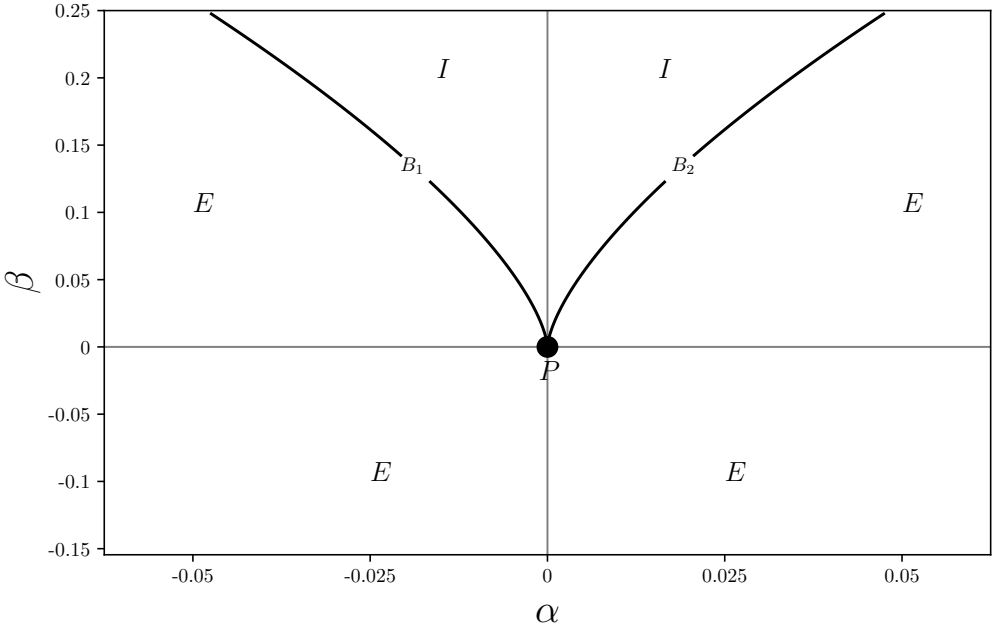


Figure 5.3: Discriminant determining the stability and number of critical points. The splitting factor $\beta$ and normal factor $\alpha$ describe the stability diagram. The bimodal regime ($I$) is separated from the unimodal regime ($E$) by two lines ($B_{1,2}$) which meet in the point $P$.

points changes at forcing values $\mu_{\pm}$. (When $D < 0$ there are three distinct real solutions which corresponds to the bimodal regime, when $D > 0$ there is only one distinct real solution, which corresponds to the unimodal regime.) When any two of the roots are the same, the number of extrema goes from 3 to 2 (or 1 if all are the same) and the solutions become degenerate (this occurs at $B_{1,2}$ in Figure 5.3).

Solving for $\alpha$ gives two solutions that are the critical values as functions of $\beta$,

$$\alpha_{\pm} = \pm \frac{2\sqrt{3}}{9} (\beta)^{3/2} \quad \text{or} \quad \alpha_{\pm} = \mp \frac{2\sqrt{3}}{9} (\beta)^{3/2},$$

with $\beta \geq 0$ for real solutions. The points $\alpha_{\pm}$ correspond to where the lines $B_{1,2}$ in Figure 5.3 are passed when moving across the stability surface.

For $\alpha_{+} < 0$ $-U(1) < 0$. This corresponds with the AMOC undergoing a collapse at $\mu_{+}$ from an on state to an off state, and the correct choice of sign is

$$\alpha_{\pm} = \mp \frac{2\sqrt{3}}{9} \left(\beta_{\pm}\right)^{3/2}, \tag{5.3}$$

with $\alpha_\pm$ and $\beta_\pm$ the values corresponding to $\mu_\pm$. Changing $\mu$ in the bifurcation diagram corresponds to moving from curve $B_2$ to curve $B_1$ and Eq. 5.3 relates the two stability parameters $\alpha$ and $\beta$ at the two critical forcing values $\mu_\pm$.

**Linear functions $\alpha, \beta$**

The value of $\beta$ does not need to be fixed (to $\alpha_\pm$ and in general there is a corresponding $\beta_\pm$ at the respective critical points. We assume linear functions for $\alpha$ and $\beta$,

$$\alpha(\mu) = \alpha_0 + \mu\,\delta\alpha$$
$$\beta(\mu) = \beta_0 + \mu\,\delta\beta,$$

reducing the dependency to these four parameters. Linear functions are the simplest non-trivial dependencies, while adding non-linear parameters introduces further unknowns, making this the most parsimonious parametrisation that captures the first order behaviour. Also, intuitively we can understand the pair $(\delta\alpha, \delta\beta)$ as the angle under which the system moves to the bifurcation point ($B_{1,2}$) in Figure 5.3), which locally only requires the values of $\alpha$ and $\beta$ up to first order. From this parametrisation we can determine the offset $\alpha_0$ and rate $\delta\alpha$ in terms of $\beta_0$ and $\delta\beta$,

$$\alpha_+ = \alpha_0 + \mu_+\delta\alpha = -\frac{2\sqrt{3}}{9}\left(\beta_+\right)^{3/2} \quad \text{and}$$
$$\alpha_- = \alpha_0 + \mu_-\delta\alpha = +\frac{2\sqrt{3}}{9}\left(\beta_-\right)^{3/2}$$

gives

$$\delta\alpha = -\frac{2\sqrt{3}}{9}\,\frac{\left(\beta_+\right)^{3/2} + \left(\beta_-\right)^{3/2}}{\mu_+ - \mu_-} \tag{5.4}$$

$$\alpha_0 = \alpha(\mu = 0) = \frac{\sqrt{3}}{9}\left[-\left(\beta_+\right)^{3/2} + \left(\beta_-\right)^{3/2}\right] - \frac{1}{2}\delta\alpha\left(\mu_+ + \mu_-\right). \tag{5.5}$$

This constrains the values of $\alpha$, leaving only $\beta$ as a free variable, which is then parameterised by $\beta_0$ and $\delta\beta$. Note that only solutions with $\beta_\pm > 0$ are valid. Also, values for $\beta_0$ and $\delta\beta_0$ that result in crossing $B_2$ in another point besides $\beta_-$ are unsuitable. (The curves $B_{1,2}$ are each intersected by a straight line in at most two points, and we require intersection at a single point only.)

### 5.2.4 Stochastic interpretation

With the deterministic framework in place, the stochastic nature can be reintroduced. The potential function can be replaced by a distribution which is the stationary distribution in the asymptotic limit (i.e. the long term behaviour of repeated sampling of the hysteresis

loop). The potential (a fourth-order polynomial) gives the probability distribution (Cobb, 1978)

$$P(x, \alpha, \beta) = Ce^{-2/\sigma^2 U(x)} = Ce^{2/\sigma^2(-1/4x^4+\beta/2x^2+\alpha x)}. \tag{5.6}$$

The factor $C = C(\alpha, \beta)$ does not have a (known) analytical expression for the general case, but can be computed numerically (and can therefore used as a factor in the likelihood function in the next section). This can be done accurately with an adaptive quadrature method (Piessens et al., 2012), though it suffers from numerical limitations. The value of $\sigma$ is a measure of intrinsic variation in the AMOC. Note that $\sigma$ is a measure of additive noise (because we assume that $\sigma$ is not dependent on $\mu$) and other choices, such as multiplicative noise, can be made (Das and Kantz, 2020). See Gardiner (2004) for a derivation of this distribution using the Fokker-Planck equation, from which also the Langevin equation can be derived. Also, note that $\sigma \to \sigma/\nu$ because of the scaling with $\nu$ we introduced in Section 5.2.1.

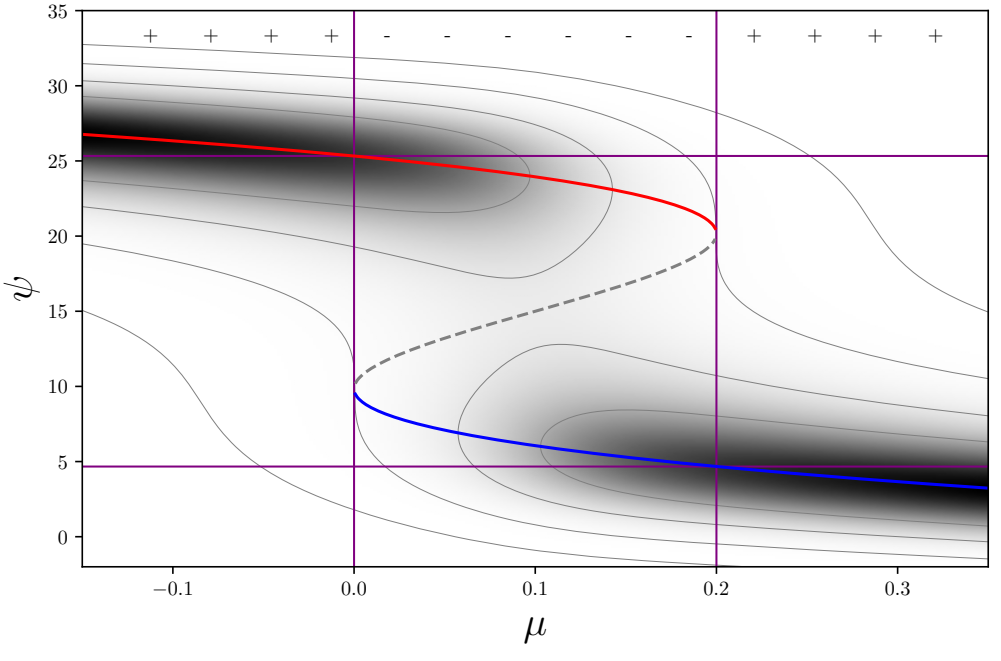


Figure 5.4: Example trajectory with corresponding distribution. Parameterised by $\lambda = 15$, $\nu = 20$, $\sigma = 0.12\nu$, $\mu_+ = 0.2$, $\mu_- = 0$, $\beta_0 = 0.2$, $\delta\beta = 0$; $\alpha_0$ and $\delta\alpha$ follow from the constraints in Eqs 5.4 and 5.5. The distribution of one of the attractor branches (red: on state, blue: off state) deforms when closer to the bifurcation points which are connected though the repellor that forms the trench of the distribution (dashed line). Top $\pm$ symbols indicate unimodal (+) or bimodal (−) regime based on the discriminant value ($D$).The value of $\sigma$ is relatively large and is chosen for clarity. The purple lines indicate the (fixed) positions of the bifurcation points.

An example bifurcation diagram with corresponding distribution is shown in Figure 5.4. The purple lines indicate the (fixed) positions of the bifurcation points. The dashed grey line marks the positions of the unstable solution (repellor) in between the two attractor branches which separates the two basins of attraction. Note that the bifurcation points are extremal in the sense that no bimodality can exists beyond them. With the trajectories being noisy and driven along the attractor, there is (always) some probability of a 'noise-induced' transition. The state shifts from one basin of attraction to the other, crossing the repellor, and the AMOC rapidly moves from one attractor to the other. For this reason, the bimodality region might be larger than is apparent from a particular sample AMOC trajectory. A larger noise level (as seen in AMOC observations Smeed et al. (2018)) would increase the likelihood of a collapse before the AMOC reaches the bifurcation point.

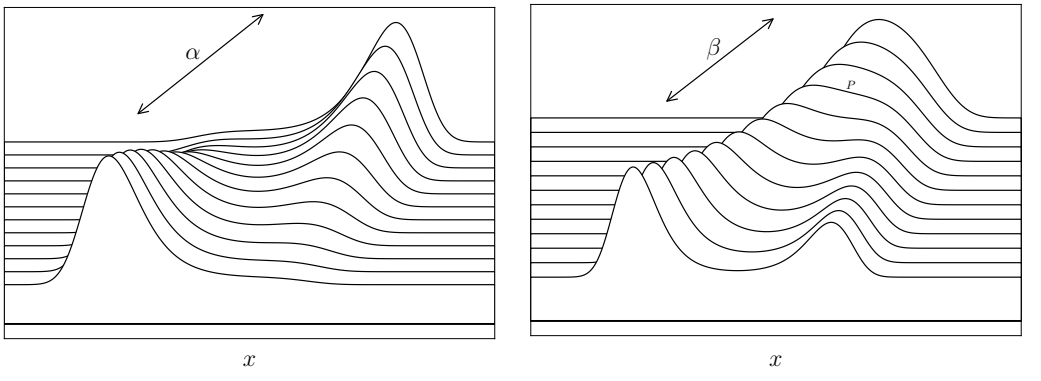


Figure 5.5: Left: Distributions from the exponential family (Eq. 5.6) where the parameter $\beta$ is kept at a fixed value and $\alpha$ is varied. The distribution transforms from unimodal (back), to bimodal (middle), to a different unimodal distribution (front). The bimodal states have a larger and a smaller mode, depending on the position within the bimodal regime. The relative strength between modes depends on $\sigma$. Right: Distributions from the exponential family (Eq. 5.6) where the parameter $\alpha$ is kept at a fixed value and $\beta$ is varied. A broad unimodal state (at the back) splits into distinct bimodal states (to the front). In the middle a critical point exists, called the cusp (point $P$ in Figure 5.3) where the split occurs.

The distributions in Figures 5.5 show that qualitatively distinct behaviour occurs when $\alpha$ or $\beta$ are varied. For both parameters, a change from a unimodal to a bimodal distribution can be seen. Each distinct shape of the distribution can be identified with one of the potential functions in Figure 5.2. In principle, a change in only one of the two structural parameters ($\alpha$ and $\beta$) can move the distribution between unimodal and bimodal forms.

We are now in a position to apply the above to collapse trajectories from climate models.

## 5.3 AMOC collapse parameter estimation

We describe how to find an optimal solution under the framework described in the previous section. Using a Bayesian optimisation procedure, estimated values of $\beta_0$ and $\delta\beta$ can be found, together with the scaling parameters $\nu$ and $\lambda$. We will also estimate the values for $\mu_\pm$, resulting in a six parameter list that describes (the upper branch) of an AMOC collapse.

The parameters $\beta_0$ and $\delta\beta$ are independent of each other, but need to cross the curves $B_{1,2}$ in Figure 5.3) to match the corresponding values for $\mu_\pm$. This constraint is satisfied by the resulting values for $\alpha_0$ and $\delta\alpha$. (This can still lead to solution candidates that are not suitable for the collapse trajectories and are eliminated in the sampling process below.) The scaling parameters are not fully independent because $\lambda < \nu$ (the offset cannot exceed the scaling) and knowing where the upper and lower branches are located already gives a rough estimate.

### 5.3.1 Parameter estimation

Cobb (1978) was able to fit the distribution in Eq. 5.6 using optimisation techniques (which were numerically unstable and not very flexible). Though the estimates for the scaling parameters $\lambda$ and $\nu$ can be quite good with this approach, estimating the trajectory parameters $\beta_0$ and $\delta\beta$ requires a more flexible method. Knowing which distribution to use, we can estimate the posterior probability distribution of the parameters given the data $\Psi(\mu)$,

$$P(\nu, \lambda, \beta_0, \delta\beta, \mu_\pm \mid \Psi).$$

Bayes' rule tells us the probability of a given observation $\Psi$ given the probability of the parameters (marginal on the left, or posterior) is proportional to the probability given the parameters (marginal on the right, or prior) and the full distribution (likelihood),

$$P(\nu, \lambda, \beta_0, \delta\beta, \mu_\pm \mid \Psi) \propto P(\Psi \mid \nu, \lambda, \beta_0, \delta\beta, \mu_\pm) \cdot P(\nu, \lambda, \beta_0, \delta\beta, \mu_\pm).$$

Sampling different values from the parameters' prior distributions will give corresponding values for the posterior distributions. A Bayesian sampler chooses successive values that tend towards greater likelihood of the model, given the observed trajectory, and will converge towards an optimal fit. Conceptually, this is what an MCMC (Markov chain Monte-Carlo) optimiser does (Bolstad, 2010). A widely used sampling algorithm is the Metropolis algorithm (Hastings, 1970; Bernardo and Smith, 2009), which we also use here. This algorithm has been implemented in many software packages (e.g. Salvatier et al., 2016; Carpenter et al., 2017).

The sampling process is time consuming because the evaluation of the potential (to calculate $P(\Psi \mid \nu, \lambda, \beta_0, \delta\beta, \mu_\pm)$) requires numerical integration (using a quadrature method), which is costly to evaluate (the exponential family of distributions cannot, in general, be evaluated analytically).

**Prior distributions**

The prior distribution of a parameter represents all the information known about that parameter before confrontation with the observed values (Bolstad, 2010). With $\nu$ and $\lambda$ transform the AMOC state variable ($\Psi$) with a shift ($\lambda$) and a scaling ($\nu$). The shift $\lambda$ cannot exceed the normalisation $\nu$, giving an upper bound on $\lambda$. Also, we note the lower limit of the lower branch, meaning $\lambda$ must be larger than this minimum value. Similarly, the scaling $\nu$ cannot be larger than the maximum value of the AMOC on the upper branch. We expect the linear parametrisation of $\alpha$ and $\beta$ introduced in the previous section to be $\mathcal{O}(1)$.

We are nonetheless still faced with infinite support on the coefficients of the expansion of the parameters ($\beta_0, \delta\beta$). We therefore transform $\beta_0$ and $\delta\beta$, with support $(-\infty, \infty)$, using the arctan function to map to $(-\pi/2, \pi/2)$. After such a transformation, we can sample from the flat prior distribution on that interval with most of the probability mass on 'reasonable' values (i.e. $\mathcal{O}(1)$). The following prior distributions are used:

$$\begin{aligned}
\nu &= U(\min(\text{AMOC}), \max(\text{AMOC})) \\
\lambda &= U(\min(\text{AMOC}), \nu) \\
\mu_+ &= U(\mu_{\text{S+}}, \mu_{\text{UP}}) \\
\mu_- &= U(\mu_{\text{DN}}, \mu_{\text{S-}}) \\
\tan(\beta_0) &= U(-\pi/2, \pi/2) \\
\tan(\delta\beta) &= U(-\pi/2, \pi/2),
\end{aligned}$$

with min(AMOC) and max(AMOC) is the minimum/maximum values in an observed collapse trajectory. $U$ is the uniform distribution on indicated intervals. The intervals values of the collapse points $\mu_\pm$ we stipulate as being bounded by where the trajectories merge ($\mu_{\text{UP}}$ and $\mu_{\text{DN}}$) and the inner values ($\mu_{\text{S-}}$ and $\mu_{\text{S+}}$) observed in the trajectories (within which bimodality is demanded, see Figure 5.6). [1]

### 5.3.2 Fitting EMIC collapse trajectories

An AMOC collapse was induced in models of intermediate complexity in Rahmstorf et al. (2005) by applying a freshwater forcing to the North Atlantic subtropical gyre region that reduced the salinity in the subpolar gyre to its north. Six of these models have a 3-D ocean components; in Figure 5.6 the trajectories of those collapses are reproduced (right column, the freshwater flux has been labelled $\mu$ here) together with their numerical derivatives (left columns in the panels). In Table 5.1 the models are listed. The forcing values of $\mu$ are known and the same for each climate model. Each model was run to equilibrium for each forcing value; there is therefore no explicit time dependence in the

[1] To exclude parameter values that lead to intersections of $\boldsymbol{B}_{1,2}$ more than once, we artificially decrease the likelihood of these values. The discriminant of the polynomial at each forcing value indicates when this is needed.

hysteresis loops shown. Both the AMOC strength and the forcing value are given in units of Sv ($=10^6\,\mathrm{m\,s^{-1}}$). Note that the bifurcation points ($\mu_\pm$) must lie within the range where the trajectories appear bimodal.

The trajectories are from the numerical Earth System Models (EMICs) Rahmstorf et al. (2005, Figure 2, bottom panel). The numerical derivatives show where the AMOC changes quickest as a response to the change in freshwater forcing. Each model has two peaks where the changes are largest, one for each change between stable branches. These peaks are located at the repellor in between the two attractors (the stable branches). At the repellor only unstable solutions exist and the AMOC is driven to a stable solution, away from these states.

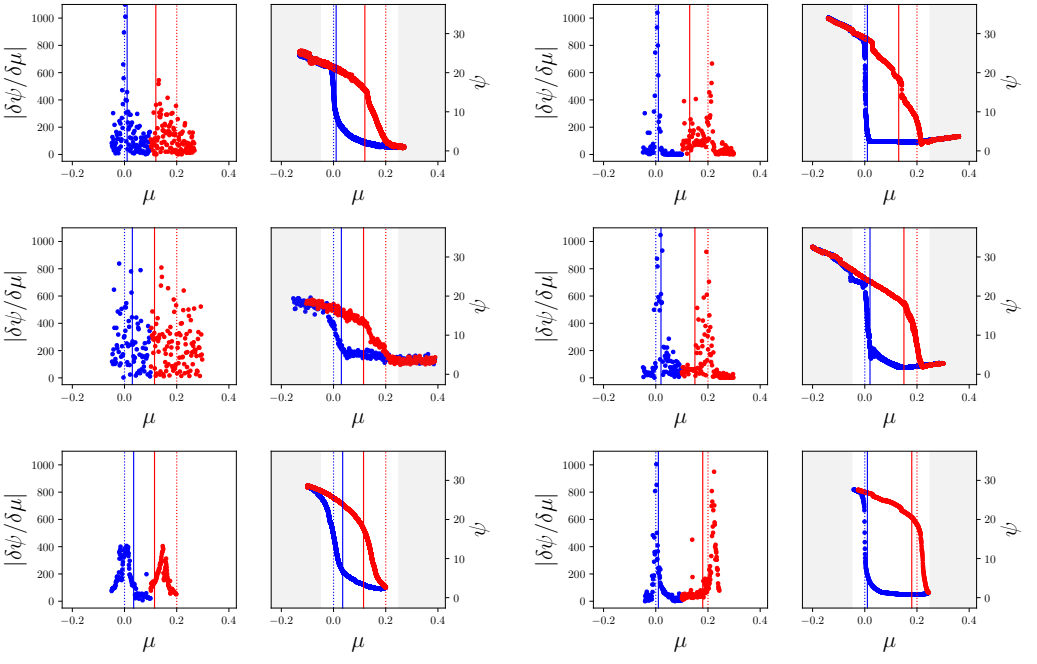


Figure 5.6: Absolute values of numerical derivatives (left) from the trajectories of AMOC strength as function of freshwater forcing to the right (taken from Rahmstorf et al. (2005, Figure 2, bottom panel), reproduced with permission from the publisher: American Geophysical Union). In red the upper branch, blue the lower branch. Left column: Bremen, ECBilt-CLIO, C-GOLDSTEIN; right column: MOM hor, MOM iso, UVic.Vertical solid lines mark $\mu = 0$ (blue) and $\mu = 0.2$ (red); vertical dashed lines mark the chosen boundary values for $\mu_\pm$. All values have units Sv.

If no other mechanisms apart from the salt advection are important we expect the bifurcation points to lie beyond the observed transition points because a noise-induced transition pushes the AMOC into the off-state sooner. (Note that although the collapse points are expected to lie before these peaks, low levels of noise will obscure this effect.)

| model | ocean component | atmosphere component | reference |
|---|---|---|---|
| Bremen | large-scale geostrophic | energy balance | Prange et al. (2003) |
| ECBilt-CLIO | 3D primitive equations | quasi-geostrophic | Goosse et al. (2001) |
| C-GOLDSTEIN | 3D simplified | energy-moisture balance | Edwards and Marsh (2005) |
| MOM hor | 3D primitive equations (MOM) | simple energy balance | Rahmstorf and Willebrand (1995) |
| MOM iso | as above, with isopycnal mixing | simple energy balance | |
| UVic | 3D primitive equations (MOM) | energy-moisture balance | Weaver et al. (2001) |

Table 5.1: Overview of models used. Each data point is independent from the others because each is the result of a quasi steady state run. The number of data points for each model was regridded onto a uniform freshwater forcing range consisting of 300 points. The summary of the type of model component and references are taken from Rahmstorf et al. (2005).

| model | $\sigma$ | $\mu_-$ | $\mu_+$ | present day |
|---|---|---|---|---|
| Bremen | 0.181 | [-0.018, 0.010] | [0.120, 0.220] | ( 0.070, 18.8)- |
| ECBilt-CLIO | 0.176 | [-0.044, 0.030] | [0.115, 0.210] | (-0.110, 18.2)+ |
| C-GOLDSTEIN | 0.122 | [-0.100, 0.035] | [0.115, 0.190] | (-0.100, 29.0)+ |
| MOM hor | 0.526 | [-0.010, 0.010] | [0.130, 0.200] | ( 0.110, 20.0)- |
| MOM iso | 0.216 | [-0.010, 0.020] | [0.150, 0.210] | ( 0.050, 22.8)- |
| UVic | 0.260 | [-0.020, 0.010] | [0.188, 0.225] | ( 0.080, 25.0)- |

Table 5.2: Overview of models, the estimated standard deviation with the upper branch fitted to a linear function (note that the original trajectories had already been smoothed), the ranges of $\mu_\pm$, the location of present day in the models, and whether the present day value is in the unimodal regime (+) or not (-). All values have units Sv.

The dashed lines indicate the regions where we will search for the optimum values of $\mu_\pm$. These differ from the fixed 0 and 0.2 values chosen by (Rahmstorf et al., 2005), who also shifted the trajectories to align on these values.

Before fitting, the upper and lower branches were extended to the left and right to fill the space of $-0.2 < \mu < 0.4$. A linear fit was use to produce additional values of the corresponding branches (at the same density of those points already present). All models then occupy the same freshwater forcing space. This is desirable because not all models have a lower branch that is fully sampled (specifically, UVic). The lower branch was extended with a negative rate of increase if the lower branch was moving upwards with increasing $\mu$ (MOM hor and MOM iso).

Our main goal is to model the transition from on-branch to the off-branch, that is, the upper right half of the hysteresis curve, and not so much the dynamics that govern the lower branch. Also, because we assume that other dynamics govern the lower branch and, our simple model has to be extended to account for those dynamics. We ignore the data on the lower branch before the collapse point so the fits would not be influenced by these points. We expect the remaining points of the trajectory to be dominated by the salt-advection mechanism.

We start by identifying some characteristic points in the trajectories in Table 5.2. The $\sigma$ (variance of the process) of the models is not given in Rahmstorf et al. (2005) or elsewhere in the literature, but was estimated as the deviation with a fitted function to the left most the top branch. (Note that smoothing was already applied in Rahmstorf et al. (2005), lowering the variance of the trajectories. Because we want to fit the collapse trajectory as given, we use the variance as evident from the data.) In principle, $\sigma$ could also be estimated as a parameter in the Bayesian optimisation, but that would unnecessarily enlarge the search space. Note that the 'off-state' of the AMOC in these models is not 0,

but $\sim$ 2Sv of AMOC strength. If the salt-advection mechanism were the only operative effect, we expect this value to be $\leq 0$. If a reverse advection cell emerges as the lower hysteresis branch, this value is negative.

In Figure 5.7 fitted distributions are shown (also tabulated in Table 5.3). As best fit parameters, we choose the mean values of the marginal posterior distributions. The dashed grey line marks the positions of the unstable solution (repellor) in between the two attractor branches which separates the two basins of attraction.

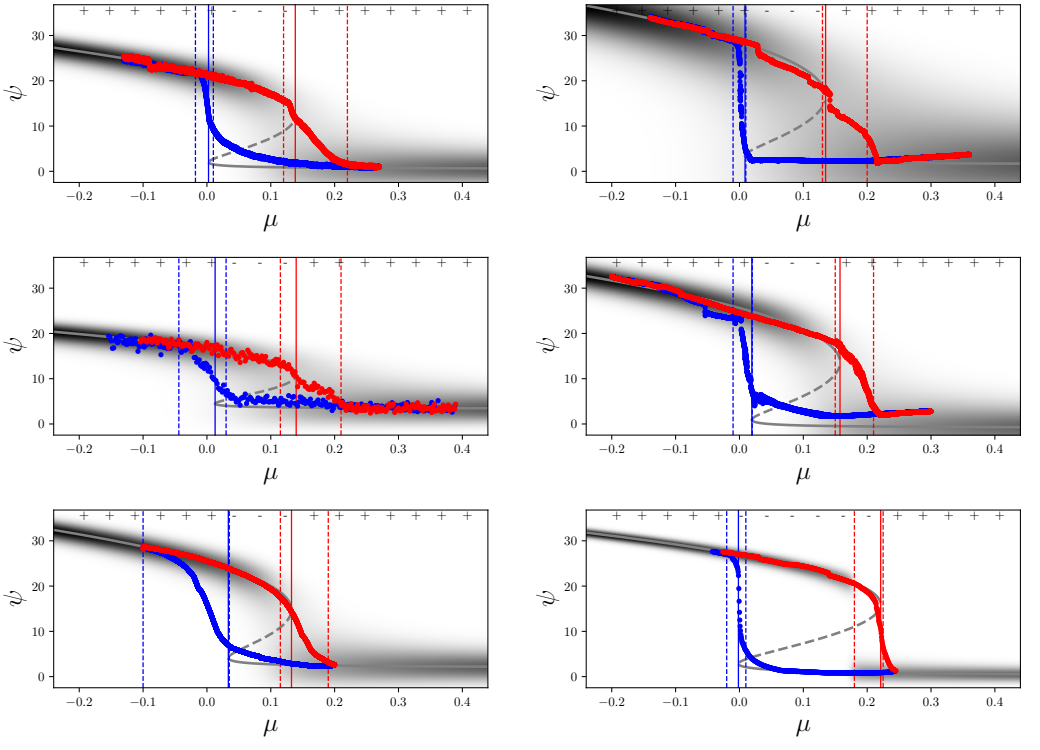


Figure 5.7: Estimated distributions under changing $\mu$. Left column: Bremen, ECBilt-CLIO, C-GOLDSTEIN; right column: MOM hor, MOM iso, UVic. Vertical dashed lines mark the chosen boundary values for $\mu_{\pm}$, with solid lines the fit values. Grey dashed line indicates the local minimum in the distribution (trench). Top $\pm$ symbols indicate the sign of the discriminant $D$ for the fitted distribution (+ for unimodal, − for bimodal). Distribution spreads have been inflated with a factor $\nu/2$ to make them visible. All values have units Sv.

The fits with a linear series through the $(\alpha, \beta)$ parameter space result in a mismatch between the behaviour seen on lower branches and that on the upper branches. This is less obvious for UVic and ECBilt-CLIO, but especially apparent for the two MOM models.

| | $\nu$ | $\lambda$ | $\beta_0$ | $\delta\beta$ | $\mu_-$ [Sv] | $\mu_+$ [Sv] | RMS dev. [Sv] |
|---|---|---|---|---|---|---|---|
| Bremen | 21.2 | 8.44 | 0.28 | -1.32 | 0.002 | 0.14 | 0.38 |
| ECBilt-CLIO | 13.8 | 8.45 | 0.26 | -1.24 | 0.013 | 0.14 | 0.60 |
| C-GOLDSTEIN | 24.2 | 10.7 | 0.27 | -1.39 | 0.033 | 0.13 | 0.48 |
| MOM hor | 28.4 | 11.7 | 0.26 | -1.31 | 0.009 | 0.13 | 0.98 |
| MOM iso | 25.7 | 8.90 | 0.32 | -1.37 | 0.019 | 0.16 | 0.83 |
| UVic | 23.5 | 10.9 | 0.35 | -0.97 | -0.002 | 0.22 | 0.81 |

Table 5.3: Mean values and standard deviations of parameters corresponding to the fitted functions in Figure 5.7. The root-mean-square deviation (a goodness of fit measure) has been determined on the upper branch up to the fitted collapse point.

## 5.4 Discussion and conclusion

We derived a simple model of AMOC collapse based on Langevin dynamics (Eq. 5.1) with a changing freshwater forcing ($\mu$) and applied this to EMIC simulated collapse trajectories taken from Rahmstorf et al. (2005). The collapse occurs at a bifurcation point $\mu_+$ which appears smaller than given in (Rahmstorf et al., 2005). A corresponding bifurcation point $\mu_-$ relates an abrupt transition back to the on-state. The AMOC also requires an offset and scaling parameter to be fitted ($\lambda$ and $\nu$). These six parameters are sufficient to describe the abrupt collapse of the AMOC as part of a hysteresis loop under varying freshwater forcing.

Any process which allows two stable states with rapid transitions between them and an asymmetric response to the forcing could in principle be described by our method. Other such geophysical processes might be ice sheet mass loss (e.g. Robinson et al., 2012), forest dieback (e.g. Staal et al., 2016), and lake turbidity (Scheffer and Van Nes, 2007).

The resurgences of the AMOC seen in the hysteresis diagrams behave differently from the collapses. The Langevin model is too simple to capture both processes. It is, however, possible to fit the change in the upper branch of the AMOC—the 'on-state'—as it moves towards a critical point and the dominant salt-advection feedback mechanism breaks down.

We note that Rahmstorf et al. (2005) determine the AMOC strength as the maximum of the meridional volume transport in the North Atlantic and might explain the asymmetry between the two branches. If for a reverse overturning cell the wrong metric has been used then the lower branch location is not correct. It is conceivable that the Langevin model results in better fits if Rahmstorf et al. (2005) had sampled $\max(|\Psi|)$ instead of $\max(\Psi)$, which would have resulted in a better metric of the lower branch. With the met-

ric used it is not apparent whether a reversed overturning cell was present or not because it was not sampled if the AMOC had taken on a negative value. It is unclear to what extent the models discussed here develop a reversed overturning circulation which can arise in 3D models (Weijer et al., 2001; Yin and Stouffer, 2007), but which can also be suppressed by atmospheric feedbacks (Yin and Stouffer (2007); however, see also Mecking et al., 2016), and strongly affected by gyre dynamics (Prange et al., 2003). These effect are not captured by the simple Langevin model proposed here, but at present it is still unclear to what extent these effects are essential in capturing the first order stability properties of the AMOC. In each case, there is no obvious way to model the asymmetry between the two branches, and obtain a full description. The two branches could be separated by associating each with a different overturning cell. The upper branch is identified with the NADW-driven cell, while a reverse cell is responsible for the lower branch. If indeed a reverse overturning cell (as described in e.g. Yin and Stouffer, 2007) dominates the lower AMOC branch, two separate overturning cells are responsible for the observed trajectories, and the two branches then cannot be expected to fit with the same parameter set.

However, another possible explanation is that (two) separate mechanisms are responsible for the upper and lower branch dependency on $\mu$. Possible mechanisms include possible mechanisms include the influence of wind-stress, North Atlantic subpolar gyre convective instability (Hofmann and Rahmstorf, 2009), or other pathways of deep water formation (Heuzé, 2017). Also, changes in the ITCZ (Intertropical Convergence Zone) due to ocean-atmosphere feedbacks are possible (Green et al., 2019); these can, in turn, can affect the salinity of the North Atlantic subtropical gyre region. However, Mecking et al. (2017) showed that for a high-resolution model the salt-advection feedback was nevertheless stronger than the ITCZ effects. Other wind coupling can occur further south through a coupling with the ACC (Antarctic Circumpolar Current) which is based on the thermal wind relation (Marshall and Johnson, 2017).

A third explanation is that deep water formation is a local process, and as a result an asymmetry is to be expected between the two branches. Local convection can, however, be subject to global controls and be associated with a sinking branch which occurs in conjunction with deep convection, but is not directly driven by it, see Spall and Pickart (2001) for a detailed discussion. The AMOC could develop a reverse cell where the overturning is driven by Antarctic Intermediate Water (AAIW), which is not part of the conceptual picture presented here (Yin and Stouffer, 2007; Jackson et al., 2017). The reverse cell introduces an asymmetry in the collapse trajectories because the driver of deep water formation is not in the North Atlantic, and might break our assumption that both the on and off branches are controlled by the same process. It is therefore difficult to estimate the return path of the AMOC if the lower branch has additional drivers from the dominant salt-advection mechanism of the upper branch. Forcing values appropriate for the lower branch might be different than those found for the upper branch.

Furthermore, the methodology used in this paper comes with difficulties in the numerical implementation. The fit procedure requires the normalisation of each distribution

in the $\mu$ time series. Because no analytic solution exist a numerical approach is needed. The numerical integration adds to the computational costs of the fits. The Markov chain method is also prone to find local optima. Also, the cost of numerical integration necessitates stopping the fits at shorter chains than (perhaps) are needed, an analytic formulation of the integrand would alleviate this but none exists to our knowledge. Modern sampling algorithms allow for gradient information to be used, which is effective when sampling a higher dimensional parameter space (the Metropolis algorithm used in this paper has greater difficulty as the dimensionality of the parameter space increases). Tighter constraints on the prior distributions could be beneficial here.

As stated in Rahmstorf et al. (2005), the EMIC trajectories had already been smoothed, resulting in a smaller variance; a smaller variance leads to distributions that are more sharply peaked. This increases the computational cost of integrating the distributions numerically. Smoothing can also add to the inertia seen in the collapses, but might be due to other reasons such as stopping the EMIC simulations before equilibration of the AMOC collapse, leaving the AMOC in a winding-down state. Also, the models in Rahmstorf et al. (2005) were integrated for 1000 model years per freshwater forcing value (which was changed in 0.05 Sv increments). If the integrations were done for an insufficient amount of time, the AMOC collapse is incomplete, leaving the measured value out of equilibrium. The intermediate points in the collapse trajectories beyond the bifurcation points indicate that either the sample points are inaccurate or other processes are involved in the AMOC.

Finally, the fitted collapse trajectories were done on an ensemble of EMICs, which arguably are not sufficiently representative of the real climate. As noted by Gent (2018), the hysteresis behaviour has not been investigated fully in models of greater complexity than EMICs; the computational cost being the prohibitive for models with high resolution (and short time steps). The hysteresis behaviour in glacial state changes has, however, been investigated in greater detail using models with simplified dynamics (e.g. Schiller et al., 1997; Zhang et al., 2017). The question arises to what extent the procedure outlined in this paper can be applied to more complicated models such as those in the CMIP archives (Taylor et al., 2012). These models do not show a full collapse trajectory like those in Rahmstorf et al. (2005), which means no sample points of the lower branch are available. Also, CMIP provides times series of forced runs. To validate our method, a transient run requires known equilibrium bifurcation points, under a slowly changing $\mu$, and include an AMOC collapse. Using a simple box model, transition probabilities for an AMOC collapse have been determined by Castellana et al. (2019). From the CMIP ensemble a similar estimate might be obtained, or at least the collapse characteristics of various models can be compared. Provided the CMIP models accurately capture the behaviour of the real AMOC and the freshwater forcing counterpart (our $\mu$) can be identified, an estimate can be made of the distance of the current climate state to the collapse point. Freshwater quantities such as $M_{\mathrm{ov}}$ have been posited (e.g. Drijfhout et al., 2011) as being suitable indicators of AMOC stability. It is possible that $M_{\mathrm{ov}}$ relates to $\mu$ and can be used to extend our method to transient runs, but at present it is unknown whether this

can be done. The inclusion of ice sheets can make a substantial difference in AMOC recovery (Ackermann et al., 2020). Also, the atmospheric freshwater transport might have a stabilising effect on the AMOC that is greater than the freshwater transports by the ocean (Lohmann, 2003). There is, however, also evidence that coupled climate models suffer from a salinity bias that favours an AMOC that is too stable (Drijfhout et al., 2011; Liu et al., 2017). These matters are outside the conceptual picture of $M_{\mathrm{ov}}$ as a stability indicator. It is therefore still an open question how probable an AMOC collapse is in more realistic models, and reality, but with the method outlined in this paper a first step could be made in answering this question.

## Acknowledgements

This work was partially funded by the European Commission's 7th Framework Programme, under Grant Agreement number 282672, EMBRACE project. The authors thank the two anonymous referees and editor Gerrit Lohmann for their valuable comments and suggestions that have improved the manuscript greatly. The authors also thank Stefan Rahmstorf for providing the original data.

# 6 Transient Atlantic Meridional Overturning Circulation response

## 6.1 Introduction

Paleo reconstructions indicate the Atlantic Meridional Overturning Circulation (AMOC) has been through collapses and resurgences in the distant past, and climate simulations show that the AMOC is expected to decrease in strength during this century (see Chapter 1 for a discussion). The question arises whether climate change in EC-Earth is currently driving the AMOC to another collapse. Chapter 5 investigated how such collapses in climate models could be parameterised as a function of a freshwater forcing for climate models that were allowed to equilibrate such as in the distant past. There are two important differences between those models and the CMIP5 models (Taylor et al., 2012) that are used to project current climate change into the future. First, there is no explicit freshwater forcing in the CMIP5 models, and Chapters 2 – 4 show what the effects would be in one particular model, EC-Earth. Second, climate change is an ongoing forcing on relatively short timescales compared to the paleo records and the models in Chapter 5.

The freshwater forcing in Chapters 2 – 4 did not bring about a collapse of the AMOC, but did weaken it further. A larger forcing might have collapsed the AMOC, but compensating mechanisms within the North Atlantic gyre structure and a, possibly, inaccurate representation of deep water formation might be important in stabilising the AMOC in EC-Earth. In this chapter, the lack of freshwater forcing from melting ice sheets is ignored and challenges that arise when modelling the AMOC out of equilibrium are explored. The various climate models in the CMIP5 ensemble show a variety of AMOC representations, not just in its pre-industrial strength, but also the rate of decline throughout the 21$^{st}$ century (Weaver et al., 2012). The freshwater budget expressed in terms of freshwater variables, such as $M_{ov}$ (Rahmstorf, 1996; Weber and Drijfhout, 2007), of these models might explain the differences and indicate why a collapse is or is not a likely outcome of climate change this century.

In Section 6.2 is sketched how Atlantic/Arctic freshwater variables might relate to AMOC stability. Also, some (implicit) assumptions about AMOC stability are discussed. Section 6.3 compares CMIP5 models' steady-state and discusses differences in evapora-

tion over the Atlantic as a (possible) model-specific bias. The forced behaviour of the CMIP5 ensemble during the 21st century after bias correction is fit to the Langevin model of Chapter 5 in Section 6.4 We end with a discussion of interpretations of the transient response in terms of the Langevin model and freshwater variables.

## 6.2 Integral freshwater variables and AMOC stability

In Figure 6.1 two diagrams show the integral freshwater variables that affect the Atlantic and Arctic freshwater budget. Integral freshwater variables (i.e. integrated over an ocean section) are preferred because they have a clear definition in ocean models and allow for comparison of the freshwater budget between models. In the diagram, the ocean sections are indicated. Of these, Bering Strait is too shallow for an overturning, but it is relevant to the freshwater budget of the Arctic. The Gibraltar Strait section does have a depth dependence (García-Lafuente et al., 2017) in its throughflow with salty water overflowing the Camarinal Sill (a natural, submerged barrier between the Atlantic and the Mediterranean) and relatively fresh water moving east above. The zonal section at Cape Agulhas at 34°S is the only substantial open ocean interface where baroclinic freshwater variables ($M_{\mathrm{ov}} + M_{\mathrm{az}}$, defined below) are important because of its extension to depth. With respect to a section's reference salinity, the salinity and velocity fields can be combined into a freshwater transport into the South Atlantic. Under steady-state conditions, this transport is part of the freshwater budget of the Atlantic and Arctic (summing all incoming components, including evaporation minus precipitation and run-off and melt, gives $\approx 0$ total freshwater transport into the Atlantic).

### 6.2.1 Advective freshwater integrals

Rahmstorf (1996) introduced a dimensional mode decomposition of the salinity/velocity field at the Cape Agulhas section and this was treated in greater detail by De Vries and Weber (2005) and Weber and Drijfhout (2007) as components in the combined Atlantic and Arctic freshwater budget. This decomposition gives the section average (0-dimensional), an average retaining depth (1-dimensional), and a remainder (2-dimensional) as section variables which can be integrated to 0-dimensional time series. Explicitly, the freshwater import across a zonal section $A$ can be written as follows when

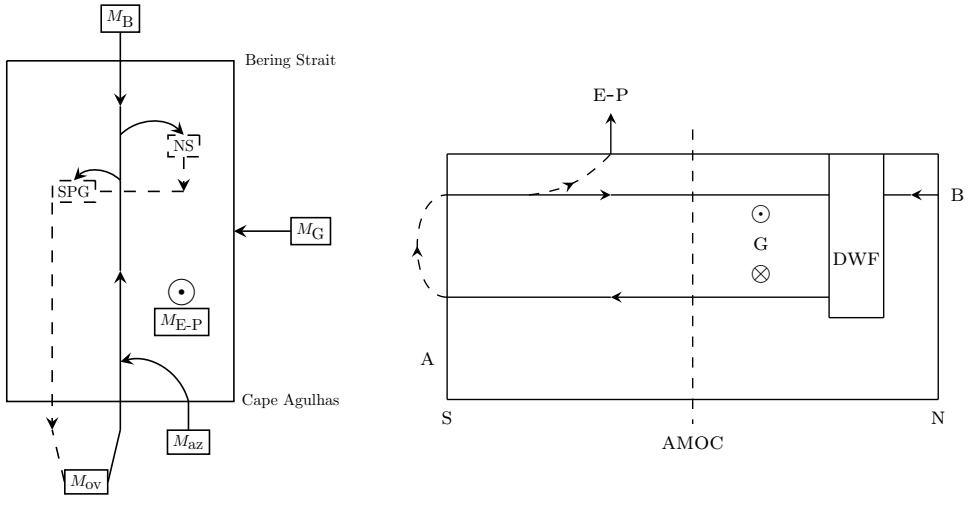


Figure 6.1: Plan and latitudinal schematic views of the Atlantic and Arctic basin. Left: top view indicating the relevant freshwater variables that exist at the basin interfaces. The deep water formation regions in the North Atlantic high latitudes are the subpolar gyre (SPG: Labrador and Irminger seas) and the Nordic Seas (NS). The Atlantic is a net evaporative basin ($M_{\mathrm{E-P}}$) but also receives freshwater due tot sea ice melt and run-off to the ocean surface. Right: a south-north diagram of the conceptual picture of the salt-advection feedback with these additional freshwater variables and deep water formation (DWF). At the Cape Agulhas section ($A$) the baroclinic freshwater transport closes the budget. The strait of Gibraltar ($G$) exports freshwater out of the Atlantic through a shallow outflow of Atlantic water and a deeper inflow of saltier Mediterranean water. Bering Strait ($B$) imports freshwater from the Pacific Ocean. Evaporation ($E$) into the basin exceeds precipitation ($P$). The dashed line indicates where the AMOC maximum is typically found.

scaling with $S_0 = \langle S \rangle$,

$$
\begin{aligned}
M'_A &= -\frac{1}{S_0} \iint_A v S \, \mathrm{d}x\mathrm{d}z \\
&= -\frac{1}{S_0} \iint_A (\langle v \rangle_x - \langle v \rangle)\langle S \rangle_x \, \mathrm{d}x\mathrm{d}z \\
&\quad - \frac{1}{S_0} \iint_A (v - \langle v \rangle_x)(S - \langle S \rangle_x) \, \mathrm{d}x\mathrm{d}z - \iint_A v \, \mathrm{d}x\mathrm{d}z \\
&=: \iint_A F_{\mathrm{ov}} + F_{\mathrm{az}} - F_{\mathrm{v}} \, \mathrm{d}x\mathrm{d}z =: M_{\mathrm{ov}} + M_{\mathrm{az}} - M_{\mathrm{v,A}};
\end{aligned} \tag{6.1}
$$

with the averaging operators as introduced in Chapter 3,

$$\langle v \rangle = \iint_A V \, \mathrm{d}x\mathrm{d}z \Big/ \iint_A \mathrm{d}x\mathrm{d}z, \quad \langle v \rangle_x = \int_A V \, \mathrm{d}x \Big/ \int_A \mathrm{d}x,$$

where $\langle v \rangle$ is 0-dimensional (barotropic), and $\langle v \rangle_x$ is 1-dimensional (retaining depth). The $M$ variables are the section-integrated $F$ (for 'field') variables. This decomposition is similar to the salt decomposition used in Chapters 3 and 5 but uses a reference salinity to convert the variables to freshwater transports instead of salt transports.

The freshwater integrals $M_{\mathrm{ov}}$ and $M_{\mathrm{az}}$ are at the Cape Agulhas section from now on; this is the section that can be drawn from Cape Agulhas, at the tip of Africa, to South America, where it cuts across the southern hemispheric subtropical gyre (the Benguela Current near Africa, and the Brazil current on the South American side). A positive value of these integral freshwater variables means a transport of freshwater into the South Atlantic. In Figure 6.2 the velocity field, salinity, field, and the fields $F_{\mathrm{ov}}$ and $F_{\mathrm{az}}$ are shown for a 50-year mean simulation (1850 – 1900) of EC-Earth. The gyre affects $M_{\mathrm{az}}$, as can be seen in the bottom-right panel of Figure 6.2. Note that the Brazil Current also imports freshwater, meaning it must export excess salt from the South Atlantic as it flows southward. Both the overturning and the gyre affect the freshwater balance into the South Atlantic, with the effect being mostly in the deep western boundary current (DWBC), which is linked to the deep water formation in the high latitudes (Peña-Molino et al., 2012).

In the bottom-left panel (Figure 6.2) a subsurface inflow, a surface outflow, and a deeper outflow shows a similar pattern as the subsurface and deeper salinity (top-right panel). The balance between the shallow export of freshwater versus the deeper import of freshwater indicates that $M_{\mathrm{ov}}$ relates to the freshening or salinifying of the Atlantic. $M_{\mathrm{az}}$ couples predominantly to a shallow inflow associated with the southern hemisphere subtropical gyre and shows similarities with both the salinity and velocity (comparing bottom-right and top-left panels). The deviation from zero in the freshwater balance needs to be balanced by other freshwater variables other than $M_{\mathrm{ov}}$ and $M_{\mathrm{az}}$ into the Atlantic and Arctic basin to maintain the reference salinity, as is the case in a steady-state climate.

### 6.2.2 Steady-state freshwater balance

The freshwater variables in the left panel of Figure 6.1 are a simplified representation of the freshwater balance. Ignoring persistent barotropic changes (such as trending changes in evaporation or precipitation over the Atlantic, see Eq. 6.1) and also ignoring the influence of the Strait of Gibraltar ($M_{\mathrm{G}}$ in Figure 6.2, see also Chapter 2) gives

$$M_{\mathrm{E-P}} = M_{\mathrm{B}} + M_{\mathrm{ov}} + M_{\mathrm{az}} - M_{\epsilon} =: M_{\mathrm{s}} - M_{\epsilon}. \tag{6.2}$$

as the freshwater balance across the interfaces of the Arctic-Atlantic (De Vries and Weber, 2005), with $M_{\epsilon}$ a remainder term. We also assume that all water taken up by the

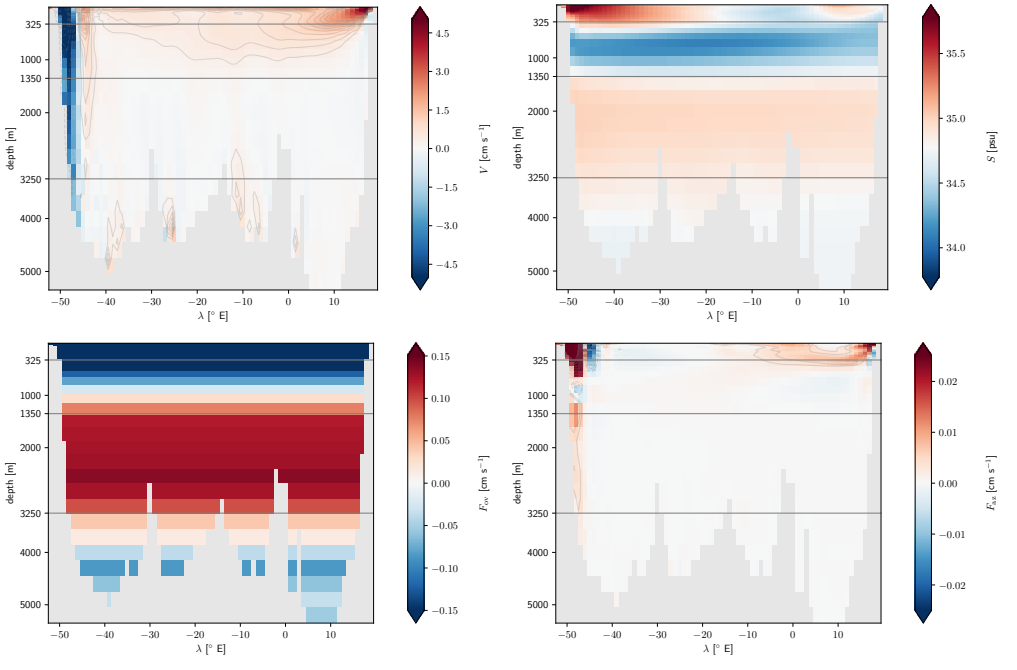


Figure 6.2: Agulhas section (34°S) annual mean (1850 – 1900) state: Top-left the velocity profile (centred at zero); top-right the salinity profile centred at the section-averaged value. Bottom-left $F_{\mathrm{ov}}$; bottom-right $F_{\mathrm{az}}$. Grey lines indicate divides in salinity as in the top-right panel.

atmosphere returns to the world ocean: there is no significant water vapour uptake by the atmosphere, land, or ice takes place and no freshwater is deposited on ice caps or results in changes in run-off, groundwater level, lakes, etc. Furthermore, any changes that affect the AMOC as a direct result of $M_{\mathrm{E-P}}$ will also affect the boundary variables. Figure 6.3 shows a subset of the CMIP5 ensemble of climate models (Taylor et al., 2012). The freshwater balance in Eq. 6.2 is fitted and the each model has a different balance between $M_{\mathrm{E-P}}$ and the advective freshwater variables. (Freshwater time series courtesy of Jennifer Mecking, as derived from the CMIP5 decomposition done in Mecking et al., 2017.) The offset of the black line is 0.05 Sv, a reasonable value for $M_{\epsilon}$ (Criado-Aldeanueva et al., 2012, estimated 0.035 Sv for the Gibraltar Strait freshwater flux). All CMIP5 models that did not have the fields available needed in the analysis here are excluded. The model GISS-E2-R (Schmidt et al., 2014) is also excluded for having an Atlantic-Arctic integrated E-P (evaporation - precipitation, $M_{\mathrm{E-P}}$)[1] an order of magnitude larger than other models.

[1]Called wfo in CMIP terminology.

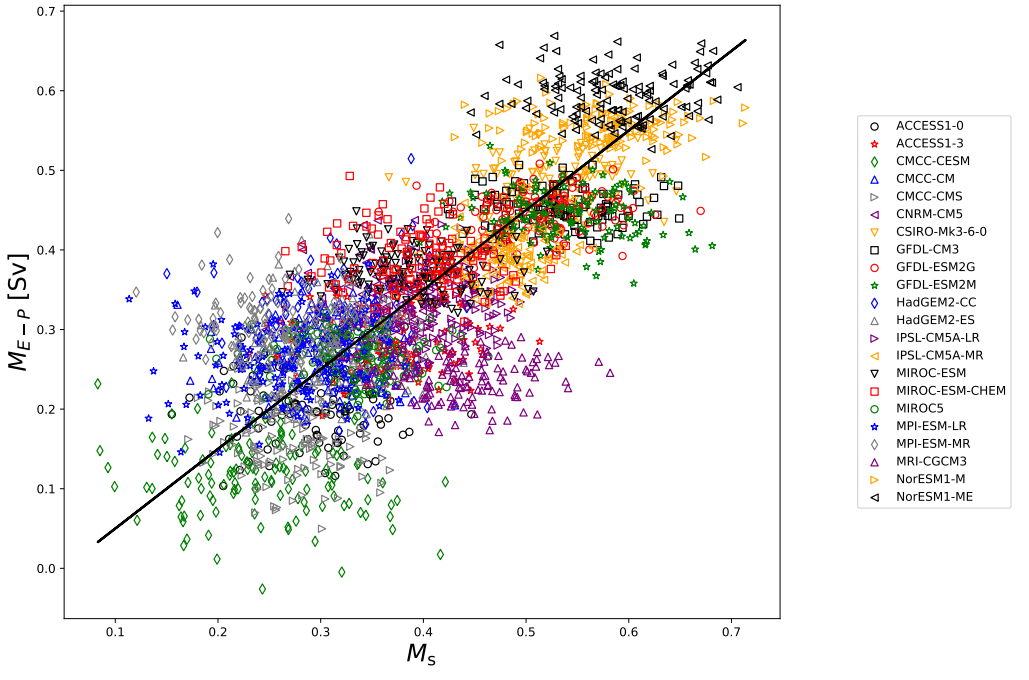


Figure 6.3: Historic (pre 2000) values $M_{\mathrm{E-P}}$ vs $M_{\mathrm{s}}$ and $M_{\mathrm{E-P}} = M_{\mathrm{s}} - 0.05$ Sv as the black line (this offset is roughly the Mediterranean component). Each symbol corresponds to the indicated CMIP5 model on the right.

An accumulation of freshwater in the North Atlantic and Arctic could weaken the AMOC and even shut it down completely (a critical transition in AMOC strength where it abruptly shifts to little or no transport). Understanding changes in the freshwater balance of the Atlantic and Arctic is therefore important for understanding AMOC stability.

### 6.2.3 Critical transitions in AMOC strength

A change in the overturning strength results in a change in the Atlantic freshwater (or salt) budget because the overturning circulation transport freshwater to or from the Southern Ocean (in a steady-state). This coupling of the AMOC to its own boundary conditions in the South Atlantic is known as the salt-advection feedback because a (hypothetical) salinity anomaly is advected in the slow, shallow thermocline northward where it is mixed into the water of cold, relatively fresh high latitudes. This mechanism was presented by Stommel (1961) as a curiosity in an idealised model and was suggested as potentially having a counterpart in the real ocean. This mechanism also exhibits hysteresis because which stable equilibrium state observed depends on whether the state is approached from a high salinity state or from a low salinity state (see Chapter 5). The (accumulated) freshwater in the Atlantic high latitudes acts as a memory of the past. The density of

sea water at the ocean surface compared to the water beneath it is a crucial factor which determines convective stability; convective instability can drive the mixing in the open ocean that produces deep water (e.g. Pickart and Spall, 2007).

If a weaker AMOC imports more freshwater, the freshwater in the shallow Atlantic increases and this should further weaken the AMOC, which is a positive feedback. The following assumptions are (implicitly) assumed to hold under the Stommel conceptual model as it was used in Chapter 5 to formulate the Langevin collapse model.

1 **single baroclinic freshwater coupling**—Freshwater variables affect the Atlantic freshwater budget, but only the overturning is part of the conceptual picture, that is:

   a Atmosphere, sea ice, and run-off ($M_{\mathrm{E-P}}$) are uncoupled;

   b Agulhas section

      i overturning ($M_{\mathrm{ov}}$) is coupled,

      ii gyre ($M_{\mathrm{az}}$) is uncoupled,

   c Bering Strait section ($M_{\mathrm{B}}$) is uncoupled,

   d Gibraltar section ($M_{\mathrm{G}}$) is uncoupled;

2 **advective equilibration**—AMOC weakening by a freshwater anomaly takes place rapidly after arrival of the anomaly in the high latitudes;

3 **weak locality**—The Atlantic freshwater budget controls the AMOC by affecting deep convection in the high latitudes directly;

4 **external insignificance**—Conditions such as windstress and eddies at ocean boundaries are not important;

5 **haline dominance**—Salinity/freshwater changes are stronger than thermal changes.

Whether or not these assumptions hold in reality or climate models, especially under climate change, is not a given. Some of the assumptions listed have been addressed in conceptual models after Stommel's; see e.g. Drijfhout et al. (2013) for a discussion of conceptual AMOC models. Each of the five assumptions is briefly discussed below, before examining the CMIP5 ensemble 21$^{\mathrm{st}}$ century projections in terms of freshwater variables.

### 6.2.4 Single baroclinic freshwater coupling

In Stommel's model, the simplest formulation ignores all freshwater coupling apart from the feedback via $M_{\mathrm{ov}}$. As noted by Mecking et al. (2017), the AMOC streamfunction

formulation is similar to $M_{ov}$, and this connection suggest that $M_{ov}$ is an important variable related to the AMOC and might indicate how the AMOC would respond to buoyancy anomalies (e.g. Drijfhout et al., 2011). If the state of the AMOC is determined by the advection of freshwater into the Atlantic, $M_{ov}$ should be an important variable in a low-dimensional description of AMOC behaviour, especially if its sign determines the possibility of a critical transition.

As shown by Cimatoribus et al. (2012), the evaporation in the South Atlantic ($M_{E-P}$) affects the freshwater budget of the Atlantic and the freshwater exchange with the Southern Ocean. As shown in Section 6.3.1, $M_{E-P}$ differs between models. This invalidates the assumption of a single freshwater coupling, although $M_{ov}$ could still be dominant in the feedback if other freshwater variables are small enough. Additionally, the Cape Agulhas section reduces to only two points in the Stommel model, only allowing $M_{ov}$, but not a variable like $M_{az}$. Exchanges mediated by the atmosphere can remain internal to the Atlantic (such as a shift in precipitation patterns, possibly associated with the Intertropical Convergence Zone, Chapter 3), or have an effect external to the basin, such as moisture transport across the Panama Isthmus. The Mediterranean influence is not significant in either the CMIP5 ensemble, or in the freshwater forcing experiments in the previous chapters. Greenland and Antarctic mass loss increases salt transport out of the basin through Bering Strait, as shown in Chapter 3. The value of $M_{ov}$ can be corrected by taking the change in freshwater exchange across the North Atlantic subpolar gyre into account: Dijkstra (2007) and Liu and Liu (2013) use the convergence of $M_{ov}$ across the SPG to implicitly account for the effect of Bering Strait as well.

The importance of evaporation and precipitation in the Atlantic and Arctic is readily seen in the CMIP5 ensemble with increasing evaporation out of the (South) Atlantic (Levang and Schmitt, 2015 show an intensification of the water cycle in CMIP5 models). Other freshwater variables than $M_{ov}$ are therefore likely important.

### 6.2.5 Advective equilibration

A distinction needs to be made between an AMOC state after equilibration on advective, or longer, timescales, and an AMOC state which is transient, possibly under a changing forcing like current changes due to human activity. Hawkins et al. (2011) show a difference between steady-state hysteresis (similar to those in Rahmstorf et al., 2005) and transient hysteresis loops. The forcing needed to collapse the AMOC under transient conditions is larger compared to steady-state simulations (0.4 Sv versus 0.2 Sv) of Hawkins et al. (2011). The advective timescale is centennial and a re-balancing is not achieved within transient timescales, meaning a greater forcing might be required to observe a critical transition on a shorter timescale.

Born and Stocker (2013) have shown that the North Atlantic subpolar gyre (SPG) region can undergo critical transitions between stable sates, with a similar description to the AMOC as in Chapter 5. The freshwater budget of the Atlantic is an important variable, but might not be directly coupled to the SPG state; it is not clear whether the

two SPG states are necessarily coupled to the two stable AMOC states. Since the SPG is an important region of deep water formation, equilibration takes place at least on SPG-critical timescales of multiple decades (Born and Stocker, 2013).

The results from climate models from Rahmstorf et al. (2005), studied in Chapter 5, indicate that this assumption of advective equilibrium is true on equilibrating timescale, presumably also for the SPG to undergo any—potentially—critical transitions. These results raise the question whether these models are sufficiently complex to adequately represent the SPG and the deep water formation process in the North Atlantic. The Atlantic cannot be considered unitary: the SPG (and Nordic Seas) are affected by local conditions of salinity and the gyre structure can be a barrier which (temporarily) shields the deep water formation state from the changes in the basin average state regarding the freshwater budget. The exchange mechanism between the SPG and the Nordic Seas is another negative feedback mechanism that can partially counteract a freshwater forcing related to (Greenland) ice sheet melt, as seen in Chapter 3.

### 6.2.6 Weak locality

Stommel (1961) assumes well mixing at all times in the box representations of both the high-density cold/fresh north and the low-density warm/salty south. For deep convection to take place, the surface waters need to converge and be cooled sufficiently to reach a high enough density that an instability of the water column sets in and homogenisation takes place to depth and mixes in the surface water. A reduction in salinity or an increase in temperature would leave the surface waters lighter and reduce deep convection, reducing the production of North Atlantic Deep Water (NADW), and consequently reduces the overturning strength.

Deep convection takes place in the Labrador and Irminger seas during winter, and also further north in the Nordic Seas (Figure 6.1 and also discussed in Chapter 4). The surface waters reaching these regions are fed by waters arriving from the south. The characteristics of these waters can therefore influence the deep water formation. From the surface down to the mixed layer depth a homogenisation of sea water takes place and deep water forms (Marshall and Schott, 1999). An increase in freshwater advected from the south would counteract this process and decrease density because salinity decreases and leads to a lower mixed layer depth and less deep water formation. Open ocean deep convection might not be the dominant process for deep water formation, however, and might take place mainly in narrow boundary currents where convergence of surface water occurs (Spall, 2008). The boundary currents are too narrow to be accurately represented in most climate models ($\mathcal{O}$(100 m) vs 100 km grid resolution). Also, the interaction with the surface through sea ice and the atmosphere will affect the surface water characteristics, and therefore deep water formation, inhibiting it through ice melt and warmer winter atmospheric temperatures.

The interaction with the winds can be important for routing salty water to the subpolar gyre and Nordic Seas (see also Chapter 4 how, especially, Greenland mass loss affects

this). A re-routing of salty water to the Nordic Seas leaves less salt available to increase seawater density in the subpolar gyre. The air/sea interaction therefore also introduces additional local dependence in the mixing/deep water formation in the North Atlantic and Arctic. The typical timescale on which the mixing takes place can be influenced by the above processes, and might be important for AMOC weakening.

### 6.2.7 External insignificance

Closure of the overturning circulation happens through upwelling in the Southern Ocean and is largely wind-driven and affected by eddies (Marshall and Speer, 2012). As discussed in Chapter 3, the Southern Ocean winds drive the supergyre (Ridgway and Dunn, 2007) in the southern hemisphere and therefore determine the wind-driven and eddy-induced exchange of water between the Southern Ocean and the South Atlantic. In particular, the return flow if the Atlantic overturning is strongly connected with the southern hemisphere supergyre (Speich et al., 2007). Climate change affects the winds and also the gyre interactions, similar to the North Atlantic gyres. Windstress can change by mass loss from Antarctica (Chapter 3), but $CO_2$ forcing alone can intensify the westerly winds in the Southern Ocean, which appear to be underestimated in the CMIP5 models (Swart and Fyfe, 2012). An increase in the windstress can change the surface inflow and affect the Atlantic freshwater budget. The return flow of the Atlantic overturning could therefore be intimately connected with the state of the Southern Ocean and its interaction with the atmosphere.

Mesoscale eddies can transport heat and salt from the Indian Ocean to the South Atlantic (Backeberg et al., 2012). Observations indicate this 'Agulhas leakage' has increased over the recent decades (Biastoch et al., 2009; Rouault et al., 2009), bringing more heat and salt into the Atlantic. Mesoscale eddies in general might be important to AMOC stability, as shown in Mecking et al. (2016) where an eddy-permitting model has a larger salt transport due to eddies in the AMOC compared to a lower resolution counterpart. In Munday et al. (2013), an eddy-permitting model shows the Antarctic circumpolar current to be less sensitive to windstress, indicating eddies in the Southern Ocean to have a stabilising effect. Numerical modelling requires substantial computational resources to simulate at the fine resolution needed to capture the dynamics of eddies in general, leaving predictions about their importance to future climate change uncertain (Hewitt et al., 2017).

### 6.2.8 Haline dominance

Density of sea water is determined by its temperature and its salinity, with a higher temperature resulting in a lower density, and higher salinity resulting in a higher density; increases in these two state variables therefore have opposite effects on density. The thermo-haline circulation is an abstracted part of the overturning which is thought of as driven by the formation of deep water (in the North Atlantic) where sea water is cooled

to the atmosphere during winter and the water density increases. As shown by Gregory et al. (2005), climate models have AMOC declines mainly driven by a reduction in high-latitude heat loss due to changes in surface thermal flux and not changes in surface freshwater flux (sea ice and evaporation-precipitation). This was also noted in Weaver et al. (2012) when studying AMOC changes in the CMIP5 ensemble under RCP8.5 forcing. A decline in AMOC might therefore not be directly causally related to changes in any freshwater variable, at least not solely. With the SPG regions further south than the Nordic Seas, it is suggestive that this mainly applies to the Labrador and Irminger Seas though. The influence of temperature is bounded because at freezing conditions no further density increase will take place by lower temperatures. It is for this reason that the Nordic Seas are less affected by thermal anomalies, as these can more easily be lost to the atmosphere due to the permanently freezing conditions and deep convection variation is determined by salinity variation (Rudels and Quadfasel, 1991).

Further south in the Labrador and Irminger Seas, only winter time is sufficiently cold to foster deep convection. Sea ice can shield the ocean from the atmosphere and a retreat of sea ice can expose more of the ocean surface and influence the deep water formation (Weijer et al., 2020). Should all Arctic sea ice disappear, this factor is no longer an influence. (See also Van der Linden et al., 2019, where changes in sea ice cover are shown to be important in modulating surface heat fluxes and mediating the effects of wind stresses on ocean currents.) Although changes in atmospheric temperatures can affect deep water formation, the SPG is only affected indirectly and internal variability is the main contributor to recent changes (Terray, 2012). This leaves freshwater as the dominant driver of AMOC stability if thermal changes are transient, and are quickly effaced through interactions with the atmosphere, whereas freshwater forcing lingers. An increasing atmospheric forcing means there is an increase in surface temperature that leads to an AMOC decline. Even though the thermal effect is largest in the initial AMOC decline, only changes in (local) salinity are part of a potential positive feedback mechanism. The changes in salinity take longer to consolidate, but could bring about an AMOC collapse after the thermal effects have weakened it.

Without a (thermal) forcing, the ocean is in a steady-state, but is represented differently in different climate models. Also under such conditions, freshwater variables can have different values in different climate models, as shown in the next section.

## 6.3 Steady-state AMOC stability

For sufficiently slow changes, the Atlantic overturning can be seen as in a steady-state. Although there is constant dynamical interaction and freshwater exchanges with the rest of the ocean and the atmosphere, there does not have to be long-term change away from a stable condition. The section-integrated volume changes, and salinity changes, between the Agulhas section and the latitude of the AMOC maximum can only be affected by changes the surface freshwater flux because the atmosphere is the only interface (ignor-

ing vertical fluxes, internal to the ocean). The AMOC streamfunction can be affected by (thermo-)haline circulation changes that change the velocity field. This means that changes to the evaporation over the Atlantic can have a direct impact on the AMOC, provided these changes are not re-routed at the surface. For instance, it is conceivable that the gyres circulation's salinity change is due to a change in $M_{\mathrm{E-P}}$, and is flushed out through Bering Strait or back to the South Atlantic gyre ($M_{\mathrm{az}}$) at the latitude of Cape Agulhas, leaving the overturning circulation (relatively) unaffected (see Cimatoribus et al., 2012). If a change in the freshwater budget is introduced, the Atlantic will adjust on advective timescales to restore the balance (unless the rest of the world ocean also undergoes a persistent change to compensate).

### 6.3.1 Evaporation differences under steady-state conditions

Different models show different behaviour to maintain the freshwater balance. In particular, there appears to be a bias in $M_{\mathrm{ov}}$ (Drijfhout et al., 2011). As seen in Figure 6.3, $M_{\mathrm{E-P}}$ varies within the CMIP5 ensemble and Figure 6.4 there appears to be a compensation between $M_{\mathrm{E-P}}$ and $M_{\mathrm{ov}}$. By accounting for this compensation in the South Atlantic, the deviation between the observed value and the models, as well as the variation within the model ensemble, might be eliminated, We should then be able to unify the freshwater import to the high Atlantic latitudes in CMIP5 models in a single equation.

Assuming that a change in the evaporation leads to a proportional change in $M_{\mathrm{ov}}$ (all models simulate the same climate during the historic period (pre 2000) just with a different evaporative bias),

$$\overline{M}_{\mathrm{ov}} = (1 - c) \times \overline{M}_{\mathrm{E-P}} + M_0, \tag{6.3}$$

with $M_0$ a constant during steady-state (the value of $\overline{M}_{\mathrm{ov}}$ if $\overline{M}_{\mathrm{E-P}} = 0$); the overbar indicates the time-average. The coefficient $c$ measures the fraction of the evaporated freshwater returning to the Southern boundary. The Atlantic is effectively too fresh where $M_{\mathrm{ov}}$ is measured due to the different balance in E-P out of the Atlantic, resulting in a bias. Then,

$$\overline{M}_{\mathrm{E-P}} = \frac{1}{1 - c} \overline{M}_{\mathrm{ov}} + M_0, \tag{6.4}$$

which can be fit (Figure 6.4) with $c = -1.0$ and $M_0 = 0.38$ Sv. An ARGO float estimate of $M_{\mathrm{ov}} = -0.11$ Sv (Garzoli et al., 2013) indicates that $\overline{M}_{\mathrm{E-P}} = 0.32$ Sv of net evaporation of the Atlantic. This value is comparable to the reanalysis net evaporation estimate of $0.33 \pm 0.04$ Sv given by Valdivieso et al. (2014) for the Atlantic and Arctic. The freshwater estimate given in Talley (2008), however, indicate a negligible value for $M_{\mathrm{ov}}$ and a net evaporation of $0.28 \pm 0.04$ Sv north of 32°S for the Atlantic and Arctic. Offsetting $\overline{M}_{\mathrm{E-P}}$ to the observed value should put all models on equal footing under steady-state conditions. How to apply this correction to the CMIP5 models is shown next.

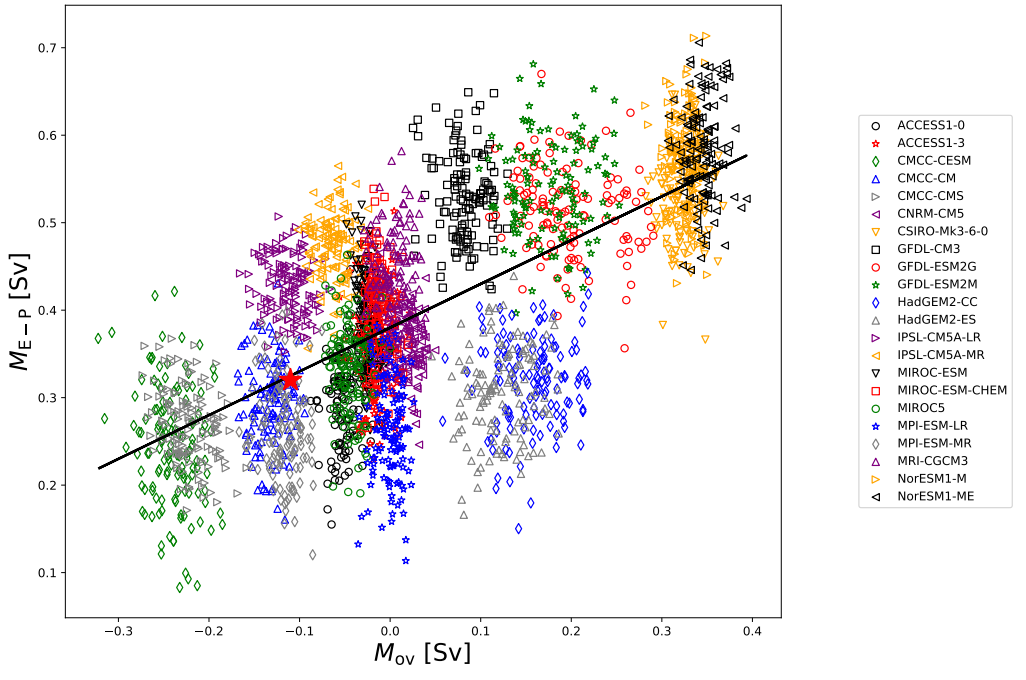


Figure 6.4: Annual historic values (pre 2000) of $M_{\mathrm{E-P}}$ versus $M_{\mathrm{ov}}$ for the indicated CMIP5 models. Black fitted line is $M_{\mathrm{E-P}} = 0.50 \times M_{\mathrm{ov}} + 0.38$ Sv. The red star indicates the observational value (-0.11, 0.32) Sv by Garzoli et al. (2013).

### 6.3.2 Agulhas $M_{\mathrm{ov}}$ correction

This relation between the Atlantic evaporation difference and the difference in $M_{\mathrm{ov}}$ values indicates a variation in how the two freshwater variables balance in the CMIP5 models. The evaporation that takes place between the Agulhas section and where the AMOC reaches a maximum can be a correction on $M_{\mathrm{ov}}$ at the latitude of Cape Agulhas. The evaporation introduces a bias between the basin boundary at Cape Agulhas and the relevant region of deep water formation. A bias-corrected version of $M_{\mathrm{ov}}$ (using the fit value $c = -1.0$ ) is

$$\overline{M}^{*}_{\mathrm{ov}} = \overline{M}_{\mathrm{ov}} - 2.0 \times \overline{M}_{\mathrm{E-P}}. \tag{6.5}$$

Typically, $\overline{M}^{*}_{\mathrm{ov}} < \overline{M}_{\mathrm{ov}}$ for CMIP5 models ($M_{\mathrm{ov}}$ time series are as used in Mecking et al., 2017), but all might be a different 'distance' away from an AMOC collapse in terms of forcing. Assuming steady-state, there is no thermal forcing with a trend and all variation between models must be due to freshwater differences.

A higher rate of evaporation in the South Atlantic corresponds to a larger $M_{\mathrm{ov}}$. This might be because $M_{\mathrm{ov}}$ registers too much freshwater in the shallow layers of the overturning going north when compared to observations. Figure 6.6 indicates that the salinity

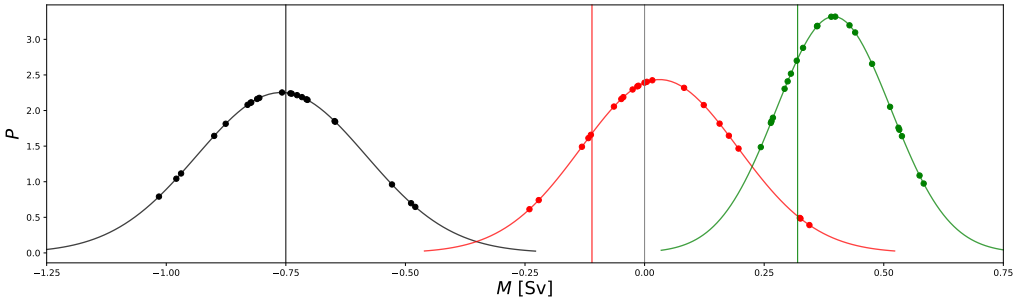


Figure 6.5: Fitted distribution of historic (pre 2000) values of $\overline{M}^{*}_{\mathrm{ov}}$ (black line), $\overline{M}_{\mathrm{ov}}$ (red line), $\overline{M}_{\mathrm{E-P}}$ (green line), according to Eq. 6.5 (all supposed to be normally distributed). Vertical line placed at $M = 0$ (models from the red distribution to the left are supposedly bistable, to the right, mono-stable). Coloured lines indicate observed values of corresponding quantity. All bias-corrected $\overline{M}_{\mathrm{ov}}$ (i.e. $\overline{M}^{*}_{\mathrm{ov}}$) are negative, indicating the AMOC to be bistable in all models in the ensemble.

field in the EN4 reanalysis differs from EC-Earth (top-right panel in Figure 6.2) where the observations indicate saltier top layers compared to the EC-Earth simulation. The evaporation in the South Atlantic removes that excess, assuming no other effects take place in that region. The value of $\overline{M}^{*}_{\mathrm{ov}}$ is negative for all CMIP5 models, and in that sense all models simulate the 'same' AMOC. If this quantity is taken as a stability indicator, with the same interpretation as $M_{\mathrm{ov}}$, all are in a bistable regime.

After correcting for an exchange between the $M_{\mathrm{ov}}$ and $M_{\mathrm{E-P}}$, different models might still behave differently under sustained forcing. The next section examines the effect of the RCP8.5 forcing scenario in the CMIP5 ensemble, and a fit is made to the Langevin model from Chapter 5.

## 6.4 Transient AMOC response under climate forcing

The response of the ocean on advective timescales allows for an equilibration between the evaporation and the freshwater field at Cape Agulhas and takes place under slow forcing changes. Forcing by human activity (mainly $CO_2$), however, takes place on timescales two orders of magnitude shorter (see Chapter 1), rapidly pushing the climate out of equilibrium. The RCP8.5 scenario results in significant warming of the atmosphere and a reduction in AMOC strength during 2005 - 2100 (Intergovernmental Panel on Climate Change, 2014b).

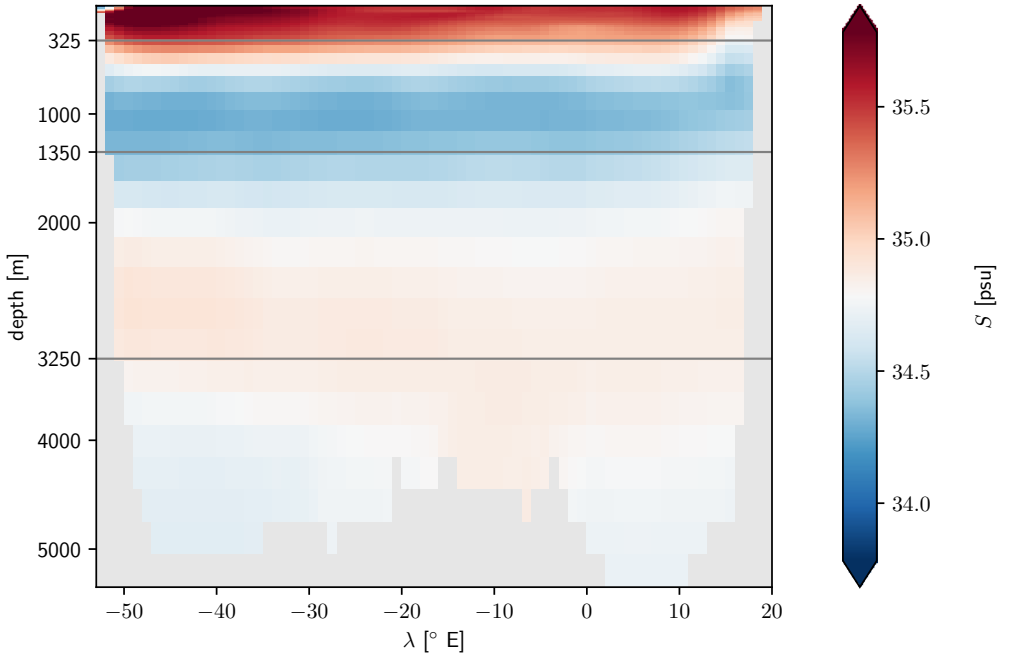


Figure 6.6: Salinity along the Agulhas section (34°S, mean of the twentieth century EN4 reanalysis; Good et al. (2013) and Gouretski and Reseghetti (2010), centred on the section average. Grey lines are the same as in Figure 6.2.

### 6.4.1 AMOC stability during the 21st century

A sustained collapse of the AMOC is not seen in the selected CMIP5 climate models (those listed in Figures 6.3 and 6.4 and included in Weaver et al., 2012), but is seen in models comparable to the Rahmstorf et al. (2005) set on similar long integration times (Hawkins et al., 2011; Bakker et al., 2016). The main difference is not the difference in level complexity between the EMICs and the CMIP5 models, but the type of experiment. In Rahmstorf et al., 2005 a constant freshwater forcing was applied for each measurement point and the models were allowed to equilibrate, while the CMIP5 ensemble uses a prescribed forcing in accordance with the RCP8.5 emission scenario during the 21st century. The lack of a collapse such as seen with the Rahmstorf et al. (2005) EMIC ensemble (Chapter 5) might relate to the time frame at which the ocean has been observed. Another important difference is that the RCP8.5 emission scenario only prescribes greenhouse gases and not a freshwater forcing. In Chapters 3 and 4 this deficiency has been addressed by the freshwater protocol from Chapter 2, but had little impact on AMOC strength. A realistic amount of (Greenland) melt might not critically affect AMOC stability this century. Should the forcing of the atmosphere stabilise, and the ocean is left

to equilibrate, an AMOC collapse might be brought about on a longer timescale, similar to those suggested by the paleo records (Barker and Knorr, 2016).

As shown by Jackson et al. (2013), the internal salt distribution within the North Atlantic changes in the CMIP5 ensemble: a build up of salinity in the subtropical Atlantic under high $CO_2$ levels leads to an AMOC recovery under reduced $CO_2$ stronger than under pre-industrial conditions. The salt build up is the result of an intensification of the hydrological cycle: increased evaporation in the subtropics and increased precipitation in the high latitudes. The subtropical salt build up, indicating a lagged response of the ocean to the atmospheric forcing, can play a role in AMOC recovery and therefore also in stabilisation. Heuzé (2017) showed that the CMIP5 ensemble displays a variety of deep water production characteristics (see also Mecking et al., 2017, for a treatment of salinity and velocity biases). In particular, the location and intensity is not in agreement with observations for the majority of models. Also, changes in freshwater to the convection areas do not seem to produce an accurate response in deep water formation and AMOC stability. This raises the question to what extent the different AMOC representations seen in these models are representative of reality. Even if a steady-state AMOC is modelled well, its response under forcing need not be. It is therefore not clear what an accurate AMOC representation is given the disagreement between models and their (collective) disagreement with reality.

Changes within the 21$^{st}$ century are short relative to the equilibration timescale of the AMOC and an ongoing forcing of both the atmosphere and the ocean will leave the ocean out of equilibrium for the foreseeable future. A collapse of the AMOC on timescales longer than the equilibration time can be connected to integral freshwater variables, as seen in Rahmstorf et al. (2005) and Hawkins et al. (2011). The behaviour on shorter timescales varies between models and is therefore not clear.

### 6.4.2 Transient forcing and the Langevin model

The models in the selected CMIP5 ensemble show strongly decreasing AMOC time series, but no collapse. The Langevin model can, however, be fitted to this set with some assumptions. The increase in surface freshwater forcing in the Arctic and SPG is the closest analogue to $\mu$ (the freshwater forcing variable used to drive the Langevin model) available in the CMIP5 ensemble runs. The maximal freshwater forcing distance between the two freshwater forcing bifurcation points ($\mu_{\pm}$) is when at 2000 $\mu_{-} = 0$, and if the prior on $\mu_{+}$ is widened to 0.4 Sv (in agreement with Figure 2(A) in Hawkins et al., 2011). Their AMOC hysteresis shows a wider loop in terms of freshwater forcing. Hawkins et al. (2011) also note that the apparent hysteresis could be an artefact of the rate at which the freshwater forcing in their simulation changes, and changes sufficiently slow leave a much narrower width on the hysteresis loop of 0.07 Sv.

To obtain a single timeseries, the CMIP5 AMOC($\mu$) series are first shifted to the ensemble mean value (pre 2000). A genetic algorithm (see e.g. Mitchell, 1996 for an introduction) which optimises the sum of the log-likelihood of the differences between a

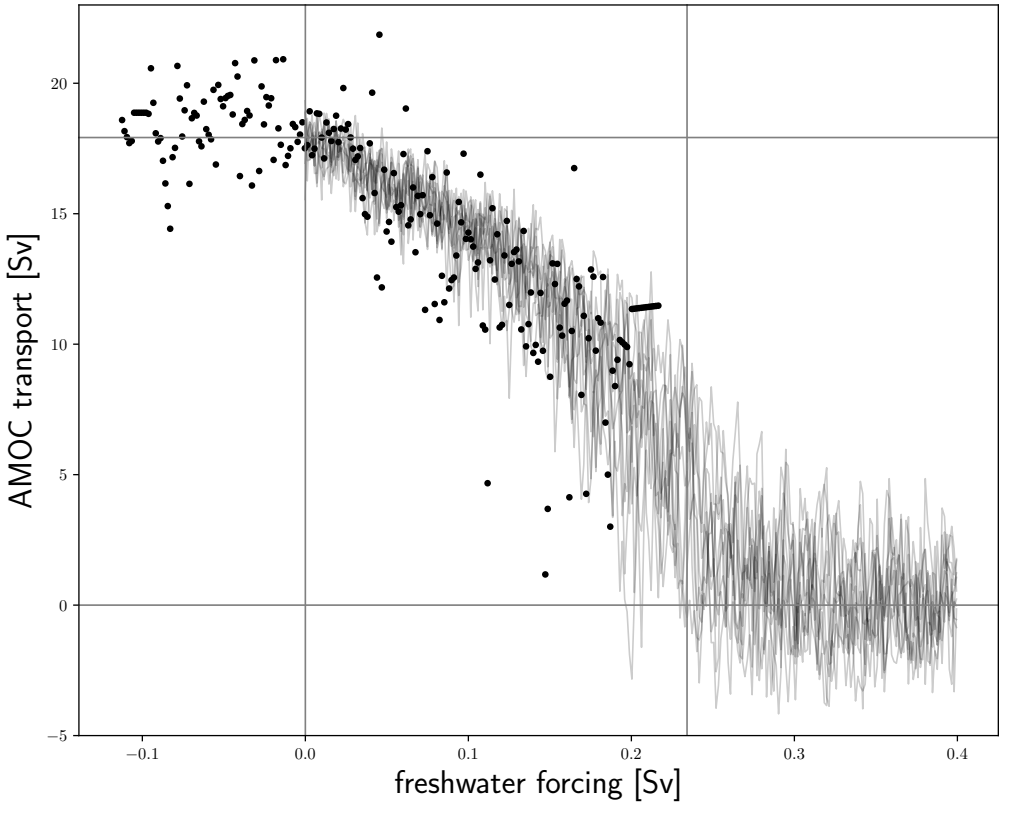


Figure 6.7: Shifted AMOC transport versus the freshwater forcing into the ocean surface north of the North Atlantic subtropical gyre at 47°N (black dots), and set of 10 realisations of a fitted Langevin model: $\nu = 11.6$, $\lambda = 3.43$, $\beta_0 = 1.32$, $\delta\beta = -5.61$, $\mu_- = 0$, $\mu_+ = 0.234$. Grey vertical lines at $\mu\pm$; horizontal lines at AMOC = 0 and AMOC= initial value (at 0 Sv).

candidate solution (see Chapter 5 for the same measure to be minimised) and the CMIP5 data points is then used to find a solution that matches the CMIP5 ensemble values to a Langevin model[2]. The Langevin model can be solved by numerical integration of its stochastic differential equation (Kasdin, 1995), which yields AMOC collapse series as realisations of the Langevin model as a stochastic process. The averaged set (dots) and 10 realisations (grey lines) are shown in Figure 6.7. To constrain the fit, a lower branch is placed at 0 Sv for $\mu > 0.4$ Sv. Note that linear extrapolation of the CMIP5 measurements already shows that the Langevin model requires a collapse at $\mu_+ < 0.4$ Sv. The AMOC

[2]Genetic algorithms are useful for when the solution landscape contains 'gaps' with inadmissible solutions, and therefore good for exploratory search, but they do not give a posterior distribution like the Markov chain approach in Chapter 5, nor do they provide an indication of solution convergence (i.e. when a non-local optimal solution has been found).

decline in the CMIP5 ensemble is also much steeper than seen in Hawkins et al. (2011) or Rahmstorf et al. (2005). Also note ensemble variation indicates some structural variance and perhaps individual models should be fit instead to find better agreement (i.e. not shifting individual time series to obtain an ensemble mean).

The time-evolution of the weakening and, possible, collapse of the AMOC as a result of climate change therefore cannot be modelled solely as a function of surface freshwater forcing. The transient forcing keeps the ocean out of equilibrium; the results of Hawkins et al. (2011) and the CMIP5 ensemble behaviour suggests that an AMOC collapse might be staved off because no new equilibrium can be reached. The AMOC might show a delayed response to elevated $CO_2$ levels, as indicated by Liu et al. (2017) where the AMOC did not collapse until 300 years after a $CO_2$ doubling. Alternatively, a transition to an AMOC off state can occur before a critical threshold, even for a moderate freshwater forcing, if applied fast enough (Lohmann and Ditlevsen, 2021). A prediction of an AMOC collapse therefore remains difficult, even if the driving freshwater forcing variables can be identified and quantified.

## 6.5 Summary and discussion

Temperature and salinity variations at the high latitude deep water formation regions, and windstress within the Atlantic and the Southern Ocean affect the Atlantic overturning (see also Chapter 1). The main driver of the AMOC might be the formation of deep water in the Atlantic high latitudes, and is at risk of shutting down abruptly due to the salt-advection feedback mechanism postulated by Stommel (1961). The salt-advection mechanism appears to have played a role in past shutdowns, but climate simulations of future climate change, such as the extended runs in CMIP5 (Weaver et al., 2012), indicate otherwise. AMOC decline as a function of the SPG-Arctic freshwater forcing is steeper in CMIP5 models than found in Chapter 5 (approximately five times larger), indicating other effects are important, and the salt-advection feedback might not be dominant on transient timescales (centennial).

There are two possible reasons for this discrepancy. First, the Stommel conceptual model might not appropriate and the Atlantic circulation does not have a salt-advection feedback mechanism where a weaker overturning leads to a buoyancy loss in the Atlantic high latitudes, subsequently leading to an even weaker AMOC; in which case, past AMOC shutdowns must have come about under different conditions, or by another mechanism. Second, climate models might not simulate the future state of the ocean well enough. Differences between models certainly exist, and their projections of the AMOC varies. Specifically, there appears to be a bias relating to the evaporation over the Atlantic and $M_{\text{ov}}$ at 34°S. Accounting for this bias does make the models more alike in their past behaviour, but other differences between the models might still be important for their transient behaviour.

The Stommel conceptual model ignores basin geometry and most ocean physics. As discussed in Section 6.2, this might be an oversimplification with respect to a possible AMOC collapse. Specifically, the freshwater routing within the ocean might counteract the effects of freshwater applied to the ocean surface and wind-driven gyre interactions can redistribute freshwater and salt. The salt-advection mechanism that is instrumental for an AMOC collapse might deviate from the direct coupling supposed by the Stommel model. Below, the assumptions discussed in Section 6.2 are summarised (indicated in brackets).

Reduced heat loss to the atmosphere affects buoyancy loss primarily in the SPG, but freshwater is more important to the Nordic Seas ('haline dominance'). A retreat of sea ice and an increase in precipitation at the high latitudes constitutes a freshwater forcing, but might not be effective due to the gyre dynamics ('advective equilibration'). A weakening of the SPG increases the deep water formation in the Nordic Seas in EC-Earth (Chapter 4) indicating a compensating mechanism due to gyre interaction. The reduction in deep water formation might, however, be mainly driven by reduced heat loss in the SPG region. The deep water formation in the SPG varies greatly among climate models (Heuzé, 2017) and there is no consensus about location, intensity, and future response to a warming atmosphere. These differences lead to uncertainty between models, and widely different projections of deep water formation and AMOC decline.

The decline of the AMOC as a function of North Atlantic surface freshwater changes seen in the CMIP5 ensemble is markedly stronger than in the freshwater-forced equilibrated experiments in Chapter 5. A collapse of the AMOC due to melting ice sheets is a real possibility, but only if the resultant meltwater can reach the deep water formation regions ('weak locality'), which might only take place on timescales longer than a century. Additionally, Atlantic freshwater import can be part of a feedback mechanism on the South Atlantic-Southern Ocean interface ('single baroclinic freshwater coupling') , but other freshwater variables, such as Bering Strait transport, can be important (Bering Strait transport can partially compensate as shown in Chapters 3 and 4). Not only does a weakening AMOC change the value of $M_{\mathrm{ov}}$, but concomitant changes in windstress also influence the Atlantic freshwater balance ('external insignificance'). A wind-driven inflow into the South Atlantic should, however, persist regardless of the state of the AMOC. Also, changes in the windstress in the North Atlantic can affect the subpolar gyre/Nordic Seas deep water formation (see Chapter 4). The Atlantic freshwater budget and AMOC might therefore be affected by different (interacting) variables that result in a loss of overturning strength and the Atlantic freshwater balance.

The simplest quantitative description of an AMOC collapse is one-dimensional, with the AMOC driven by a single free variable. In Chapter 5 the Langevin equation forms the basis for such a description, where changes in the AMOC are due to a surface freshwater forcing only. The Langevin model has two parameters ($\alpha$ and $\beta$) that describe how the AMOC is positioned relative to its two stable branches, as well a scaling and offset parameter ($\lambda$ and $\nu$) to de-dimensionalise the formulation. To reduce the dimensionality of the model to one, a linear relation between $\alpha$ and $\beta$ was assumed, both parameters being

functions of the freshwater forcing. The Langevin model agrees with the Stommel conceptual model, but not with the projections of CMIP5 models (as shown in Section 6.4) under the assumption that only freshwater changes in the North Atlantic subpolar gyre region and Arctic drive the AMOC changes. The AMOC is projected to collapse too soon, compared to the weakening, but stable AMOC, projected by CMIP5 models. It might be possible to extend the Langevin model to also match the time-evolution of the AMOC under less stringent assumptions than those made in Chapter 5.

We can speculate that the parameter $\alpha$ might relate to high latitude buoyancy loss due to thermal effects, as a change in $\alpha$ will not push the AMOC to a critical transition, and can be interpreted as the lack of the salt-advection feedback. Changes in $\beta$, however, can lead to a critical transition and might be better suited to relate to buoyancy loss due to freshwater changes. Another possibility is that both $\alpha$ and $\beta$ relate to essentially the same process of high latitude buoyancy loss, but represent different routes through which local salinity is impacted; specifically, the surface forcing versus the advected freshwater or salt by means of the gyres and overturning (these would relate to $M_{\mathrm{az}}$ and $M_{\mathrm{ov}}$). The parameters $\lambda$ and $\nu$ are constant in Chapter 5, but, in principle, they could depend on time and possibly also be related to thermal changes; in which case, the AMOC could decline steadily without an accelerated loss of stability. The AMOC decline in Figure 6.7 likely cannot be expressed as a function of a single freshwater variable and some stabilisation takes place to allow the AMOC to weaken, but not collapse under the RCP8.5 emission scenario. Also, other emission scenarios might affect the AMOC and the freshwater variables differently. In which case, the AMOC might decline less steeply, but become more unstable as the forcing progresses.

In summary, the Langevin model requires a revision for it to be applicable to time-dependent, RCP8.5-forced AMOC weakening, as opposed to equilibrated and surface freshwater-forced AMOC collapse trajectories for which it was originally developed. Model-dependent conditions within the Atlantic might be important to adequately model weakening, and possible collapse, of the AMOC time series in climate model projections. Time series of integral freshwater variables, such as changes in Atlantic evaporation and precipitation, might be key drivers, but which variables are sufficient to accurately model AMOC stability remains uncertain.

## Acknowledgements

Thanks go out to Wilco Hazeleger and Sybren Drijfhout for helpful comments, suggestions, and corrections that have improved this chapter.

# 7 Synthesis

For over a century and a half emissions of $CO_2$ due to the burning of fossil fuels have increased. Although the immediate effects on the atmosphere can be measured, effects that take place on longer timescales are much more difficult to track. The ocean is arguably the most important part because its much larger heat capacity compared to the atmosphere, due to its interaction with the atmosphere and the cryosphere.

As shown in the previous chapters, the ocean responds in a varied way to melting ice sheets. Ocean currents and salinity distributions are affected, and non-linear changes can take place. It is the non-linearity that makes prediction of the future so difficult. Not only is it necessary to resort to scenario-based modelling (Chapter 2) with its inherent uncertainties, but the resultant numerical projections are tentative at best.

This chapter summarises the relevant points from the previous chapters, followed by a critique and research outlook.

## 7.1 Ice sheet melt and ocean adjustment

In Chapter 2 a method to introduce a freshwater forcing to the top of the ocean that mimics ice loss from the polar ice sheets in coupled climate models was described. Processes that increase mass loss from glacier retreat are explicitly projected into the future (up to the year 2100) along a set of storylines that make up a scenario of future melt and mass loss through iceberg calving. The introduction of an iceberg pattern allows for more distant effects of freshwater to affect the ocean, away from the source ice sheets. Preliminary additional results indicate that the Atlantic overturning circulation is only mildly affected by the freshwater.

Chapters 3 and 4 use the forcing approach and analyse an ensemble of simulations in a so called ramp-up/ramp-down experiment. The ramp-up phase is the same as in Chapter 2, and the ramp-down extends the forcing time series (the freshwater scenario and the RCP8.5 greenhouse gases emission scenario) by mirroring about the year 2100. The reason for doing so is that lagged effects in the ocean become more noticeable and the short-term effects (largely) cancel.

Chapter 3 shows that the added freshwater dilutes the entire ocean by increasing total volume. In the Atlantic, the initial dilution mainly comes from Greenland freshwater,

but the increase in mass is counteracted by the mass flux across the boundaries of the Atlantic, with the outflow from the South Atlantic into the Southern Ocean becoming larger than the inflow through Bering Strait. The combined effect is an export of salt from the Arctic and Atlantic Ocean to the Southern Ocean. The overturning circulation increases freshwater import into the South Atlantic, while the South Atlantic subtropical gyre exports salt and imports freshwater. The arrival of freshwater from Antarctica results in an increase of the gyre contribution. Individual runs where the northern and southern hemisphere freshwater forcing field were separated indicate that the freshening of the Atlantic due to freshwater coming from Greenland is partially counteracted by the Antarctic mass loss, and which affects the sea surface height gradient across Bering Strait. Also, the Greenland mass loss has a barotropic effect, while the Antarctic mass loss mainly affects the overturning. This is intuitive because freshwater applied to the ocean surface is advected by shallow and surface currents and introduces a baroclinic effect at a distance, but there is an (immediate) barotropic effect by changing the sea surface height locally with the addition of more water.

Chapter 4 delved more deeply in the adjustment processes within the Arctic and Atlantic Oceans and gives an explanation for the limited AMOC weakening seen previously. The strongest circulation change occurs in the western North Atlantic subpolar gyre and in the Nordic Seas where a decrease in the subpolar gyre and an increase in the Nordic Seas is intimately connected. Associated with these counteracting changes in both circulation systems, the AMOC change is relatively weak compared to the North Atlantic subpolar gyre strength decrease. The deep water formation due to convection in the North Atlantic's Labrador and Irminger Seas reduces during the experiment, but is enhanced in the Nordic seas in the Arctic, resulting in little additional weakening of the AMOC as it is fed by both regions (the overflow across the Iceland-Scotland ridge connects the Nordic Seas deep water to the NADW). A feedback between the ocean sea surface temperatures and the westerly winds is an important mechanism in this shift. The Greenland mass loss introduces a freshwater anomaly to the subpolar gyre, weakening the gyre circulation strength. The weakened subpolar gyre shifts to the west, allowing the subtropical gyre to the south to expand. This gyre rearrangement allows the North Atlantic Current to bring water to the Nordic Seas that would otherwise have been transported to the subpolar gyre. Consequently, the sea surface temperature in the Nordic Seas increases, but decreases in the Labrador and Irminger Seas. This means the gradient of the sea surface temperatures has changed, which enhances the westerly winds. The winds, in turn, enhance the gyre strength in the Nordic Seas. Although the Greenland mass loss is the instigator of an initial gyre adjustment, a coupled sea surface/winds stress response enhances the effect, allowing for a sustained compensation of the deep water formation that inhibits a further AMOC strength decrease which would otherwise have occurred if the Labrador and Irminger Seas region were the only source of deep water.

Chapters 3 and 4 showed that polar ice sheet melt does not merely dilute the ocean and hamper deep convection, but that adjustments take place on both the boundary of the Atlantic and its interior. A complicated picture of internal feedbacks and changes in

salt distribution indicates that the AMOC response is not a simple, direct relation to the amount of ice sheet melt that takes place (on top of the RCP8.5 emission scenario).

Chapter 5 studied the collapse characteristics of the AMOC seen in an older generation of climate models (EMICs). These models are simpler but are less computationally demanding, which allowed the a large ensemble by Rahmstorf et al. (2005) to be simulated. A range of freshwater forcing values was applied to the North Atlantic subtropical region and for each value, each model was run to a quasi-equilibrium state. At a model-specific forcing value (0.1 – 0.2 Sv) a rapid change as a function of the forcing value is seen. Additionally, reducing the forcing again from these collapsed states and running these model to a new equilibrium state shows a dependence on the history with the AMOC remaining in a collapsed state, even at negative forcing values. In other words, the AMOC state, as a function of freshwater, shows hysteresis.

Two scaling parameters, two critical points for the freshwater forcing, and two stability parameters (to describe a linear change) are sufficient to fit a stochastic process based in the Langevin equation to the hysteresis loops. The Langevin equation is used to model the salt-advection feedback that had been proposed (Stommel, 1961; Rahmstorf, 1996) as the mechanism that could be responsible for AMOC bistability. The conceptual picture of a potential function with two 'wells' can then be turned into a quantitative description which describes the state of the AMOC as a function of a persistent freshwater forcing. This description does not help to predict an AMOC collapse from climate models because the timescale in which the ocean adjusts is not clear (the equilibration time). Also, the freshwater variable that would the direct cause of the AMOC decline is not known.

## 7.2 Critique

Research related to climate change does not have the luxury of time and is for this reason rather unfortunate compared to other modern science. Earth, and in particular the ocean, is a complicated system to model where the difference of scale between relevant processes hinders a complete description. Large-scale structures such as the AMOC and the wind-driven gyres can be recovered in simulations, but not necessarily through the right underlying mechanisms. Whether deep water formation is mainly in the SPG interior or in the boundary currents (e.g. Katsman et al., 2018) is a case in point. Increasing model resolution might alleviate some of these problems (see Hirschi et al., 2020). In line with increased resolution, an adaptive resolution where the modelling grid undergoes subdivision and fusion of gridcells where needed (called adaptive mesh refinement, see e.g. Blayo and Debreu, 1999) might prove advantageous by putting computational power where it is needed most.

A more fundamental problem is the lack of modelling of some physical processes altogether. The absence of ice sheet modelling is an obvious defect which ignores the most important interactions with the cryosphere and cannot be addressed by mimicking

its effects on the ocean like the approach in Chapter 2 because feedbacks are ignored and the reliance on scenarios is limiting.

Climate change in recent history has been gradual, and has not seen abrupt changes (like a declining AMOC on its upper stable branch). Early climate models have been fairly successful at projecting the warming seen today, even though they were far less sophisticated than modern models (e.g. Sawyer, 1972; Hansen et al., 1988). The ocean's thermal inertia has so far suppressed effects of recent climate change, but might become the dominant driver of future climate change. Because over 90% of excess energy due to human activity has been taken up by the ocean (Von Schuckmann et al., 2020), proper modelling of how the ocean stores that heat, and the limits to its capacity to do so, is needed. The true test of climate simulation would come when abrupt changes, such as a possible AMOC collapse, are seen in reality; it is under such circumstances that the steady changes seen so far—that have been modelled well—radically change. It is possible that the drivers of abrupt changes (non-linear dynamics) are not relevant to project gradual climate change, but are dominant for feedbacks that determine future change away from the current quasi-steady regime. In essence this is what the Langevin model shows: one well in the potential function are dominant under low forcing values and the other well becomes dominant when reaching a critical transition, even effacing the original quasi-steady state. In other words, the previously subordinate effects of little importance become leading in determining the behaviour from that point on. The steady changes can be modelled accurately under the steady regime by ignoring subordinate effects, but breaks down when these effect become dominant drivers. This might be relevant for other climate tipping elements as well (see also Valdes, 2011, on uncertainty about modelling future, forced climate behaviour).

With climate models' increasing complexity, the subordinate drivers should also be modelled, either by explicit inclusion (e.g. coupling an ice sheet module), or implicitly by increased resolution or secondary effects of another phenomenon. The trade-off, however, is that increased complexity also means an increase in parameter space, which leads to greater structural uncertainty. As shown by Mecking et al. (2016), increasing resolution of an ocean model (0.25° horizontal) allows for better representation of mesoscale eddies, which counterbalance a salt transport seen in a lower resolution counterpart. The AMOC collapses in this model and remains in a stable off state for 450 years, but without a reverse overturning cell as previously found by Stouffer and Manabe (2003) or the southward shift of the ITCZ typically seen in lower resolution models (Zhang and Delworth, 2005). Both the eddy effects and the absence of a reverse THC cell are arguably a better representation, directly related to higher resolution. There is a risk of counteracting effects that show apparent agreement at a larger scale when comparing simulation to observation. The diverse representation of deep water formation in the North Atlantic in CMIP5 models (Heuzé, 2017) is an example of this. The AMOC in climate models arguable agrees well with reality, but the driving processes and their geometry, perhaps, do not. The possibility remains that these mismatches become more salient in the fu-

ture if it turns out they are important for accurate representation away from the current (somewhat) stable climate.

A lack of consensus among current simulations exposes a structural uncertainty in climate simulators. It is possible that higher resolution and better representation of subscale processes will lead to convergence, hopefully matching observations. Climate simulations do appear to represent large scale circulations such as the AMOC, but without accurate representation of the causal drivers we cannot confidently claim that the projections into the future are reliable.

Another problem is the lack of causal understanding in the typical experiments done. A hierarchy of models that increase in complexity could provide more insight in the causal structure of the large-scale changes seen and identify which causal relations are persistent from a certain level of complexity upward (or disappear). Related is the need for ensembles of simulations. Though ensembles are now standard, large ensembles that cover most of the variation are needed to find the common responses, and possible bifurcations.

Climate models are defined using many lines of cobbled together computer code, and require substantial computational resources to operate. The evolution of the codebase inevitably leads to add-ons and varying ad hoc approaches and implementations. This leads to obfuscation and also imposes a barrier to further development. Ideally, a hierarchy of models can be generated from a single abstract codebase through parametrisation such as resolution and the inclusion/exclusion of physical effects. (Physics-informed deep learning might be able to replace subgrid-scale heuristics; see e.g. Brajard et al. (2021) and Kashinath et al. (2021).) Resources are always limited, and time to develop and run climate models is scarce, as are the financial means to construct and maintain the supercomputer clusters needed for the calculations. By designing experiments to explicitly study the effects of structural changes (at a certain level of complexity) causal relations should be easier to identify. This does, however, require a more flexible method of defining climate models and a, possibly substantial, refactoring of existing code.

It might be the case that fundamental risks associated with climate change cannot be assessed before they hit in reality. We might not have the requisite resources or modelling capabilities and capacity to predict an AMOC collapse. What is clear, however, is that changes are ongoing. Theoretical considerations, simulations, and an accumulation of observations (see Chapter 1 for examples) all show changes in the climate compared to our pre-industrial past.

### 7.2.1 Research outlook

Even within the limitations of the experimental set-up of the previous chapters, more work can be done that might prove insightful. In particular, it is not clear what freshwater variable might cause an AMOC collapse. The deep water formation regions undergo freshening due to sea ice melt and increased precipitation, but increased evaporation to the south would increase the salinity of water moving north. A simple model such as in

Chapter 5 does not apply to the transient response seen in the CMIP5 ensemble. Also, freshwater re-routing and salt build up in the lower North Atlantic latitudes can delay the salt-advection (positive) feedback and sustain or restart North Atlantic Deep Water (NADW) formation. Further experiments with more fine-grained control over both might prove useful in separating these effects.

Only one climate model, EC-Earth, was studied in detail. Clearly, using of a variety of models, each with their own characteristics, would be valuable for comparison. Additionally, a more diverse set of scenarios ought to be compared to determine the sensitivity of the results to the choices made.

Extending the Langevin model from Chapter 5 to include a surface forcing and an advective forcing (possibly interpretable in terms of the stability parameters $\alpha$ and $\beta$) might allow for a wider range of AMOC responses to be fitted; this would relax the assumption of a linear parametrisation across the stability landscape. Explicitly modelling the dependence between the SPG deep water formation and the Nordic Seas, though a further increase in complexity, might capture some essential dynamics that allows for severe weakening of the AMOC without inducing a collapse. Whether or not this can be achieved as a formulation in terms of integral freshwater variables remains an open question.

Ongoing observation of the ocean will constrain climate models in the near future. In particular, the RAPID array (Moat et al., 2020b) and the Overturning in the Subpolar North Atlantic Program (OSNAP—Lozier et al., 2017; Li et al., 2017) will help to constrain climate models and future states of the AMOC. Also, observations of deep water formation in the North Atlantic and Nordic Seas should match their representation in climate models. If both the drivers of the AMOC and the development of the AMOC itself in climate models align with what is seen in observations we can be more confident that the projections are accurate. Additionally, observations in the South Atlantic/Southern Ocean would be beneficial. Although observation of the South Atlantic and Southern Ocean does take pace (e.g. the ARGO floats—Roemmich et al., 2009), the continuous measurement of the overturning, like RAPID, is still missing. If the Southern Ocean/South Atlantic interface is important to AMOC stability, monitoring changes in this region will be useful to constrain the AMOC state and its future development.

## Acknowledgements

Thanks go out to Wilco Hazeleger and Sybren Drijfhout for helpful comments, suggestions, and corrections that have improved this chapter.

# Acronyms & initialisms

| | |
|---|---|
| **AABW** | Antarctic Bottom Water |
| **AAIW** | Antarctic Intermediate Water |
| **ACC** | Antarctic Circumpolar Current |
| **AMOC** | Atlantic Meridional Overturning Circulation |
| **ARC** | Agulhas Return Current |
| **CCM** | coupled climate codel |
| **CMIP** | coupled model intercomparison project |
| **DSOW** | Denmark Strait Overflow Water |
| **DWBC** | Deep Western Boundary Current |
| **DWF** | deep water formation |
| **EAIS** | East Antarctic Ice Sheet |
| **ECMWF** | European Centre for Medium Range Weather Forecasting |
| **EMIC** | Earth model of intermediate complexity |
| **EPRI** | evaporation precipitation run-off sea ice |
| **GCM** | general circulation model/global climate model |
| **GHG** | greenhouse gases |
| **GIN** | Greenland-Iceland-Norway Sea (Nordic seas) |
| **IFS** | Integrated Forecast System |

**MOC** Meridional Overturning Circulation

**NAC** North Atlantic Current

**NADW** North Atlantic Deep Water

**NEMO** Nucleus for European Modelling of the Ocean

**NH** Northern Hemisphere

**PSU** practical salinity unit [$g\,kg^{-1}$]

**RCP** representative concentration pathway

**SH** Southern Hemisphere

**SMB** surface mass balance

**SSH** sea surface height

**SST** sea surface temperature

**WAIS** West Antarctic Ice Sheet

# Symbols

| | |
|---|---|
| $P$ | Pressure [kg m$^{-1}$ $s^{-2}$] |
| Å | Ångström [m$^{-10}$] |
| $S$ | salinity [psu] |
| $T$ | temperature [ °C] |
| $U$ | zonal velocity [m s$^{-1}$] |
| $V$ | meridional velocity [m s$^{-1}$] |
| $W$ | vertical velocity [m s$^{-1}$] |
| $\rho$ | density [kg m$^{-3}$] |
| $CO_2$ | carbon dioxide [ppm] |
| Gt | Gigatonne [$10^{12}$ kg] |
| Sv | Sverdrup [$10^6$ m$^3$ $s^{-1}$] |

# Glossary

**Advection**

The transport of some property of a fluid by the motion of the fluid itself; in particular, the (horizontal) transport of salt by the ocean.

**Anomaly**

Difference between effect and control of for instance two simulations.

**Baroclinic**

Velocity field that varies with depth; the baroclinic component of the velocity is the total minus the barotropic component.

**Barotropic**

Velocity field that is uniform with depth.

**Basal melt**

Melting at the base of a glacier.

**Basin**

A body of water that has some depths not in direct contact with the open ocean.

**Convection**

Mass motions within a fluid resulting in transport and mixing of the properties of that fluid.

**Current**

Regular motion in the ocean, cyclic or otherwise steady stream; can be due to density gradients or wind-driven.

**Decoupling**

When interaction between two (physical) quantities ceases.

**Detrainment**

Water exchange from the seasonal pycnocline to the mixed layer above.

**Diapycnal**

At an angle to an isopycnal.

**Eddy**

Closed circulation motion shed by an ocean current–oceanic weather.

**Ekman transport**

Transport that results when the Coriolis force and wind drag forces balance; typically only in the top 100m of the ocean (the Ekman layer).

**Entrainment**

Water exchange from the mixed layer to the seasonal pycnocline below.

**Eustatic sea level rise**

The sea level rise due to the addition of water to the ocean.

**Forcing**

A value external to the model–typically a time series–to either explicitly set a state variable or add to it.

**Geostrophic balance**

Balance between Coriolis force and horizontal pressure-gradient forces. The geostrophic current follow the isobars of the pressure gradient.

**Halocline**

The layer between a fresh and salty layer with a steep salinity gradient.

**Halosteric sea level rise**

The sea level rise due to the expansion of sea water by a change in salinity; a lowering of salinity from current conditions results in a increase of volume by a decrease in density.

**Hövmuller diagram**

longitude versus time diagram of an average or sum over a latitude band.

**Isopycnal**

A constant density surface; also, along an isopycnal.

**Meridional**

Direction parallel to a line of longitude; along a meridian.

**Mixed layer**

Top ocean layer where salinity, temperature, and density are vertically nearly uniform due to turbulent mixing processes; typically 100 m - 20 0m thick, below which the pycnocline begins.

**Model**

Set of mathematical equations, or their definition in computer code, or the numerical simulation that results after computation, all used interchangeably.

**Obduction**

Upward movement of water from the permanent pycnocline to the seasonal pycnocline above; the water then becomes influenced by the atmosphere.

**Section**

2-Dimensional plane from the ocean surface to depth.

**Sill**

Submerged ridge that separates a basin's body of water below the sill depth.

**Subduction**

Downward movement of water from the seasonal pycnocline to the permanent pycnocline below.

**Thermocline**

The layer between a warm and cold layer with a steep temperature gradient.

**Thermosteric sea level rise**

The sea level rise due to the expansion of sea water by a change temperature; an increase in the mean temperature from current conditions results in an expansion of volume by a decrease in density.

**Vorticity**

Local rotation of a fluid parcel; the curl of the velocity vector.

**Water mass**

Body of water with a common origin (e.g. convection in a particular region); can be identified by its ($S$, $T$) characteristics.

**Water mass formation**

Interaction with air-sea fluxes or mixing builds up a body of water with a particular density ($S$, $T$).

**Zonal**

Direction parallel to a line of latitude; i.e. easterly or westerly.

# Bibliography


Aagaard, K. and Carmack, E. C. (1989). "The role of sea ice and other fresh water in the Arctic circulation". In: *Journal of Geophysical Research: Oceans* 94.C10, pp. 14485–14498. ISSN: 2156-2202. DOI: 10.1029/JC094iC10p14485.

Aagaard, K., Weingartner, T. J., Danielson, S. L., Woodgate, R. A., Johnson, G. C., and Whitledge, T. E. (2006). "Some controls on flow and salinity in Bering Strait". In: *Geophysical Research Letters* 33.19. ISSN: 1944-8007. DOI: 10.1029/2006GL026612.

Ackermann, L., Danek, C., Gierz, P., and Lohmann, G. (2020). "AMOC Recovery in a Multicentennial Scenario Using a Coupled Atmosphere-Ocean-Ice Sheet Model". In: *Geophysical Research Letters* 47.16, e2019GL086810.

Alley, R. B., Horgan, H. J., Joughin, I., Cuffey, K. M., Dupont, T. K., Parizek, B. R., Anandakrishnan, S., and Bassis, J. (2008). "A Simple Law for Ice-Shelf Calving". In: *Science* 322.5906, p. 1344. DOI: 10.1126/science.1162543.

Amundson, J. M. and Truffer, M. (Dec. 2010). "A unifying framework for iceberg-calving models". In: *Journal of Glaciology* 56.199, pp. 822–830. DOI: 10.3189/002214310794457173.

Backeberg, B. C., Penven, P., and Rouault, M. (2012). "Impact of intensified Indian Ocean winds on mesoscale variability in the Agulhas system". In: *Nature Climate Change* 2.8, pp. 608–612.

Bakker, P. et al. (2016). "Fate of the Atlantic Meridional Overturning Circulation: Strong decline under continued warming and Greenland melting". In: *Geophysical Research Letters* 43.23.

Bamber, J., Van den Broeke, M., Ettema, J., Lenaerts, J., and Rignot, E. (2012). "Recent large increases in freshwater fluxes from Greenland into the North Atlantic". In: *Geophysical Research Letters* 39.19. ISSN: 1944-8007. DOI: 10.1029/2012GL052552.

Bamber, J. L., Oppenheimer, M., Kopp, R. E., Aspinall, W. P., and Cooke, R. M. (2019). "Ice sheet contributions to future sea-level rise from structured expert judgment". In: *Proceedings of the National Academy of Sciences* 116.23, pp. 11195–11200.

Barker, S. and Knorr, G. (2016). "A paleo-perspective on the AMOC as a tipping element". In: *PAGES Magazine* 24.1, pp. 14–15.

Bartoli, G., Hönisch, B., and Zeebe, R. E. (2011). "Atmospheric CO2 decline during the Pliocene intensification of Northern Hemisphere glaciations". In: *Paleoceanography* 26.4.

Beal, L. M., De Ruijter, W. P., Biastoch, A., Zahn, R., et al. (2011). "On the role of the Agulhas system in ocean circulation and climate". In: *Nature* 472.7344, pp. 429–436.

Beckmann, A. and Goosse, H. (2003). "A parameterization of ice shelf–ocean interaction for climate models". In: *Ocean Modelling* 5.2, pp. 157–170. ISSN: 1463-5003. DOI: 10.1016/S1463-5003(02)00019-7.

Bereiter, B., Eggleston, S., Schmitt, J., Nehrbass-Ahles, C., Stocker, T. F., Fischer, H., Kipfstuhl, S., and Chappellaz, J. (2015). "Revision of the EPICA Dome C CO2 record from 800 to 600 kyr before present". In: *Geophysical Research Letters* 42.2, pp. 542–549.

Berglund, N. and Gentz, B. (2002). "Metastability in simple climate models: pathwise analysis of slowly driven Langevin equations". In: *Stochastics and Dynamics* 2.03, pp. 327–356.

Bernardo, J. and Smith, A. (2009). *Bayesian Theory*. Wiley Series in Probability and Statistics. Wiley. ISBN: 9780470317716.

Biastoch, A., Böning, C. W., Schwarzkopf, F. U., and Lutjeharms, J. (2009). "Increase in Agulhas leakage due to poleward shift of Southern Hemisphere westerlies". In: *Nature* 462.7272, pp. 495–498.

Bigg, G. R., Wadley, M. R., Stevens, D. P., and Johnson, J. A. (1996). "Prediction of iceberg trajectories for the North Atlantic and Arctic oceans". In: *Geophysical Research Letters* 23.24, pp. 3587–3590. ISSN: 1944-8007. DOI: 10.1029/96GL03369.

— (1997). "Modelling the dynamics and thermodynamics of icebergs". In: *Cold Regions Science and Technology* 26.2, pp. 113–135. ISSN: 0165-232X. DOI: 10.1016/S0165-232X(97)00012-8.

Bindoff, N. L. et al. (2007). "Observations: oceanic climate change and sea level". In: *Climate Change 2007: The Physical Science Basis*. Ed. by Solomon, S., Qin, D., Manning, M., Chen, Z., Marquis, M., Averyt, K., Tignor, M., and Miller, H. Cambridge University Press.

Birkhoff, G. and Mac Lane, S. (1970). *A survey of modern algebra*. Macmillan New York, p. 437.

Blayo, E. and Debreu, L. (1999). "Adaptive mesh refinement for finite-difference ocean models: first experiments". In: *Journal of Physical Oceanography* 29.6, pp. 1239–1250.

Boers, N. (2021). "Observation-based early-warning signals for a collapse of the Atlantic Meridional Overturning Circulation". In: *Nature Climate Change* 11.8, pp. 680–688.

Bolstad, W. M. (2010). *Understanding computational Bayesian statistics*. Vol. 644. John Wiley & Sons.

Böning, C. W., Behrens, E., Biastoch, A., Getzlaff, K., and Bamber, J. L. (2016). "Emerging impact of Greenland meltwater on deepwater formation in the North Atlantic Ocean". In: *Nature Geoscience* 9.7, pp. 523–527.

Born, A. and Mignot, J. (2012). "Dynamics of decadal variability in the Atlantic subpolar gyre: a stochastically forced oscillator". In: *Climate dynamics* 39.1-2, pp. 461–474.

Born, A., Stocker, T. F., and Sandø, A. B. (2016). "Transport of salt and freshwater in the Atlantic Subpolar Gyre". In: *Ocean Dynamics* 66.9, pp. 1051–1064.

Born, A. and Stocker, T. F. (Oct. 2013). "Two Stable Equilibria of the Atlantic Subpolar Gyre". In: *J. Phys. Oceanogr.* 44.1, pp. 246–264. DOI: 10.1175/jpo-d-13-073.1.

Boucher, O., Halloran, P. R., Burke, E. J., Doutriaux-Boucher, M., Jones, C. D., Lowe, J., Ringer, M. A., Robertson, E., and Wu, P. (2012). "Reversibility in an Earth System model in response to $CO_2$ concentration changes". In: *Environmental Research Letters* 7.2, p. 024013.

Bouillon, S., Maqueda, M. A. M., Legat, V., and Fichefet, T. (2009). "An elastic–viscous–plastic sea ice model formulated on Arakawa B and C grids". In: *Ocean Modelling* 27.3-4, pp. 174–184.

Boulton, C. A., Allison, L. C., and Lenton, T. M. (2014). "Early warning signals of Atlantic Meridional Overturning Circulation collapse in a fully coupled climate model". In: *Nature communications* 5.1, pp. 1–9.

Bradley, R. S. (1999). *Paleoclimatology: reconstructing climates of the Quaternary*. Elsevier.

Brajard, J., Carrassi, A., Bocquet, M., and Bertino, L. (2021). "Combining data assimilation and machine learning to infer unresolved scale parametrization". In: *Philosophical Transactions of the Royal Society A* 379.2194, p. 20200086.

Brodeau, L. and Koenigk, T. (2016). "Extinction of the northern oceanic deep convection in an ensemble of climate model simulations of the 20th and 21st centuries". In: *Climate Dynamics* 46.9-10, pp. 2863–2882.

Broecker, W. S. (1997). "Thermohaline circulation, the Achilles heel of our climate system: Will man-made CO2 upset the current balance?" In: *Science* 278.5343, pp. 1582–1588.

Broecker, W. S., Bond, G., Klas, M., Bonani, G., and Wolfli, W. (1990). "A salt oscillator in the glacial Atlantic? 1. The concept". In: *Paleoceanography* 5.4, pp. 469–477.

Broecker, W. S., Peteet, D. M., and Rind, D. (1985). "Does the ocean-atmosphere system have more than one stable mode of operation?" In: *Nature* 315.6014, pp. 21–26.

Brook, E. J. and Buizert, C. (2018). "Antarctic and global climate history viewed from ice cores". In: *Nature* 558.7709, pp. 200–208.

Bulgin, C. E., Merchant, C. J., and Ferreira, D. (2020). "Tendencies, variability and persistence of sea surface temperature anomalies". In: *Scientific Reports* 10.1, pp. 1–13.

Caesar, L., Rahmstorf, S., Robinson, A., Feulner, G., and Saba, V. (2018). "Observed fingerprint of a weakening Atlantic Ocean overturning circulation". In: *Nature* 556.7700, pp. 191–196.

Carpenter, B. et al. (2017). "Stan: A Probabilistic Programming Language". In: *Journal of Statistical Software, Articles* 76.1, pp. 1–32. DOI: 10.18637/jss.v076.i01.

Castellana, D., Baars, S., Wubs, F. W., and Dijkstra, H. A. (2019). "transition probabilities of noise-induced transitions of the Atlantic ocean circulation". In: *Scientific Reports* 9.1, pp. 1–7.

Chang, W.-L., Smith, R. B., Wicks, C., Farrell, J. M., and Puskas, C. M. (2007). "Accelerated uplift and magmatic intrusion of the Yellowstone caldera, 2004 to 2006". In: *Science* 318.5852, pp. 952–956.

Church, A. et al. (2013). *Sea Level Change. In: Climate Change 2013: The Physical Science Basis. Contribution of Working Group I to the Fifth Assessment Report of the Intergovernmental Panel on Climate Change*. Cambridge University Press.

Cimatoribus, A., Drijfhout, S., Toom, M. den, and Dijkstra, H. (2012). "Sensitivity of the Atlantic meridional overturning circulation to South Atlantic freshwater anomalies". In: *Climate Dynamics* 39.9-10, pp. 2291–2306. ISSN: 0930-7575. DOI: 10.1007/s00382-012-1292-5.

Cobb, L. (1978). "Stochastic catastrophe models and multimodal distributions". In: *Systems Research and Behavioral Science* 23.4, pp. 360–374.

— (1980). "Estimation theory for the cusp catastrophe model". In: *Proceedings of the American Statistical Association*, pp. 772–776.

Collins, M. et al. (2013). "Long-term climate change: Projections, commitments and irreversibility". In: *Climate Change 2013: The Physical Science Basis. Contribution of Working Group I to the Fifth Assessment Report of the Intergovernmental Panel on Climate Change*. Cambridge, UK: Cambridge University Press, pp. 1029–1136. DOI: 10.1017/CBO9781107415324.024.

Criado-Aldeanueva, F., Soto-Navarro, F. J., and García-Lafuente, J. (2012). "Seasonal and interannual variability of surface heat and freshwater fluxes in the Mediterranean Sea: Budgets and exchange through the Strait of Gibraltar". In: *International Journal of Climatology* 32.2, pp. 286–302.

Dakos, V., Scheffer, M., Van Nes, E. H., Brovkin, V., Petoukhov, V., and Held, H. (2008). "Slowing down as an early warning signal for abrupt climate change". In: *Proceedings of the National Academy of Sciences* 105.38, pp. 14308–14312. DOI: 10.1073/pnas.0802430105.

Dansgaard, W., Clausen, H., Gundestrup, N., Hammer, C., Johnsen, S., Kristinsdottir, P., and Reeh, N. (1982). "A new Greenland deep ice core". In: *Science* 218.4579, pp. 1273–1277.

Dansgaard, W. et al. (1993). "Evidence for general instability of past climate from a 250-kyr ice-core record". In: *Nature* 364.6434, p. 218.

Das, M. and Kantz, H. (June 2020). "Stochastic resonance and hysteresis in climate with state-dependent fluctuations". In: *Phys. Rev. E* 101 (6), p. 062145. DOI: 10.1103/PhysRevE.101.062145.

De Boer, A. M., Graham, R. M., Thomas, M. D., and Kohfeld, K. E. (2013). "The control of the Southern Hemisphere Westerlies on the position of the Subtropical Front". In: *Journal of Geophysical Research: Oceans* 118.10, pp. 5669–5675.

De Boer, A. M. and Nof, D. (2004). "The Bering Strait's grip on the northern hemisphere climate". In: *Deep Sea Research Part I: Oceanographic Research Papers* 51.10, pp. 1347–1366.

De Verdiére, C. A. (1989). "On the interaction of wind and buoyancy driven gyres". In: *Journal of Marine Research* 47.3, pp. 595–633. DOI: 10.1357/002224089785076172.

De Vries, P. and Weber, S. L. (2005). "The Atlantic freshwater budget as a diagnostic for the existence of a stable shut down of the meridional overturning circulation". In: *Geophysical Research Letters* 32.9. ISSN: 1944-8007. DOI: 10.1029/2004GL021450.

DeConto, R. M. and Pollard, D. (2016). "Contribution of Antarctica to past and future sea-level rise". In: *Nature* 531.7596, pp. 591–597.

Den Toom, M., Dijkstra, H. A., Weijer, W., Hecht, M. W., Maltrud, M. E., and Van Sebille, E. (2014). "Sensitivity of a strongly eddying global ocean to North Atlantic freshwater perturbations". In: *Journal of Physical Oceanography* 44, pp. 464–481. DOI: 10.1175/jpo-d-12-0155.1.

Deshayes, J., Curry, R., and Msadek, R. (2014). "CMIP5 model intercomparison of freshwater budget and circulation in the North Atlantic". In: *Journal of Climate* 27.9, pp. 3298–3317.

Dijkstra, H. A. (2007). "Characterization of the multiple equilibria regime in a global ocean model". In: *Tellus A* 59.5, pp. 695–705.

Ditlevsen, P. D. and Johnsen, S. J. (2010). "Tipping points: Early warning and wishful thinking". In: *Geophysical Research Letters* 37.19. L19703. ISSN: 1944-8007. DOI: 10.1029/2010GL044486.

Drijfhout, S. S., Weber, S. L., and Van der Swaluw, E. (2011). "The stability of the MOC as diagnosed from model projections for pre-industrial, present and future climates". In: *Climate Dynamics* 37.7, pp. 1575–1586.

Drijfhout, S. (2015). "Competition between global warming and an abrupt collapse of the AMOC in Earth's energy imbalance". In: *Scientific Reports* 5.14877. DOI: 10.1038/srep14877.

Drijfhout, S. S., Marshall, D. P., and Dijkstra, H. A. (2013). "Chapter 11 - Conceptual Models of the Wind-Driven and Thermohaline Circulation". In: *Ocean Circulation and Climate*. Ed. by Siedler, G., Griffies, S. M., Gould, J., and Church, J. A. Vol. 103. International Geophysics. Academic Press, pp. 257–282. DOI: https://doi.org/10.1016/B978-0-12-391851-2.00011-8.

Drouin, K. L. and Lozier, M. S. (2019). "The surface pathways of the South Atlantic: Revisiting the cold and warm water routes using observational data". In: *Journal of Geophysical Research: Oceans* 124.10, pp. 7082–7103.

Dukhovskoy, D., Yashayaev, I., Proshutinsky, A., Bamber, J., Bashmachnikov, I., Chassignet, E., Lee, C., and Tedstone, A. (2019). "Role of Greenland freshwater anomaly in the recent freshening of the subpolar North Atlantic". In: *Journal of Geophysical Research: Oceans* 124.5, pp. 3333–3360.

Durgadoo, J. V., Loveday, B. R., Reason, C. J., Penven, P., and Biastoch, A. (2013). "Agulhas leakage predominantly responds to the Southern Hemisphere westerlies". In: *Journal of Physical Oceanography* 43.10, pp. 2113–2131.

ECMWF (2006). *IFS documentation*. URL: http://www.ecmwf.int/research/ifsdocs/CY31R1/index.html.

Eden, C., Jochum, M., and Danabasoglu, G. (2009). "Effects of diffferent closures for thickness diffusivity". In: *Ocean Modelling* 26.1 - 2, pp. 47–59.

Edwards, N. R. and Marsh, R. (2005). "Uncertainties due to transport-parameter sensitivity in an efficient 3-D ocean-climate model". In: *Climate dynamics* 24.4, pp. 415–433.

Eyring, V., Bony, S., Meehl, G. A., Senior, C. A., Stevens, B., Stouffer, R. J., and Taylor, K. E. (2016). "Overview of the Coupled Model Intercomparison Project Phase 6 (CMIP6) experimental design and organization". In: *Geoscientific Model Development* 9.5, pp. 1937–1958. DOI: 10.5194/gmd-9-1937-2016.

Falcon-Lang, H. and Cantrill, D. (2001). "Leaf phenology of some mid-Cretaceous polar forests, Alexander Island, Antarctica". In: *Geological Magazine* 138.1, pp. 39–52.

Feldmann, J. and Levermann, A. (2015). "Collapse of the West Antarctic Ice Sheet after local destabilization of the Amundsen Basin". In: *Proceedings of the National Academy of Sciences* 112.46, pp. 14191–14196.

Fettweis, X., Franco, B., Tedesco, M., Angelen, J. H. van, Lenaerts, J. T. M., Van den Broeke, M. R., and Gallée, H. (2013). "Estimating the Greenland ice sheet surface mass balance contribution to future sea level rise using the regional atmospheric climate model MAR". In: *The Cryosphere* 7.2, pp. 469–489. DOI: 10.5194/tc-7-469-2013.

Fichefet, T. and Morales Maqueda, M. (1997). "Sensitivity of a global sea ice model to the treatment of ice thermodynamics and dynamics." In: *J Geophys Res* 102.646, pp. 609–12. DOI: 10.1029/97JC00480.

Foster, G. L., Royer, D. L., and Lunt, D. J. (2017). "Future climate forcing potentially without precedent in the last 420 million years". In: *Nature communications* 8.1, pp. 1–8.

Fu, Y., Li, F., Karstensen, J., and Wang, C. (2020). "A stable Atlantic Meridional Overturning Circulation in a changing North Atlantic Ocean since the 1990s". In: *Science advances* 6.48, eabc7836.

Fyke, J., Sergienko, O., Löfverström, M., Price, S., and Lenaerts, J. T. (2018). "An overview of interactions and feedbacks between ice sheets and the Earth system". In: *Reviews of Geophysics* 56.2, pp. 361–408.

Ganachaud, A. and Wunsch, C. (2000). "Improved estimates of global ocean circulation, heat transport and mixing from hydrographic data". In: *Nature* 408.6811, p. 453.

García-Lafuente, J., Naranjo, C., Sammartino, S., Sánchez-Garrido, J. C., and Delgado, J. (2017). "The Mediterranean outflow in the Strait of Gibraltar and its connection with upstream conditions in the Alborán Sea". In: *Ocean Science* 13.2, pp. 195–207.

Gardiner, C. W. (2004). *Handbook of stochastic methods for physics, chemistry and the natural sciences*. Third. Vol. 13. Springer Series in Synergetics. Springer-Verlag, pp. xviii+415. ISBN: 3-540-20882-8.

Garrison, T. S. (2011). *Essentials of oceanography*. 6th ed. Cengage Learning.

Gary, S. F., Lozier, M. S., Böning, C. W., and Biastoch, A. (2011). "Deciphering the pathways for the deep limb of the Meridional Overturning Circulation". In: *Deep Sea Research Part II: Topical Studies in Oceanography* 58.17, pp. 1781–1797.

Garzoli, S. L., Baringer, M. O., Dong, S., Perez, R. C., and Yao, Q. (Jan. 2013). "South Atlantic meridional fluxes". In: *Deep Sea Research Part I: Oceanographic Research Papers* 71.0, pp. 21–32.

Gent, P. R. (2018). "A commentary on the Atlantic meridional overturning circulation stability in climate models". In: *Ocean Modelling* 122, pp. 57–66.

Gent, P. R. and Mcwilliams, J. C. (1990). "Isopycnal mixing in ocean circulation models". In: *Journal of Physical Oceanography* 20.1, pp. 150–155.

Gill, A. (1982). *Atmosphere-Ocean Dynamics*. International Geophysics. Elsevier Science. ISBN: 9780080570525.

Gillard, L. C., Hu, X., Myers, P. G., and Bamber, J. L. (2016). "Meltwater pathways from marine terminating glaciers of the Greenland ice sheet". In: *Geophysical Research Letters*. ISSN: 1944-8007. DOI: 10.1002/2016GL070969.

Good, S. A., Martin, M. J., and Rayner, N. A. (2013). "EN4: Quality controlled ocean temperature and salinity profiles and monthly objective analyses with uncertainty estimates". In: *Journal of Geophysical Research: Oceans* 118.12, pp. 6704–6716.

Goosse, H., Selten, F., Haarsma, R., and Opsteegh, J. (2001). "Decadal variability in high northern latitudes as simulated by an intermediate-complexity climate model". In: *Annals of Glaciology* 33, pp. 525–532.

Gouretski, V. and Reseghetti, F. (2010). "On depth and temperature biases in bathythermograph data: Development of a new correction scheme based on analysis of a global ocean database". In: *Deep Sea Research Part I: Oceanographic Research Papers* 57.6, pp. 812–833.

Green, B., Marshall, J., and Campin, J.-M. (2019). "The 'sticky' ITCZ: ocean-moderated ITCZ shifts". In: *Climate dynamics* 53.1-2, pp. 1–19.

Green, J. and Schmittner, A. (2015). "Climatic consequences of a Pine Island Glacier collapse". In: *Journal of Climate* 28.23, pp. 9221–9234.

Gregory, J. M. and Huybrechts, P. (July 2006). "Ice-sheet contributions to future sea-level change". In: *Philosophical Transactions of the Royal Society A: Mathematical, Physical and Engineering Sciences* 364.1844, pp. 1709–1732. ISSN: 1471-2962. DOI: 10.1098/rsta.2006.1796.

Gregory, J. M. et al. (2005). "A model intercomparison of changes in the Atlantic thermohaline circulation in response to increasing atmospheric $CO_2$ concentration". In: *Geophysical Research Letters* 32.12. ISSN: 1944-8007. DOI: 10.1029/2005GL023209.

Greve, R. and Blatter, H. (2009). *Dynamics of Ice Sheets and Glaciers*. Advances in Geophysical and Environmental Mechanics and Mathematics. Springer-Verlag. ISBN: 978-3-642-03414-5. DOI: 10.1007/978-3-642-03415-2.

Hanna, E., Huybrechts, P., Steffen, K., Cappelen, J., Huff, R., Shuman, C., Irvine-Fynn, T., Wise, S., and Griffiths, M. (Jan. 2008). "Increased Runoff from Melt from the Greenland Ice Sheet: A Response to Global Warming". In: *J. Climate* 21.2, pp. 331–341. DOI: 10.1175/2007JCLI1964.1.

Hanna, E. et al. (2013). "Ice-sheet mass balance and climate change". In: *Nature* 498.7452, pp. 51–59.

Hansen, J., Fung, I., Lacis, A., Rind, D., Lebedeff, S., Ruedy, R., Russell, G., and Stone, P. (1988). "Global climate changes as forecast by Goddard Institute for Space Studies three-dimensional model". In: *Journal of geophysical research: Atmospheres* 93.D8, pp. 9341–9364.

Hansen, J., Sato, M., Russell, G., and Kharecha, P. (2013). "Climate sensitivity, sea level and atmospheric carbon dioxide". In: *Philosophical Transactions of the Royal Society A: Mathematical, Physical and Engineering Sciences* 371.2001, p. 20120294.

Hartmann, D. L. (2016). *Global Physical Climatology*. 2nd ed. Elsevier Science. ISBN: 0123285313,978-0-12-328531-7.

Haskins, R. K., Oliver, K. I., Jackson, L. C., Wood, R. A., and Drijfhout, S. S. (2019). "Temperature domination of AMOC weakening due to freshwater hosing in two GCMs". In: *Climate Dynamics* 54.1-2, pp. 273–286.

— (2020). "Temperature domination of AMOC weakening due to freshwater hosing in two GCMs". In: *Climate Dynamics* 54.1-2, pp. 273–286.

Hastings, W. K. (1970). "Monte Carlo sampling methods using Markov chains and their applications". In: *Biometrika* 57.1, pp. 97–109. DOI: 10.1093/biomet/57.1.97.

Hawkins, E., Smith, R. S., Allison, L. C., Gregory, J. M., Woollings, T. J., Pohlmann, H., and De Cuevas, B. (2011). "Bistability of the Atlantic overturning circulation in a global climate model and links to ocean freshwater transport". In: *Geophysical Research Letters* 38.10.

Hazeleger, W. et al. (2012). "EC-Earth V2.2: description and validation of a new seamless earth system prediction model". English. In: *Climate Dynamics* 39.11, pp. 2611–2629. ISSN: 0930-7575. DOI: 10.1007/s00382-011-1228-5.

Hazeleger, W. et al. (Oct. 2010). "EC-Earth: A Seamless Earth-System Prediction Approach in Action". In: *Bulletin of the American Meteorological Society* 91.10, pp. 1357–1363. ISSN: 0003-0007. DOI: 10.1175/2010BAMS2877.1.

Held, H. and Kleinen, T. (2004). "Detection of climate system bifurcations by degenerate fingerprinting". In: *Geophysical Research Letters* 31.23.

Hellmer, H. H., Kauker, F., Timmermann, R., Determann, J., and Rae, J. (May 2012). "Twenty-first-century warming of a large Antarctic ice-shelf cavity by a redirected coastal current". In: *Nature* 485.7397, pp. 225–228. ISSN: 0028-0836. DOI: 10.1038/nature11064.

Helm, V., Humbert, A., and Miller, H. (2014). "Elevation and elevation change of Greenland and Antarctica derived from CryoSat-2". In: *The Cryosphere* 8.4, pp. 1539–1559. DOI: 10.5194/tc-8-1539-2014.

Heuzé, C. (2017). "North Atlantic deep water formation and AMOC in CMIP5 models". In: *Ocean Science Discussions* 2017, pp. 1–22. DOI: 10.5194/os-2017-2.

Hewitt, H. T. et al. (2017). "Will high-resolution global ocean models benefit coupled predictions on short-range to climate timescales?" In: *Ocean Modelling* 120, pp. 120–136.

Hirschi, J. J.-M. et al. (2020). "The Atlantic meridional overturning circulation in high-resolution models". In: *Journal of Geophysical Research: Oceans* 125.4, e2019JC015522.

Hofmann, M. and Rahmstorf, S. (2009). "On the stability of the Atlantic meridional overturning circulation". In: *Proceedings of the National Academy of Sciences* 106.49, pp. 20584–20589.

Holland, D. M., Thomas, R. H., Young, B. de, Ribergaard, M. H., and Lyberth, B. (Oct. 2008). "Acceleration of Jakobshavn Isbræ triggered by warm subsurface ocean waters". In: *Nature Geosci* 1.10, pp. 659–664. ISSN: 1752-0894. DOI: 10.1038/ngeo316.

Holliday, N. P. et al. (2020). "Ocean circulation causes the largest freshening event for 120 years in eastern subpolar North Atlantic". In: *Nature communications* 11.1, pp. 1–15.

Hu, A., Meehl, G. A., Han, W., Otto-Bliestner, B., Abe-Ouchi, A., and Rosenbloom, N. (2015). "Effects of the Bering Strait closure on AMOC and global climate under different background climates". In: *Progress in Oceanography* 132, pp. 174–196.

Hu, A., Meehl, G. A., Han, W., and Yin, J. (2011). "Effect of the potential melting of the Greenland Ice Sheet on the Meridional Overturning Circulation and global climate in the future". In: *Deep Sea Research Part II: Topical Studies in Oceanography* 58.17-18, pp. 1914–1926.

Hu, A., Meehl, G. A., and Han, W. (2007). "Role of the Bering Strait in the thermohaline circulation and abrupt climate change". In: *Geophysical Research Letters* 34.5. L05704, n/a–n/a. DOI: 10.1029/2006GL028906.

Hu, A., Meehl, G. A., Han, W., Yin, J., Wu, B., and Kimoto, M. (2013). "Influence of Continental Ice Retreat on Future Global Climate". In: *Journal of Climate* 26.10, pp. 3087–3111. DOI: 10.1175/JCLI-D-12-00102.1.

Hu, A., Otto-Bliesner, B. L., Meehl, G. A., Han, W., Morrill, C., Brady, E. C., and Briegleb, B. (2008). "Response of thermohaline circulation to freshwater forcing under present-day and LGM conditions". In: *Journal of Climate* 21.10, pp. 2239–2258.

Hu, A. et al. (2012). "Role of the Bering Strait on the hysteresis of the ocean conveyor belt circulation and glacial climate stability". In: *Proceedings of the National Academy of Sciences* 109.17, pp. 6417–6422.

Hurrell, J. W. (1995). "Decadal trends in the North Atlantic Oscillation: Regional temperatures and precipitation". In: *Science* 269.5224, pp. 676–679.

Hurrell, J. W., Kushnir, Y., Ottersen, G., and Visbeck, M. (2003). "An overview of the North Atlantic oscillation". In: *Geophysical Monograph-American Geophysical Union* 134, pp. 1–36.

Intergovernmental Panel on Climate Change (2014a). *Climate Change 2014 – Impacts, Adaptation and Vulnerability: Part A: Global and Sectoral Aspects: Working Group II Contribution to the IPCC Fifth Assessment Report*. Vol. 1. Cambridge University Press. DOI: 10.1017/CBO9781107415379.

— (2014b). "Observations: Ocean Pages". In: *Climate Change 2013 – The Physical Science Basis: Working Group I Contribution to the Fifth Assessment Report of the Intergovernmental Panel on Climate Change*. Cambridge University Press, pp. 255–316. DOI: 10.1017/CBO9781107415324.010.

Jackson, L. C., Schaller, N., Smith, R. S., Palmer, M. D., and Vellinga, M. (2013). "Response of the Atlantic meridional overturning circulation to a reversal of greenhouse gas increases". In: *Climate Dynamics*. DOI: 10.1007/s00382-013-1842-5.

Jackson, L., Smith, R. S., and Wood, R. (2017). "Ocean and atmosphere feedbacks affecting AMOC hysteresis in a GCM". In: *Climate Dynamics* 49.1-2, pp. 173–191.

Jenkins, A. and Holland, D. (2007). "Melting of floating ice and sea level rise". In: *Geophysical Research Letters* 34.16. ISSN: 1944-8007. DOI: 10.1029/2007GL030784.

Johnsen, S., Clausen, H. B., Dansgaard, W., Fuhrer, K., Gundestrup, N., Hammer, C. U., Iversen, P., Jouzel, J., Stauffer, B., et al. (1992). "Irregular glacial interstadials recorded in a new Greenland ice core". In: *Nature* 359.6393, pp. 311–313.

Joughin, I. and Alley, R. B. (Aug. 2011). "Stability of the West Antarctic ice sheet in a warming world". In: *Nature Geosci* 4.8, pp. 506–513. ISSN: 1752-0894. DOI: 10.1038/ngeo1194.

Joughin, I., Smith, B. E., and Medley, B. (2014). "Marine ice sheet collapse potentially under way for the Thwaites Glacier Basin, West Antarctica". In: *Science* 344.6185, pp. 735–738.

Jouzel, J. et al. (2007). "Orbital and millennial Antarctic climate variability over the past 800,000 years". In: *science* 317.5839, pp. 793–796.

Jüling, A., Viebahn, J. P., Drijfhout, S. S., and Dijkstra, H. A. (2018). "Energetics of the Southern Ocean Mode". In: *Journal of Geophysical Research: Oceans* 123.12, pp. 9283–9304.

Karstensen, J. and Lorbacher, K. (2011). "A practical indicator for surface ocean heat and freshwater buoyancy fluxes and its application to the NCEP reanalysis data". In: *Tellus A* 63.2. ISSN: 1600-0870.

Kasdin, N. J. (1995). "Runge-Kutta algorithm for the numerical integration of stochastic differential equations". In: *Journal of Guidance, Control, and Dynamics* 18.1, pp. 114–120.

Kashinath, K. et al. (2021). "Physics-informed machine learning: case studies for weather and climate modelling". In: *Philosophical Transactions of the Royal Society A* 379.2194, p. 20200093.

Katsman, C. A. et al. (2011). "Exploring high-end scenarios for local sea level rise to develop flood protection strategies for a low-lying delta-The Netherlands as an example". In: *Climatic Change* 109.3-4, pp. 617–645. ISSN: 0165-0009.

Katsman, C., Drijfhout, S., Dijkstra, H., and Spall, M. (2018). "Sinking of dense North Atlantic waters in a global ocean model: Location and controls". In: *Journal of Geophysical Research: Oceans* 123.5, pp. 3563–3576.

Katsman, C., Hazeleger, W., Drijfhout, S., Oldenborgh, G., and Burgers, G. (2008). "Climate scenarios of sea level rise for the northeast Atlantic Ocean: a study including the effects of ocean dynamics and gravity changes induced by ice melt". In: *Climatic Change* 91 (3-4), pp. 351–374. ISSN: 0165-0009. DOI: 10.1007/s10584-008-9442-9.

Keeling, C. D., Bacastow, R. B., Bainbridge, A. E., Ekdahl Jr, C. A., Guenther, P. R., Waterman, L. S., and Chin, J. F. (1976). "Atmospheric carbon dioxide variations at Mauna Loa observatory, Hawaii". In: *Tellus* 28.6, pp. 538–551.

Khatiwala, S. et al. (2013). "Global ocean storage of anthropogenic carbon". In: *Biogeosciences* 10.4, pp. 2169–2191. DOI: 10.5194/bg-10-2169-2013.

Kleinen, T., Held, H., and Petschel-Held, G. (2003). "The potential role of spectral properties in detecting thresholds in the Earth system: application to the thermohaline circulation". In: *Ocean Dynamics* 53.2, pp. 53–63.

Kopp, R., Mitrovica, J., Griffies, S., Yin, J., Hay, C., and Stouffer, R. (2010). "The impact of Greenland melt on local sea levels: A partially coupled analysis of dynamic and static equilibrium effects in idealized water-hosing experiments". In: *Climatic Change* 103.3, pp. 619–625.

Kuhlbrodt, T., Griesel, A., Montoya, M., Levermann, A., Hofmann, M., and Rahmstorf, S. (2007). "On the driving processes of the Atlantic meridional overturning circulation". In: *Reviews of Geophysics* 45.2.

Kwasniok, F. and Lohmann, G. (Dec. 2009). "Deriving dynamical models from paleoclimatic records: Application to glacial millennial-scale climate variability". In: *Phys. Rev. E* 80 (6), p. 066104. DOI: 10.1103/PhysRevE.80.066104.

Lauderdale, J. M., Dutkiewicz, S., Williams, R. G., and Follows, M. J. (2016). "Quantifying the drivers of ocean-atmosphere CO2 fluxes". In: *Global Biogeochemical Cycles* 30.7, pp. 983–999.

Lavender, K. L., Davis, R. E., and Owens, W. B. (2000). "Mid-depth recirculation observed in the interior Labrador and Irminger seas by direct velocity measurements". In: *Nature* 407.6800, pp. 66–69.

Le Bars, D., Drijfhout, S., and De Vries, H. (2017). "A high-end sea level rise probabilistic projection including rapid Antarctic ice sheet mass loss". In: *Environmental Research Letters* 12.4, p. 044013.

Le Corre, M., Gula, J., and Tréguier, A.-M. (2020). "Barotropic vorticity balance of the North Atlantic subpolar gyre in an eddy-resolving model". In: *Ocean Science* 16.2, pp. 451–468. DOI: 10.5194/os-16-451-2020.

Lee, C.-T. A. et al. (2013). "Continental arc–island arc fluctuations, growth of crustal carbonates, and long-term climate change". In: *Geosphere* 9.1, pp. 21–36.

Lemons, D., Gythiel, A., and Langevin's, P. (1908). "paper "Sur la théorie du mouvement brownien [On the theory of Brownian motion]"". In: *CR Acad. Sci.(Paris)* 146, pp. 530–533.

Lenton, T. M., Held, H., Kriegler, E., Hall, J. W., Lucht, W., Rahmstorf, S., and Schellnhuber, H. J. (2008). "Tipping elements in the Earth's climate system". In: *Proceedings of the national Academy of Sciences* 105.6, pp. 1786–1793. DOI: 10.1073/pnas.0705414105.

Lenz, E. (1845). "Bermerkungen über die Temperatur des Weltmeeres in verschiedenen Tiefen". In: *Bulletin de la Classe Physico-Mathématique de l'Académie Impériale des Sciences de Saint-Pétersbourg* 5, pp. 67–74.

Levang, S. J. and Schmitt, R. W. (2015). "Centennial Changes of the Global Water Cycle in CMIP5 Models". In: *Journal of Climate* 28.16, pp. 6489–6502. DOI: 10.1175/JCLI-D-15-0143.1.

Li, F., Lozier, M. S., and Johns, W. E. (2017). "Calculating the Meridional Volume, Heat, and Freshwater Transports from an Observing System in the Subpolar North Atlantic: Observing System Simulation Experiment". In: *Journal of Atmospheric and Oceanic Technology* 34.7, pp. 1483–1500. DOI: 10.1175/JTECH-D-16-0247.1.

Li, G., Cheng, L., Zhu, J., Trenberth, K. E., Mann, M. E., and Abraham, J. P. (2020). "Increasing ocean stratification over the past half-century". In: *Nature Climate Change* 10.12, pp. 1116–1123.

Liou, K.-N. (2002). *An introduction to atmospheric radiation*. 2nd ed. Elsevier.

Lisiecki, L. E. and Raymo, M. E. (2005). "A Pliocene-Pleistocene stack of 57 globally distributed benthic $\delta$18O records". In: *Paleoceanography* 20.1.

Liu, W. and Liu, Z. (2013). "A diagnostic indicator of the stability of the Atlantic meridional overturning circulation in CCSM3". In: *Journal of Climate* 26.6, pp. 1926–1938.

Liu, W., Xie, S.-P., Liu, Z., and Zhu, J. (2017). "Overlooked possibility of a collapsed Atlantic Meridional Overturning Circulation in warming climate". In: *Science Advances* 3.1, e1601666.

Livina, V. N., Kwasniok, F., and Lenton, T. M. (2010). "Potential analysis reveals changing number of climate states during the last 60 kyr." In: *Climate of the Past* 6.1.

Lohmann, G. (2003). "Atmospheric and oceanic freshwater transport during weak Atlantic overturning circulation". In: *Tellus A: Dynamic Meteorology and Oceanography* 55.5, pp. 438–449.

Lohmann, J. and Ditlevsen, P. D. (2021). "Risk of tipping the overturning circulation due to increasing rates of ice melt". In: *Proceedings of the National Academy of Sciences* 118.9.

Lohmann, K. et al. (2014). "The role of subpolar deep water formation and Nordic Seas overflows in simulated multidecadal variability of the Atlantic meridional overturning circulation". In: *Ocean Science* 10, pp. 227–241.

Lorbacher, K., Marsland, S. J., Church, J. A., Griffies, S. M., and Stammer, D. (2012). "Rapid barotropic sea level rise from ice sheet melting". In: *Journal of Geophysical Research: Oceans* 117.C6. ISSN: 2156-2202. DOI: 10.1029/2011JC007733.

Lozier, M. S. et al. (2019). "A sea change in our view of overturning in the subpolar North Atlantic". In: *Science* 363.6426, pp. 516–521.

Lozier, M. S. et al. (2017). "Overturning in the Subpolar North Atlantic Program: A New International Ocean Observing System". In: *Bulletin of the American Meteorological Society* 98.4, pp. 737–752. DOI: 10.1175/BAMS-D-16-0057.1.

Luyten, J. and Stommel, H. (1986). "Gyres Driven by Combined Wind and Buoyancy Flux". In: *Journal of Physical Oceanography* 16.9, pp. 1551–1560. DOI: 10.1175/1520-0485(1986)016<1551:GDBCWA>2.0.CO;2.

Madec, G. (2008). "NEMO ocean engine". In: *Note du Pole de modelisation, Institut Pierre-Simon Laplace (IPSL), France* 27, pp. 1288–1619.

Manabe, S. and Stouffer, R. (1988). "Two stable equilibria of a coupled ocean-atmosphere model". In: *Journal of Climate* 1.9, pp. 841–866.

Marotzke, J. (1997). "Boundary mixing and the dynamics of three-dimensional thermohaline circulations". In: *Journal of Physical Oceanography* 27.8, pp. 1713–1728.

Marsh, R. et al. (2015). "NEMO-ICB (v1. 0): interactive icebergs in the NEMO ocean model globally configured at eddy-permitting resolution". In: *Geoscientific Model Development* 8.5, pp. 1547–1562.

Marsh, R., Desbruyères, D., Bamber, J. L., Cuevas, B. A. de, Coward, A. C., and Aksenov, Y. (2010). "Short-term impacts of enhanced Greenland freshwater fluxes in an eddy-permitting ocean model". In: *Ocean Science* 6.3, pp. 749–760. DOI: 10.5194/os-6-749-2010.

Marshall, D. P. and Johnson, H. L. (2017). "Relative strength of the Antarctic Circumpolar Current and Atlantic Meridional Overturning Circulation". In: *Tellus A: Dynamic Meteorology and Oceanography* 69.1, p. 1338884. DOI: 10.1080/16000870.2017.1338884.

Marshall, J. and Schott, F. (1999). "Open-ocean convection: Observations, theory, and models". In: *Reviews of geophysics* 37.1, pp. 1–64.

Marshall, J. and Speer, K. (2012). "Closure of the meridional overturning circulation through Southern Ocean upwelling". In: *Nature Geoscience* 5.3, pp. 171–180.

Martin, T. and Adcroft, A. (2010). "Parameterizing the fresh-water flux from land ice to ocean with interactive icebergs in a coupled climate model". In: *Ocean Modelling* 34.3–4, pp. 111–124. ISSN: 1463-5003. DOI: 10.1016/j.ocemod.2010.05.001.

McCarthy, G. D. et al. (2015). "Measuring the Atlantic meridional overturning circulation at 26 N". In: *Progress in Oceanography* 130, pp. 91–111.

McDougall, T. et al. (2009). "The international thermodynamic equation of seawater 2010 (teos-10): Calculation and use of thermodynamic properties". In: *Global Ship-based Repeat Hydrography Manual, IOCCP Report No* 14.

Mecking, J., Drijfhout, S., Jackson, L., and Andrews, M. (2017). "The effect of model bias on Atlantic freshwater transport and implications for AMOC bi-stability". In: *Tellus A: Dynamic Meteorology and Oceanography* 69.1, p. 1299910.

Mecking, J., Drijfhout, S., Jackson, L., and Graham, T. (2016). "Stable AMOC off state in an eddy-permitting coupled climate model". In: *Climate Dynamics* 47.7-8, pp. 2455–2470.

Meehl, G. et al. (2007). *Climate Change 2007: The Physical Science Basis. Contribution of Working Group 1 to the Fourth Assessment Report of the Intergovernmental Panel on Climate Change*. Cambridge University Press.

Meinshausen, M. et al. (2017). *Historical greenhouse gas concentrations for climate modelling (CMIP6)*.

Menviel, L., Timmermann, A., Timm, O. E., and Mouchet, A. (2010). "Climate and biogeochemical response to a rapid melting of the West Antarctic Ice Sheet during interglacials and implications for future climate". In: *Paleoceanography and Paleoclimatology* 25.4, PA4231.

Mernild, S. H. and Liston, G. E. (Sept. 2012). "Greenland Freshwater Runoff. Part II: Distribution and Trends, 1960-2010". In: *Journal of Climate* 25, pp. 6015–6035. DOI: 10.1175/JCLI-D-11-00592.1.

Mitchell, M. (1996). *An introduction to genetic algorithms*. MIT press.

Moat, B. I. et al. (2020a). "Pending recovery in the strength of the meridional overturning circulation at 26° N". In: *Ocean Science* 16.4, pp. 863–874. DOI: 10.5194/os-16-863-2020.

Moat, B., Frajka-Williams, E., Smeed D.A.and Rayner, D., Sanchez-Franks, A., Johns, W., Baringer, M., Volkov, D., and Collins, J. (2020b). "Atlantic meridional overturning circulation observed by the RAPID-MOCHA-WBTS (RAPID-Meridional Overturning Circulation and Heatflux Array-Western Boundary Time Series) array at 26N from 2004 to 2018 (v2018.2)". In: *British Oceanographic Data Centre*. DOI: 10.5285/aa57e879-4cca-28b6-e053-6c86abc02de5.

Morrill, C., Ward, E. M., Wagner, A. J., Otto-Bliesner, B. L., and Rosenbloom, N. (2014). "Large sensitivity to freshwater forcing location in 8.2 ka simulations". In: *Paleoceanography* 29.10, pp. 930–945.

Motyka, R. J., Truffer, M., Fahnestock, M., Mortensen, J., Rysgaard, S., and Howat, I. (Feb. 2011). "Submarine melting of the 1985 Jakobshavn Isbræ floating tongue and the triggering of the current retreat". In: *Journal of Geophysical Research* 116.F1, F01007+. ISSN: 0148-0227. DOI: 10.1029/2009jf001632.

Mouginot, J., Rignot, E., Bjørk, A. A., Van den Broeke, M., Millan, R., Morlighem, M., Noël, B., Scheuchl, B., and Wood, M. (2019). "Forty-six years of Greenland Ice Sheet mass balance from 1972 to 2018". In: *Proceedings of the National Academy of Sciences* 116.19, pp. 9239–9244.

Munday, D. R., Johnson, H. L., and Marshall, D. P. (2013). "Eddy Saturation of Equilibrated Circumpolar Currents". In: *Journal of Physical Oceanography* 43.3, pp. 507–532. DOI: 10.1175/JPO-D-12-095.1.

Murray-Wallace, C. V. and Woodroffe, C. D. (2014). "Pleistocene sea-level changes". In: *Quaternary Sea-Level Changes: A Global Perspective*. Cambridge University Press, pp. 256–319. DOI: 10.1017/CBO9781139024440.007.

Murton, J. B., Bateman, M. D., Dallimore, S. R., Teller, J. T., and Yang, Z. (2010). "Identification of Younger Dryas outburst flood path from Lake Agassiz to the Arctic Ocean". In: *Nature* 464.7289, pp. 740–743.

Nikurashin, M. and Vallis, G. (2012). "A theory of the interhemispheric meridional overturning circulation and associated stratification". In: *Journal of Physical Oceanography* 42.10, pp. 1652–1667.

Nowicki, S. M., Payne, A., Larour, E., Seroussi, H., Goelzer, H., Lipscomb, W., Gregory, J., Abe-Ouchi, A., and Shepherd, A. (2016). "Ice sheet model intercomparison project (ISMIP6) contribution to CMIP6". In: *Geoscientific Model Development* 9.12, pp. 4521–4545.

Otto-Bliesner, B. L. and Brady, E. C. (2010). "The sensitivity of the climate response to the magnitude and location of freshwater forcing: last glacial maximum experiments". In: *Quaternary Science Reviews* 29.1, pp. 56–73.

Palter, J. B. (2015). "The role of the Gulf Stream in European climate". In: *Annual review of marine science* 7, pp. 113–137.

Paolo, F. S., Fricker, H. A., and Padman, L. (2015). "Volume loss from Antarctic ice shelves is accelerating". In: *Science* 348.6232, pp. 327–331.

Pedlosky, J. (1996). *Ocean Circulation Theory*. Springer Science & Business Media.

Peeters, F. J., Acheson, R., Brummer, G.-J. A., De Ruijter, W. P., Schneider, R. R., Ganssen, G. M., Ufkes, E., and Kroon, D. (2004). "Vigorous exchange between the Indian and Atlantic oceans at the end of the past five glacial periods". In: *Nature* 430.7000, pp. 661–665.

Peña-Molino, B., Joyce, T. M., and Toole, J. M. (2012). "Variability in the deep western boundary current: Local versus remote forcing". In: *Journal of Geophysical Research: Oceans* 117.C12.

Pfeffer, W. T., Harper, J. T., and O'Neel, S. (Sept. 2008). "Kinematic Constraints on Glacier Contributions to 21st-Century Sea-Level Rise". In: *Science* 321.5894, pp. 1340–1343. DOI: 10.1126/science.1159099.

Pickart, R. S. and Spall, M. A. (Sept. 2007). "Impact of Labrador Sea Convection on the North Atlantic Meridional Overturning Circulation". In: *Journal of Physical Oceanography* 37.9, pp. 2207–2227. ISSN: 0022-3670. DOI: 10.1175/JPO3178.1.

Piessens, R., Doncker-Kapenga, E. de, Überhuber, C., and Kahaner, D. (2012). *Quadpack: A Subroutine Package for Automatic Integration*. Springer Series in Computational Mathematics. Springer Berlin Heidelberg. ISBN: 9783642617867.

Pörtner, [ et al. (In press). *IPCC, 2019: IPCC Special Report on the Ocean and Cryosphere in a Changing Climate*.

Poston, T. and Stewart, I. (1978). *Catastrophe theory and its applications*. Surveys and reference works in mathematics. Pitman. ISBN: 9780273010296.

Prange, M., Lohmann, G., and Paul, A. (2003). "Influence of vertical mixing on the thermohaline hysteresis: Analyses of an OGCM". In: *Journal of Physical Oceanography* 33.8, pp. 1707–1721.

Pritchard, H. D., Arthern, R. J., Vaughan, D. G., and Edwards, L. A. (2009). "Extensive dynamic thinning on the margins of the Greenland and Antarctic ice sheets". In: *Nature* 461.7266, pp. 971–975.

Rahmstorf, S. (1996). "On the freshwater forcing and transport of the Atlantic thermohaline circulation". In: *Climate Dynamics* 12.12, pp. 799–811.

— (2000). "The thermohaline ocean circulation: A system with dangerous thresholds?" In: *Climatic Change* 46.3, pp. 247–256.

— (2002). "Ocean circulation and climate during the past 120,000 years". In: *Nature* 419.6903, pp. 207–214.

Rahmstorf, S. and Willebrand, J. (1995). "The role of temperature feedback in stabilizing the thermohaline circulation". In: *Journal of Physical Oceanography* 25.5, pp. 787–805.

Rahmstorf, S. et al. (2005). "Thermohaline circulation hysteresis: A model intercomparison". In: *Geophysical Research Letters* 32.23.

Reason, C. and Power, S. (1994). "The influence of the Bering Strait on the circulation in a coarse resolution global ocean model". In: *Climate Dynamics* 9.7, pp. 363–369.

Rhein, M., Steinfeldt, R., Kieke, D., Stendardo, I., and Yashayaev, I. (2017). "Ventilation variability of Labrador Sea Water and its impact on oxygen and anthropogenic carbon: a review". In: *Philosophical Transactions of the Royal Society A: Mathematical, Physical and Engineering Sciences* 375.2102, p. 20160321.

Riahi, K., Rao, S., Krey, V., Cho, C., Chirkov, V., Fischer, G., Kindermann, G., Nakicenovic, N., and Rafaj, P. (2011). "RCP 8.5—A scenario of comparatively high greenhouse gas emissions". In: *Climatic Change* 109.1-2, p. 33.

Richardson, P. L. (2008). "On the history of meridional overturning circulation schematic diagrams". In: *Progress in Oceanography* 76.4, pp. 466–486.

Ridgway, K. and Dunn, J. (2007). "Observational evidence for a Southern Hemisphere oceanic supergyre". In: *Geophysical Research Letters* 34.13.

Rignot, E. (2006). "Changes in ice dynamics and mass balance of the Antarctic, Ice Sheet". In: *Philos. Trans. R. Soc. London, Ser. A* 364, pp. 1637–1656.

Rignot, E., Jacobs, S., Mouginot, J., and Scheuchl, B. (2013). "Ice-Shelf Melting Around Antarctica". In: *Science* 341.6143, pp. 266–270. DOI: 10.1126/science.1235798.

Rignot, E. and Kanagaratnam, P. (2006). "Changes in the Velocity Structure of the Greenland Ice Sheet". In: *Science* 311, pp. 986–990.

Rignot, E., Velicogna, I., Van den Broeke, M. R., Monaghan, A., and Lenaerts, J. (Mar. 2011). "Acceleration of the contribution of the Greenland and Antarctic ice sheets to sea level rise". In: *Geophys. Res. Lett.* 38, p. L05503. DOI: 10.1029/2011GL046583.

Rignot, E., Bamber, J. L., Van den Broeke, M. R., Davis, C., Li, Y., van de Berg, W. J., and Van Meijgaard, E. (Feb. 2008). "Recent Antarctic ice mass loss from radar in-

terferometry and regional climate modelling". In: *Nature Geosci* 1.2, pp. 106–110. ISSN: 1752-0894. DOI: 10.1038/ngeo102.

Rignot, E. and Jacobs, S. S. (2002). "Rapid Bottom Melting Widespread near Antarctic Ice Sheet Grounding Lines". In: *Science* 296.5575, pp. 2020–2023. DOI: 10.1126/science.1070942.

Rignot, E., Koppes, M., and Velicogna, I. (Feb. 2010). "Rapid submarine melting of the calving faces of West Greenland glaciers". In: *Nature Geoscience* 3.3, pp. 187–191. ISSN: 1752-0894. DOI: 10.1038/ngeo765.

Rignot, E., Mouginot, J., Morlighem, M., Seroussi, H., and Scheuchl, B. (2014). "Widespread, rapid grounding line retreat of Pine Island, Thwaites, Smith, and Kohler glaciers, West Antarctica, from 1992 to 2011". In: *Geophysical Research Letters* 41.10, pp. 3502–3509.

Robinson, A., Calov, R., and Ganopolski, A. (2012). "Multistability and critical thresholds of the Greenland ice sheet". In: *Nature Climate Change* 2.6, pp. 429–432.

Roemmich, D., Johnson, G. C., Riser, S., Davis, R., Gilson, J., Owens, W. B., Garzoli, S. L., Schmid, C., and Ignaszewski, M. (2009). "The Argo Program: Observing the global ocean with profiling floats". In: *Oceanography* 22.2, pp. 34–43. DOI: 10.5670/oceanog.2009.36.

Rohde, R. A. and Hausfather, Z. (2020). "The Berkeley Earth land/ocean temperature record". In: *Earth System Science Data* 12.4, pp. 3469–3479.

Rouault, M., Penven, P., and Pohl, B. (2009). "Warming in the Agulhas Current system since the 1980's". In: *Geophysical Research Letters* 36.12.

Roullet, G. and Madec, G. (2000). "Salt conservation, free surface, and varying levels: A new formulation for ocean general circulation models". In: *Journal of Geophysical Research: Oceans* 105.C10, pp. 23927–23942. ISSN: 2156-2202. DOI: 10.1029/2000JC900089.

Rudels, B. and Quadfasel, D. (1991). "Convection and deep water formation in the Arctic Ocean-Greenland Sea system". In: *Journal of Marine Systems* 2.3-4, pp. 435–450.

Rye, C. D., Garabato, A. C. N., Holland, P., Meredith, M., Nurser, A. G., Coward, A. C., and Webb, D. J. (Mar. 2014). "Evidence of increased glacial melt in Antarctic coastal sea level rise". In: *Nature*.

Salvatier, J., Wiecki, T. V., and Fonnesbeck, C. (2016). "Probabilistic programming in Python using PyMC3". In: *PeerJ Computer Science* 2, e55.

Sasgen, I., Wouters, B., Gardner, A. S., King, M. D., Tedesco, M., Landerer, F. W., Dahle, C., Save, H., and Fettweis, X. (2020). "Return to rapid ice loss in Greenland and record loss in 2019 detected by the GRACE-FO satellites". In: *Communications Earth & Environment* 1.1, pp. 1–8.

Sawyer, J. S. (1972). "Man-made carbon dioxide and the "greenhouse" effect". In: *Nature* 239.5366, pp. 23–26.

Scambos, T. A., Bohlander, J. A., Shuman, C. A., and Skvarca, P. (2004). "Glacier acceleration and thinning after ice shelf collapse in the Larsen B embayment, Antarc-

tica". In: *Geophysical Research Letters* 31.18. ISSN: 1944-8007. DOI: 10.1029/2004GL020670.

Scheffer, M. and Van Nes, E. H. (2007). "Shallow lakes theory revisited: various alternative regimes driven by climate, nutrients, depth and lake size". In: *Shallow lakes in a changing world*. Springer, pp. 455–466.

Schiller, A., Mikolajewicz, U., and Voss, R. (1997). "The stability of the North Atlantic thermohaline circulation in a coupled ocean-atmosphere general circulation model". In: *Climate Dynamics* 13.5, pp. 325–347.

Schmidt, G. A. et al. (2014). "Configuration and assessment of the GISS ModelE2 contributions to the CMIP5 archive". In: *Journal of Advances in Modeling Earth Systems* 6.1, pp. 141–184.

Scholz, C. A. et al. (2007). "East African megadroughts between 135 and 75 thousand years ago and bearing on early-modern human origins". In: *Proceedings of the National Academy of Sciences* 104.42, pp. 16416–16421.

Seidov, D., Haupt, B. J., Barron, E. J., and Maslin, M. (2001). "Ocean Bi-Polar Seesaw and Climate: Southern Versus Northern Meltwater Impacts". In: *The oceans and rapid climate change: Past, present, and future, Geophys. Monogr. Ser., vol. 126, edited by D. Seidov, B. J. Haput, and M. Maslin*, pp. 147–167.

Sgubin, G., Swingedouw, D., Drijfhout, S., Hagemann, S., and Robertson, E. (Nov. 2014). "Multimodel analysis on the response of the AMOC under an increase of radiative forcing and its symmetrical reversal". In: *Climate Dynamics*. DOI: 10.1007/s00382-014-2391-2.

Sgubin, G., Swingedouw, D., Drijfhout, S., Mary, Y., and Bennabi., A. (2017). "Abrupt cooling over the North Atlantic in modern climate models". In: *Nature Communications* 8. DOI: 10.1038/ncomms14375.

Shepherd, A. and Wingham, D. (2007). "Recent Sea-Level Contributions of the Antarctic and Greenland Ice Sheets". In: *Science* 315.5818, pp. 1529–1532. DOI: 10.1126/science.1136776.

Shepherd, A. et al. (2012). "A Reconciled Estimate of Ice-Sheet Mass Balance". In: *Science* 338.6111, pp. 1183–1189. DOI: 10.1126/science.1228102.

Shepherd, A. et al. (2019). "Trends in Antarctic Ice Sheet elevation and mass". In: *Geophysical Research Letters* 46.14, pp. 8174–8183.

Sijp, W. P. and England, M. H. (2008). "The effect of a northward shift in the southern hemisphere westerlies on the global ocean". In: *Progress in Oceanography* 79.1, pp. 1–19.

Sijp, W. P., Gregory, J. M., Tailleux, R., and Spence, P. (2012). "The key role of the western boundary in linking the AMOC strength to the North-South pressure gradient". In: *Journal of Physical Oceanography* 42.4, pp. 628–643.

Smeed, D. et al. (2018). "The North Atlantic Ocean is in a state of reduced overturning". In: *Geophysical Research Letters* 45.3, pp. 1527–1533.

Sørensen, L. S., Simonsen, S. B., Forsberg, R., Khvorostovsky, K., Meister, R., and Engdahl, M. E. (2018). "25 years of elevation changes of the Greenland Ice Sheet from

ERS, Envisat, and CryoSat-2 radar altimetry". In: *Earth and Planetary Science Letters* 495, pp. 234–241.

Spall, M. A. (Dec. 2008). "Buoyancy-Forced Downwelling in Boundary Currents". In: *Journal of Physical Oceanography* 38.12, pp. 2704–2721. ISSN: 0022-3670. DOI: 10.1175/2008JPO3993.1.

Spall, M. A. and Pickart, R. S. (2001). "Where Does Dense Water Sink? A Subpolar Gyre Example". In: *Journal of Physical Oceanography* 31.3, pp. 810–826. DOI: 10.1175/1520-0485(2001)031<0810:WDDWSA>2.0.CO;2.

Speich, S., Blanke, B., and Cai, W. (2007). "Atlantic meridional overturning circulation and the Southern Hemisphere supergyre". In: *Geophysical Research Letters* 34.23.

Spence, P., Saenko, O. A., Sijp, W., and England, M. H. (Apr. 2013). "North Atlantic Climate Response to Lake Agassiz Drainage at Coarse and Ocean Eddy-Permitting Resolutions". In: *Journal of Climate* 26.8, pp. 2651–2667. ISSN: 0894-8755. DOI: 10.1175/JCLI-D-11-00683.1.

Staal, A., Dekker, S. C., Xu, C., and Van Nes, E. H. (2016). "Bistability, spatial interaction, and the distribution of tropical forests and savannas". In: *Ecosystems* 19.6, pp. 1080–1091.

Stammer, D., Agarwal, N., Herrmann, P., Köhl, A., and Mechoso, C. (2011). "Response of a Coupled Ocean–Atmosphere Model to Greenland Ice Melting". In: *Surveys in geophysics*, pp. 1–22.

Stammer, D. (2008). "Response of the global ocean to Greenland and Antarctic ice melting". In: *Journal of Geophysical Research: Oceans* 113.C6. ISSN: 2156-2202. DOI: 10.1029/2006JC004079.

Starr, A. et al. (2021). "Antarctic icebergs reorganize ocean circulation during Pleistocene glacials". In: *Nature* 589.1, pp. 236–241. DOI: 10.1038/s41586-020-03094-7.

Sterl, A. et al. (2012). "A look at the ocean in the EC-Earth climate model". In: *Climate Dynamics* 39.11, pp. 2631–2657.

Stewart, R. H. (2008). *Introduction to physical oceanography*. Robert H. Stewart.

Stocker, T. (2011). *Introduction to climate modelling*. Springer Science & Business Media.

Stocker, T. F. and Johnsen, S. J. (2003). "A minimum thermodynamic model for the bipolar seesaw". In: *Paleoceanography* 18.4. 1087. ISSN: 1944-9186.

Stommel, H. (1961). "Thermohaline convection with two stable regimes of flow". In: *Tellus* 13, p. 224.

Stouffer, R. and Manabe, S. (2003). "Equilibrium response of thermohaline circulation to large changes in atmospheric CO2 concentration". In: *Climate Dynamics* 20.7-8, pp. 759–773.

Stouffer, R. J. et al. (2006). "Investigating the causes of the response of the thermohaline circulation to past and future climate changes". In: *Journal of Climate* 19.8, pp. 1365–1387.

Stouffer, R. J., Seidov, D., and Haupt, B. J. (2007). "Climate Response to External Sources of Freshwater: North Atlantic versus the Southern Ocean". In: *Journal of Climate* 20.3, pp. 436–448. DOI: 10.1175/JCLI4015.1.

Swart, N. and Fyfe, J. C. (2012). "Observed and simulated changes in the Southern Hemisphere surface westerly wind-stress". In: *Geophysical Research Letters* 39.16.

Swingedouw, D., Rodehacke, C. B., Behrens, E., Menary, M., Olsen, S. M., Gao, Y., Mikolajewicz, U., Mignot, J., and Biastoch, A. (Aug. 2013a). "Decadal fingerprints of freshwater discharge around Greenland in a multi-model ensemble". In: *Climate Dynamics* 41, pp. 695–720. DOI: 10.1007/s00382-012-1479-9.

Swingedouw, D., Fichefet, T., Goosse, H., and Loutre, M.-F. (2009). "Impact of transient freshwater releases in the Southern Ocean on the AMOC and climate". In: *Climate dynamics* 33.2-3, pp. 365–381.

Swingedouw, D., Rodehacke, C. B., Behrens, E., Menary, M., Olsen, S. M., Gao, Y., Mikolajewicz, U., Mignot, J., and Biastoch, A. (2013b). "Decadal fingerprints of freshwater discharge around Greenland in a multi-model ensemble". In: *Climate dynamics* 41.3-4, pp. 695–720.

Swingedouw, D., Rodehacke, C. B., Olsen, S. M., Menary, M., Gao, Y., Mikolajewicz, U., and Mignot, J. (2015). "On the reduced sensitivity of the Atlantic overturning to Greenland ice sheet melting in projections: a multi-model assessment". In: *Climate dynamics* 44.11-12, pp. 3261–3279.

Talley, L. D. (2008). "Freshwater transport estimates and the global overturning circulation: Shallow, deep and throughflow components". In: *Progress in Oceanography* 78.4, pp. 257–303.

— (2011). *Descriptive physical oceanography: an introduction*. 6th ed. Academic press.

Tans, P. and Keeling, R. (Mar. 2021). *Global Monitoring Laboratory - Carbon Cycle Greenhouse Gases*. URL: https://www.esrl.noaa.gov/gmd/ccgg/trends/data.html.

Taylor, K. E., Stouffer, R. J., and Meehl, G. A. (Apr. 2012). "An Overview of CMIP5 and the Experiment Design". In: *Bulletin of the American Meteorological Society* 93.4, pp. 485–498. ISSN: 0003-0007. DOI: 10.1175/BAMS-D-11-00094.1.

Terray, L. (2012). "Evidence for multiple drivers of North Atlantic multi-decadal climate variability". In: *Geophysical research letters* 39.19.

Thomas, R., Frederick, E., Krabill, W., Manizade, S., and Martin, C. (May 2006). "Progressive increase in ice loss from Greenland". In: *Geophysical Research Letters* 33.10, pp. L10503+. ISSN: 0094-8276. DOI: 10.1029/2006GL026075.

— (2009). "Recent changes on Greenland outlet glaciers". In: *Journal of Glaciology* 55.189, pp. 147–162.

Thorpe, R. B., Gregory, J. M., Johns, T. C., Wood, R. A., and Mitchell, J. F. B. (2001). "Mechanisms Determining the Atlantic Thermohaline Circulation Response to Greenhouse Gas Forcing in a Non-Flux-Adjusted Coupled Climate Model". In: *Journal of Climate* 14.14, pp. 3102–3116. DOI: 10.1175/1520-0442(2001)014<3102:MDTATC>2.0.CO;2.

Timmermans, M.-L., Toole, J., and Krishfield, R. (2018). "Warming of the interior Arctic Ocean linked to sea ice losses at the basin margins". In: *Science Advances* 4.8. DOI: 10.1126/sciadv.aat6773.

Treguier, A.-M., Deshayes, J., Lique, C., Dussin, R., and Molines, J.-M. (2012). "Eddy contributions to the meridional transport of salt in the North Atlantic". In: *Journal of Geophysical Research: Oceans* 117.C5, pp. 18–26.

Valcke, S., Caubel, A., Vogelsang, R., and Declat, D. (2004). *OASIS 3 User's Guide*. Technical Report TR/CMGC/04/68. Toulouse, France: CERFACS.

Valdes, P. (2011). "Built for stability". In: *Nature Geoscience* 4.7, pp. 414–416.

Valdivieso, M., Haines, K., Zuo, H., and Lea, D. (2014). "Freshwater and heat transports from global ocean synthesis". In: *Journal of Geophysical Research: Oceans* 119.1, pp. 394–409.

Vallis, G. K. (2019). *Essentials of atmospheric and oceanic dynamics*. Cambridge University Press.

Van den Berk, J. and Drijfhout, S. (2014). "A realistic freshwater forcing protocol for ocean-coupled climate models". In: *Ocean Modelling* 81.0, pp. 36–48. ISSN: 1463-5003. DOI: 10.1016/j.ocemod.2014.07.003.

Van den Berk, J., Drijfhout, S., and Hazeleger, W. (2019). "Atlantic salinity budget in response to Northern and Southern Hemisphere ice sheet discharge". In: *Climate Dynamics* 52.9-10, pp. 5249–5267.

— (2021a). "Characterisation of Atlantic meridional overturning hysteresis using Langevin dynamics". In: *Earth System Dynamics* 12.1, pp. 69–81.

— (2021b). "Circulation adjustment in the Arctic and Atlantic in response to Greenland and Antarctic mass loss". In: *Climate Dynamics* 57.7, pp. 1689–1707. DOI: 10.1007/s00382-021-05755-3.

Van den Broeke, M. R., Bamber, J., Lenaerts, J., and Rignot, E. (Sept. 2011). "Ice Sheets and Sea Level: Thinking Outside the Box". In: *Surveys in Geophysics* 32.4-5, pp. 495–505.

Van den Hurk, B. et al. (2007). "New climate change scenarios for the Netherlands". In: *Water science and technology* 56.4, pp. 27–33.

Van der Linden, E., Le Bars, D., Bintanja, R., and Hazeleger, W. (Oct. 2019). "Oceanic heat transport into the Arctic under high and low CO2 forcing". In: *Climate dynamics* 53.7-8, pp. 4763–4780. DOI: 10.1007/s00382-019-04824-y.

Vellinga, M. and Wood, R. A. (Aug. 2002). "Global Climatic Impacts of a Collapse of the Atlantic Thermohaline Circulation". In: *Climatic Change* 54.3, pp. 251–267. ISSN: 1573-1480. DOI: 10.1023/A:1016168827653.

Vizcaino, M. (2014). "Ice sheets as interactive components of Earth System Models: progress and challenges". In: *Wiley Interdisciplinary Reviews: Climate Change* 5.4, pp. 557–568. ISSN: 1757-7799. DOI: 10.1002/wcc.285.

Von Schuckmann, K. et al. (2020). "Heat stored in the Earth system: where does the energy go?" In: *Earth System Science Data* 12.3, pp. 2013–2041. DOI: 10.5194/essd-12-2013-2020.

Wang, C. and Beckmann, A. (2007). "Investigation of the impact of Antarctic ice-shelf melting in a global ice-ocean model (ORCA2-LIM)". In: *Annals of Glaciology* 46.1, pp. 78–82. DOI: 10.3189/172756407782871602.

Wary, M., Eynaud, F., Swingedouw, D., Masson-Delmotte, V., Matthiessen, J., Kissel, C., Zumaque, J., Rossignol, L., and Jouzel, J. (2017). "Regional seesaw between the North Atlantic and Nordic Seas during the last glacial abrupt climate events". In: *Climate of the Past* 13.6, pp. 729–739.

Weaver, A. J. et al. (2001). "The UVic Earth System Climate Model: Model description, climatology, and applications to past, present and future climates". In: *Atmosphere-Ocean* 39.4, pp. 361–428.

Weaver, A. J. et al. (2012). "Stability of the Atlantic meridional overturning circulation: A model intercomparison". In: *Geophysical Research Letters* 39.20. ISSN: 1944-8007. DOI: 10.1029/2012GL053763.

Weber, S. L. and Drijfhout, S. S. (2007). "Stability of the Atlantic Meridional Overturning Circulation in the Last Glacial Maximum climate". In: *Geophysical Research Letters* 34.22. ISSN: 1944-8007. DOI: 10.1029/2007GL031437.

Weijer, W., Maltrud, M. E., Hecht, M. W., Dijkstra, H. A., and Kliphuis, M. A. (2012). "Response of the Atlantic Ocean circulation to Greenland Ice Sheet melting in a strongly-eddying ocean model". In: *Geophysical Research Letters* 39.9. ISSN: 1944-8007. DOI: 10.1029/2012GL051611.

Weijer, W., Cheng, W., Garuba, O. A., Hu, A., and Nadiga, B. (2020). "CMIP6 models predict significant 21st century decline of the Atlantic Meridional Overturning Circulation". In: *Geophysical Research Letters* 47.12, e2019GL086075.

Weijer, W., De Ruijter, W. P., and Dijkstra, H. A. (2001). "Stability of the Atlantic overturning circulation: Competition between Bering Strait freshwater flux and Agulhas heat and salt sources". In: *Journal of Physical Oceanography* 31.8, pp. 2385–2402.

Weijer, W., De Ruijter, W. P., Sterl, A., and Drijfhout, S. S. (2002). "Response of the Atlantic overturning circulation to South Atlantic sources of buoyancy". In: *Global and Planetary Change* 34.3-4, pp. 293–311.

Weijer, W. et al. (2019). "Stability of the Atlantic Meridional Overturning Circulation: A review and synthesis". In: *Journal of Geophysical Research: Oceans* 124.8, pp. 5336–5375.

Wood, R. A., Keen, A. B., Mitchell, J. F., and Gregory, J. M. (1999). "Changing spatial structure of the thermohaline circulation in response to atmospheric $CO_2$ forcing in a climate model". In: *Nature* 399.6736, pp. 572–575.

Woodgate, R. A., Aagaard, K., and Weingartner, T. J. (2006). "Interannual changes in the Bering Strait fluxes of volume, heat and freshwater between 1991 and 2004". In: *Geophysical Research Letters* 33.15. ISSN: 1944-8007. DOI: 10.1029/2006GL026931.

Wouters, B., Drijfhout, S., and Hazeleger, W. (2012). "Interdecadal North-Atlantic meridional overturning circulation variability in EC-EARTH". In: *Climate dynamics* 39.11, pp. 2695–2712.

Yang, Q., Dixon, T. H., Myers, P. G., Bonin, J., Chambers, D., Van den Broeke, M., Ribergaard, M. H., and Mortensen, J. (2016). "Recent increases in Arctic freshwater flux affects Labrador Sea convection and Atlantic overturning circulation". In: *Nature communications* 7.1, pp. 1–8.

Yashayaev, I. and Loder, J. W. (2017). "Further intensification of deep convection in the Labrador Sea in 2016". In: *Geophysical Research Letters* 44.3, pp. 1429–1438.

Yin, J. and Stouffer, R. J. (2007). "Comparison of the Stability of the Atlantic Thermohaline Circulation in Two Coupled Atmosphere–Ocean General Circulation Models". In: *Journal of Climate* 20.17, pp. 4293–4315. DOI: 10.1175/JCLI4256.1.

Zachos, J. C., Dickens, G. R., and Zeebe, R. E. (2008). "An early Cenozoic perspective on greenhouse warming and carbon-cycle dynamics". In: *Nature* 451.7176, pp. 279–283.

Zhang, R. and Delworth, T. L. (2005). "Simulated tropical response to a substantial weakening of the Atlantic thermohaline circulation". In: *Journal of Climate* 18.12, pp. 1853–1860.

Zhang, R., Delworth, T. L., Rosati, A., Anderson, W. G., Dixon, K. W., Lee, H.-C., and Zeng, F. (2011). "Sensitivity of the North Atlantic Ocean Circulation to an abrupt change in the Nordic Sea overflow in a high resolution global coupled climate model". In: *Journal of Geophysical Research: Oceans* 116.C12. C12024. ISSN: 2156-2202. DOI: 10.1029/2011JC007240.

Zhang, X., Knorr, G., Lohmann, G., and Barker, S. (2017). "Abrupt North Atlantic circulation changes in response to gradual CO 2 forcing in a glacial climate state". In: *Nature Geoscience* 10.7, pp. 518–523.

# Index